Development of Balanced Mixture Design Index Parameters and the Flex Suite of Performance Analysis Tools for Asphalt Pavements—Volume I

PUBLICATION NO. FHWA-HRT-24-112

JUNE 2024

U.S. Department of Transportation
Federal Highway Administration

Research, Development, and Technology
Turner-Fairbank Highway Research Center
6300 Georgetown Pike
McLean, VA 22101-2296

FOREWORD

Highway agencies need to construct durable, long-lasting pavements that maximize highway investments and satisfy user expectations. These needs drive highway owners to investigate and improve the way they test and evaluate pavement materials. Owner agencies want to move beyond the traditional quality assurance specification focus on the as-constructed product quality toward specifications that evaluate long-term durability and performance across the asset's life. This report describes Federal Highway Administration research efforts to develop mechanistic-based performance testing and analysis tools for the purpose of understanding fundamental pavement performance and easing deployment of performance tests and associated analysis and evaluation tools to understand long-term performance. The research team developed two performance test indexes to support balanced mixture design concepts and provide agencies information and tools to evaluate their mixtures and pavements: S_{app}, the cyclic fatigue index parameter, for cracking, and the Rutting Strain Index for rutting. This report presents a framework for the asphalt mixture performance tester-based performance tests and indexes for balanced mix design. The Maine Department of Transportation, Missouri Department of Transportation, and Western Federal Land Highway Division also conducted three shadow projects. Three Microsoft® Excel®-based analysis tools were developed to aid equipment data transfer and the analysis of the test results, indexes, and pavement structure.

Jean A. Nehme, Ph.D., P.E.
Director, Office of Infrastructure
Research and Development

Notice

This document is disseminated under the sponsorship of the U.S. Department of Transportation in the interest of information exchange. The U.S. Government assumes no liability for the use of the information contained in this document.

Non-Binding Contents

Except for the statutes and regulations cited, the contents of this document do not have the force and effect of law and are not meant to bind the States or the public in any way. This document is intended only to provide information regarding existing requirements under the law or agency policies.

Quality Assurance Statement

The Federal Highway Administration (FHWA) provides high-quality information to serve Government, industry, and the public in a manner that promotes public understanding. Standards and policies are used to ensure and maximize the quality, objectivity, utility, and integrity of its information. FHWA periodically reviews quality issues and adjusts its programs and processes to ensure continuous quality improvement.

Disclaimer for Product Names and Manufacturers

The U.S. Government does not endorse products or manufacturers. Trademarks or manufacturers' names appear in this document only because they are considered essential to the objective of the document. They are included for informational purposes only and are not intended to reflect a preference, approval, or endorsement of any one product or entity.

TECHNICAL REPORT DOCUMENTATION PAGE

1. Report No. FHWA-HRT-24-112	2. Government Accession No.	3. Recipient's Catalog No.
4. Title and Subtitle Development of Balanced Mixture Design Index Parameters and the Flex Suite of Performance Analysis Tools for Asphalt Pavements—Volume I		5. Report Date June 2024 6. Performing Organization Code:
7. Author(s) Y. Richard Kim (0000-0003-3295-977X), B. Shane Underwood (0000-0002-7223-3968), Murthy N. Guddati (0000-0002-4134-3435), Amir Ghanbari (0000-0003-3828-8065), Behrooz Keshavarzi, Yizhuang David Wang (0000-0002-5149-9898), Jaehoon Jeong (0000-0001-8692-4965), Douglas Mocelin (0000-0002-7670-6136), Felipe Do Canto Pivetta, and Nooralhuda F. Saleh (0000-0003-2847-4999)		8. Performing Organization Report No.
9. Performing Organization Name and Address North Carolina State University Department of Civil, Construction, and Environmental Engineering Campus Box 7908 Raleigh, NC 27695		10. Work Unit No. 11. Contract or Grant No. DTFH61-13-C-00025
12. Sponsoring Agency Name and Address Office of Infrastructure Research and Development Federal Highway Administration 6300 Georgetown Pike McLean, VA 22101-2296		13. Type of Report and Period Covered Final Report; September 2013–August 2021 14. Sponsoring Agency Code HRDI-20
15. Supplementary Notes The contracting officer's representative was Matthew Corrigan (HRDI-20; ORCID: 0000-0002-1230-8462).		

16. Abstract

This report documents research to advance mechanistic models, performance analysis and evaluation, and design methodologies to aid agency efforts to understand asphalt pavement performance. The research team developed FlexMAT™ version 2.1 and FlexPAVE™ version 2.0 as the material-level and pavement-level analysis tools, respectively. FlexPAVE 2.0 includes the simplified viscoelastic continuum damage model for fatigue and thermal cracking, the permanent strain shift model for rutting, and the NCHRP 09-54 aging models. FlexMAT 2.1 develops the input material properties for FlexPAVE 2.0 seamlessly. S_{app} and the Rutting Strain Index are the cracking and rutting indexes, respectively, which aid balanced mix design (BMD) and improve performance analysis. These two indexes' threshold values are a function of traffic level, using more than 100 different asphalt mixtures. The team used the four corners concept to develop performance-volumetrics and index-volumetrics relationships to use as the foundation for BMD methods. The team employed Bayesian inference-based Markov Chain Monte Carlo technique uncertainty analysis to develop a reliability framework for distress predictions using FlexPAVE 2.0 and also developed PASSFlex™ to support the steps of a performance evaluation on a project. One of the performance protocols the TFRS-01 project recommended was implemented into PASSFlex. The research team performed three shadow projects in concert with the Western Federal Lands Highway Division, Maine Department of Transportation, and Missouri Department of Transportation to introduce the asphalt mixture performance tester suite of performance tests and performance models. This volume is the first in a series. The other volume in the series is FHWA-HRT-24-111: *Development of Balanced Mixture Design Index Parameters and the Flex Suite of Performance Analysis Tools for Asphalt Pavements—Volume II.*

17. Key Words	18. Distribution Statement
FlexMAT, FlexPAVE, PASSFlex, thermal cracking, S-VECD, shift model, S_{app}, RSI, PVR, IVR, balanced mix design, shadow project, reliability, performance specification, PRS	No restrictions. This document is available to the public through the National Technical Information Service. Springfield, VA 22161. https://www.ntis.gov

19. Security Classif. (of this report)	20. Security Classif. (of this page)	21. No. of Pages	22. Price
Unclassified	Unclassified	270	N/A

Form DOT F 1700.7 (8-72) Reproduction of completed page authorized

SI* (MODERN METRIC) CONVERSION FACTORS

APPROXIMATE CONVERSIONS TO SI UNITS

Symbol	When You Know	Multiply By	To Find	Symbol
		LENGTH		
in	inches	25.4	millimeters	mm
ft	feet	0.305	meters	m
yd	yards	0.914	meters	m
mi	miles	1.61	kilometers	km
		AREA		
in^2	square inches	645.2	square millimeters	mm^2
ft^2	square feet	0.093	square meters	m^2
yd^2	square yard	0.836	square meters	m^2
ac	acres	0.405	hectares	ha
mi^2	square miles	2.59	square kilometers	km^2
		VOLUME		
fl oz	fluid ounces	29.57	milliliters	mL
gal	gallons	3.785	liters	L
ft^3	cubic feet	0.028	cubic meters	m^3
yd^3	cubic yards	0.765	cubic meters	m^3
	NOTE: volumes greater than 1,000 L shall be shown in m^3			
		MASS		
oz	ounces	28.35	grams	g
lb	pounds	0.454	kilograms	kg
T	short tons (2,000 lb)	0.907	megagrams (or "metric ton")	Mg (or "t")
		TEMPERATURE (exact degrees)		
°F	Fahrenheit	5 (F-32)/9 or (F-32)/1.8	Celsius	°C
		ILLUMINATION		
fc	foot-candles	10.76	lux	lx
fl	foot-Lamberts	3.426	$candela/m^2$	cd/m^2
		FORCE and PRESSURE or STRESS		
lbf	poundforce	4.45	newtons	N
lbf/in^2	poundforce per square inch	6.89	kilopascals	kPa

APPROXIMATE CONVERSIONS FROM SI UNITS

Symbol	When You Know	Multiply By	To Find	Symbol
		LENGTH		
mm	millimeters	0.039	inches	in
m	meters	3.28	feet	ft
m	meters	1.09	yards	yd
km	kilometers	0.621	miles	mi
		AREA		
mm^2	square millimeters	0.0016	square inches	in^2
m^2	square meters	10.764	square feet	ft^2
m^2	square meters	1.195	square yards	yd^2
ha	hectares	2.47	acres	ac
km^2	square kilometers	0.386	square miles	mi^2
		VOLUME		
mL	milliliters	0.034	fluid ounces	fl oz
L	liters	0.264	gallons	gal
m^3	cubic meters	35.314	cubic feet	ft^3
m^3	cubic meters	1.307	cubic yards	yd^3
		MASS		
g	grams	0.035	ounces	oz
kg	kilograms	2.202	pounds	lb
Mg (or "t")	megagrams (or "metric ton")	1.103	short tons (2,000 lb)	T
		TEMPERATURE (exact degrees)		
°C	Celsius	1.8C+32	Fahrenheit	°F
		ILLUMINATION		
lx	lux	0.0929	foot-candles	fc
cd/m^2	candela/m2	0.2919	foot-Lamberts	fl
		FORCE and PRESSURE or STRESS		
N	newtons	2.225	poundforce	lbf
kPa	kilopascals	0.145	poundforce per square inch	lbf/in^2

*SI is the symbol for International System of Units. Appropriate rounding should be made to comply with Section 4 of ASTM E380. (Revised March 2003)

TABLE OF CONTENTS

LIST OF FIGURES

LIST OF TABLES

LIST OF ABBREVIATIONS

AASHTO	American Association of State Highway and Transportation Officials
ABC	aggregate base course
ABR	asphalt binder replacement
AC	asphalt content
ALF	Accelerated Load Facility
AMAC	asphalt mixture aging-cracking
AMPT	asphalt mixture performance tester
ANOVA	analysis of variance
APA	asphalt pavement analyzer
AQC	acceptance quality characteristics
ATCA	asphalt thermal cracking analyzer
AV	air void
BMD	balanced mix design
CALUW	coarse aggregate loose unit weight
COV	coefficient of variance
CR-TB	crumb rubber-terminal blend
CTC	coefficient of thermal contraction
CTE	coefficient of thermal expansion
CUW	chosen unit weight
CZM	cohesive zone model
DCT	disc-shaped compact tension
DF	damage factor
DMR	dynamic modulus ratio
DPSE	dissipated pseudostrain energy
EICM	Enhanced Integrated Climatic Model
ESAL	equivalent single-axle load
FFE	Fourier finite element
FHWA	Federal Highway Administration
GUI	graphical user interface
HMA	hot-mix asphalt
HPG	high performance grade
HWT	Hamburg wheel-tracking
iRLPD	incremental repeated load permanent deformation
IVR	index-volumetrics relationship
KEC	Korea Expressway Corporation
K-S	Kolmogorov-Smirnov test
LOE	line of equality
LTA	long-term aged
LTPP	Long-Term Pavement Performance program
LVDT	linear variable differential transformer
LWP	left wheel path
MaineDOT	Maine Department of Transportation
MCMC	Markov Chain Monte Carlo
MEPDG	*Mechanistic-Empirical Pavement Design Guide*

MERRA-2	Modern-Era Retrospective Analysis for Research and Applications, Version 2
MESAL	million equivalent single-axle load
MIT	Manitoba Infrastructure and Transportation
MnROAD	Minnesota's Cold Weather Pavement Testing Facility
NCAT	National Center for Asphalt Technology
NCDOT	North Carolina Department of Transportation
NCHRP	National Cooperative Highway Research Program
NCSU	North Carolina State University
NMAS	nominal maximum aggregate size
OGFC	open-graded friction course
PAM	pavement aging model
PAV	pressure aging vessel
PEMD	performance-engineered mix design
PG	performance grade
PID	proportional integral derivative
PLD	predicted life difference
PMA	polymer-modified asphalt
PPO	predictive BMD performance optimum
PRS	performance-related specifications
PVR	performance-volumetrics relationship
QA	quality assurance
RAP	reclaimed asphalt pavement
RAS	reclaimed asphalt shingle
RSI	Rutting Strain Index
RTFO	rolling thin film oven
RWP	right wheel path
SBS	styrene butadiene styrene
Section 508	Section 508 of the Rehabilitation Act of 1973
SHRP	Strategic Highway Research Program
SMA	stone matrix asphalt
SSR	stress sweep rutting (test method)
STA	short-term aged
S-VECD	simplified viscoelastic continuum damage
SVO	Superpave volumetric optimum
TCAP	thermal cracking analysis package
TRLPD	triaxial repeated load permanent deformation
TSRST	thermal stress restrained specimen test
TSS	triaxial stress sweep
t–TS	time–temperature superposition
VECD	viscoelastic continuum damage
VFA	voids filled with asphalt
VMA	voids in mineral aggregate
WMA	warm-mix asphalt
2S2P1D	two springs, two parabolic elements, one dashpot

EXECUTIVE SUMMARY

Over the past few decades, the research team developed advanced models for asphalt concrete under complex loading conditions, to achieve accurate pavement performance evaluations and predictions. These material models can accurately capture various critical phenomena, such as microcrack-induced damage (critical for fatigue modeling), strain-rate temperature interdependence, permanent deformation behavior (critical for high-temperature modeling), and damage reduction during rest periods between loads. The resultant mechanistic models can evaluate fatigue cracking, permanent deformation (rutting), and healing and are referred to as the simplified viscoelastic continuum damage (S-VECD) model, the shift model, and the healing model, respectively.[1,2,3] A suite of test methods accompanies these mechanistic models. These test methods are designed for use by an asphalt mixture performance tester (AMPT) and have been adopted by the American Association of State Highway and Transportation Officials (AASHTO) as standards.[4]

The research efforts presented in this report were designed to advance the deployment of the Federal Highway Administration's performance testing and evaluation of asphalt pavements. These efforts can be categorized as follows:

- Development of a thermal cracking model.
- Development of the S_{app} index and the Rutting Strain Index (RSI) as the cracking and rutting indexes, respectively.
- Development of FlexMAT™ version 2.1.[5]
- Development of FlexPAVE™ version 2.0.[6]
- Development of performance-volumetrics relationships (PVRs) and index-volumetrics relationships (IVRs).
- Development of AMPT balanced mix design (BMD) methods.
- Reliability analysis of cracking damage and rut depth predictions.
- Development of PASSFlex™.[7]
- Demonstration of field shadow projects.

This Executive Summary provides a brief overview of each of these efforts.

THERMAL CRACKING MODEL

Researchers conducting this study developed a thermal cracking analysis framework, FlexTC, that employs the S-VECD model to characterize asphalt mixture behavior at low temperatures.[8] FlexTC's use of the S-VECD model allows the prediction of both fatigue cracking (top-down and bottom-up cracking) and thermal cracking using a single set of test methods.

One of the important material properties for thermal cracking prediction is the coefficient of thermal contraction (CTC). FlexTC uses three levels to determine the CTC of an asphalt mixture. Level 1 assumes direct measurements of the mixture's CTC using ZERODUR®.[9,10] Level 2 estimates the CTC of the mixture using the voids in mineral aggregate (VMA) of the mixture, aggregate bulk specific gravity, the CTC of the mineral aggregate in the mixture, and the CTC of the binder. Level 3 uses a similar approach to level 2, but instead of using the measured binder CTCs as inputs, level 3 estimates the CTCs using the low-temperature performance grade (PG) of the binder.

The algorithm that FlexTC uses to determine the crack depth in a pavement subjected to thermal fluctuations models the asphalt layer as a layer composed of sublayers of uniaxial rods with fixed ends.[8] The boundary condition for each uniaxial rod is the same as the boundary condition used in the thermal stress restrained specimen test (TSRST). Therefore, research efforts focused on developing a methodology to predict the fracture of asphalt concrete specimens in the TSRST. These efforts resulted in the development of a dissipated pseudostrain energy (DPSE)-based failure criterion. The DPSE failure criterion can be characterized using the AMPT dynamic modulus and cyclic fatigue tests, which also serve as the characterization tests for fatigue cracking (both bottom-up and top-down cracking).

The research team verified the developed FlexTC framework using the material properties and field performance of eight cells from Minnesota's Cold Weather Pavement Testing Facility (MnROAD).[8,11] The MnROAD cells (and corresponding mixtures) are designed to evaluate various mix design factors for reclaimed asphalt pavement (RAP) and reclaimed asphalt shingle mixtures. Therefore, the eight MnROAD cells this study used were paired based on the target mix factor. A comparison of the predicted and observed thermal cracking performance of two paired cells resulted in reasonably good agreement.

The research team has implemented the three different levels for CTC determination and the verified FlexTC algorithm in FlexMAT version 2.1 and FlexPAVE version 2.0, respectively. (See references 5, 6, 8, and 9.)

THE S_{app} INDEX AND THE RUTTING STRAIN INDEX

As the paving industry moves toward BMD, index parameters are receiving more attention from researchers and practitioners. With this phenomenon in mind, the research team developed S_{app} and RSI index parameters for cracking and rutting by simplifying the S-VECD model and permanent strain shift model, respectively.

S_{app} accounts for the effects of a mixture's modulus and toughness on the mixture's fatigue resistance and is a measure of the amount of fatigue damage the mixture can tolerate under loading. Higher S_{app} values indicate better fatigue resistance. The S_{app} value is determined at the average temperature of the high and low PGs, as given in LTPPBind Online at the location for the project of interest: −3 °C.[12] S_{app} threshold values were determined for different traffic levels using 105 mixtures that include hot mix asphalt (HMA) mixtures with varying percentages of RAP, warm mix asphalt (WMA) mixtures with different technologies, and polymer-modified asphalt (PMA) mixtures. These threshold values apply to surface, intermediate, and base course mixtures. The research team found the S_{app} value to be sensitive to mixture factors

(e.g., aggregate gradation, binder content, RAP content, binder grade, and type of binder modifier), compaction, and aging and meets general expectations with respect to the effects of these parameters on fatigue cracking performance.

The RSI is the average permanent strain (in percent) and is defined as the ratio of the permanent deformation in an asphalt layer to the thickness of that layer at the end of a 20-yr period over which 30 million 18-kip equivalent single-axle load repetitions are applied to a standard pavement structure. A mixture with lower RSI values has more rutting resistance than a mixture with higher RSI values.

Because permanent deformation in asphalt pavements is a function of temperature, stress level, and loading time, which all change with pavement depth, the research team used FlexPAVE to run an array of conditions to develop the stress and loading time profiles of standard pavement structures.[6] To calculate RSI values under realistic temperature profiles, the user selects a city (in a U.S. territory or State) closest to the project location in FlexMAT.[5] Then FlexMAT extracts the temperature profile across the entire depth of the pavement structure from a database created using Enhanced Integrated Climatic Model (EICM) simulations that include 20 yr (1996–2015) of air temperature data from the National Aeronautics and Space Administration Modern-Era Retrospective Analysis for Research and Applications, Version 2 (MERRA-2) dataset.[13,14] FlexMAT uses the shift model to calculate the permanent strain in each sublayer of asphalt (using the temperature and the precalculated stress and loading time for that sublayer) and produces the RSI value within a few seconds. RSI threshold values were determined using 79 mixtures that include the HMA mixtures with varying RAP contents and volumetric properties, WMA mixtures with different technologies, and PMA mixtures. The RSI value was found to decrease with a coarser gradation, lower asphalt binder content, higher RAP content, and higher compaction density (lower air void content).

FlexMAT calculates S_{app} and RSI values using AMPT test results.[5] The test results generated to determine the S_{app} and RSI values for a given mixture can be used in FlexPAVE for long-term pavement performance predictions.[6] This link is the main difference between the S_{app} and RSI parameters and other BMD indexes.

FLEXMAT VERSION 2.1

FlexMAT is designed to take output files from the AMPT and perform all the complex calculations required for the mechanistic material models.[5] During this project, the research team made various improvements to FlexMAT Cracking and FlexMAT Rutting version 1.1.[15,16] The version number for the resulting FlexMAT is version 2.1. The following list summarizes the improvements made and capabilities added to FlexMAT Cracking:

- Fitting the dynamic modulus data to the two springs, two parabolic elements, one dashpot (2S2P1D) model using generalized reduced gradient nonlinear fitting with a multistart configuration.

- Defining the failure of the cyclic fatigue test data as the maximum value of stress times the number of loading cycles.

- Including the three levels needed to determine the CTC.
- Including the three levels needed to determine the rheological aging index values for the National Cooperative Highway Research Program (NCHRP) 09-54 aging models.[17]
- Calculating the DPSE as a function of the reduced strain rate for the thermal cracking analysis.
- Including a bridge routine to import data from previous versions of FlexMAT.[5]
- Selecting a city for S_{app} determination.
- Including data quality indicators.
- Including U.S. customary units.
- Adding a dynamic modulus table that is compatible with AASHTOWare Pavement ME.[18]
- Ensuring Section 508 of the Rehabilitation Act of 1973 (Section 508) compliance.[19]

The following list summarizes the improvements made and capabilities added to FlexMAT Rutting:[16]

- Expanding the temperature database to 20 yr using 2,798 stations from MERRA-2.[14]
- Including U.S. customary units.
- Including a bridge routine to import data from previous versions of FlexMAT.[5]
- Ensuring Section 508 compliance.[19]

In addition to these improvements and added capabilities, the research team developed and implemented a universal input data structure in both FlexMAT programs, so FlexMAT can be used with any loading machine if the machine can generate test results according to the universal data structure.[5] Also, FlexMAT version 2.1 generates output files that can be used in FlexPAVE versions 1.1 and 2.0, thus allowing the use of the previous FlexPAVE version.[5,6,20]

The S_{app} and RSI values are calculated using FlexMAT, thus making FlexMAT an important element in index-based BMD and index-based performance-related specifications (PRS) protocols.[5]

PRELIMINARY TRANSFER FUNCTIONS FOR FLEXPAVE VERSION 1.1

The research team developed preliminary transfer functions for fatigue cracking and rut depth predictions using 39 pavement sections from 4 field projects: 5 sections from the National Center for Asphalt Technology (NCAT) test track in Alabama, United States (data are from the NCAT's 2009 research cycle); 14 sections from the 2016 MnROAD project in Minnesota, United States; 4 sections from the Manitoba Transportation and Infrastructure test road in Manitoba, Canada; and 16 sections from the Korean Expressway Corporation test road in Yeoju, South Korea. (See

references 11, 21, 22, and 23.) The research team used the suite of AMPT performance tests on all the original asphalt mixtures used in the construction of these pavement sections. The test results were analyzed by FlexMAT, and the performance of these pavement sections was analyzed using FlexPAVE version 1.1.[5,20] In general, the research team found reasonable agreement between the observed and predicted performance. This comparison resulted in preliminary transfer functions for fatigue cracking and rutting. This project refers to these transfer functions as preliminary because the amount of data used in the development of these functions was limited.

FLEXPAVE VERSION 2.0

The following list summarizes the significant improvements made to FlexPAVE version 1.1, which resulted in FlexPAVE version 2.0:[6,20]

- Implementing full finite element analysis instead of the layered analysis in FlexPAVE version 1.1.[20]
- Including the NCHRP 09-54 aging models.[17]
- Including the DPSE-based thermal cracking model.
- Including the seasonal effects of unbound materials.
- Including EICM with the MERRA-2 database.[13,14]
- Including a graphical user interface based on Microsoft® Excel®.[24]
- Ensuring Section 508 compliance.[19]

In summary, FlexPAVE version 2.0 allows the user to predict fatigue cracking, thermal cracking, and rutting with the effects of aging.[6] FlexPAVE version 2.0 uses the results from the same test methods to predict both fatigue cracking and thermal cracking. FlexPAVE's major strength is that FlexPAVE uses not only realistic loading and climatic conditions but also material characterization methods that are much simpler than other mechanistic-empirical asphalt pavement analysis methodologies.

PERFORMANCE-VOLUMETRICS RELATIONSHIP AND INDEX-VOLUMETRICS RELATIONSHIP

The paving community's move toward mechanistic-empirical pavement design, BMD, and PRS raises the importance of performance testing asphalt concrete more than ever. Mechanistic models typically require detailed material property information that can be time-consuming to measure. This time becomes even more critical considering how often the properties need to be measured for PRS, where construction variability must be evaluated on a lot-by-lot basis. To complete the full testing and analysis of each lot, the agency may spend several workdays on laboratory tests to determine the material properties. Owing to these challenges, state-of-the-practice technologies primarily utilize volumetric methods for asphalt mixture design and quality control and assurance specifications. These volumetric methods have a great advantage over those based on mechanistic properties, because the volumetric properties can be measured quickly, and the results can be used to make production adjustments if necessary. However, volumetric methods' disadvantage is that although volumetric-based methods are related to performance, the specific relationship to performance for a given mixture is unknown.

To address this issue for PRS, the research team developed the PVR and IVR. This development effort began with the finding that the volumetric properties measured at the design number of gyrations during quality assurance (QA) procedures and in-place density can be combined into two in-place volumetric properties, i.e., in-place VMA (VMA_{IP}) and in-place voids filled with asphalt (VFA) (VFA_{IP}). The research team also found a linear relationship between performance (cracking and rutting) and these two in-place volumetric properties. This relationship can be best established using the four corners approach. The four corners are the volumetric conditions located furthest apart from each other in the VMA_{IP} versus VFA_{IP} space but within the limit for mixture acceptance. The four corners approach is based on the finding that the performance of an asphalt mixture at any volumetric condition can be predicted if the performance of the mixture at the four corners is measured. This study used several mixtures, both laboratory-mixed and plant-produced, to characterize and verify the PVRs and IVRs.

The major benefits of PVR and IVR are as follows:

- PVR and IVR allow engineers to continue to use current test methods and equipment for QA purposes.
- PVR and IVR allow material characterization to be completed in a short period during the mixture design and QA processes.
- PVR and IVR bridge the gap between the volumetric properties and performance of asphalt mixtures and allow engineering judgment in mixture design and QA processes to be based on performance.

ASPHALT MIXTURE PERFORMANCE TESTER BALANCED MIX DESIGN

The successful development and verification of PVR and IVR allowed the research team to use those relationships in BMD. In addition, the ability of PVR and IVR to predict the performance of a mixture at various gradations, binder contents, and air void contents enabled the resultant BMD to optimize the mixture for both aggregate gradation and binder content for a given set of aggregate stockpiles and binder. In this project, the research team developed three tiers of BMD based on the AMPT suite of performance tests. Tiers 1 and 2 use the S_{app} and RSI parameters, whereas tier 3 uses the pavement life that FlexPAVE predicted.[6] In tier 1, the S_{app} and RSI values of the design mix are measured and compared against the threshold values for the given traffic to determine pass or fail. Tier 2 BMD is similar to the tier 3 predictive BMD. The main difference is that tier 2 uses the IVR concept, and all the tests and analyses are performed at a fixed design air void content (e.g., 4 percent), thus requiring the AMPT performance tests to be performed at two points rather than at four corners.

For purposes of tier 2 BMD, the IVR function is considered as the volumetric relationship for different gradations at the fixed design air void content (4 percent) at the design compaction level. For the general IVR function based on the four corners concept, three coefficients are considered as the fitting coefficients needed to calibrate the IVR. However, at the fixed design air void content, due to the intercorrelation of the VMA, VFA, and fixed design air void content, the IVR function can be calibrated using only two fitting coefficients.

The mixture characterization in tier 3 is the most demanding of the three tiers. Tier 3 uses PVRs characterized using the pavement life predicted from FlexPAVE at the four corners volumetric conditions.[6] That is, fatigue cracking and rutting PVRs are used to determine the optimal combination of aggregate gradation and asphalt content for a given set of aggregate stockpiles and binder. Although the required mixture characterization efforts in tier 3 BMD are much greater than those in tier 2, the data generated in tier 3 provide information about the changes in mixture performance that occur as the air void content changes. Therefore, the data generated for tier 3 BMD can be readily used for developing payment provisions in PRS.

In contrast to the design methodology employed for other BMD methods, tiers 2 and 3 of the AMPT-based BMD methods allow users to determine the optimal combination of aggregate gradation and asphalt content for a given set of aggregate and binder.

RELIABILITY ANALYSIS

Although mechanistic-based methods strive to systematically account for the physical properties and active mechanisms in a pavement, these methods are not perfect representations of the real system. As such, the mechanistic prediction of pavement performance is an inherently uncertain approach. The research team evaluated the known uncertainties as those uncertainties pertain to model characterization and the propagation of these uncertainties into long-term pavement performance simulations. Specifically, the research team used the Bayesian inference-based Markov Chain Monte Carlo (MCMC) method to investigate the ways that the uncertainties from the S-VECD and rutting shift model input parameters propagate to pavement performance simulation errors.[25] The goal was to estimate the reliability of the %Cracking and rut depth predictions in pavement simulations. For this purpose, the research team used mixtures of varying composition and behaviors (in both the mean and the uncertainty of these behaviors) and performed thousands of FlexPAVE simulations using different levels of material property variability, climate, loading, and structural conditions.[6]

For %Cracking, research team analyzed the material variations and found that their analysis yielded a simplified and predictable relationship with the uncertainty in long-term performance predictions. Thus, the research team characterized and verified simplified expressions involving parameters readily calculable from laboratory experiments (linear viscoelastic, damage, and failure criteria). The predictive models can predict the propagation of the testing variability to %Cracking variations at any desired level of reliability with more than 98 percent accuracy (less than 2 percent error).

For rutting, the research team developed an even more simplified approach using the same algorithm used to determine RSI. Here the error in material variation was found to propagate at a rate of approximately 1.5 to 3.5 times that of the variation in viscoplastic strain observed in the AASHTO TP 134 experiments.[26] The research team also concluded that to improve the accuracy of the test results, a ruggedness study should be undertaken to identify the effects of the SSR test factors on the shift model's coefficients. When the ruggedness study on AASHTO TP 134 will be done, the effect of sample-to-sample variability on the model coefficients could be studied. Therefore, the limits for the Bayesian inference-based MCMC method could be selected based on the more robust analysis.

PASSFLEX

PASSFlex is software based on Microsoft Excel that combines FlexMAT and FlexPAVE into a PRS framework to support the user (e.g., agencies, contractors, and researchers) in the different steps of a PRS-based project. (See references 5, 6, 7, and 24.) PASSFlex was designed to offer the user five main features:

- Development of a local database of mixtures based on AMPT testing.
- Development of PRS using a choice of protocol.
- Mix approval based on an index or on performance.
- QA evaluation by measured acceptance quality characteristics and calibrated volumetric relationships.
- A toolbox that contains FlexMAT and FlexPAVE in a single environment.[5,6]

This report takes one of the three protocols developed under the auspices of the TFRS-01 project, *Quality Assurance (QA) Aspects of Performance Related Specifications (PRS)*, and uses that protocol to describe the various elements of PASSFlex and how those elements work together to develop tables for payment provisions, which constitute the most critical element in successful PRS.[7,27]

SHADOW PROJECTS

The research team undertook three shadow projects in concert with the Western Federal Lands Highway Division, Maine Department of Transportation, and Missouri Department of Transportation, respectively, to introduce the AMPT suite of performance tests and PRS models to State departments of transportation. The research team used samples from ongoing construction projects to develop PVRs and to evaluate the PVRs' accuracy as a function of mixture volumetrics and in-place density values. The data from the shadow projects have no bearing on currently specified payments to contractors; however, agencies and the research team can use the results of the shadow projects to evaluate the PRS methods in realistic environments and prepare agencies for the deployment of PRS in the future.

The general steps involved in a shadow project include the following activities:

- Two-day, hands-on AMPT workshop.
- AMPT training at the agency's laboratory.
- Proficiency testing.
- Shadow project selection.
- Acquisition of construction samples and QA data.
- Selection of the four corners volumetric conditions.
- AMPT testing and data analysis using FlexMAT and FlexPAVE.[5,6]
- PVR and IVR development.
- Evaluation of the effects of construction variability on pavement performance.

The analysis results for the shadow project data clearly demonstrate the importance of in-place density on a pavement's cracking and rutting performance. The analysis found much less variation for binder content and aggregate gradation. The PVRs and IVRs that the research team generated using the construction samples from the shadow projects were verified using the AMPT performance test results from an independent set of construction samples. However, future research should include laboratory-mixed and laboratory-compacted mixtures to evaluate the effects of binder content and aggregate gradation.

CHAPTER 1. INTRODUCTION

Highway agencies in the United States spend billions annually to rehabilitate or reconstruct asphalt pavements that have reached low serviceability threshold limits. Considering this level of investment, stakeholders should ask whether:

- These rehabilitated or reconstructed pavements have performed as expected.
- Construction costs are commensurate with real-world pavement performance.

The next generation of quality assurance (QA) specifications being deployed by the Federal Highway Administration (FHWA) addresses these questions.

Today, most highway agencies use QA specifications for the construction of asphalt pavements. The typical acceptance quality characteristics (AQCs) in these specifications include asphalt content, gradation, laboratory air void content, and in-place density. These measurable AQCs impact pavement performance. To account for construction variability, most highway agencies use pay factors in their QA specifications based on percent within limits. The current QA specifications are limited because those specifications do not directly evaluate the effect of asphalt mixture deviations on the pavement's performance; instead, the current QA specifications use AQC limits to adjust the payment based on a statistical evaluation of the as-constructed asphalt pavement properties relative to the design specifications. Thus, payment incentives are based on process control in the production and placement of the pavement to reduce variability and not on the pavement's performance. Once researchers validate and calibrate performance prediction models, highway agencies can use the specifications that researchers develop to determine performance-adjusted payment provisions that link design to construction and payment to reflect the expected and constructed pavement performance.

Like the current QA specifications, performance specifications require contractor quality control and management and agency verification and acceptance activities throughout the production and placement of the pavement. Final acceptance of the pavement is based on random statistical sampling of the mixture and its measured quality level on a lot-by-lot basis for the specified AQCs. Performance-related specifications (PRS) differ from current QA specifications by using mechanistic-empirical pavement performance models to quantify the relationship between the AQCs and subsequent pavement performance. Highway agencies use these performance prediction models to provide rational payment adjustments based on an assessment of the measured quality and variability of the product. The payment adjustments are related to the difference between the as-designed and as-constructed pavement life. From this perspective, performance specifications better align design requirements with construction by focusing on characteristics that relate more directly to performance and by promoting an improved understanding and a shared responsibility for performance among all parties. Performance, quality, and costs are uniquely connected through modeling to analyze tradeoffs and determine how these elements impact performance and pavement service life.

In addition to directly linking design and construction and providing payment incentives and disincentives that are justified through the reduction or extension of pavement life, PRSs offer the following benefits:

- Industry and agencies are continually looking for ways to innovate to improve pavement performance, and performance specifications and analysis tools provide a platform for agency or industry-initiated innovation. The ability to innovate can provide contractors with a competitive advantage, which can ultimately lead to cost savings and greater returns.

- Performance specifications transfer some of the performance risk from the agency to the contractor in return for allowing the contractor to be more innovative and more competitive, which in the long run will result in improved and more efficient construction practices, thus reducing long-term costs to the agency.

This report describes the various research efforts, performance tests, and analysis tools for the purpose of understanding fundamental performance and facilitating deployment of performance tests and evaluation. Chapter 2 presents a summary of the aging models that researchers have developed under the auspices of National Cooperative Highway Research Program (NCHRP) 09-54, and the low-temperature cracking model.[17] Chapter 3 describes the research efforts to develop the cracking index, S_{app}, and rutting index, the Rutting Strain Index (RSI). Chapter 4 introduces FlexMAT™ version 2.1 as the material-level analysis software.[5] Chapter 5 presents the research efforts to advance the structural model by developing preliminary transfer functions for FlexPAVE™ version 1.1 and FlexPAVE version 2.0.[6,20] In volume II of this report, chapter 1 introduces the concepts of a performance-volumetrics relationship (PVR) and index-volumetrics relationship (IVR).[28] Volume II chapter 2 presents the framework for the Asphalt Mixture Performance Tester (AMPT) balanced mix design (BMD) method. Volume II chapter 3 presents reliability analyses for both cracking and rutting and the development of PASSFlex™ as a software program to develop PRS.[7] Volume II chapter 4 describes the three shadow projects that the Maine Department of Transportation (MaineDOT), Missouri Department of Transportation, and Western Federal Lands Highway Division conducted with guidance from the research team. Finally, volume II chapter 10 provides conclusions and future research recommendations.

CHAPTER 2. ASPHALT MATERIAL MODEL DEVELOPMENT

AGING MODELS

The research team conducted a comprehensive study of asphalt mixture aging under NCHRP 09-54 and will implement the findings of the study in the PRS with the expectation of yielding more accurate performance predictions.[17] Two of the main outcomes of NCHRP 09-54 go hand-in-hand to predict the evolution of asphalt mixture properties for any field aging condition, climate, and pavement depth. The two outcomes are the pavement aging model (PAM) and the asphalt mixture aging-cracking (AMAC) model. PAM is based on rigorous oxidation kinetics modeling. This model can predict the evolution of a rheological aging index for any field aging condition, climate, and pavement depth given only two material-dependent inputs. The AMAC model predicts changes in an asphalt mixture's linear viscoelastic and cyclic fatigue properties with aging from the reference short-term aged (STA) mixture properties using the predicted rheological aging index values obtained from PAM.

Pavement Aging Model

Equation 1 through equation 8 show PAM. The predicted rheological aging index property is log |*G**| at 64 °C, 10 rad/s. (See references 29–32.) Equation 1, equation 2, and equation 3 show oxidation kinetics information that was calibrated as a function of pavement depth for a wide range of pavement sections, including sections that contain both conventional hot mix asphalt (HMA) and other materials, for example, reclaimed asphalt pavement (RAP), warm mix asphalt (WMA), and polymer-modified asphalt (PMA). Equation 4 through equation 7 show the depth-dependent field calibration of the kinetics model, which was carried out using both conventional HMA and other materials (i.e., RAP, WMA, and PMA) prepared at the optimum asphalt content. Researchers conducted a systematic study of the mixture's morphology and analyzed the findings to calibrate an adjustment to the PAM predictions as a function of deviation from the Superpave™ optimum asphalt content, as shown in equation 8. A 2021 report by Kim et al. provides further details about the development and calibration of this model.[32]

$$\log|G^*|_{kinetics} = \log|G^*|_0 + M\left[1-\frac{k_c}{k_f}\right]\left(1-\exp\left(-k_f t\right)\right)+k_c M t \quad (1)$$

$$k_f = A_f \exp\left(\frac{-E_{af}}{RT}\right) \quad (2)$$

$$k_c = A_c \exp\left(\frac{-E_{ac}}{RT}\right) \quad (3)$$

$$\log|G^*|_{t,z} = \log|G^*|_0 + M\left(\frac{0.916z + AP_{\max}}{z+1}\right)\left(1 - e^{-N \times AP_t}\right) \quad (4)$$

$$AP_t = \frac{\log|G^*|_{kinetics,t} - \log|G^*|_0}{M} \quad (5)$$

$$AP_{\max} = \frac{4.5 - \log|G^*|_0}{M} \quad (6)$$

$$N = 0.477e^{-0.226 \times AP_{t=10}} \quad (7)$$

$$\log|G^*|_{field,adj} = \log|G^*|_{field} \times (1 - 0.149 \times \%AC_{dev}) \quad (8)$$

Where:

$|G^*|_{kinetics}$ = long term aged (LTA) binder shear modulus at 64 °C and 10 rad/s (kPa).
$|G^*|_0$ = STA binder shear modulus at 64 °C and 10 rad/s (kPa).
k_f = rate of fast reaction.
k_c = rate of constant reaction.
A_f = fast reaction frequency factor, considered a regression parameter equal to 1.25×10^3.
A_c = constant reaction frequency factor, considered a regression parameter equal to 3.68×10^7.
E_{af} = fast reaction activation energy, considered a regression parameter equal to 95.04.
E_{ac} = constant reaction activation energy, considered a regression parameter equal to 62.21.
R = universal gas constant or ideal gas constant equal to 0.008314 (kJ/mol K).
T = pavement temperature (Kelvin).
t = reaction time (days).
M = fitting parameter related to fast reaction reactive material.
$|G^*|_{t,z}$ = LTA binder shear modulus after depth-dependent calibration at 64 °C and 10 rad/s (kPa).
$|G^*|_{kinetics,t}$ = LTA binder shear modulus calculated at the pavement surface at time t (kPa).
AP_t = aging parameter at the pavement surface at time t (kPa).
$AP_{t=10}$ = aging parameter at the pavement surface calculated at 10 yr of aging (kPa).
z = pavement depth (cm).
$|G^*|_{t,z,adj}$ = LTA binder shear modulus after deviation from optimum asphalt content calibration at 64 °C and 10 rad/s (kPa).
$\%AC_{dev}$ = asphalt content of interest minus the Superpave optimum asphalt content (percent).

Hierarchical Input Level System for Pavement Aging Model

PAM requires as inputs the hourly pavement temperature data from the Enhanced Integrated Climate Model (EICM), the material-dependent parameter *M*, and log |*G**| (64 °C, 10 rad/s) at the STA condition.[13] The material-dependent parameters (*M* and log |*G**| at STA) can be determined at three levels of accuracy. These levels comprise the hierarchical input level system that makes PAM more amenable to practical applications given the users' different testing capabilities. The three levels, presented in the following sections from highest level of accuracy to lowest level of accuracy, make use of the following information and methods:

- Loose mixture aging.
- Rolling thin film oven (RTFO) and pressure aging vessel (PAV) aging.
- Binder performance grade (PG).

Input Level 1

In input level 1, the log |*G**| (64 °C, 10 rad/s) at STA conditions is obtained by aging loose mixture in the oven at 135 °C for 4 h and then extracting, recovering, and testing the binder. The parameter *M* is obtained by measuring log |*G**| at STA conditions and at multiple long term aged (LTA) conditions by aging loose mixture in an oven at 95 °C, then extracting, recovering, and testing the binder.[32–34] The value of *M* in equation 1 is then determined via optimization such that the predicted log |*G**| values match the measured values. Any laboratory LTA duration can be considered to obtain log |*G**| to calibrate *M* if the duration allows for binder log |*G**| values that are well dispersed on the oxidation time-scale. The aging durations should allow binder log |*G**| values that belong to the constant region in the kinetics plot of |*G**| versus aging duration so that the oxidation kinetics data obtained are meaningful and reproducible.

Input Level 2

Level 2 equates loose mixture kinetics and binder kinetics obtained from RTFO and PAV tests and is empirical in nature. For a total of eight different binders, the log |*G**| (64 °C, 10 rad/s) obtained after RTFO aging was found to be equal to the log |*G**| obtained from testing binder extracted and recovered from loose mixture aged at the STA condition (4 h at 135 °C). Similarly, the log |*G**| obtained after RTFO aging and 40 h in the PAV were found to be equal to the log |*G**| obtained from testing binder extracted and recovered from loose mixture aged at the LTA condition of 6 d in the oven at 95 °C.

Thus, level 2 requires aging the binder using the RTFO and PAV (40 h). These two levels of aging are equivalent to loose mixture STA and 6 d of LTA in the oven at 95 °C. The log |*G**| beyond 6 d of aging is proportional to the log |*G**| at 6 d of aging and can be obtained using equation 9.

$$\log\left|G^*_{iD}\right| = \log\left|G^*_{6D}\right| \times 1.02635^{i-6} \quad for\ i \geq 6 \tag{9}$$

Knowing log |*G**| at 0 d and 6 d and beyond, *M* can be obtained by optimizing equation 1 such that the predicted log |*G**| values match the estimated ones obtained from RTFO and 40-h PAV aging. The 2021 report by Kim et al. provides details and examples of the fit.[32]

Input Level 3

Level 3 is a less accurate alternative for determining the material-specific parameters, compared to levels 1 and 2, and is to convert the binder high performance grade (HPG) to both log |*G**| (64 °C, 10 rad/s) at STA conditions and *M*.

The log |*G**| (64 °C, 10 rad/s) at STA conditions can be obtained through the empirical equation 10. *M* can be obtained through the empirical equation 11.

$$\log|G^*| = \frac{6.552}{1+\left(\frac{HPG}{107.167}\right)^{-4.068}} \tag{10}$$

$$M = \frac{0.94}{1+\left(\frac{HPG}{82.68}\right)^{7.96}} \tag{11}$$

Estimation of Pavement Aging Model Inputs for Reclaimed Asphalt Pavement Mixtures

The material-dependent parameters (*M* and log |*G**| at STA conditions) for RAP-containing mixtures can be determined at two levels of accuracy. The two levels, level 1 and level 3, presented in the following sections from highest to lowest level of accuracy, make use of loose mixture aging and the binder PG, respectively.

Input Level 1

The log |*G**| at STA conditions for RAP-containing mixtures can be obtained by aging the RAP-containing loose mixture for 4 h at 135 °C in the oven followed by extraction, recovery, and testing of the binder.

To obtain *M* of the RAP-containing mixture, the RAP-containing mixture should be aged at STA conditions and for multiple LTA durations at 95 °C in the oven followed by extraction, recovery, and testing of the binder. *M* in equation 1 is then optimized such that the predicted log |*G**| values match the measured values. Recall that any laboratory LTA duration can be considered to calibrate *M* if the duration provides binder log |*G**| values that are well dispersed on the oxidation time-scale. The aging durations should provide binder log |*G**| values that belong to the constant region of the kinetics plot so that the oxidation kinetics obtained are meaningful and reproducible.

Input Level 3

Virgin mixture parameters can be obtained the same as described for level 1 for virgin mixtures. RAP parameters can be obtained as described in the following paragraphs. Equation 12 and equation 13 would then be used to obtain the RAP-containing mixture parameters (blend of virgin and RAP parameters).

$$\log|G^*|_{0,Blend} = (1-ABR)\log|G^*|_{0,Binder} + ABR \times \log|G^*|_{0,RAP} \quad (12)$$

$$M_{Blend} = (1-X_{RAP})M_{Binder} + X_{RAP}M_{RAP} \quad (13)$$

Where:

$|G^*|_{0,Binder}$ = dynamic shear modulus of STA virgin binder.
$|G^*|_{0,RAP}$ = dynamic shear modulus of STA 100 percent RAP binder.
$|G^*|_{0,Blend}$ = dynamic shear modulus of STA RAP blended binder.
ABR = asphalt binder replacement.
M_{Blend} = fitting parameter related to fast reaction reactive material of the blend.
M_{Binder} = fitting parameter related to fast reaction reactive material of the STA virgin binder.
M_{RAP} = fitting parameter related to fast reaction reactive material of the RAP.
X_{RAP} = mass fraction of the RAP.
$(1-X_{RAP})$ = mass fraction of the virgin binder.

The log $|G^*|$ at STA conditions for RAP can be obtained using equation 10 if the HPG of the RAP is known. Alternatively, if the HPG is not known, the HPG can be estimated using PAM by assuming the virgin binder kinetics. The 2021 report by Kim et al. provides a set of maps that show the HPG of RAP for any location in the United States, assuming different virgin binder log $|G^*|$ values at STA conditions and M.[32] After obtaining the RAP HPG from the maps, the log $|G^*|$ at STA conditions for RAP is obtained using equation 10.

The M of RAP can be obtained using equation 11 if the HPG of the RAP is known. Alternatively, if the HPG is not known, a similar approach to that used to obtain log $|G^*|$ at STA conditions for RAP can be used After obtaining the RAP HPG from the maps, the log $|G^*|$ at STA conditions for RAP is obtained using equation 11.

Asphalt Mixture Aging-Cracking Model

The LTA properties of asphalt mixtures can be predicted given the STA mixture properties combined with PAM predictions of the log $|G^*|$ evolution. This framework is built on the method currently implemented in Pavement ME that uses a reduced frequency concept based on time-aging superposition to model the effect of aging on a mixture's modulus.[18] With time-aging superposition, the end results from characterization are a single governing master curve, a time-temperature shift factor function, and an aging shift factor function. The predictive framework for modeling the changes in asphalt mixture fatigue properties is based on a similar concept to that used for modulus prediction.

Modulus Prediction

The horizontal shift is achieved by calculating a reduced frequency using equation 16 that relies on two shift factors. The isotherms are shifted due to the effect of not only temperature but also age level. A time-temperature shift (t-TS) factor, singly, would shift the isotherms to a reference temperature. A common form of the t-TS factor function is shown in equation 14. A time-aging shift (tAS) factor, on the other hand, would shift the isotherms to a reference age level. Equation 15 is a form of the tAS factor function where log |*G**| acts as an aging state variable. The calculated reduced frequency obtained from equation 16 then can be input into the sigmoidal function shown in equation 17 to determine the mixture dynamic modulus at the desired temperature and aging level. The evaluation of this method using the two springs, two parabolic elements, one dashpot (2S2P1D) model instead of the sigmoidal function for the modulus is yet to be conducted.

In practice, the sigmoidal fitting parameters (δ, α, β, γ) and the t-TS fitting parameters (α_1, α_2) should be determined via nonlinear optimization to minimize the error between the storage modulus sigmoidal predictions and measured data that correspond to the STA condition only. Time-temperature shifting should be conducted in the storage modulus (E') domain rather than in the dynamic modulus ($|E^*|$) domain to construct the master curves. Because the STA storage modulus data can be used to fit the sigmoidal function and t-TS factor function, the tAS function is the only other component needed to predict the storage modulus at any other aging level given an aging model to predict the log |*G**| evolution with aging. With the log |*G**| known, the fitting parameter *c* is effectively the only parameter needed to predict the LTA storage modulus value.

Two levels of accuracy can be employed to obtain the parameter *c*. For the first level, *c* can be estimated to be the slope between the t-TS factors (log (a_T)) and the difference in log |*G**|. The data needed to create this relationship include the mixture dynamic modulus at STA conditions and the binder dynamic shear modulus at STA conditions at 10 rad/s and at mixture testing temperatures. For the second level, if the binder dynamic shear modulus value at STA conditions at 10 rad/s and at mixture testing temperatures is not available, then a universal *c* value of 1.71 can be used to calculate the tAS factors. The 2021 report by Kim et al., a 2017 article by Rad et al., and the 2020 article by Saleh et al. provide more information about the development of this approach.[32,34,35]

$$\log(a_T) = \alpha_1 \left(T - T_{ref}\right)^2 + \alpha_2 \left(T - T_{ref}\right) \tag{14}$$

$$\log(a_A) = c \times (\log|G^*|_{LTA} - \log|G^*|_{STA(ref)}) \tag{15}$$

$$f_r = f \times a_T \times a_A \tag{16}$$

$$log(|E^*|) = \delta + \frac{\alpha}{1 + e^{\beta + \gamma \log(f_r)}} \quad (17)$$

Where:

a_T = t-TS factor at a given temperature.
T = temperature (°C).
T_{ref} = reference temperature (°C).
α_1, α_2 = fitting parameters.
a_A = tAS factor at a given age level.
$|G^*|_{LTA}$ = dynamic shear modulus at a certain LTA condition and at 64 °C and 10 rad/s predicted from PAM.
$|G^*|_{STA(ref)}$ = dynamic shear modulus at reference STA condition and at 64 °C and 10 rad/s
c = fitting parameter.
f_r = reduced frequency (Hz).
f = frequency (Hz).
$|E^*|$ = dynamic modulus (kPa).
δ, α, β, γ = fitting parameters.

Fatigue Properties Prediction

The prediction of fatigue properties involves the prediction of the damage characteristic curve and the failure criterion (D^R). A similar concept to the master curve shifting process presented earlier is used here to predict the damage characteristic curve, where a shift factor is defined in terms of the change in log $|G^*|$, as shown in equation 18. The mixture cyclic fatigue test results at the STA condition and predictions of log $|G^*|$ allow the shift factor a_A in equation 18 to be calculated, which then allows the damage characteristic curve to be predicted as a function of age level using equation 19.

$$\log(a_A)_{fatigue} = 0.2025 \times (\log|G^*|_{LTA} - \log|G^*|_{STA(ref)}) \quad (18)$$

$$C = 1 - (C_{11} / a_A^{C_{12}}) S^{C_{12}} \quad (19)$$

Where:

a_A = shift factor for the damage characteristic curve.
$|G^*|_{LTA}$ = dynamic shear modulus at a certain long-term aging condition and at 64 °C and 10 rad/s.
$|G^*|_{STA(ref)}$ = dynamic shear modulus at reference short-term aging condition and at 64 °C and 10 rad/s.
C = pseudo secant modulus (from this point on pseudostiffness for simplicity).
S = amount of fatigue damage in the specimen.
C_{11}, C_{12} = fitting parameters of STA damage characteristic curve.

The change in the failure criterion, D^R, also can be predicted as a function of aging level, which is based on changes in log $|G^*|$ due to aging. Equations 20 through 22 are established to predict the decrease in D^R with aging. The 2021 report by Kim et al. provides details regarding the development of these equations.(32)

$$D^R{}_{LTA} = D^R{}_{STA} - (D^R{}_{STA} - 0.1)e^{\frac{1.44\left(\log|G^*|_{LTA} - 4.5\right)}{\left(\max\Delta\log|G^*|\right)\left(\Delta\log|G^*|\right)}} \quad (20)$$

$$\max\Delta\log|G^*| = 4.5 - \log|G^*|_{STA(ref)} \quad (21)$$

$$\Delta\log|G^*| = \log|G^*|_{LTA} - \log|G^*|_{STA(ref)} \quad (22)$$

Where:

$D^R{}_{LTA}$ = predicted failure criterion at a certain LTA condition.
$D^R{}_{STA}$ = measured failure criterion at STA condition.
$|G^*|_{LTA}$ = dynamic shear modulus at a certain LTA condition and at 64 °C and 10 rad/s.
$|G^*|_{STA(ref)}$ = dynamic shear modulus at reference STA condition and at 64 °C and 10 rad/s.

THERMAL CRACKING MODEL

Thermal cracking is the predominant failure mode for pavement sections that have been constructed in cold regions where significant air temperature drops induce stress in the pavement layers.(36) This type of stress, hereafter referred to as thermal stress, causes damage, referred to as thermal damage. Once the level of damage exceeds the mixture's tolerance threshold, macrocracks begin to form in asphalt pavement sections. Moreover, significant fluctuations in the daily air temperature also lead to the accumulation of damage within pavement section sublayers and lower the pavement's capacity for resistance to cracking as the pavement ages. Both severe thermal shots and daily thermal fluctuations work together to create transverse cracks. This phenomenon is not limited to cold regions. Thermal cracking often occurs in warm regions where stiff binder is used to resist permanent deformation.(37)

Thermal cracking depends on many parameters, including the pavement's structure, the asphalt mixture properties, environmental loading, and pavement aging. Thermal cracking is considered to be top-down cracking in which the induced thermal contraction has a gradient throughout the depth of the pavement and each sublayer is restrained against movement in the longitudinal direction.(38,39) The asphalt sections experience contraction and expansion when the sections are subjected to daily air temperature fluctuations. Cooling events cause the material to contract and, because of the long length of the pavement section (in the direction of traffic flow) and the width of the pavement section, the plane-strain condition is dominant and tension stress is induced in the pavement layers. The magnitude of the induced stress depends on the rate of the temperature drop, the current temperature, the tendency of the mixture to contract, and the mixture's stiffness.

This section introduces methodologies to determine the coefficient of thermal contraction (CTC). Next, this section describes a predictive methodology for fracture in the thermal stress restrained specimen test (TSRST). This methodology utilizes the dissipated pseudostrain energy (DPSE) based failure criterion, which can be predicted using simplified viscoelastic continuum damage (S-VECD) theory. Finally, the predictive methodology for fracture in the TSRST is implemented into the structural analysis framework, named FlexTC.[9] The research team used the thermal cracking performance of Minnesota's Cold Weather Pavement Testing Facility (MnROAD) mixtures and sections to verify the predictive methodology for the TSRST and FlexTC.[9,11]

Determination of the Coefficient of Thermal Contraction for Asphalt Mixtures

Among all the parameters that affect the magnitude of thermal stress in asphalt mixtures, the CTC is the factor that determines the amount of contraction that asphalt mixtures undergo for any given temperature drop. As a result, the CTC is a critical input parameter for predicting the damage associated with thermal cracking in asphalt pavement sections. The study that was conducted as part of the calibration of the thermal cracking model in the American Association of State Highway and Transportation Officials (AASHTO) Mechanistic Empirical Pavement Design Guide (MEPDG) software emphasizes the importance of the CTC for predicted crack spacing.[40]

This study comprises both an experimental study to measure the CTCs of asphalt mixtures and an analytical study to develop predictive models of CTCs based on constituent material properties. Three levels of analysis are proposed for measuring and predicting the CTCs of asphalt concrete mixtures. The CTC of an asphalt mixture should be measured directly at level I. Because level I may require extra testing and additional testing equipment, level II suggests a simple yet efficient formulation (a composite model) for predicting mixture CTCs. This method requires measured binder CTCs *a priori*. Level III analysis groups binders based on their low PG (LPG) and uses average CTC values for each group. In level III analysis, the estimated binder CTC is input into the composite model to predict the CTC of the mixture. Then, the validity and accuracy of the different methods are investigated based on comparisons of the measured and predicted CTC values. To study the effect of error in the mixture CTC predictions, the research team compared the induced thermal stress in a representative volume element sample subjected to thermal variation using the measured CTC or predicted CTC from level II or III analyses. Before this report describes the work in this study in detail, the following two sections summarize previous research efforts to measure and predict the CTC of asphalt mixtures.

Measuring the Coefficient of Thermal Contraction of Asphalt Mixtures

Researchers have long known that the CTC is a function of temperature. (See references 41–46.) Several researchers developed various test methods to measure the CTC of asphalt mixtures. For example, Stoffels and Kwanda used the resistance strain gauge method to capture the CTC variation of asphalt mixtures for temperatures ranging from 0 °C to −25 °C.[47] However, the installation of strain gauges on specimens makes this approach cumbersome, and thus, other researchers have not adopted this methodology. Mehta, Christensen, and Stoffels used linear variable differential transducers (LVDTs) to measure the CTC of asphalt concrete as part of indirect tensile strength testing.[48] The Mehta, Christensen, and Stoffels study of three different mixtures and an aluminum sample obtained values that agreed with the values reported by

Stoffels and Kwanda. Zeng and Shields attached LVDTs to asphalt concrete beam specimens (51 mm × 51 mm × 340 mm) and applied temperatures ranging from −40 °C to 40 °C to measure the thermal deformation of the asphalt mixtures.[49] Based on the measured data, Zeng and Shields concluded that thermal deformation cannot be approximated by a linear function, which means that the CTC is a nonlinear function of temperature. Bahia and Anderson developed a hyperbolic relationship to express the volume changes of binder when binder is subjected to temperature variation, expressed here as equation 23.[50] Several researchers have used this relationship to fit measured data. (See references 36, 43, 51, and 52.) Therefore, because of its widespread usage and accuracy, the research team decided to adopt this relationship to fit the measured data in this research.

$$v = c_v + CTC_g \times (T - T_g) + R \times (CTC_L - CTC_g) \times Ln\left(1 + \exp\left(\frac{T - T_g}{R}\right)\right) \quad (23)$$

Where:

v = specific volume change.
c_v = a constant.
R = regression constant that is related to the rate of volume change at or near the glass transition temperature.
T = test temperature (°C).
T_g = glassy temperature (°C).
CTC_L, CTC_g = coefficients of thermal contraction greater than and less than the glassy temperature, respectively.

Later, Bahia and a research group at the University of Wisconsin, Madison, developed a test setup for measuring the CTCs of asphalt mixtures that consists of a control chamber where an asphalt sample is placed on a frictionless Teflon® base.[43] The researchers attached an asphalt sample to two LVDTs at its ends and placed a beam (65 mm × 65 mm × 380 mm) in a temperature-controlled chamber to measure the mixture CTC. The test starts at 40 °C and finishes at −80 °C with a rate of 1 °C/min. Marasteanu et al. placed a dummy sample in the chamber to record the surface and inside temperatures during testing.[36] The samples Marasteanu et al. used were compacted by a kneading compactor and sawn to the required size. (A kneading compactor is unable to bring the sample air void content close to the air void content of asphalt mixtures in the field, where the air void content drops significantly because of passing traffic a few years after construction.) Later, Bahia, Tabatabaee, and Velasquez used samples sawn and glued from Superpave gyratory-compacted asphalt mixture samples.[45] This test setup is called the asphalt thermal cracking analyzer (ATCA) test. The ATCA test is laborious because the ATCA test requires the gluing of sawn samples to form the test specimen. The ATCA can measure two sets of properties in each run:

- The fracture temperature of an asphalt sample that is restrained at both ends and experiences damage as the temperature decreases.
- The CTC of another sample that is free to deform as the temperature drops.

The high temperature drop rate imposes a considerable temperature gradient within the sample. The ATCA test does not provide a tool to measure the temperature inside the samples; therefore, the air temperature is used to calculate the CTC of the mixture.

Alavi developed the uniaxial thermal stress and strain test after making modifications to the TSRST and measured the CTC of the mixture during this test.[53] Alavi included two samples that were side-cored from the Superpave gyratory-compacted sample and glued them together to make a long enough specimen that would fit inside the temperature chamber. In this test, the researchers placed the sample on top of a frictionless pad and attached the sample to two LVDTs at its ends. The researchers placed the sample horizontally and used the horizontal sample in addition to a vertical restrained sample. Once the test starts at 25 °C and the air temperature inside the chamber drops at the rate of −10 °C/h, the longitudinal deformation of the horizontal unrestrained specimen is recorded. Researchers can use these measurements to find the CTCs of asphalt mixtures.[54]

Islam and Tarefder measured the CTC and coefficient of thermal expansion (CTE) of asphalt mixtures in the laboratory.[46] Islam and Tarefder used the temperature range of −20 °C to 55 °C and field-cored and laboratory Superpave gyratory-compacted samples to study the variations in the CTCs and CTEs as a function of temperature. Islam and Tarefder also investigated the effects of anisotropy, air void content, aggregate gradation, and aggregate source. These researchers attached two LVDTs to cylindrical samples (100 mm in diameter and 150 mm in height) and measured the CTCs and CTEs of the asphalt mixtures. Islam and Tarefder used lithium aluminosilicate glass-ceramic, also known as ZERODUR®, to calibrate the LVDTs.[10] ZERODUR has low CTC and CTE values and thus can be used to calibrate LVDTs. Through statistical hypothesis tests, Islam and Tarefder concluded that the CTC and CTE are independent of anisotropic effects. This finding can help develop a predictive model by modeling the asphalt behavior only in one direction. Through statistical hypothesis tests, Islam and Tarefder also concluded that air void content and aggregate gradation do not affect the CTC, but that aggregate geology does affect the CTC and CTE.

Bahia and Anderson developed a dilatometry system to measure the thermo-volumetric properties of asphalt binder.[50] This system consists of two capillary tubes filled with ethyl alcohol located above the binder sample. The volumetric variation of the binder due to an imposed temperature change changes the amount of alcohol in the tubes. The test starts at 40 °C and finishes at −76 °C. The system subjects binder samples to a cooling rate of 1 °C/min. For each run of the test, users can take two measurements. Details about this test are available elsewhere.[50] Correlating the temperature-dependent behavior of an asphalt mixture to its constituent binder seems a reasonable strategy. Binder thermo-volumetric properties play a critical role in the dependency of asphalt mixture thermal deformation on the governing temperature.

Akentuna proposed the Ohio CTE device that consists of two LVDTs with flat tips fixed at the top sides of an aluminum frame.[55] The device fixes the LVDTs in such a way that the LVDTs are mutually perpendicular and coincide with the diameter of the test specimen. Users can obtain each test sample from a Superpave gyratory-compacted sample.

Predicting the Coefficient of Thermal Contraction of Asphalt Mixtures

Jones and Darter developed a volumetric equation to predict CTCs and CTEs.[56] The relationship that Jones and Darter developed, expressed here as equation 24, considers the volumetric thermal variations of the aggregate and binder separately and sums the values to obtain the linear CTC and CTE of asphalt mixtures. Jones and Darter assumed that the contributions from the binder and aggregate are proportional to their corresponding volumetric portion.

$$B_{mixture} = \frac{V_{AC} \times CTC_{binder} + V_{aggregate} \times CTC_{aggregate}}{3V_{total}} \quad (24)$$

Where:

V_{AC} = binder content.
CTC_{binder} = thermal coefficient of contraction for the binder.
$V_{aggregate}$ = aggregate volume content.
$CTC_{aggregate}$ = thermal coefficient of contraction for the aggregate.

Lytton et al. later modified Jones et al.'s relationship to take into account the effect of air voids. Their modified equation is shown here as equation 25.[57]

$$B_{mixture} = \frac{\left(V_{AC} + V_{AIR}\right) \times CTC_{binder} + V_{aggregate} \times CTC_{aggregate}}{3V_{total}} \quad (25)$$

Where V_{AIR} is air void content.

A study conducted as part of the Strategic Highway Research Program (SHRP) used the CTC value of 3.45×10^{-4} (1/°C) to represent the CTC of binder.[58] Although using a constant CTC value for binder regardless of the dominant temperature has long been proved to be incorrect, the idea of using a constant value for binder thermo-volumetric properties suggests a method to categorize different binders into separate groups and use a constant set of numbers to represent each group.

Kim et al. proposed a composite model to predict the CTC of asphalt mixtures.[44] Their model approximates an asphalt mixture as a composite that consists of aggregate, asphalt binder, and air voids. Kim et al. used the Hirsch model to consider the contributions of binder, aggregate, and air void to determine the thermal deformation of asphalt mixtures.[59] Kim et al. assumed that the orthotropic nature of asphalt mixtures does affect the thermal deformation responses of asphalt mixtures and, as a result, Kim et al. considered an idealized packing and a three-dimensional phase diagram of the aggregate and the asphalt binder. Kim et al. also considered the volume fraction of the binder phase and the aggregate phase to be proportional to the cubic power of the relative length of each phase. Equations 26 and 27 describe this assumption.

$$L^3_{aggregate} = 1 - \frac{VMA}{100} \rightarrow L_{aggregate} = \sqrt[3]{1 - \frac{VMA}{100}}$$

(26)

$$L_{binder} = 1 - L_{aggregate} = 1 - \sqrt[3]{1 - \frac{VMA}{100}}$$

(27)

Where:

VMA = void in mineral aggregate.

$L_{aggregate}$ = representative length of the aggregate.

Kim et al. assumed that the areas of the binder and aggregate phases are proportional to the square power of their corresponding lengths, and can be obtained from equations 28 and 29.[44] According to the Islam and Tarefder study, the anisotropic effect can be ignored and, as a result, the Kim, Wargo, and Powers approach could be simplified and the relationship rewritten in one dimension.[46]

$$A_{aggregate} = L^2_{aggregate} = 1 - \left(\sqrt{1 - \frac{VMA}{100}} \right)^{\frac{2}{3}}$$

(28)

$$A_{binder} = L^2_{binder} = \left(\frac{VMA}{100} \right)^{\frac{2}{3}}$$

(29)

Where:

$A_{aggregate}$ = area of the aggregate.

A_{binder} = area of the binder.

Alavi conducted a comprehensive study to investigate the effects of mixture volumetric properties on the CTCs of mixtures.[37,60] Alavi extracted important factors regarding the mixtures' thermal deformation and measured the CTCs of mixtures in uniaxial thermal stress and strain tests and proposed regression equations to correlate the liquid CTC (CTC_L), glassy CTC (CTC_g), and glass transition temperature (T_g) of mixtures with other volumetric properties. Alavi assumed a universal constant curvature (R) for all the mixtures. Alavi also included the low shear modulus of unaged binder, asphalt binder content, and aggregate gradation in the regression relationships.[53]

Alavi also studied the correlations among the CTC_L, CTC_g, and T_g as a function of aging and represented aging using the carbonyl content of the mixture and tried to correlate the variation of the aforementioned parameters to the carbonyl level.[37] Although this approach can simplify the

measurement procedure for practical purposes, the low R^2 values of the regression relationships make the accuracy of the approach questionable.

Teymourpour and Bahia used the finite element method to develop a semiempirical model to estimate the CTCs and CTEs of asphalt mixtures.[61] Teymourpour and Bahia used dilatometric testing to obtain the glass transition temperature of the mastic and digital images of mixture specimens to represent the internal aggregate structure of the asphalt mixture. The general structure of the model is based on the Hirsch model wherein the asphalt mixture modulus is linked to volumetric properties. The proposed model assumes that the mixture CTE is a weighted average of the upper and lower theoretical bounds of the CTE. Teymourpour and Bahia calculated the theoretical bounds based on the volume fractions and the modulus value of each phase and used an empirical approach to show the contribution of each phase. Equations 30 through 34 expresses the mathematical definition of this methodology.

$$CTC_{mixture}^{liquid} = CTC_{upper}^{liquid} \times F_{liquid} + CTC_{lower}^{liquid} \times \left(1 - F_{liquid}\right) \tag{30}$$

$$CTC_{mixture}^{glassy} = CTC_{upper}^{glassy} \times F_{glassy} + CTC_{lower}^{glassy} \times \left(1 - F_{glassy}\right) \tag{31}$$

$$F_{liquid} = (0.7 - 0.31 \times \beta) \times E_{liquid}^{100 \times CTC_L} \tag{32}$$

$$F_{glassy} = (0.98 - 0.29 \times \beta) \times E_{aggregate}^{20 \times CTC_{glassy}} \tag{33}$$

$$\beta = \frac{number\ of\ contact\ zones\ of\ the\ mixtures}{770} \tag{34}$$

Where:

$CTC_{mixture}^{liquid}$ = mixture CTC above the glassy temperature.
CTC_{upper}^{liquid} = upper limit for the mixture CTC for temperatures above the glassy temperature.
F_{liquid} = contribution factor for temperatures above the glassy temperature.
CTC_{lower}^{liquid} = lower limit for the mixture CTC at temperatures below the glassy temperature.
$CTC_{mixture}^{glassy}$ = mixture CTC for temperatures below the glassy temperature.
CTC_{upper}^{glassy} = upper limit for the mixture CTC for temperatures below the glassy temperature.
CTC_{lower}^{glassy} = lower limit for the mixture CTC for temperatures below the glassy temperature.
F_{glassy} = contribution factor for temperatures below the glassy temperature.

According to equations 30 to 34, the developed methodology considers the aggregate-to-aggregate contact points as a parameter that can affect the CTC of mixtures. Teymourpour and Bahia used IPass software to obtain this parameter by processing scanned images of the sample surface.[62] The requirement of the aggregate-to-aggregate contact points adds to the efforts required to predict the CTC of mixtures. The procedure proposed by Teymourpour and Bahia assumes that the CTC of mixtures comes from the contribution of parallel and series models.[61] In a study undertaken to modify the Hirsch model, Christensen and Bonaquist found that the effect of a series model in the formulation can be ignored for most mixtures.[63] This finding motivated the research team to examine the contribution of parallel and series models introduced in the Teymourpour and Bahia model separately and determine their significance for predicting the CTCs of mixtures.[61]

In the first step of the research presented in this study, the research team gathered data that were measured and reported in the literature and then built a dataset.[42,43,58] The research team can use the dataset to examine the validity and accuracy of any proposed models and, as a result, this report refers to the dataset as the first dataset.

Based on the work of Kim et al. and Marasteanu et al., the research team decided to investigate the contribution of parallel and series models separately to predict the CTCs of mixtures.[43,44] The parallel model assumes that the aggregate and binder phases are positioned in parallel to each other whereas the series model assumes that the aggregate and binder phases are acting independently in a series. The main motivation behind modeling the thermal deformation of mixtures using one-dimensional models is the conclusion drawn by Islam and Tarefder that the anisotropic effect is negligible.[46] According to the Christensen and Bonaquist study, the contribution from each model should be examined separately to make sure that the final model is sufficient and efficient.[63]

For this study, the research team examined the accuracy of the two aforementioned mechanisms, parallel and series, in predicting the CTC of mixtures through comparisons of information in the database. The series model requires the relaxation modulus of the binder, $G(t)$, a priori. Because this parameter is not measured in routine mixture characterization procedures, the research team decided to backcalculate this parameter through other suggested approaches and selected the Hirsch, modified Hirsch, and 2S2P1D models for this purpose. The research team tested the accuracy of the proposed methodology using mixtures that have a wide range of thermo-volumetric properties, tested the different mixtures, and measured their thermo-volumetric properties. These measurements comprise the second dataset.

Materials and Testing

This section describes the mixture properties, test procedure for level I analysis, samples of the measurements, and fitting results. The research team used two datasets to examine the validity and accuracy of the level II and III analyses. Because the temperature dependency of asphalt mixtures depends on the binder, the research team decided to divide the testing procedure into three different analysis levels. The classifications are based on the amount of work required to measure the mixture CTC or its binder. Each level requires the following different measurement efforts:

- Level I: The mixture CTC is measured directly. This level requires test equipment that can apply temperatures up to −60 °C with a monotonic and predefined rate of loading.
- Level II: The binder CTC is measured to predict the mixture CTC. This level requires the mixture volumetrics, aggregate elastic modulus, aggregate thermal properties, and mixture dynamic modulus.
- Level III: The binder CTC is taken from the developed database. This level requires all the parameters mentioned for level II.

The first dataset consists of measured data from MnROAD mixtures that are reported in Marasteanu et al.[11,43,64] The measured CTCs for both the binders and mixtures are reported for this dataset. Details regarding specimen dimensions and testing procedures are explained elsewhere.

Table 1 and table 2 present the binder and mixture information included in the first dataset, respectively (first dataset). The term Cell Name in the first dataset refers to the mixture that was used for constructing a segment of a road in a field experiment at the MnROAD testing facility.[11,64] Table 3 presents details of the mixture properties included in the second dataset.

Table 1. Binder information for first dataset.

Cell Name	T_g (°C)	CTC_g (1/°C)	CTC_L (1/°C)	R
Cell 3	−27.4	2.97E-05	5.48E-04	6.6
Cell 19	−21	3.35E-04	5.56E-04	2.8
Cell 20	−17.4	1.77E-04	7.93E-04	6.9
Cell 22	−20.2	3.30E-04	7.70E-04	2.7
Cell 33	−18.4	3.40E-04	6.90E-04	3.1
Cell 34	−20.7	4.90E-04	9.60E-04	13.1
Cell 35	−17.8	2.60E-04	6.90E-04	4.5

Table 2. Mixture information for first dataset.

Cell Name	VMA (percent)	Air Void (percent)	T_g (°C)	CTC_g (1/°C)	CTC_L (1/°C)	R
Cell 3	15.2	4	−25.3	9.93E-06	9.93E-06	6.9
Cell 19	16.2	4	−25.3	1.33E-05	3.86E-05	4.7
Cell 20	16.1	4	−20.5	1.40E-05	5.00E-05	4.9
Cell 22	14.8	3.7	−28.7	9.40E-06	4.00E-05	2.6
Cell 33	16.4	4.2	−26.8	6.90E-06	5.10E-05	6
Cell 34	16.2	4.2	−22.2	1.30E-05	5.10E-05	6.2
Cell 35	16.5	4	−25.6	1.40E-05	5.00E-05	3.5

Table 3. Mixture information for second dataset.

Mixture Number	Mixture Name	VMA	Additive	RAP Content (percent)	Binder Grade	Air Void (percent)
1	NC RS9.5B WMA	15.8	NA	30	PG 58-28	4
2	MIT-Advera	15.2	Advera	0	PG 64-22	3.0
3	MIT-Sasobit	15	Sasobit	0	PG 58-28	3.2
4	MIT-Evotherm	14.9	Evotherm	0	PG 58-28	3.8
5	MIT RAP 50SB	15.5	NA	50	PG 52-34	5.7
6	NY 9.5	15.3	NA	0	PG 64-22	3.2
7	NY 19	17.1	NA	0	PG 54-22	5

NC = North Carolina; MIT = Manitoba Infrastructure and Transportation; NY = New York; NA = not applicable.

Figure 1 shows the variation in CTC of the binders and mixtures in the first dataset. As the temperature varies, both the HMA and the sensor components in the LVDTs undergo thermal deformation. To obtain a true estimation of the asphalt mixture properties, the thermal deformation of LVDTs should be calculated separately and then subtracted from the measurements.

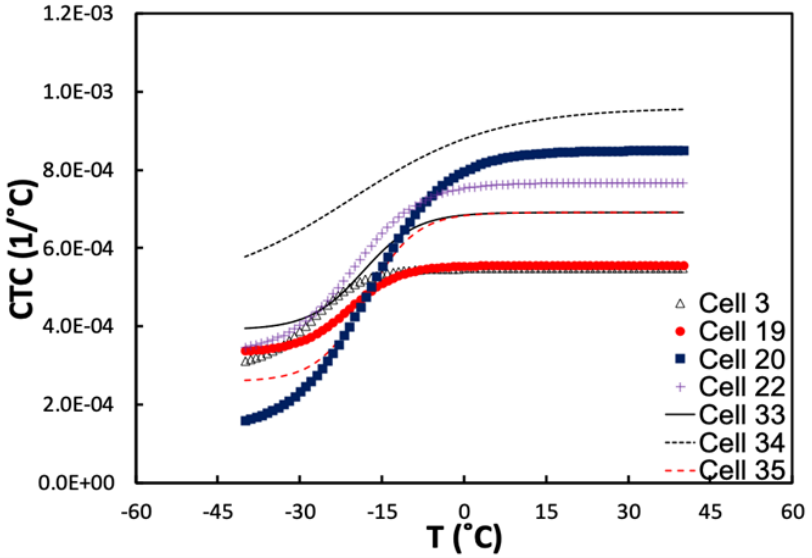

0 °C = 32 °F; T = temperature.

A. Binder.

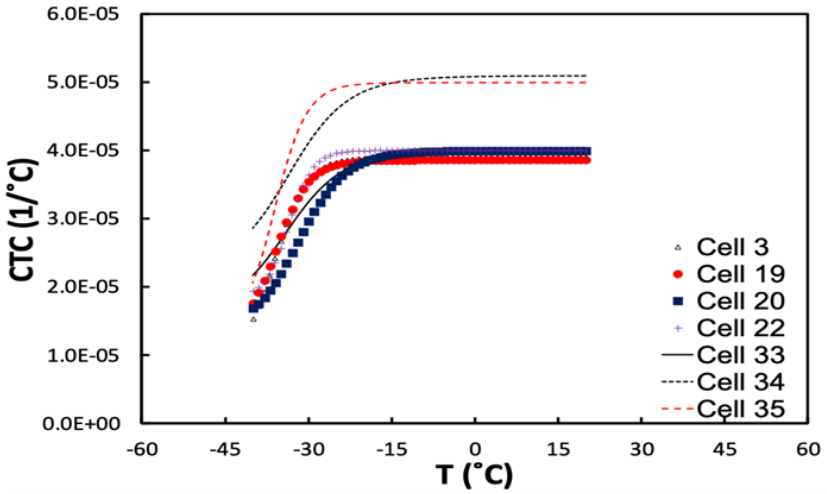

B. Mixture.

Figure 1. Graphs. CTC plots for binders and mixtures in the first dataset.[65]

For the measurements taken in this study, researchers used a ZERODUR sample to calibrate the LVDT deformation as the temperature dropped.[10] Figure 2-A and figure 2-B show the LVDTs attached to the ZERODUR sample and asphalt concrete sample, respectively. After all four LVDTs were attached to the ZERODUR sample, the sample was placed in the temperature chamber until the sample reached the equilibrium temperature of 22 °C. The research team used a Material Testing System (MTS-810), which is capable of changing the temperature in a controlled manner, in this study.[66] The research team selected −30 °C/h as the temperature rate

and measured the LVDT recordings throughout the test. Figure 3 presents the LVDT readings while the LVDTs were attached to the ZERODUR sample. Table 4 presents the calibration results. The LVDTs show positive (expansion) results on a decrease in temperature. The ZERODUR sample did not contract due to a decrease in temperature, whereas the steel rods in the LVDT did contract. Because the ends of the LVDT were glued to the ZERODUR sample, the sensor spring expanded to facilitate the contraction of the steel rods. Therefore, with a decrease in temperature, the LVDTs show an expansion output if the material does not contract.

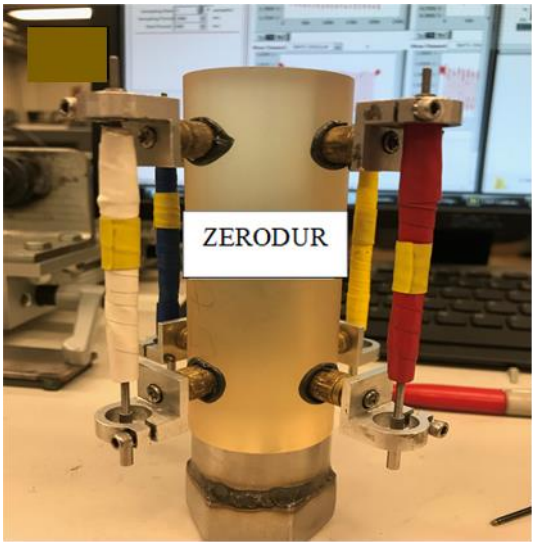

A. ZERODUR sample.

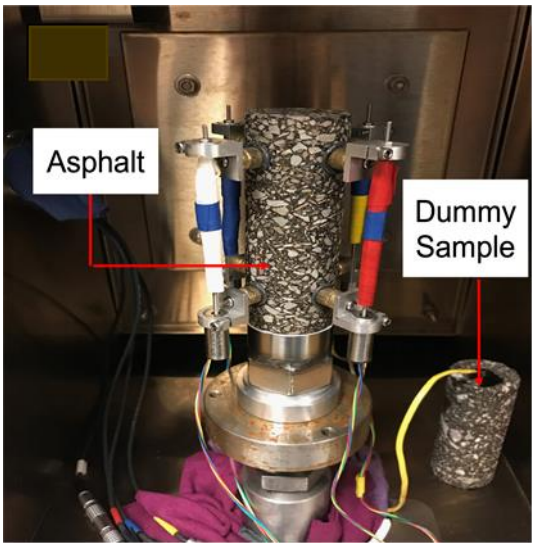

B. Asphalt concrete sample.

Figure 2. Photos. LVDTs attached to samples.[(65)]

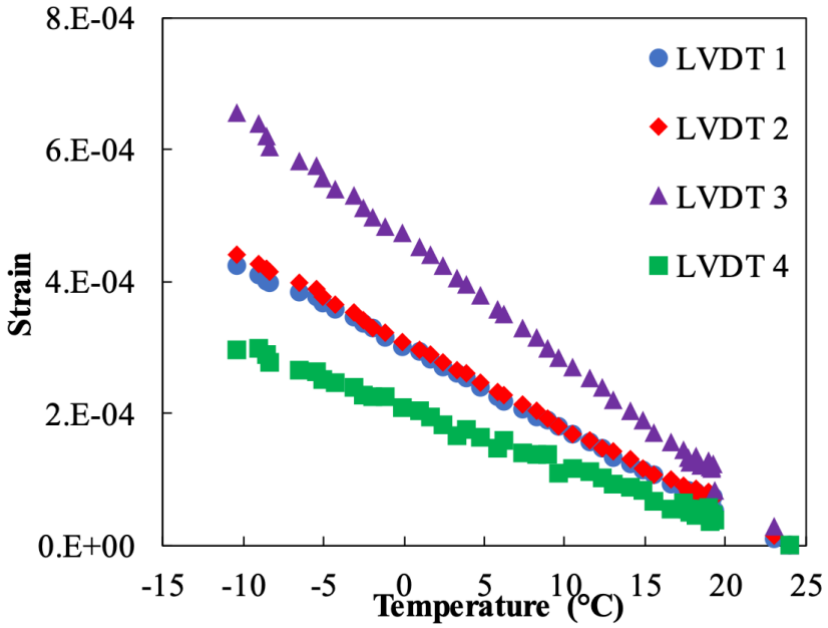

Figure 3. Graph. LVDT strain readings while LVDTs attached to ZERODUR sample and subjected to constant temperature drop.[65]

Table 4. Results of LVDT calibration.

LVDT	Slope (Strain/°C)
LVDT 1	−1.26E-05
LVDT 2	−1.28E-05
LVDT 3	−1.85E-05
LVDT 4	−8.87E-06

For the CTC measurements of the asphalt mixture sample, shown in figure 2-B, 38-mm diameter specimens were used. The sample dimensions and details regarding mixture fabrication, coring, and cutting are reported in Castorena et al.[67] The specimen is placed on top of a Teflon pad to minimize the friction. A dummy sample is positioned in the chamber to record the temperature during the test. At the start of the test, the specimens and the dummy sample are kept at 22 °C for 20 min to reach a stable temperature. After conditioning, the air inside the chamber is decreased at a rate of −30 °C/h and lowered to −65 °C. During the test, the LVDT measurements are recoded using National Instruments™ LabView® software.[68] A thermocouple records the air temperature, the temperature inside the dummy sample, and the surface temperature of the dummy sample during each run.

After correcting the LVDT readings, the research team fitted the results to equation 23 to find the thermo-volumetric properties of the mixtures. Figure 4 presents examples of the LVDT readings, temperature variations, and fitting results. Table 15 presents the fitting results. The research team used averages of the inside and surface temperatures to fit the recorded data. The temperature the research team used to plot the data shown in figure 4 is the average temperature.

The research team used MathWorks® MATLAB® nonlinear Curve Fitting Toolbox™ to fit equation 23 to the measurements by minimizing the sum of squared error.[69]

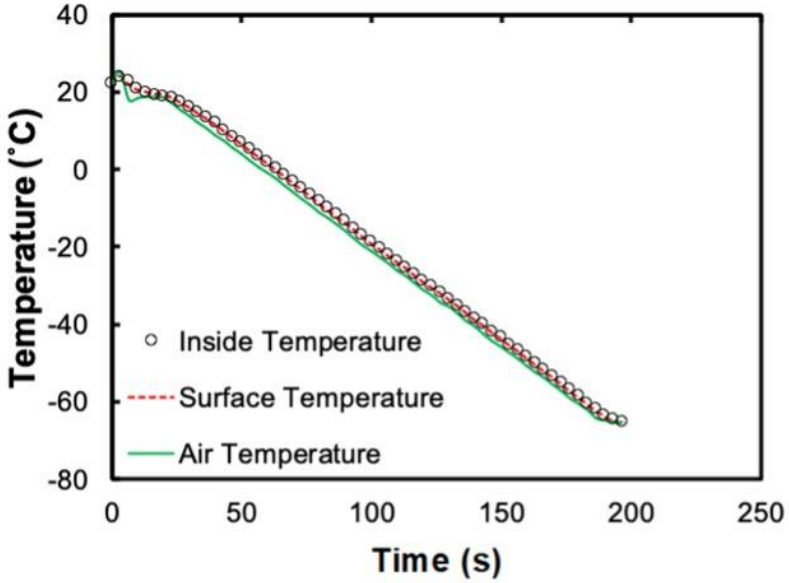

A. LVDT readings.

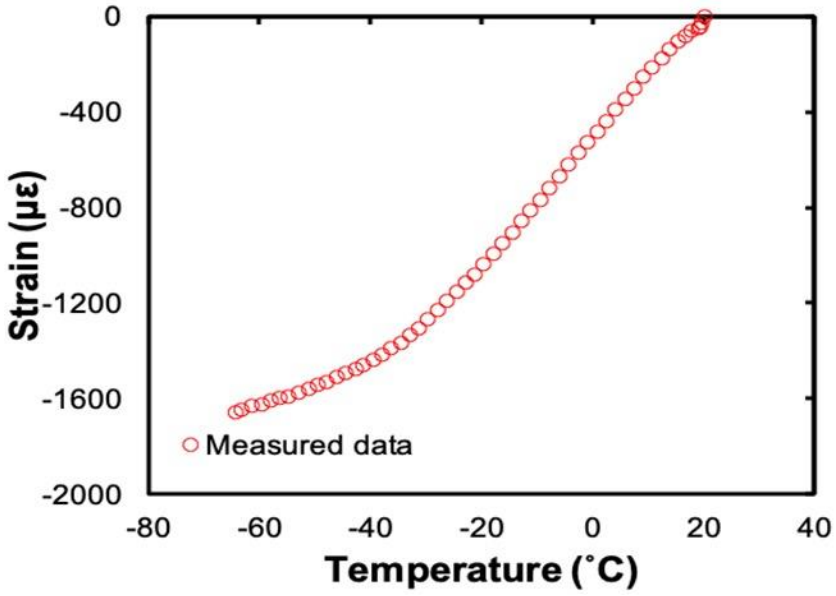

B. Temperature variation.

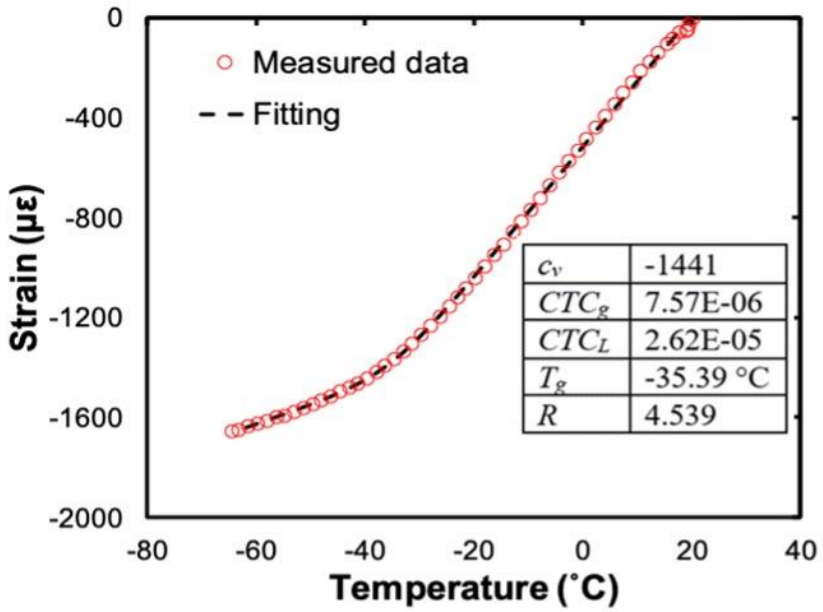

C. Fitting results.

Figure 4. Graphs. Measurement data and fitting results for NY 9.5 mixture.[65]

Table 5. Fitting results for mixtures tested.

Mix	c_v	CTC_g (1/°C)	CTC_L (1/°C)	T_g (°C)	R
NY 9.5	−1441	7.57E-06	2.63E-05	−35.39	4.538
NY 19	2.229	7.59E-06	2.02E-05	−34.4	2.229
Rs 9.5B	2.683	8.03E-06	2.27E-05	−29.03	2.683
MIT 50SB	4.483	6.08E-06	2.08E-05	−34.29	4.483
MIT Advera	1.306	6.17E-06	2.04E-05	−38.22	1.306
MIT Sasobit	1.714	4.53E-06	1.92E-05	−37.25	1.714
MIT Evotherm	1.609	7.73E-06	2.35E-05	−39	1.609

c_v = constant; CTG_g = glassy CTC; CTC_L = liquid CTC; T_g = glassy temperature; R = regression constant.

Based on the measured data reported in different studies, the research team constructed a dataset for the thermo-volumetric properties (CTC_g, CTC_L, T_g) of the binders and arranged them based on the LPG. Figure 5 presents the constructed dataset.

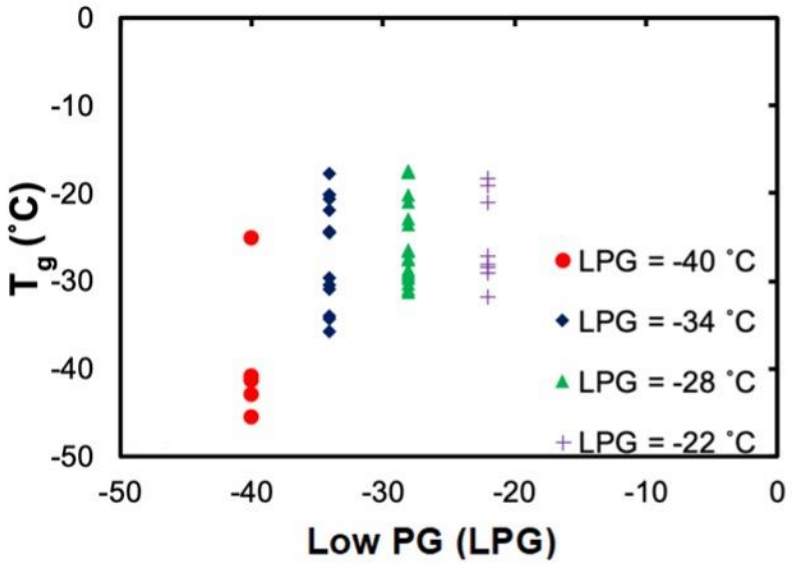

A. Glassy temperature (T_g).

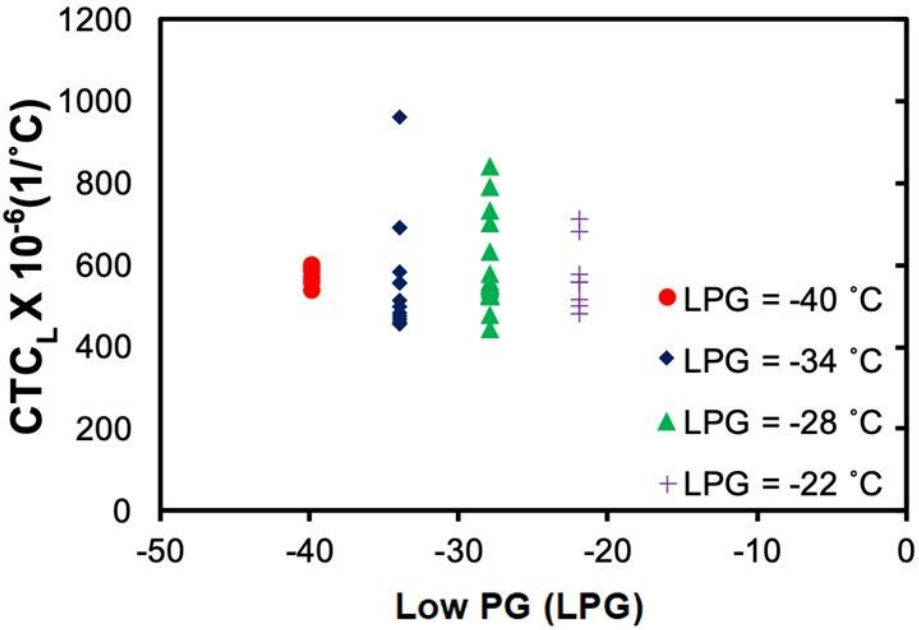

B. Liquid CTC (CTC_L).

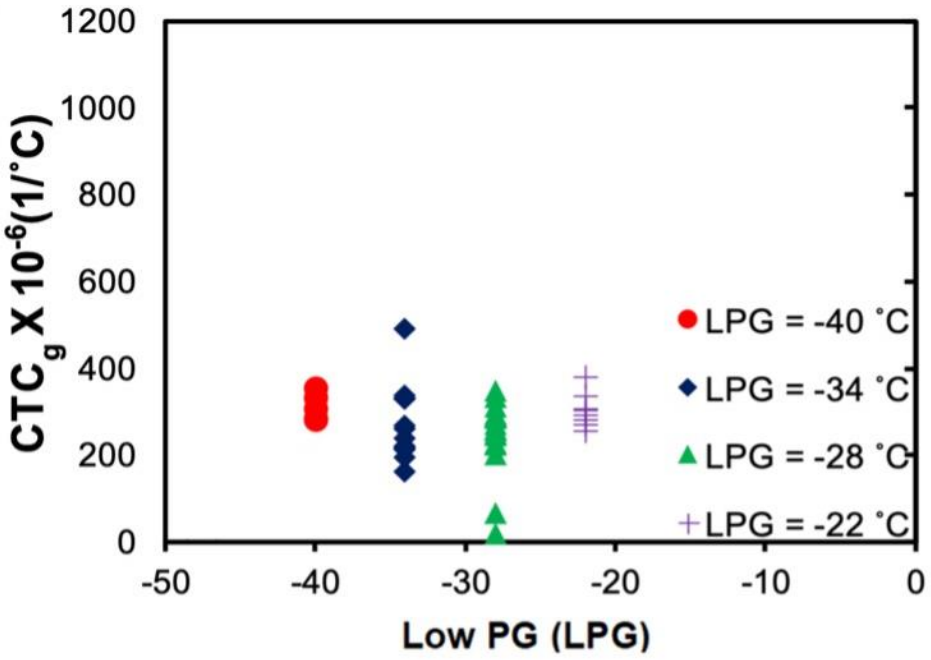

C. Glassy CTC (CTC_g).

Figure 5. Graphs. Classification of binder thermo-volumetric properties based on LPG.[(65)]

For the first experimental campaign, the temperature of the sample was not reported. To consider the temperature gradient within the sample during the test, the research team decided to solve the heat equation, equation 35, and select the temperature in the middle of the sample as the representative temperature.

$$\frac{\partial T}{\partial t} = \kappa \frac{\partial^2 T}{\partial x^2} \tag{35}$$

Where:

T = temperature.
t = time.
κ = thermal diffusivity.
x = spatial coordinate.

Equation 35 is solved by using the finite difference method to find the temperature gradient within the sample as a function of time. The thermal diffusivity is assumed to be equal to 5e-7 m^2/°C. This value is within the range of reported values for asphalt mixtures. Figure 6 shows the temperature gradient within the sample for different air temperature drop rates. Figure 7 presents the calculated average temperatures of the sample and air temperature.

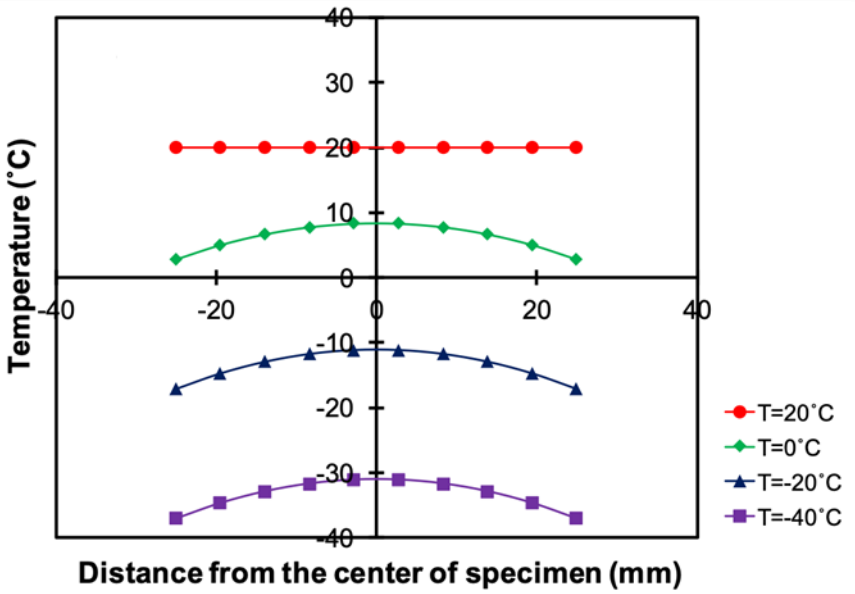

10 mm = 0.4 inches.

A. −60 °C/h.

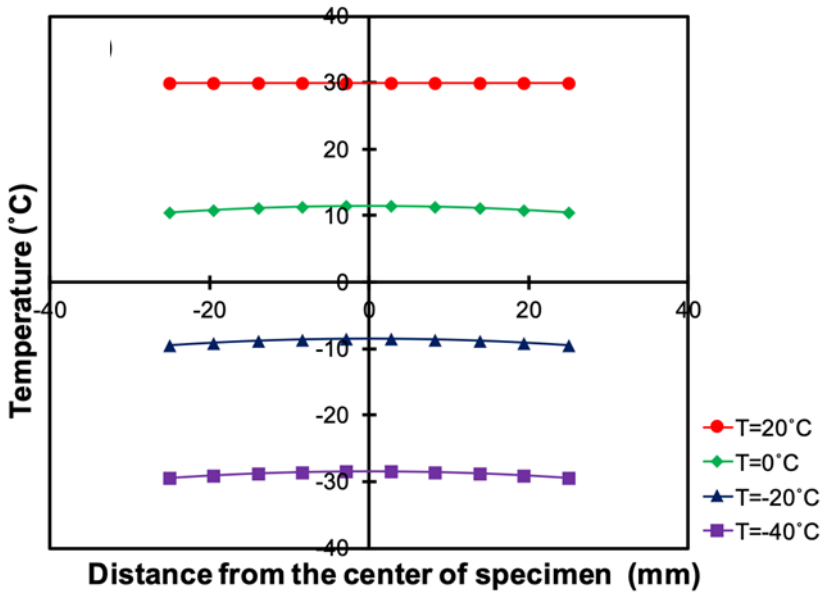

B. −10 °C/h.

Figure 6. Graphs. Temperature gradients within the sample at different instances of time for different rates of air temperature change.[(65)]

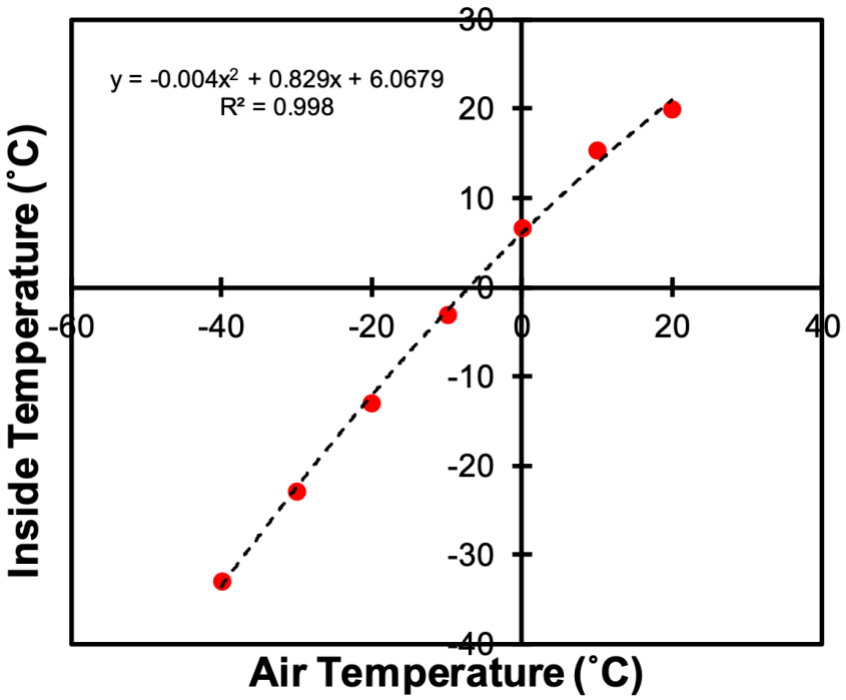

Figure 7. Graph. Averaged temperature evolution as a function of time.[65]

Methodology Used to Predict Mixture Coefficient of Thermal Contraction

This section derives and explains the basic formulation of the aforementioned composite model and also discusses different approaches for backcalculating the shear modulus ($|G(\omega)|$) values of mixtures from the given dynamic modulus data. Finally, this section draws comparisons between the parallel and series models.

An asphalt concrete mixture is a particulate composite material that consists of a single continuous phase (asphalt binder) and a single discontinuous particulate phase (aggregate). Researchers have developed simple methods to illustrate the principle of the behavior of a particulate composite under an external perturbation. Figure 8-A and figure 8-B show the simplest models in which the composite elements are positioned either in a series or in parallel, respectively, with respect to the external load.

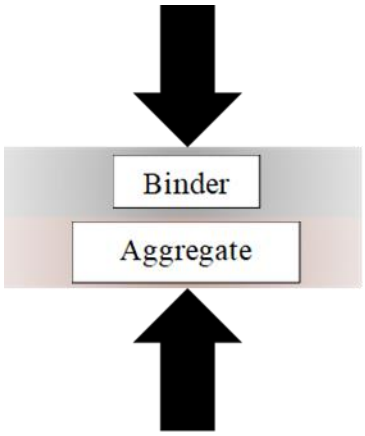

A. Series model.

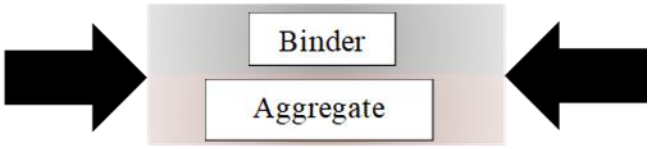

B. Parallel model.

Figure 8. Illustrations. Schematic view of composite elements in asphalt mixtures.[(65)]

Users can obtain different models through different assumptions about the relative position of these parallel and series models with respect to each other.

For the series model, once the binder and aggregate are positioned in a series, their deformation under external temperature variations can be considered independently. The total deformation can be calculated as equation 36.

$$l_{mixture} CTC_{mixture} VT = l_{binder} CTC_{binder} \Delta T + l_{aggregate} CTC_{aggregate} \Delta T \rightarrow$$

$$CTC_{mixture} = \frac{l_{binder}}{l_{mixture}} \times CTC_{binder} + \frac{l_{aggregate}}{l_{mixture}} \times CTC_{aggregate}$$

(36)

Where:

$l_{mixture}$ = representative length of the mixture.
$CTC_{mixture}$ = CTC of the mixture.
ΔT = temperature drop.
l_{binder} = representative length of the binder.
CTC_{binder} = CTC of the binder.
$l_{aggregate}$ = representative length of the aggregate.
$CTC_{aggregate}$ = CTC for the aggregate.

The volume fraction of the aggregate in an asphalt mixture can be assumed as equation 37.

$$Aggregate\,volume\ fraction = 1 - \frac{VMA}{100}$$

(37)

The relative length of the aggregate and binder in an asphalt mixture can be expressed as $\sqrt[3]{1-\frac{VMA}{100}}$ and $\sqrt[3]{\frac{VMA}{100}}$, respectively. Substituting these assumptions into equation 36 gives equation 38.

$$CTC_{mixture} = \sqrt[3]{\frac{VMA}{100}} \times CTC_{binder} + \sqrt[3]{1-\frac{VMA}{100}} \times CTC_{aggregate}$$

(38)

In the parallel model, due to the relative difference in thermal deformation between the aggregate and binder, an internal force occurs at the interface. Figure 9 shows the internal friction that occurs at the interface of the aggregate and binder.

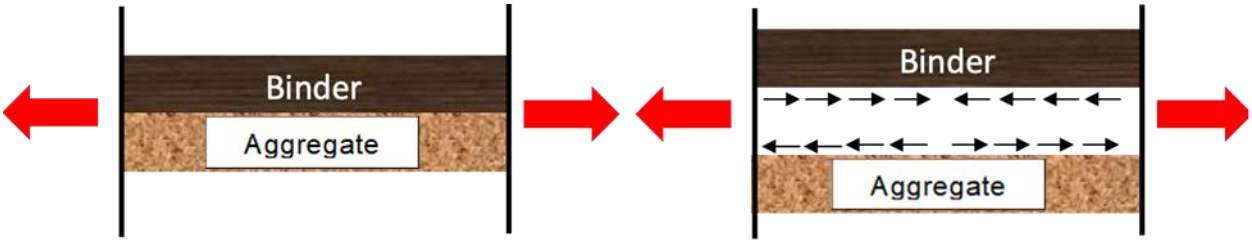

Figure 9. Illustration. Schematic view of building block of parallel model and internal force that occurs at the interface.[65]

Equation 39 expresses the displacement continuity between these two phases.

$$l_{mixture} \times CTC_{mixture} \times \Delta T = l_{mixture} \times CTC_{aggregate} \times \Delta T + \frac{F \times l_{mixture}}{A_{aggregate} \times E_{aggregate}} = l_{mixture} \times CTC_{binder} \times \Delta T - \frac{F \times l_{mixture}}{A_{binder} \times E_{binder}} \quad (39)$$

Where:

$A_{aggregate}$ = representative area of the aggregate.
A_{binder} = representative area of the binder.
F = internal force that is induced due to the difference in the relative contraction of the aggregate and binder.
$E_{aggregate}$ = elastic modulus of the aggregate.
E_{binder} = viscoelastic modulus of the binder.

Equation 39 can be simplified by removing the internal force between the two phases. Equation 40 expresses the final form for the two phases.

$$CTC_{mixture} = \frac{CTC_{aggregate} \times A_{aggregate} \times E_{aggregate} + CTC_{binder} \times A_{binder} \times E_{binder}(t)}{A_{aggregate} \times E_{aggregate} + A_{binder} \times E_{binder}(t)} \quad (40)$$

Equation 40 indicates that the parallel model requires the elastic modulus and CTC of the aggregate. Christensen and Bonaquist developed equation 41 to calculate the aggregate elastic modulus from the aggregate bulk specific gravity (G_{sb}).[63]

$$E_{aggregate} = 5,073 \times G_{sb}^{2.02} \quad (41)$$

The mixtures that were used in this research contain granite aggregate; the CTC of such aggregate is assumed to be 9e-6 (1/°C).[70]

As can be understood from equation 40, the parallel model does need the binder relaxation modulus, $E(t)$, to be given *a priori*. The binder relaxation modulus can be calculated from the binder shear modulus by converting the data obtained in the frequency domain to the time domain. Because the binder frequency sweep test is not commonly used in asphalt characterization procedures, the research team investigated different methods for backcalculating binder shear modulus data from given mixture dynamic modulus data.

The research team considered the following models for backcalculating the shear modulus of binder from the given dynamic modulus data:

- The Hirsch model.
- A modified Hirsch model.
- The 2S2P1D model.

Equation 42 and equation 43 show the Hirsch model, which requires the VMA, voids filled with asphalt (VFA), and the binder shear modulus, $|G^*|$, to predict the mixture dynamic modulus.

$$\left|E^*\right| = P_c \times \left(29,400 \times \left(1 - \frac{VMA}{100} \right) + 3 \times \left|G^*\right| \times \frac{VMA \times VFA}{10,000} \right) + \left(1 - P_c\right) \times \left(\frac{1 - \frac{VMA}{100}}{29,400} + \frac{VMA}{3 \times VFA \times \left|G^*\right|_{binder}} \right) \quad (42)$$

$$P_c = \frac{\left(0.138 + \frac{VFA \times 3 \times \left|G^*\right|_{binder}}{VMA} \right)^{0.58}}{36.2 + \left(0.138 + \frac{VFA \times 3 \times \left|G^*\right|_{binder}}{VMA} \right)^{0.58}} \quad (43)$$

The modified Hirsch model is shown as equation 44 and equation 45.

$$\left|E^*\right|_{mixture} = P_c \times \left(E_{aggregate} \times \left(1 - \frac{VMA}{100} \right) + 3 \times \left|G^*\right|_{binder} \times \frac{VMA \times VFA}{10,000} \right) \quad (44)$$

$$P_c = H_1 + \left(1 - H_1\right) \frac{\exp\left(H_2 + H_3 \times Ln\left(\frac{VFA}{100} \times \left|G^*\right|_{binder} \right) + H_4 \times VMA \times H_5 \times Ln\left(\varepsilon\right) \right)}{1 + \exp\left(H_2 + H_3 \times Ln\left(\frac{VFA}{100} \times \left|G^*\right|_{binder} \right) + H_4 \times VMA + H_5 \times Ln\left(\varepsilon\right) \right)} \quad (45)$$

This study used eight different mixtures that were studied as part of the New England High Reclaimed Asphalt Pavement Pooled Fund project to examine the accuracy of the different methods for predicting binder shear modulus data.[71] Sabouri et al. reported the volumetric properties of those mixtures.[72] Dynamic modulus measurements were taken of the mixtures at North Carolina State University and shear modulus tests of the extracted and recovered binders

were conducted at the University of Rutgers.[73] Table 6 presents details about the Vermont mixtures that were included in the New England project. VTa and VTe represent two different sources for the mixtures and the number after them is the percent of RAP in the mix. The research team fitted the measured dynamic moduli values using the 2S2P1D model developed by Olard and Di Benedetto.[74] The report by Daniel et al. provides details regarding the measurements of the shear moduli of the binders.[73]

Table 6. Summary of mixtures used to backcalculate binder shear modulus values from mixture dynamic modulus values.

Mix	Virgin PG	NMAS (mm)	RAP Content (percent)	VMA	VFA	G_{sb}
VTa00	52-34	9.5	0	20.2	76.3	2.744
VTa20	52-34	9.5	20	18.8	81.9	2.723
VTa30	52-34	9.5	30	17.7	82.9	2.713
VTa40	52-34	9.5	40	18	77.8	2.703
VTe00	64-28	9.5	0	20.3	71.5	2.744
VTe20	64-28	9.5	20	18.7	79.7	2.723
VTe30	64-28	9.5	30	19.1	75.9	2.713
VTe40	64-28	9.5	40	18.2	76.4	2.703

NMAS = nominal maximum aggregate size; G_{sb} = bulk specific gravity.

Figure 10 presents comparisons of the backcalculated and measured shear modulus values of the eight different Vermont mixtures. Figure 10 shows that the Hirsch and modified Hirsch methods overpredict the actual measured binder modulus values. This observation agrees with data reported in Sakhaiefar et al. in which the dynamic modulus values predicted using these two methods underpredicted the corresponding measured values.[54]

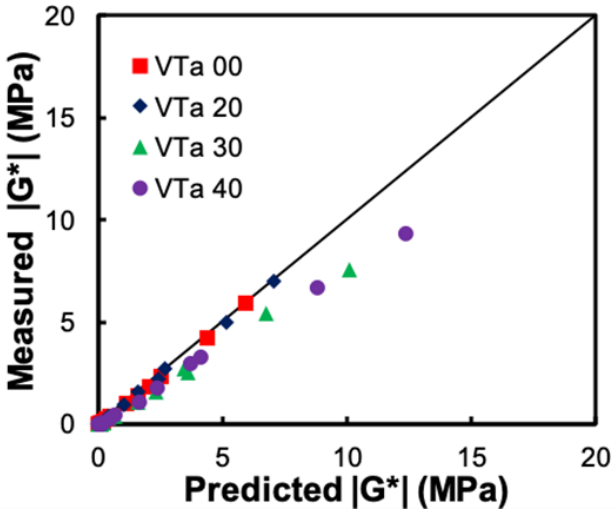

1 MPa = 145.04 psi.

A. Shear modulus values of binder in VTa mixtures backcalculated from the Hirsch model.

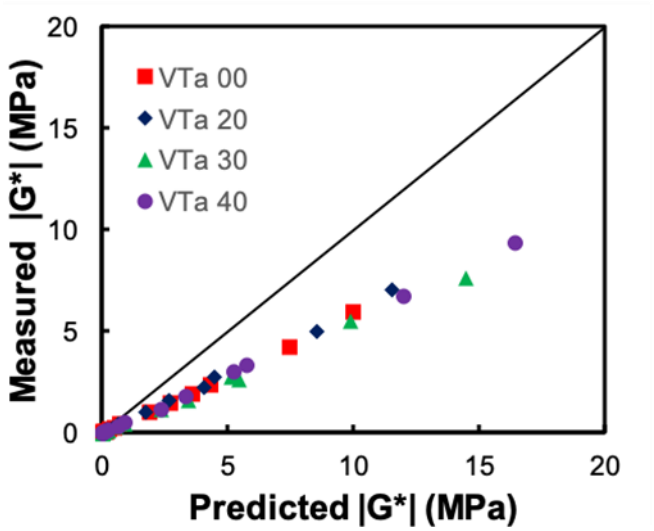

B. Shear modulus values of binder in VTa mixtures backcalculated from the modified Hirsch model.

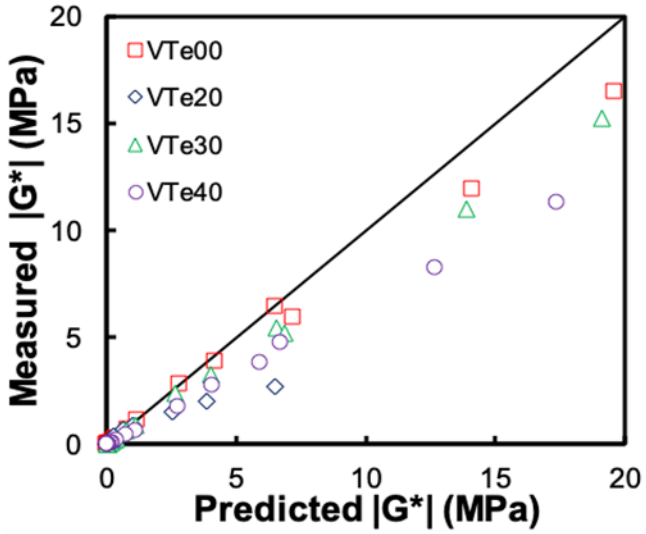

C. Shear modulus values of binder in VTe mixtures backcalculated from the Hirsch model.

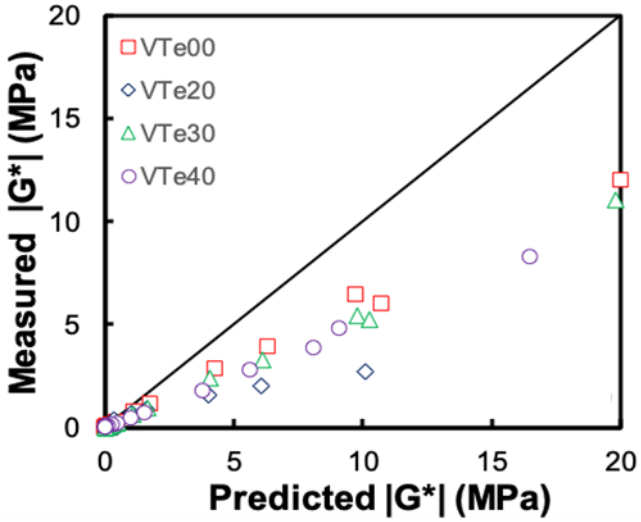

D. Shear modulus values of binder in VTe mixtures backcalculated from the modified Hirsch model.

Figure 10. Graphs. Comparison between backcalculated and measured binder shear modulus (|G*|) data for eight mixtures obtained using the Hirsch and modified Hirsch models.(65)

Olard and Di Benedetto proved that the parameters obtained from fitting mixture dynamic modulus data and binder data correlate with the 2S2P1D formula. Equations 46 and 47 express the 2S2P1D formula for mixtures.(74)

$$E^*(\omega) = E_0 + \frac{E_\infty - E_0}{1 + \delta(i\omega\tau)^{-\kappa} + (i\omega\tau)^{-h} + (i\omega\tau)^{-1}} \quad (46)$$

$$\tau = \tau_0 a_T \quad (47)$$

Where:

i = square root of −1.
a_T = t-TS factor for mixtures.
E_0 = lower asymptote of the mixture modulus.
E_∞ = glassy modulus of the mixture.
δ, τ_0, k, and h = fitting parameters.

A Marasteanu et al. report provides details regarding the physical meanings of the 2S2P1D fitting parameters.(43)

Equation 48 and equation 49 show the 2S2P1D formula for binders.

$$E^*_{binder} = E_{0-binder} + \frac{E_{\infty-binder} - E_{0-binder}}{1 + \delta(i\omega\tau)^{-k} + (i\omega\tau)^{-h} + (i\omega\beta\tau_{binder})^{-1}} \quad (48)$$

$$\tau_{binder} = \tau_{0\_binder} \times a_T \quad (49)$$

Where:

$E_{0\text{-}binder}$ = lower asymptote value of the binder elastic modulus.
E_{∞_binder} = binder glassy modulus.

The measured data show that the $E_{0\text{-}binder}$ value is low and can be ignored in comparison with all the other parameters.(74) Olard and Di Benedetto and Marasteanu et al. proved that the δ, k, h, and β parameters are equal for any mixture and its binder.(43)

Also, Underwood and Kim have proven that the t-TS factor is the same for mixtures and binders.(75) The only remaining parameter is the τ_0 parameter, which is the characteristic time of a material and has been shown to differ between mixtures and binders. Olard and Di Benedetto tried to find a relationship between the τ_0 of binders and mixtures, as expressed in equation 50.(74)

$$\tau_{0-mixture} = 10^{2.66} \times \tau_{0-binder} \quad (50)$$

Olard and Di Benedetto stated that this relationship is empirical and depends on the mix design and aging conditions during mixing.(74) Later, Marasteanu et al. studied additional mixtures and introduced equation 51 for relating the characteristic times of binders and mixtures.(43)

$$\tau_{0-mixture} = 10^{3.17} \times \tau_{0-binder} \quad (51)$$

Marasteanu et al. tested different binder grades and mixtures with different aggregate types that contained those binders.(43) Marasteanu et al. concluded that the characteristic time of a binder and mixture depends on the mixture design. This research used equation 51 to correlate the characteristic times of mixtures and binders.

Substituting all the fitted parameters from the mixture dynamic modulus fitting in the 2S2P1D formula gives equation 52 and equation 53, which expresses the relationship between the binder properties that can be obtained from fitting the 2S2P1D relationship to the mixture dynamic modulus data. This research assumes the binder shear glassy modulus to have a global value of 2 GPa. This value is similar to the measured data from the Olard and Di Benedetto study.(74) Poisson's ratio of the binder is assumed to be 0.5.

$$\frac{E^*_{binder}}{E_{G\_binder}} = \frac{1}{1+\delta_{mixture}\times\left(i\omega\tau_{0,binder}a_T\right)^{-h_{mixture}}+\left(i\omega\tau_{0,binder}a_T\right)^{-k_{mixture}}+\left(i\omega\tau_{0,binder}a_T\right)^{-1}} \tag{52}$$

$$E_{G\_binder} = 2{,}000\times 2\times(1+0.5) = 6{,}000\ MPa \tag{53}$$

Where:

E^*_{binder} = viscoelastic moduli of binder.
$E_{G\text{-}binder}$ = glassy moduli of binder.
ω = radial frequency.
τ, h, k, δ = fitting parameters related to the 2S2P1D model.
a_T = t-TS factor for the mixture.
i = squared root of −1.

The 2S2P1D fitting parameters (h, k, δ) can be obtained from fitting the mixture dynamic modulus data to the 2S2P1D formula (Olard and Di Beneditto).(74) τ can be obtained from fitting the mixture dynamic modulus measurements and then converting them to the corresponding values for binder using equation 51.

The research team used equation 52 to backcalculate the elastic modulus, shear modulus, and phase angle of the binder for the Vermont mixtures. Figure 11 presents comparisons of the predicted values using the 2S2P1D approach and the measured values. Figure 11 proves that the 2S2P1D formula can predict the shear modulus and phase angle of binders. This formula can be used to backcalculate the binder shear modulus and phase angle from the given measured dynamic modulus data of a mixture.

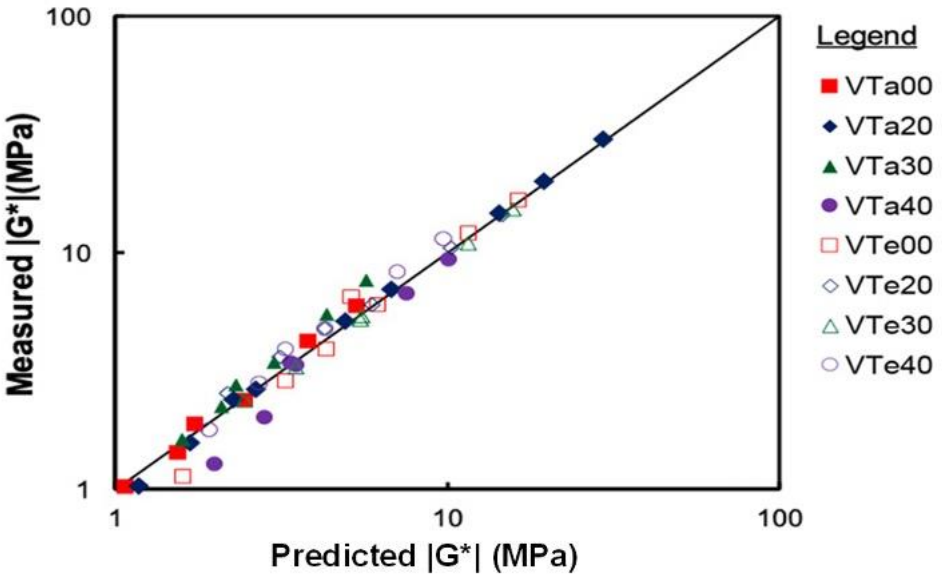

A. |*G**| comparison in log-log scale.

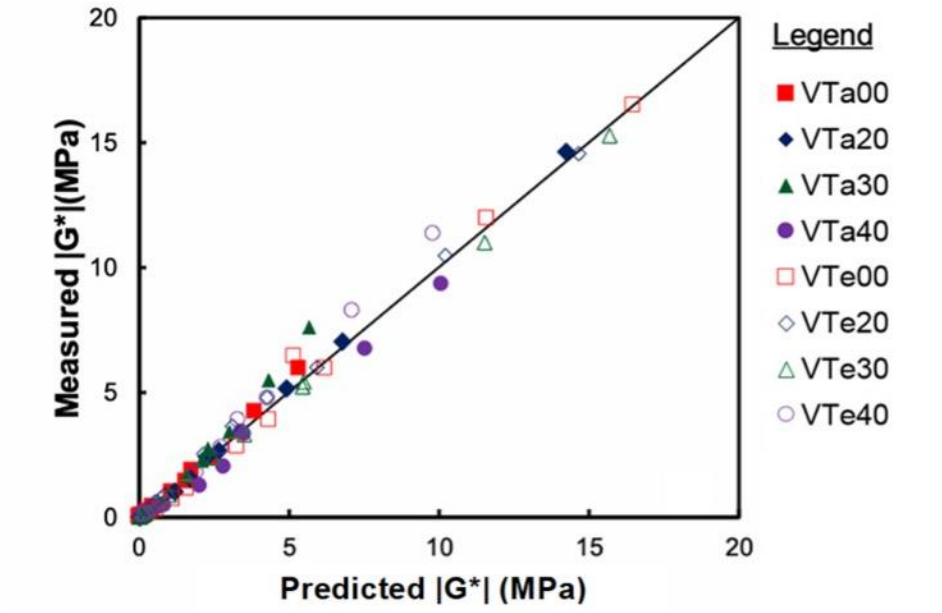

B. |*G**| comparison in arithmetic scale.

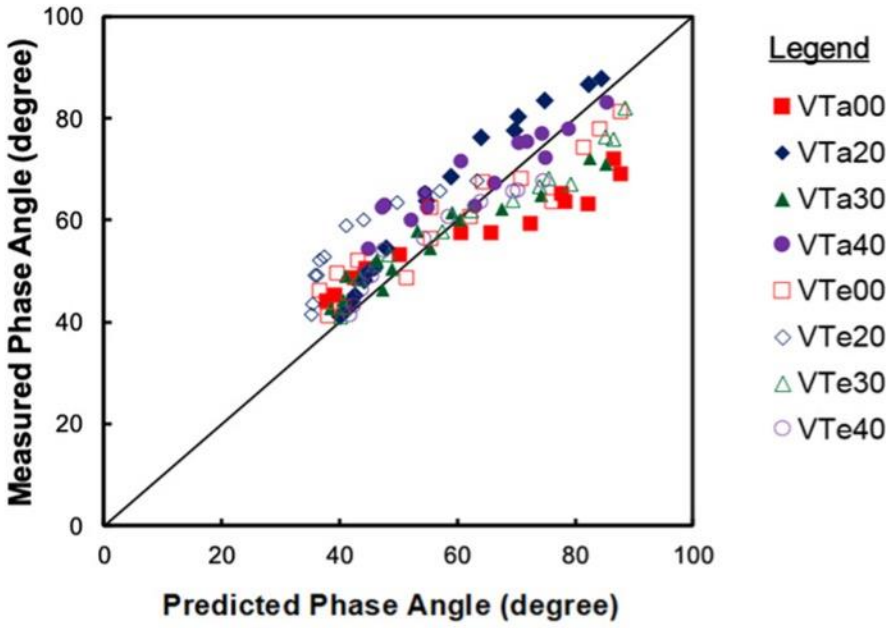

C. Phase angle comparison.

Figure 11. Graphs. Comparisons of predicted shear modulus |G*| and phase angle data for Vermont mixtures using the 2S2P1D approach with measured data.[(65)]

As can be observed, the relaxation modulus or $E(t)$ of the binder is a required parameter for predicting the CTC of a mixture. The research team used the collocation method to convert the elastic modulus of binder in the frequency domain to the relaxation modulus of binder in the time domain. Equation 54 and equation 55 express the Prony series form of the shear modulus in the time domain and the storage modulus in the frequency domain.

$$E(t) = E_{\infty} + \sum_{j=1}^{m} E_j \exp\left(-\frac{t}{\rho_j}\right) \tag{54}$$

$$E'(\omega) = E_{\infty} + \sum_{j=1}^{m} \frac{\omega^2 \rho_j^2 E_j}{\omega^2 \rho_j^2 + 1} \tag{55}$$

Finding the binder's relaxation modulus $E(t)$ from the given dynamic modulus of the mixture allows comparisons of the predicted CTC values obtained from the parallel and series models with the actual measured values, as presented in figure 12.

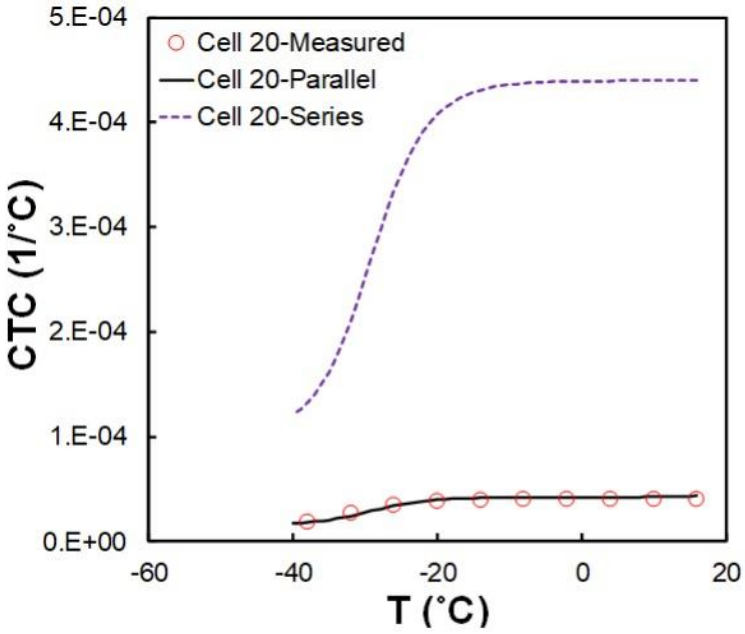

A. Cell 20.

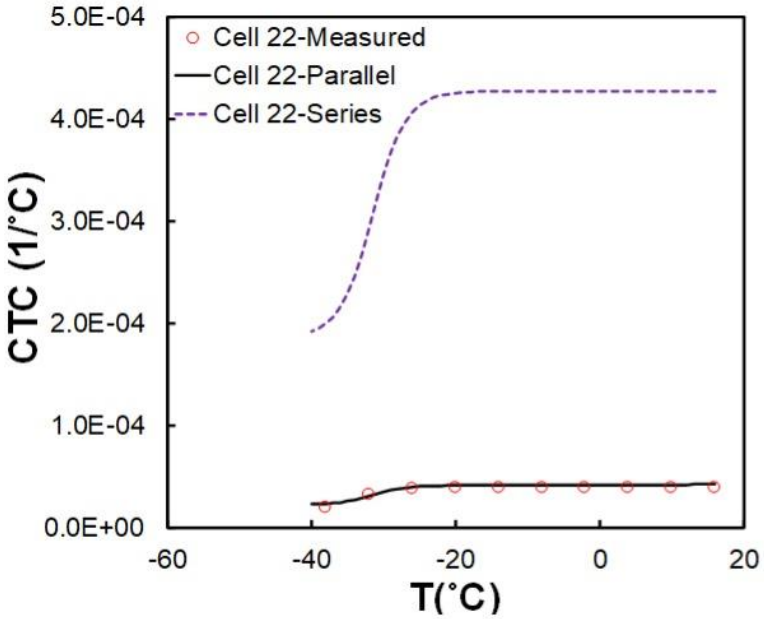

B. Cell 22.

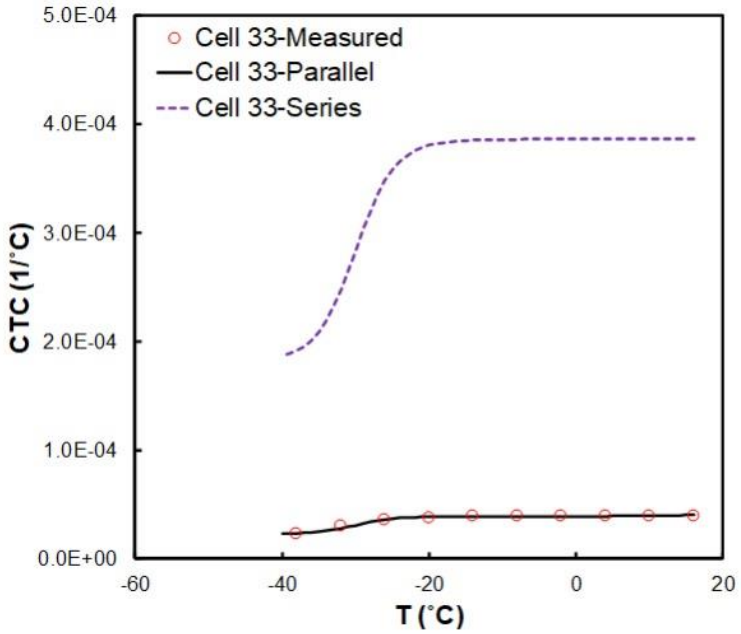

C. Cell 33.

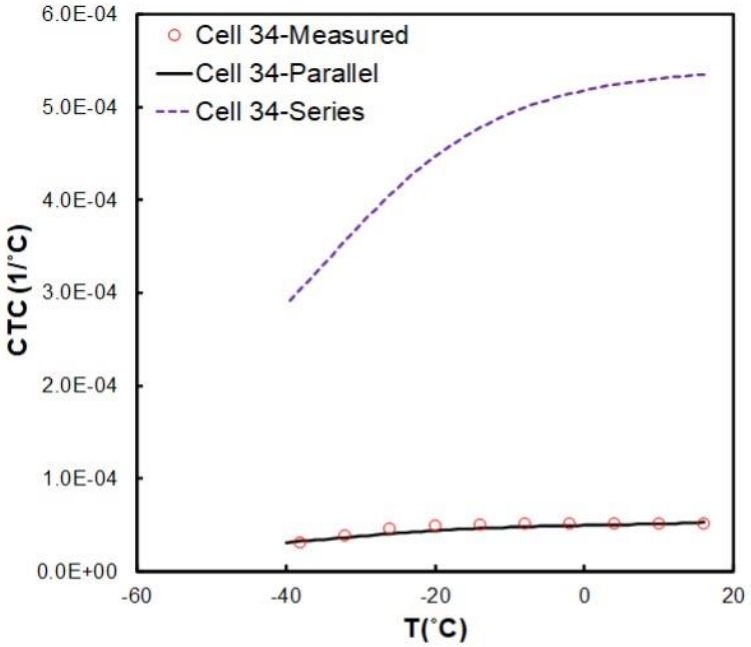

D. Cell 34.

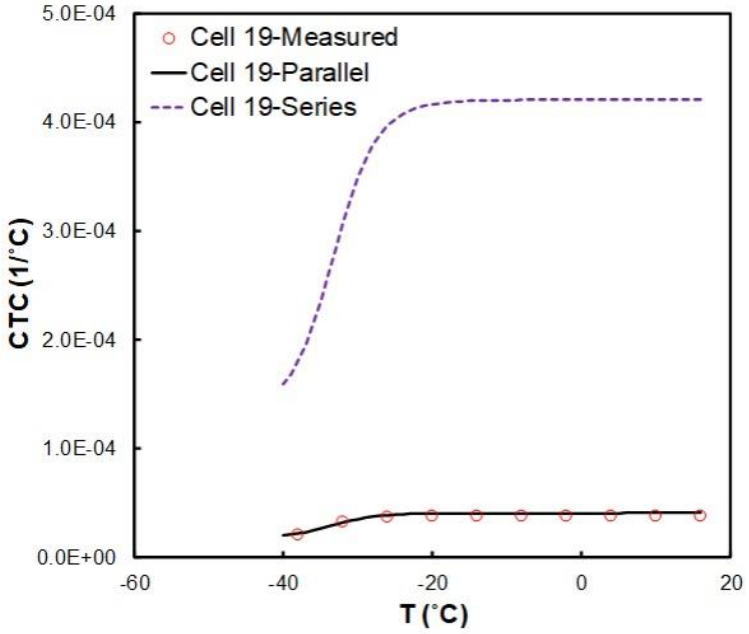

E. Cell 19.

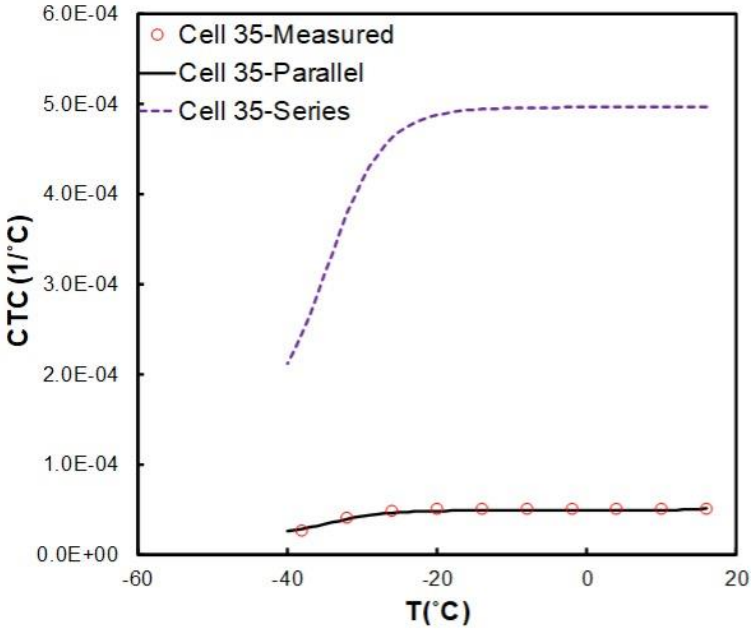

F. Cell 35.

Figure 12. Graphs. Comparisons of predicted CTCs obtained from parallel and series models with actual measured values.[(65)]

Results and Discussion

Figure 13 presents a comparison between the measurements and predictions for level II analysis of the CTC parameter for the temperature range of 20 °C to −40 °C. As shown, the proposed methodology can capture the CTC variation with good accuracy. Although level II analysis requires the measured CTC of the binder a priori, level III uses the clustering method to obtain the thermo-volumetric properties of the binder. Figure 14 presents comparisons between the predictions obtained from level III analysis and measurements from the two datasets of the mixtures. More scatter can be observed in figure 14 than in figure 13. The scatter in the high CTC value ranges shown in figure 14 requires further analysis to determine the effect of this error on the accuracy of the induced stress predictions in asphalt pavements.

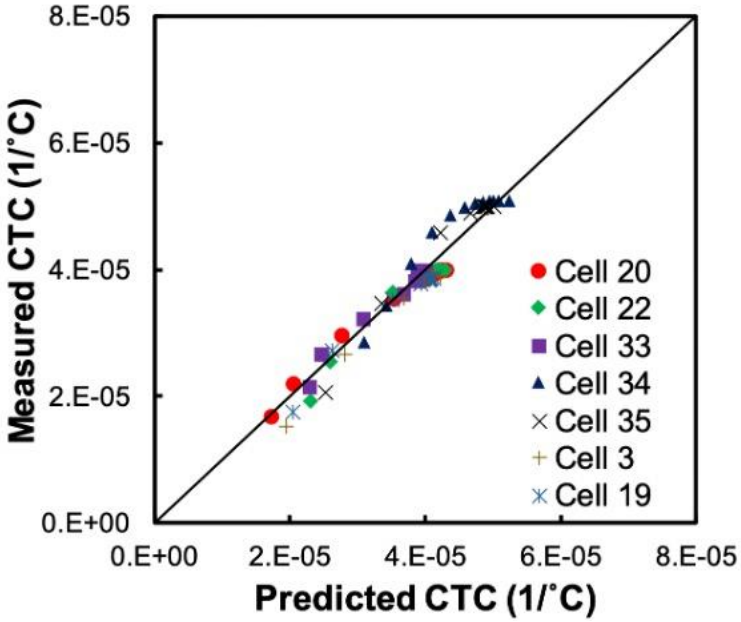

Figure 13. Graph. Comparison of predicted CTCs obtained from equation 40 (level II) and measured data obtained from Marasteanu et al.[(65)]

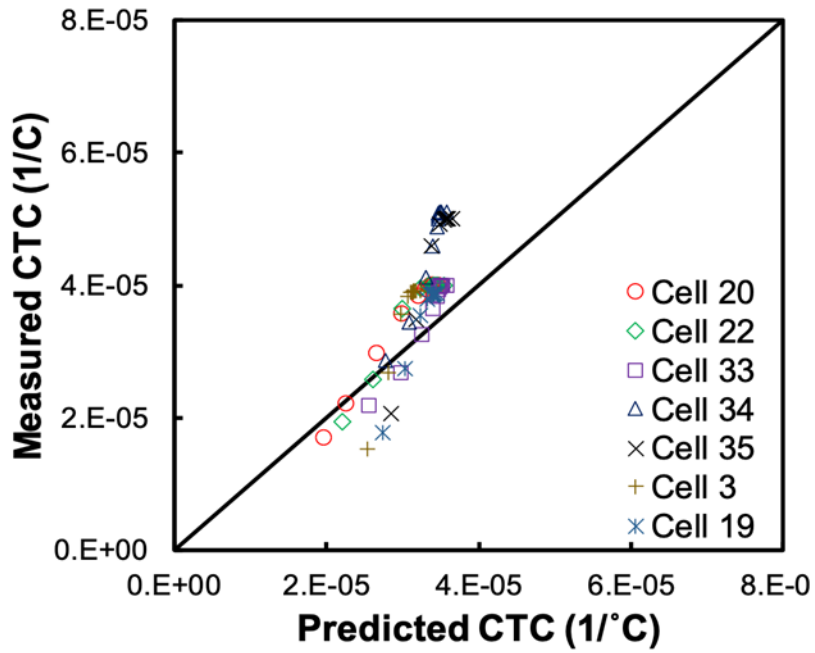

A. Data obtained from Marasteanu et al.

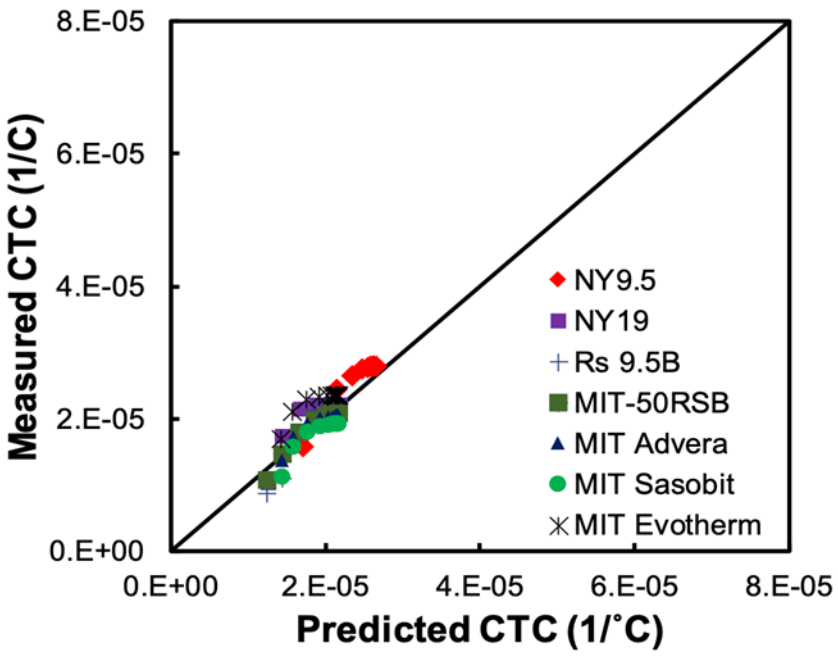

B. Data obtained from North Carolina State University researchers.

Figure 14. Graphs. Comparison of predicted CTCs of mixtures obtained from level III analysis and measured data.[(65)]

To evaluate the effect of the error shown in figure 14 on thermal stress in asphalt pavements, a typical structure is considered for predicting the thermal distribution. The research team used EICM software to calculate the temperature distribution in the pavement sections based on the given air temperature data.[13,76] The pavement structure used in the EICM has a 4-inch thick asphalt layer on top of a 12-inch thick aggregate base layer.

Figure 15 presents a comparison between the stress predicted from the measured CTCs (level I) and the predicted CTCs obtained from levels II and III for the first and second datasets. Figure 15-A proves the ability of the level II analysis. Figure 15-A and figure 15-C present comparisons of the stress values obtained based on level III analysis and the corresponding stress values calculated from level I analysis. The comparison proves that level III analysis can match the results of level I analysis.

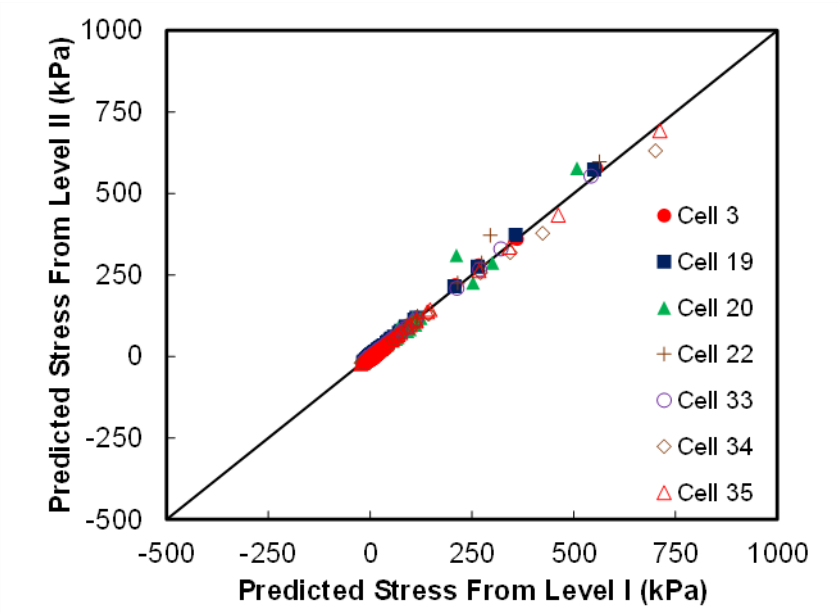

1 kPa = 0.145 psi.

A. Obtained from levels I and II for first dataset.

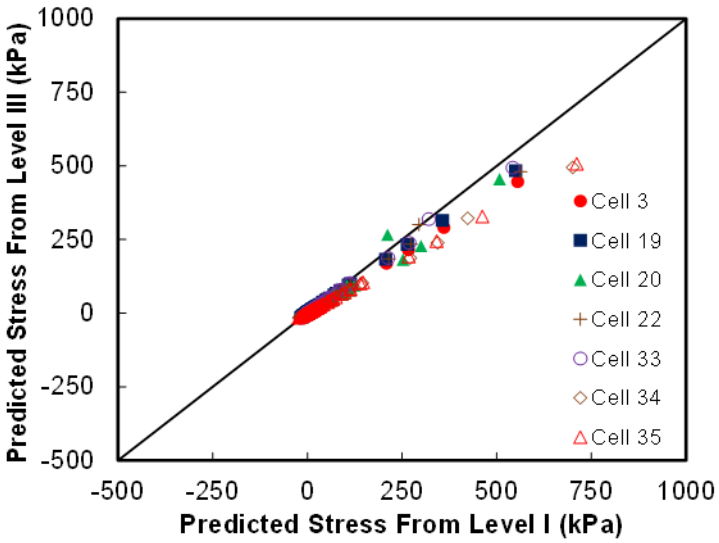

B. Obtained from levels I and III for first dataset.

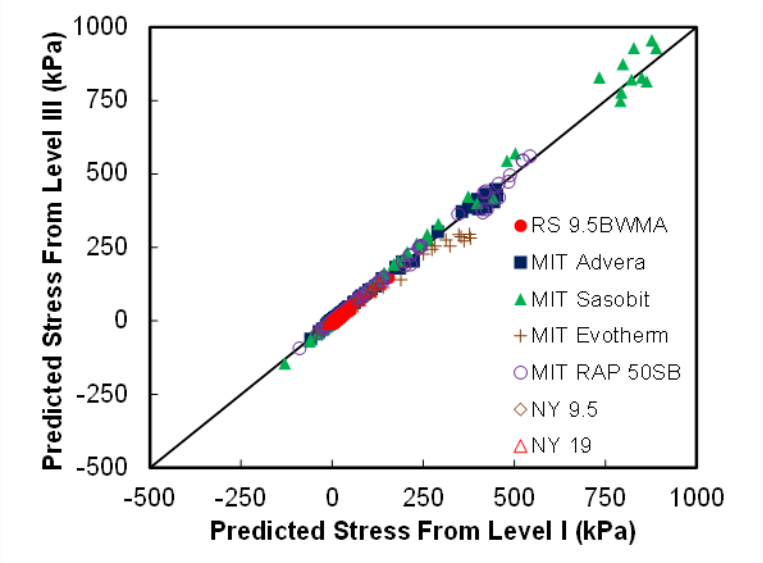

Note: RS9.5BWMA is a 9.5 mm surface mixture with warm-mix additive and PG 64-22 binder.

C. Obtained from levels I and III for second dataset.

Figure 15. Graphs. Comparison of predicted thermal stress values.[(65)]

Summary

This section presents the results of an experimental study to measure the CTCs of asphalt mixtures and the results of an analytical study to predict the mixture CTC from given volumetric and mechanical properties. The CTC describes how mixtures behave when subjected to thermal

variation, and thus is a fundamental parameter for thermal cracking analysis. The test developed to measure the CTCs was successful and all the approaches developed for this study provided reasonable predictions of this parameter and will allow fewer testing requirements.

Three levels of analysis were developed in this study. Level I is used to measure the CTC of a mixture, which requires a device that can control the temperature at a given rate. In addition, to eliminate LVDT contraction during the test, level I requires LVDTs to be calibrated against thermal deformation before mixture testing. The research team used a ZERODUR sample for this task.[10]

Both level II and level III are analytical methods in which the CTC can be obtained with reduced testing effort. Level II employs a simple yet efficient method (a composite model) that can predict the mixture CTC for a broad range of temperatures. The model requires the aggregate modulus of elasticity, aggregate CTC, mixture volumetric properties, and binder relaxation modulus and thermo-volumetric properties. The research team investigated different methods for backcalculating the binder modulus from the given mixture modulus. The 2S2P1D formulation was able to provide a good estimation of the binder modulus and phase angle. Also, the binder thermo-volumetric properties measured and reported in the literature can be grouped based on their low PG, which comprises level III analysis.[65]

The mixtures included in the experimental plan to measure the CTCs cover a broad range of binder PG, additives, and RAP content. The research team also predicted the CTCs of those mixtures using the composite model and level III analysis. The results indicate that level III can provide reasonable predictions of mixture CTCs for a wide range of temperatures, with minimal testing effort. The research team also verified level II through predicting the data reported in the literature that include both mixture and binder measurements. Level II can provide a good approximation of the measurements analyzed in level I without the need for CTC tests.

To study the effect of error in the mixture CTC predictions, the research team compared the induced thermal stress in a representative volume element sample subjected to thermal variation using the measured CTC or predicted CTC from level II or III analyses. The stress predicted using level II and III agree with the stress predicted using level I, proving the accuracy of the approaches presented herein.

Predicting Thermal Stress Restrained Specimen Test Fracture Using the Dissipated Pseudostrain Energy Criterion

TSRST is one of a few tests that can simulate thermal loading in the field.[77–79] Conducting TSRSTs is a time-consuming task, therefore, a methodology is needed to predict the fracture temperature of asphalt mixtures that is measured by TSRSTs. This study utilized DPSE, which can be predicted using S-VECD theory, as a failure criterion to predict the fracture temperature of asphalt mixtures. The results show that the DPSE failure criterion can differentiate the mixtures' thermal cracking performance based on differences in the mixtures' volumetric properties. The results also show that the predicted mixture performance matches the field rankings reasonably well. The next section presents a brief review of the TSRST and gives details about the predictive methodology.

Literature Review on Thermal Stress Restrained Specimen Tests

In TSRSTs, the asphalt concrete specimen is subjected to cooling while its ends are restrained from any movement. This restriction is similar to thermal loading in the field, where asphalt material, due to the long length of the pavement in the traffic direction, is restrained at both ends. Due to the imposed restriction in TSRSTs, thermal stress occurs in the asphalt concrete sample. That is, as the temperature decreases in the test chamber, thermal stress builds up and damage occurs in the asphalt concrete specimen. At a certain temperature, the sample is unable to support any more loading and fails.[80] This report refers to the temperature and stress associated with this failure as the fracture temperature and fracture stress, respectively.

Researchers developed the TSRST as part of the SHRP.[79] Jung and Vinson studied the effects of binder type, aging level, and cooling rate on TSRST results (i.e., the fracture stress and fracture temperature) and found that an increase in the cooling rate leads to an increase in fracture stress. Jung and Vinson found a similar trend for fracture temperature. These researchers also found that aging increases the fracture temperature while decreasing the fracture stress and that the fracture temperature shows less variability than the fracture stress. Therefore, fracture temperature is used as the index criterion for low-temperature mixture evaluations.

The uniaxial thermal stress and strain test, developed by Morian, is a modification of TSRST where the loading platen and gluing technique are altered and an additional unrestrained sample is used to determine the thermal strain of the mixture sample.[81] The restrained and unrestrained samples are subjected concurrently to temperature variation.

Alavi studied the fracture properties of different mixtures as a function of aging and related aging to the carbonyl content in the mixture.[77] Alavi found that aging can significantly increase the fracture temperature and decrease the fracture stress.[80] Alavi defined crack initiation stress as the point at which the material shows the highest modulus value. Crack initiation is believed to indicate the time at which microdamage starts in the material. Alavi developed a relationship to correlate the crack initiation in the material with the carbonyl level.

Jung and Vinson applied the cooling rate of −10 °C/h, which various researchers have since adopted because applying that rate decreases the testing time.[78] Cortez found that the maximum daily cooling rate ranges from −1.4 °C/h to −2.7 °C/h based on analysis of measured pavement temperature data obtained at several Long-Term Pavement Performance (LTPP) program road sections located in mountain regions (i.e., Nevada, Utah, Idaho, Arizona, Colorado, and New Mexico).[81] As a result of this overestimation of the cooling rate, the fracture temperatures measured by TSRSTs using the cooling rate of −10 °C/h may not accurately represent the thermal cracking performance of in-service pavements.

Chehab and Kim used viscoelastic continuum damage (VECD) theory to predict the induced stress in TSRSTs and the fracture stress and fracture temperature.[79] Chehab and Kim measured the strength and failure strain of asphalt concrete using uniaxial direct tension monotonic tests at a constant reduced strain rate to construct strength and failure strain master curves, respectively. Both the strength and failure strain master curves can be expressed as a function of reduced strain rate and can cover a broad range of rates and temperatures. Chehab and Kim intersected the induced stress and thermal strain curves predicted for the TSRST with the measured strength

and failure strain master curves and expressed the intersection points as the failure. Average values of the fracture parameters obtained using the strength and failure strain criteria were in good agreement with the measured values.

Measurement of the fracture temperature is a cumbersome task that requires substantial testing effort. The fracture temperature measured in TSRSTs is a function of cooling rate and the temperature at which the test starts. These factors make developing a predictive methodology that can predict the TSRST fracture temperature rather than measuring the fracture temperature through the TSRST desirable. Another advantage of a predictive methodology is that the fracture temperature under a wide range of temperatures and cooling rates can be estimated without having to perform many TSRSTs. Based on this need, Keshavarzi and Kim developed the DPSE failure criterion that is based on S-VECD theory and showed that the fracture temperature and fracture stress predicted using the DPSE failure criterion and the S-VECD model are in good agreement with the values measured by the TSRST.[82] One of the major advantages of this predictive methodology is that the material properties required for the thermal fracture predictions can be obtained from AMPT dynamic modulus and cyclic fatigue tests, which are used to characterize fatigue cracking (both top-down and bottom-up cracking) using the S-VECD model.[83,84] That is, researchers can use a single set of tests to predict both fatigue cracking (both top-down and bottom-up) and thermal cracking. The ability of the DPSE failure criterion to differentiate (and rank) the performance of eight pavement sections constructed at MnROAD is proven in this study of the cracking potential of asphalt mixtures with different mixture factors.[11,64] To evaluate the DPSE failure criterion further, the research team aged the asphalt mixtures at two levels, STA and LTA, and followed the procedure suggested by NCHRP 09-54 for aging the mixtures in the laboratory.[17]

Study Mixtures

The research team selected eight mixtures from the 2016 MnROAD cracking study and used those mixtures to construct the surface layer of MnROAD pavement sections with a 12.5-cm thick asphalt layer.[11,64] The pavement sections have 79 cm of combined base and subgrade. Table 7 presents the properties of the mixtures used in this study.

Table 7. Properties of MnROAD mixtures.

Mixture ID	RAP (percent)	RAS (percent)	NMAS (mm)	AC (percent)	Binder Grade	Design Air Voids (percent)
Cell 16	20	5	9.5	5.0	PG 64S-22	4
Cell 17	10	5	9.5	5.3	PG 64S-22	4
Cell 18	20	0	9.5	5.1	PG 64S-22	4
Cell 19	20	0	9.5	5.7	PG 64S-22	3
Cell 20	30	0	12.5	5.0	PG 52S-34	4
Cell 21	20	0	9.5	5.2	PG 58H-34	4
Cell 22	20	0	12.5	5.4	PG 58H-34	4
Cell 23	15	0	12.5	5.2	PG 64E-34	4

AC = asphalt content.

As mentioned, aging affects the different thermal cracking mechanisms. Therefore, the effects of aging should be included in the mixture characterization protocol. This study followed the standard method for performance testing of asphalt mixtures proposed by NCHRP 09-54 to simulate a minimum of two levels of aging: LTA and STA.[17] This aging procedure was developed, calibrated, and validated using component materials of pavement sections that were subjected to up to 21 yr of field aging.[85] The MnROAD mixtures were aged for 3 d to cover the aging evolution of the surface layers in the MnROAD sections for 4 yr.[11,64] The MnROAD sections were constructed in August 2016 and the condition survey used in this study was conducted in April 2019, which is approximately 2.7 yr after construction. Therefore, 3 d of aging, which corresponds to 4 yr of aging in service, were too long to represent the mixtures' conditions at the time of the condition survey. This study's eight mixtures were tested at each aging level to obtain their linear viscoelastic and fatigue properties.

Required Material Properties and Test Methods

Coefficient of Thermal Contraction

The drop in a test chamber's air temperature is the driving factor for failing mixtures used in TSRSTs. The temperature variation can be translated to induced thermal strain through the CTC parameter, defined here as equation 56.

$$\varepsilon_{total} = \varepsilon_{mechanical} + \varepsilon_{thermal} = 0 \rightarrow \varepsilon_{mechanical} = -CTC \times \left(T - T_0\right) \tag{56}$$

Where:

ε_{total} = total strain induced in the specimen and kept constant (i.e., zero) during the test.
$\varepsilon_{mechanical}$ = mechanical strain.
$\varepsilon_{thermal}$ = thermal strain.
T = temperature.
T_0 = starting temperature for the TSRST.

The CTC determines how much strain is imposed on the material and, as a result, has a significant effect on the predicted thermal cracking performance of pavement sections. This study compares the fracture temperatures predicted from the measured and predicted CTCs of the study mixtures. The rest of this section summarizes the measurement and prediction methodologies.

CTC of the study mixtures is measured using the ZERODUR method described in the previous section.[10] Equation 57 presents the CTC function used to fit the measured CTC values.

$$CTC\left(T\right) = CTC_g + \left(CTC_l - CTC_g\right) \times \frac{e^{\frac{T - T_g}{R}}}{1 + e^{\frac{T - T_g}{R}}} \tag{57}$$

The asphalt mixture samples were subjected to a constant rate of temperature drop of −30 °C/h. Each test was started at 20 °C and ended at −40 °C. Four LVDTs were attached to the specimen to record the thermal strain during thermal loading. For the CTC measurements taken in this study, the research team used a ZERODUR sample, which has insignificant thermal contraction, to determine the deformation of the LVDTs as the temperature dropped, which the team in turn used to adjust the LVDT measurements obtained from the sample.[10] The research team used a dummy sample placed inside the test chamber to record the temperatures at the center and surface of the sample and the air temperature. The team averaged the center and surface temperatures of the dummy sample and used that average as the material's temperature.

The research team used equation 58 to fit the thermal strain data and find the CTC parameters.

$$l = c_v + CTC_g \times \left(T - T_g\right) + R \times \left(CTC_l - CTC_g\right) \times Ln\left(1 + \exp\left(\frac{T - T_g}{R}\right)\right) \quad (58)$$

Where:

l = sample length.
c_v = constant.

The CTCs of the study mixtures are also predicted using the algorithm suggested by Keshavarzi et al. and presented in the previous Methodology Used to Predict Mixture Coefficient of Thermal Contraction section.[65]

The binder modulus (E_{binder}) is backcalculated from the mixture modulus using the 2S2P1D method. CTC_{binder} is obtained from a database that was developed using characteristics of various binders and binder CTC measurements reported in the literature.[65] The database presents the binder CTC parameters (i.e., CTC_g, CTC_l, T_g, and R) as a function of the LPG of the binder. Details about these properties are available elsewhere.[65]

Dynamic Modulus and Phase Angle

The degree of the stress development is a function of the CTC and the material's stiffness. Researchers have studied and suggested various methods to predict mixture stiffness for a wide range of temperatures and frequencies based on different function forms or volumetric properties.[74,86,87] The North Carolina State University research team also investigated different forms of dynamic modulus master curves and t-TS factors and found that together the 2S2P1D function (equation 46) for the mixture dynamic modulus master curve and a second-order polynomial function (equation 59) for the t-TS factor are able to predict the mixture's dynamic modulus and phase angle at temperatures lower than the test temperatures suggested by AASHTO TP 132 (4 °C, 20 °C, and 40 °C).[88]

$$\log(a_T) = a_1 T^2 + a_2 T + a_3$$

(59)

Where:

E^* = complex modulus.
E_0 = fluid modulus of the asphalt mixture (lower asymptote).
E_∞ = glassy modulus.
ω = loading frequency.
i = square root of −1.
δ, τ_0, k, h, β = model coefficients that are specific to the mixture.
a_T = the t-TS factor.
a_1, a_2, a_3 = t-TS function coefficients.

In this study, dynamic modulus tests were carried out using an AMPT according to AASHTO TP 132.[89] Small test specimens, 38 mm in diameter and 110 mm in height, cut and cored from a gyratory-compacted sample 150 mm in diameter and 180 mm in height, were fabricated according to AASHTO PP 99.[90] The eight study mixtures were tested at three temperatures (4 °C, 20 °C, and 40 °C) and at six test frequencies ranging from 0.1 to 25 Hz.

Failure Criterion

Induced stress depends on the material's stiffness and level of damage. The S-VECD model is a framework that has gained attention because it can keep track of the material's integrity.[91] The S-VECD model framework can predict the evolution of microdamage within a material using parameters that are measurable at the macroscale.[29] S-VECD theory, which is based on Schapery's work potential theory, which was built on thermodynamic principles, quantifies damage by defining an internal state variable (S).[92] Keshavarzi and Kim showed that the induced stress within a representative volume element sample in a uniaxial direct tension monotonic test can be predicted by using the data measured in a uniaxial direct tension cyclic fatigue test. Keshavarzi and Kim later measured the DPSE of mixtures and correlated the DPSE to the induced reduced strain rate in a uniaxial direct tension monotonic test (shown in equation 61), as described in equation 60.

$$DPSE = \int_0^{\xi_f} \varepsilon_R^2 \times (1 - C) d\xi \le a(C_0) \times \varepsilon_r^{\bullet b(C_0)}$$

(60)

$$\varepsilon_r^g = CTC \times \frac{\Delta T}{\Delta t} \times a_T$$

(61)

Where:

ε_R = pseudostrain.
C = pseudostiffness.
ξ = reduced time.

C_0 = current damage level.
a, b =material properties that depend on the damage level.
ε_r = reduced strain rate.
ΔT = difference in temperature.
Δt = difference in time.

The research team conducted cyclic fatigue testing using an AMPT in accordance with AASHTO TP 133.[93] The testing frequency was 10 Hz. Multiple tests were conducted for each mixture at different strain levels.

Predictive Methodology for Fracture Used in Thermal Stress Restrained Specimen Test

This section uses the DPSE failure criterion to predict the TSRST fracture temperature. The heat equation, equation 62, can be solved numerically to calculate the temperature distribution within the sample.

$$\frac{\partial T}{\partial t} = k\frac{\partial^2 T}{\partial t^2} \tag{62}$$

Where:
T = temperature
k = heat diffusivity
t = time.

Equation 63 and equation 64 are used to keep track of the material integrity, C, during the test.

$$\frac{dC}{dt} = \lambda\left(1-C\right)^{(1+\alpha)\left(1-\frac{1}{C_{12}}\right)} \times \left(\int_o^t E\left(t-\xi\right)\frac{d}{d\xi}\left(CTC\times\left(T-T_0\right)\right)d\xi\right)^{2\alpha} \tag{63}$$

$$\lambda = \left(\frac{1}{2}\times C_{11}\times C_{12}\right)^{1+\alpha} \times \left(\frac{1}{C_{11}}\right)^{(1+\alpha)\left(1-\frac{1}{C_{12}}\right)} \tag{64}$$

Where:
C = pseudostiffness and represents material integrity.
t = reduced time.
C_{11}, C_{12}, α = material parameters.
E = mixture's relaxation modulus.
ξ = integration parameter.
T_0 = temperature at which the test starts.

This study assumes that T_0 = 5 °C for all the simulations. Knowing the evolution of C, the DPSE can be calculated from equation 60. The intersection of the DPSE evolution curve with the failure criterion curve can be used to detect failure. The reduced strain rate, expressed as equation 61, at the time of failure can be obtained from the point of intersection. Knowing the relationship between the reduced stain rate and specimen surface temperature, the fracture temperature then can be calculated.

Results and Discussion

Figure 16 and figure 17 present the test data obtained for the MnROAD test sections, referred to as cells in the figure legend.[11,64] These data include the dynamic modulus master curves, phase angle master curves, time-temperature shift factors, damage characteristic curves, average of the measured CTC values, and predicted DPSE failure envelope for all the STA and LTA tested materials. The dynamic modulus value is the average of two values, the damage characteristic curve is the average of three curves, and the CTC is the average of two measurements taken from sample replicates.

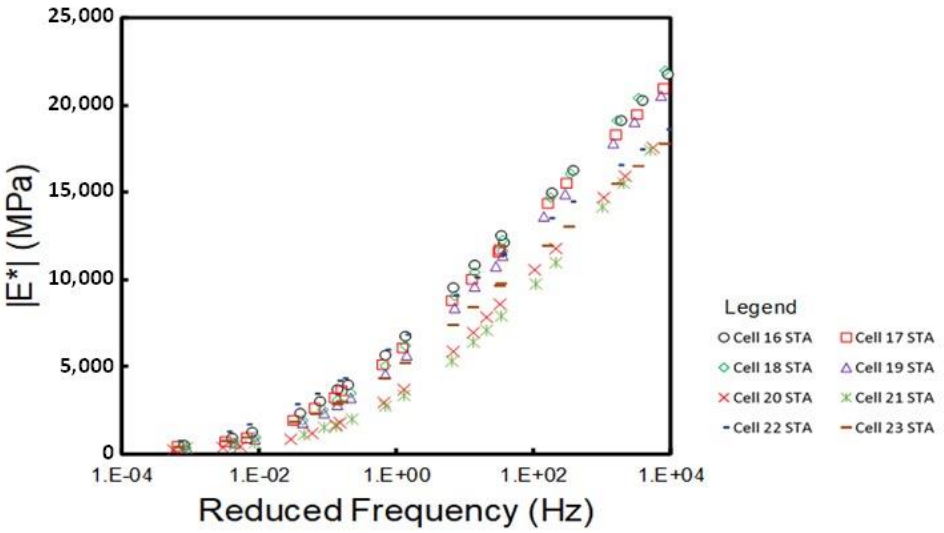

1 MPa = 145.04 psi.

A. Dynamic modulus master curves.

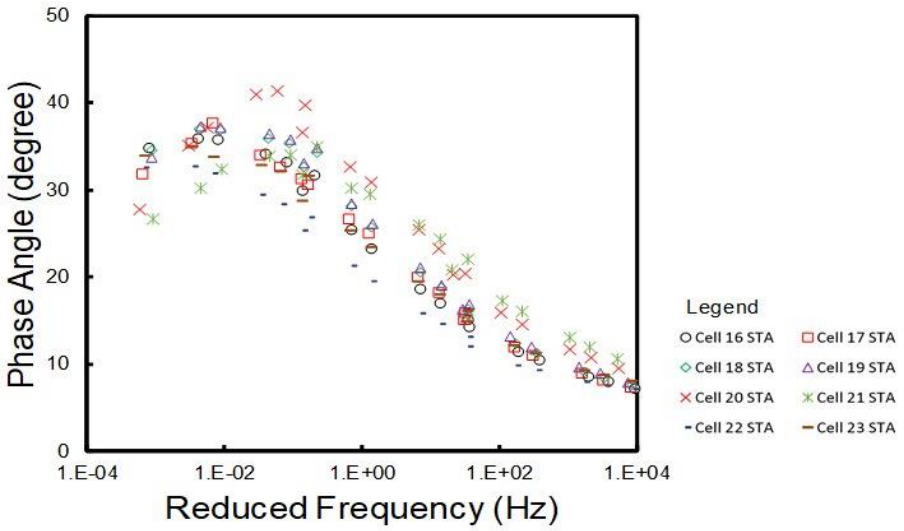

B. Phase angle master curves.

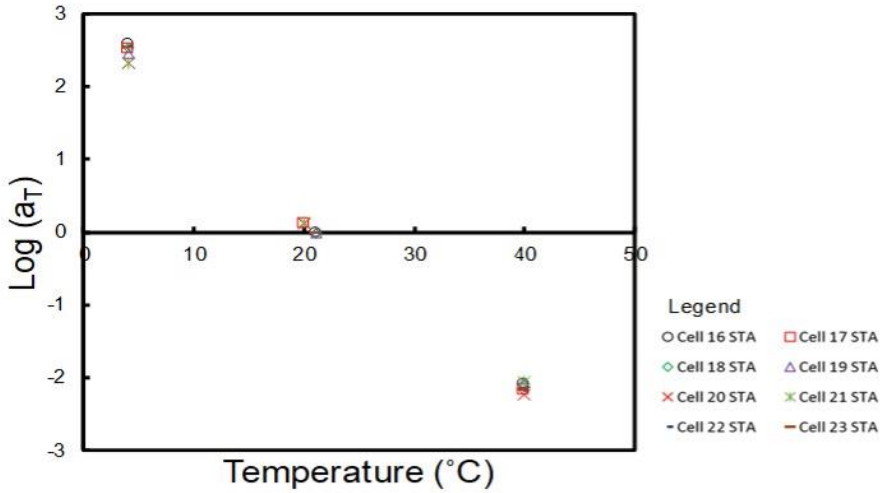

C. Time-temperature shift factors.

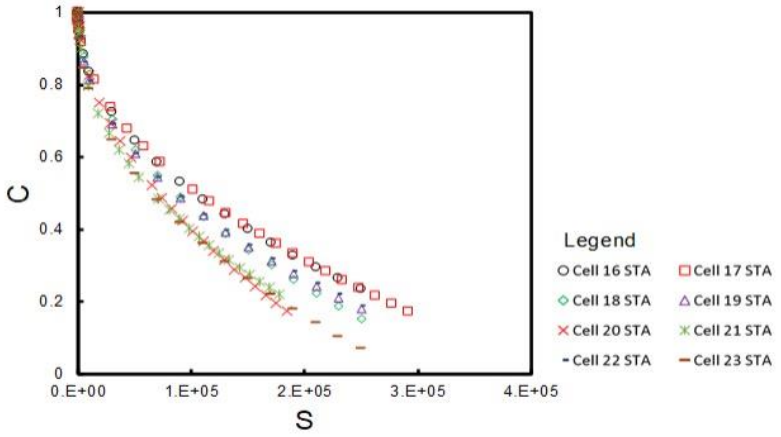

D. Damage characteristic curves.

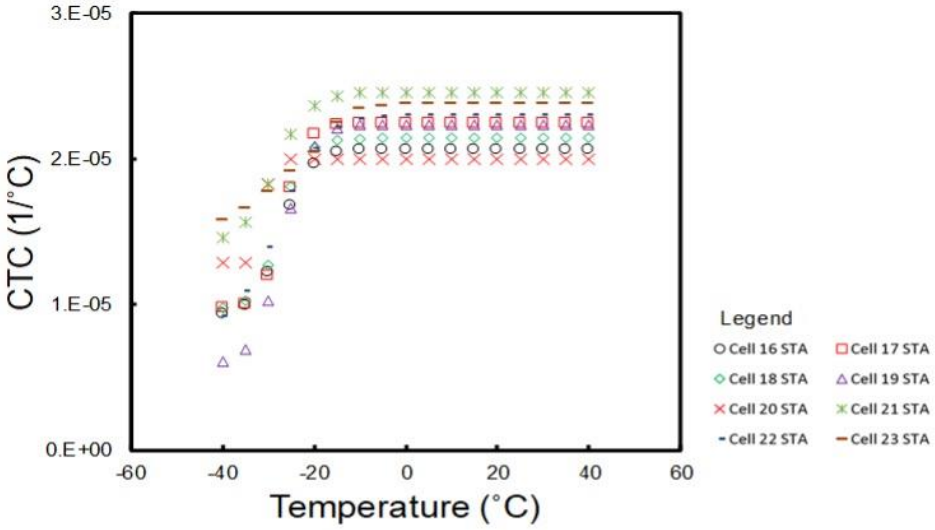

E. Averaged measured CTCs as a function of temperature.

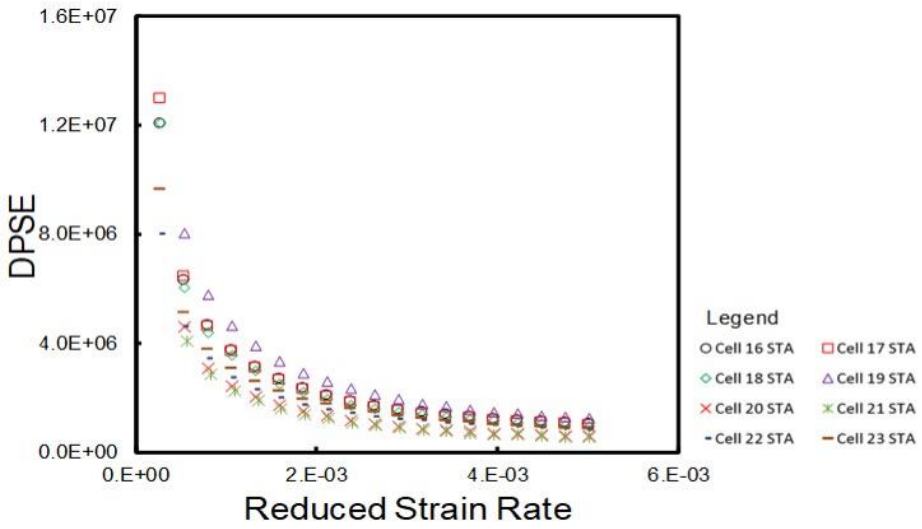

F. Predicted DPSE failure envelopes.

Figure 16. Graphs. Measured material properties at STA conditions for MnROAD sections.[94]

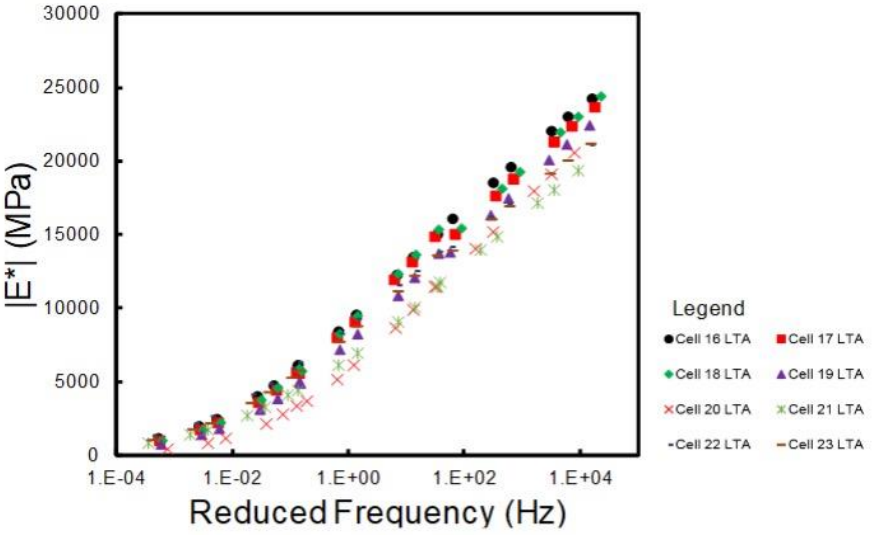

1 MPa = 145.04 psi.

A. Dynamic modulus master curves.

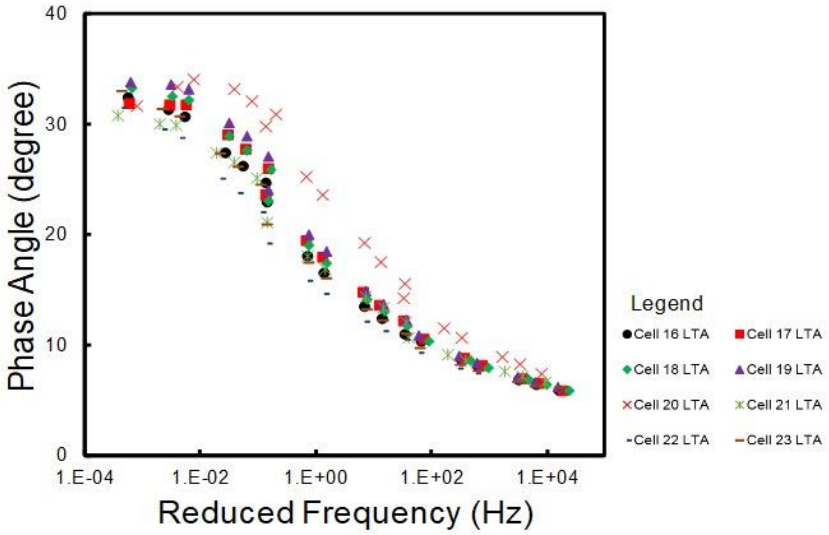

B. Phase angle master curves.

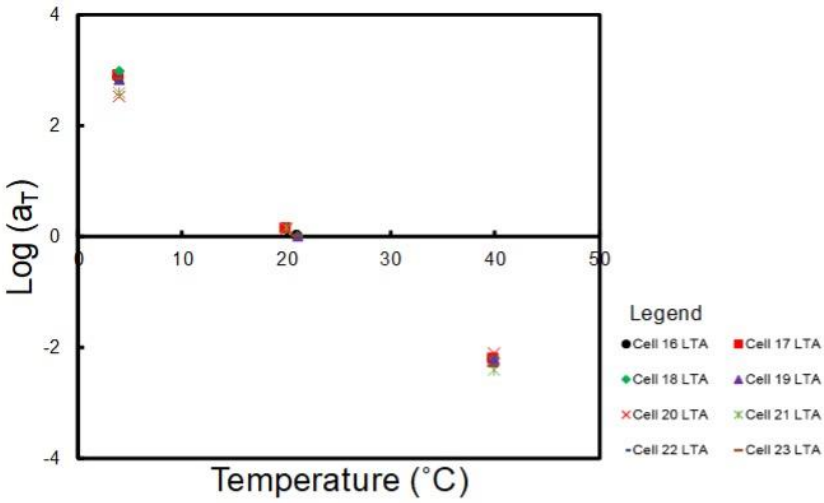

C. Time-temperature shift factors.

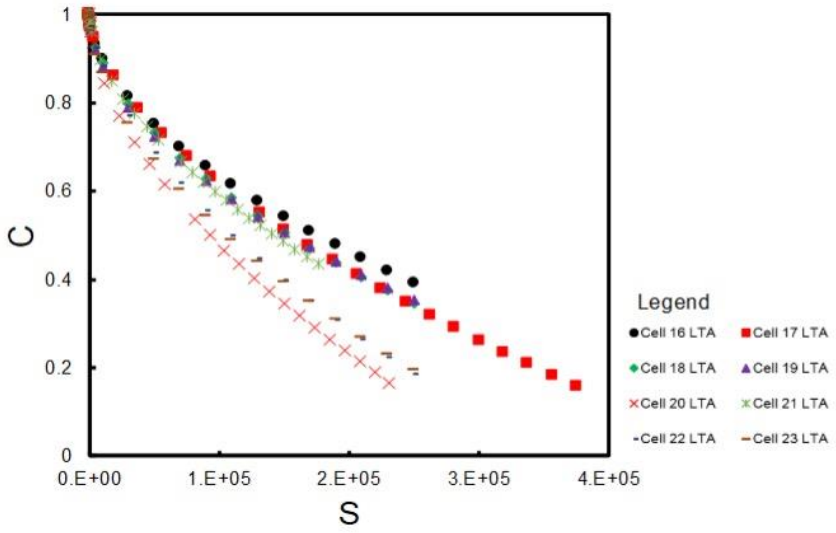

D. Damage characteristic curves.

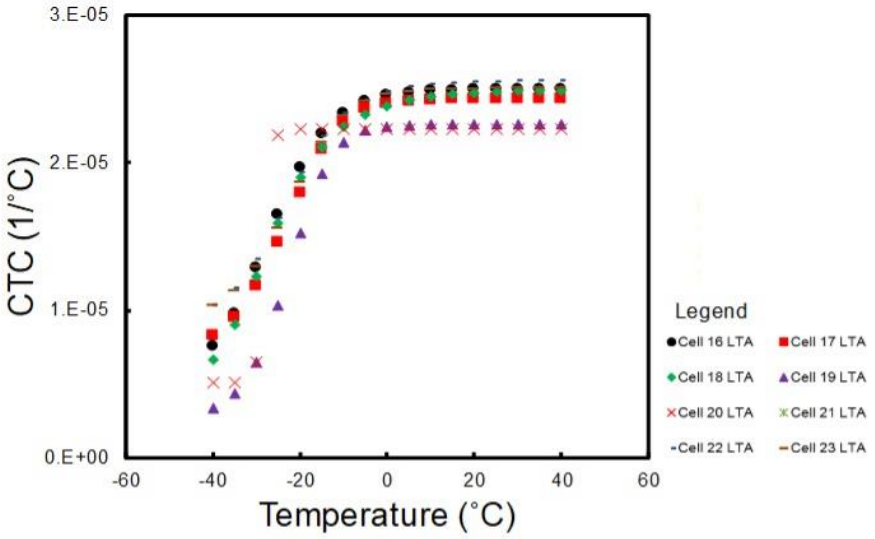

E. Averaged CTCs as a function of temperature.

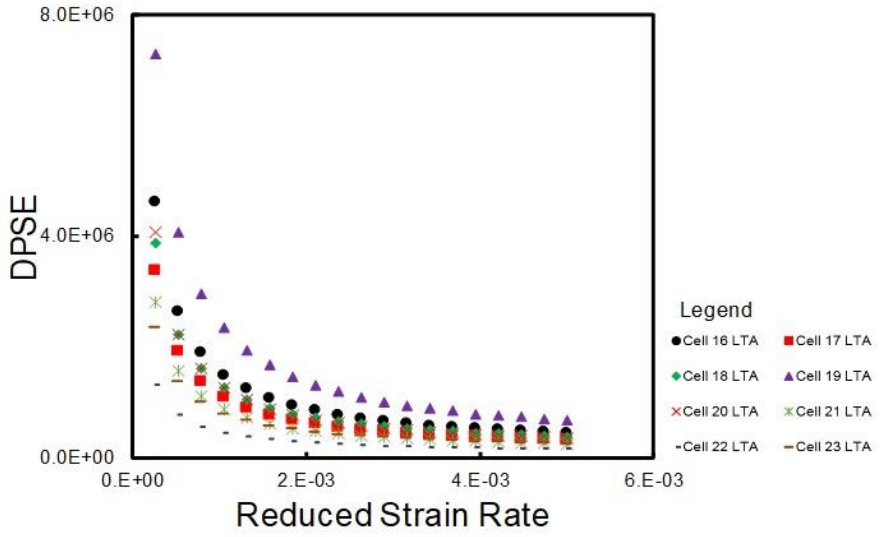

F. Predicted DPSE failure envelopes.

Figure 17. Graphs. Measured material properties at LTA conditions for MnROAD sections.(94)

Table 8 presents the results of the fitting of the CTC measurements to equation 58. The values shown in table 8 are used in equation 57 to determine the CTC values at different temperatures.

Table 8. Measured and predicted CTC of study mixtures at STA and LTA conditions.

Cell	Aging Level	CTC_l (10^{-6}/°C)	CTC_g (10^{-6}/°C)	T_g (°C)	R
Cell 16	STA	20.67/ 20.30	9.25/ 8.75	−26.96/ −26.85	2.94/ 2.74
Cell 16	LTA	25.00/ 25.81	2.30/ 4.48	−27.26/ −26.42	6.98/ 6.80
Cell 17	STA	22.43/ 22.43	9.77/ 9.77	−26.45/ −26.45	2.26/ 2.26
Cell 17	LTA	24.37/ 21.03	7.74/ 8.40	−22.96/ −19.62	5.83/ 4.81
Cell 18	STA	21.44/ 22.53	9.71/ 10.64	−27.33/ −27.02	2.54/ 2.80
Cell 18	LTA	23.82/ 29.24	3.37/ 1.40	−26.21/ −28.59	7.27/ 11.46
Cell 19	STA	30.60/ 19.92	2.73/ 5.63	−21.00/ −25.14	8.00/ 2.87
Cell 19	LTA	22.65/ 24.80	3.15/ 1.10	−22.51/ −24.68	4.73/ 5.08
Cell 20	STA	24.36/ 20.03	2.15/ 12.87	−25.60/ −30.83	5.20/ 0.74
Cell 20	LTA	29.43/ 22.30	3.40/ 5.19	−23.45/ −30.40	8.30/ 0.79
Cell 21	STA	24.59/ 24.59	14.22/ 14.22	−28.47/ −28.47	3.74/ 3.58
Cell 21	LTA	29.25/ 18.93	10.87/ 13.61	−26.50/ −30.40	4.52/ 9.16
Cell 22	STA	21.93/ 21.93	3.16/ 3.16	−29.99/ −29.99	5.23/ 5.23
Cell 22	LTA	28.03/ 28.03	7.96/ 7.94	−23.47/ −23.47	9.11/ 9.11
Cell 23	STA	23.57/ 23.57	9.75/ 9.75	−28.00/ −28.00	6.25/ 6.25
Cell 23	LTA	24.37/ 25.76	9.10/ 9.97	−23.49/ −21.35	6.80/ 5.55

T_g = glassy temperature; R = regression constant.
Note: The first and second numbers in each cell are the measured and predicted CTCs, respectively.

The predicted mixture CTC values in table 8 were obtained using the following steps:

- The aggregate and binder properties were determined based on findings from Keshavarzi et al. (which are summarized in the Coefficient of Thermal Contraction section).[65]
- Binder CTC values were calculated as a function of temperature from equation 57 using the binder CTC parameters (i.e., CTC_g, CTC_l, T_g, and R) obtained from the binder CTC database using the low-temperature PG of the binders.
- Temperature-dependent CTC_{binder} values and backcalculated E_{binder}, which is also temperature-dependent, were input to equation 40 to predict $CTC_{mixture}$.
- The predicted $CTC_{mixture}$ values were fitted using equation 57 to determine the mixture CTC parameters shown in table 8.

Table 9 and table 10 summarize all the aggregate and binder properties used in the prediction of $CTC_{mixture}$.

Table 9. Aggregate properties used to predict the mixture CTC.

Cell Number	Aggregate CTC	Aggregate Relative Area	Aggregate *E* (GPa)
Cell 16	9E-06	0.90	37.19
Cell 17	9E-06	0.90	37.36
Cell 18	9E-06	0.90	37.13
Cell 19	9E-06	0.90	37.13
Cell 20	9E-06	0.90	36.99
Cell 21	9E-06	0.90	37.13
Cell 22	9E-06	0.90	36.11
Cell 23	9E-06	0.90	37.19

Table 10. Binder properties used to predict the mixture CTC.

Cell Number	Binder CTC_l (10^{-6}/°C)	Binder CTC_g (10^{-6}/°C)	Binder T_g (°C)	Binder *R*	Binder Relative Area
Cell 16	600	170	−25	6	0.28
Cell 17	600	170	−25	6	0.28
Cell 18	600	170	−25	6	0.28
Cell 19	600	170	−25	6	0.28
Cell 20	600	250	−27	6	0.28
Cell 21	600	250	−27	6	0.28
Cell 22	600	250	−27	6	0.27
Cell 23	600	250	−27	6	0.27

T_g= glassy temperature; R = the regression constant.

Figure 18-A and figure 18-B present comparisons of the measured and predicted CTCs for the study mixtures at STA and LTA conditions, respectively.

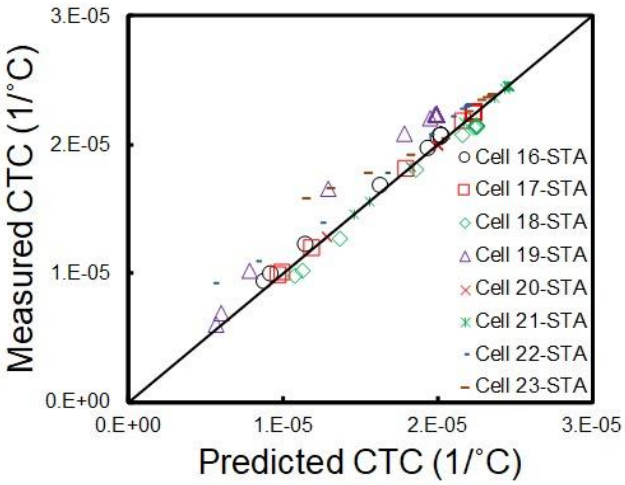

A. STA.

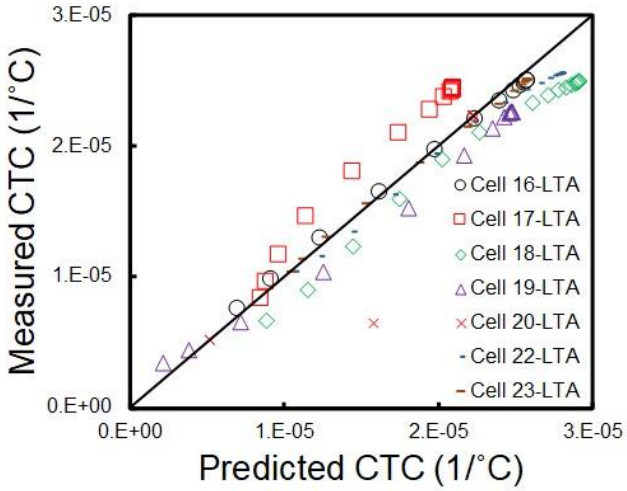

B. LTA.

Figure 18. Graphs. Comparison of measured and predicted CTCs of MnROAD mixtures.[(94)]

Figure 19 presents comparisons of the measured material properties between the STA and LTA conditions for the cell 16 mixture as a representative mixture. Figure 19-A shows a significant increase in the dynamic modulus value when the aging duration is increased. The increase in

mixture stiffness reflects the higher magnitude of thermal stress applied to the mixture, which in turn diminishes its performance. Figure 19-B shows that the phase angle, on the other hand, drops when the age level increases. The phase angle, which can be linked to mixture viscosity, represents the ability of a mixture to relieve stress. Thus, a reduction in phase angle corresponds to less chance that the mixture can relieve stress. The t-TS factor determines the reduced strain rate that is applied to the material. Figure 19-C shows that aging causes an increase in the t-TS factor at lower temperatures. This phenomenon makes the applied reduced rate (equation 61) higher for aged materials and makes them more susceptible to cracking. Figure 19-D shows that the damage characteristic curves exhibit an upward shift with aging. This outcome is expected because the damage characteristic curves of stiffer materials tend to be located higher in the *C* versus *S* graph than the curves of softer materials. Figure 19-E presents a comparison of the predicted DPSE values, which constitutes the failure criterion, as the aging level increases from STA to LTA conditions. As is apparent from figure 19-E, aging decreases the tolerable DPSE of asphalt mixtures for a wide range of frequencies. Figure 19-F presents the CTCs measured for two aging levels. In sum, figure 19 indicates that aging can significantly increase the applied thermal stress by increasing the mixture's modulus value, can decrease the mixture's ability to relieve thermal stress, and can diminish the capacity of a mixture to resist thermal damage.

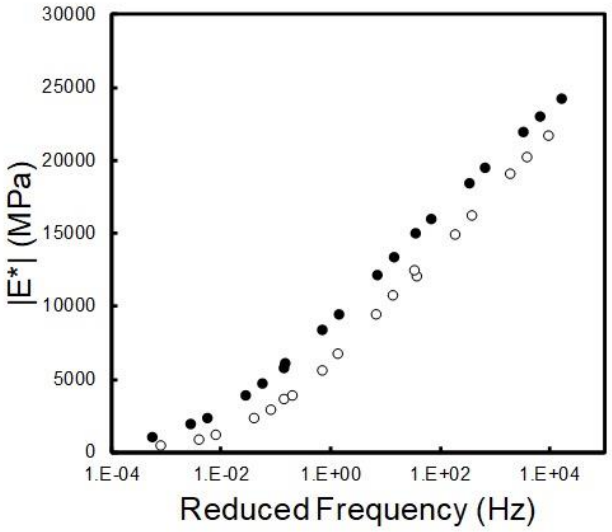

1 MPa = 145.04 psi.
Note: Open circles are STA and filled circles are LTA.

A. Measured dynamic modulus master curves.

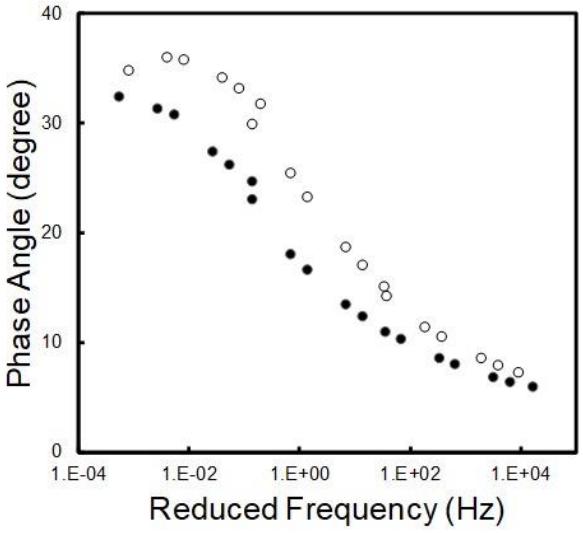

1 MPa = 145.04 psi.
Note: Open circles are STA and filled circles are LTA.

B. Measured phase angle master curves.

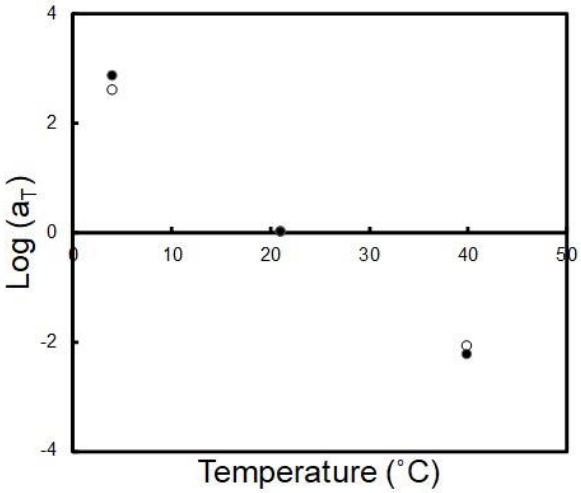

1 MPa = 145.04 psi.
Note: Open circles are STA and filled circles are LTA.

C. Measured time-temperature shift factors.

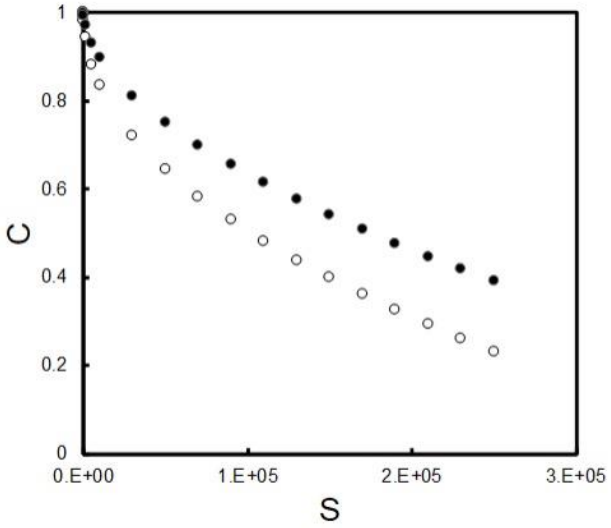

1 MPa = 145.04 psi.
Note: Open circles are STA and filled circles are LTA.

D. Measured damage characteristic curves.

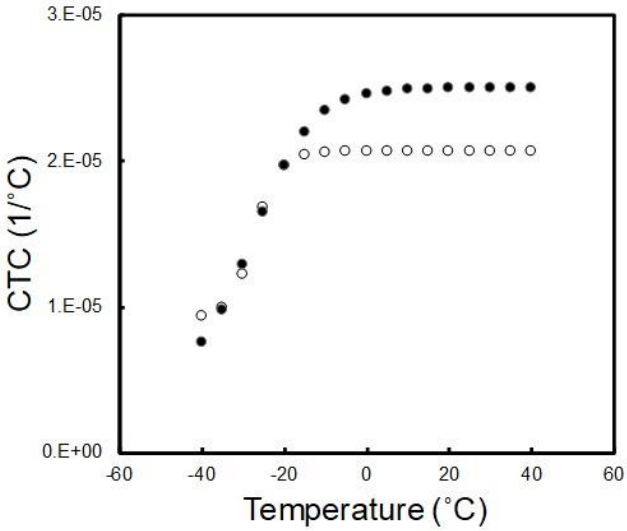

1 MPa = 145.04 psi.
Note: Open circles are STA and filled circles are LTA.

E. Predicted DPSE values.

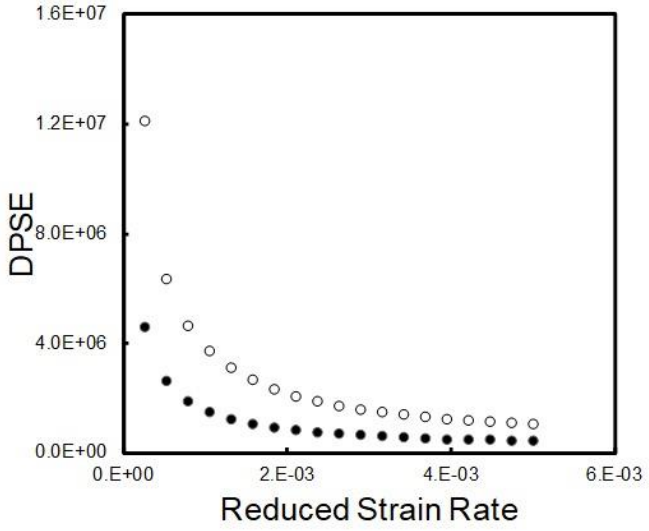

1 MPa = 145.04 psi.
Note: Open circles are STA and filled circles are LTA.

F. Measured CTC values.

Figure 19. Graphs. Comparisons between material properties under STA and LTA conditions for cell 16.[(94)]

Figure 20 presents the number of transverse cracks observed in the field along with the predicted TSRST fracture temperatures for both STA and LTA conditions. The eight cells are ordered from left to right in the figure from most transverse cracks to fewest transverse cracks. Also, the absolute values of the fracture temperatures are used in the figure and the taller bars for the fracture temperature indicate better performing cells. Therefore, the trends for the number of transverse cracks and fracture temperature should be the opposite if the fracture temperature prediction methodology works well.

Figure 20 reveals two observations. First, aging significantly increases the fracture temperature for all the mixtures. Although this outcome is the case for almost all the mixtures, cell 23 shows less sensitivity to aging than the other cells. The polymer modification technology used for this mixture is the reason cell 23 is less prone to aging. Second, the predicted fracture temperatures at the STA condition in general follow the opposite (i.e., correct) trend to the trend for the number of transverse cracks, whereas the LTA condition does not work as well as the STA condition. This discrepancy is probably due to the fact that the LTA condition used in this study represents the mixtures' aged condition at the time the transverse cracking measurements were taken. In other words, the STA condition should be able to represent the mixture's condition over 2.7 yr in service better than the LTA condition that represents the mixture's condition at 4 yr, as shown in table 11 where the climatic aging index determines the extent of aging for field conditions.

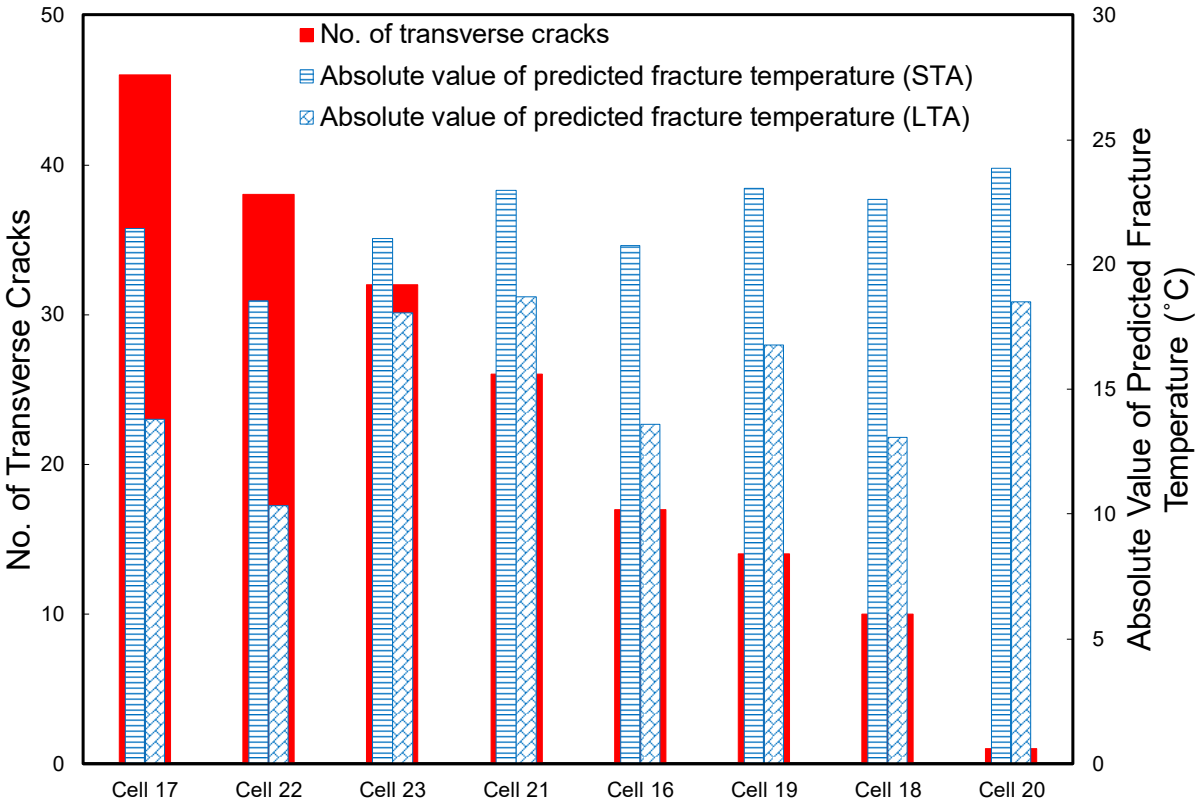

Figure 20. Graph. Number of transverse cracks observed in the field for selected MnROAD sections and predicted fracture temperatures at STA and LTA conditions.[94]

Table 11. Climatic aging index values in days as functions of time and depth for MnROAD sections.

Minnesota Depth (mm)	Year 0	Year 2	Year 4	Year 8	Year 15
6	0	1.4	2.7	5.4	10.2
18	0	0.8	1.7	3.3	6.2
30	0	0.6	1.3	2.6	4.8
42	0	0.5	1.1	2.2	4.1

Figure 21 compares the predicted fracture temperatures using the measured and predicted CTC values for the MnROAD mixtures.[11,64] As shown, the predictive relationship for the mixture CTC slightly underpredicts the measured fracture temperatures, which gives an extra safety factor.

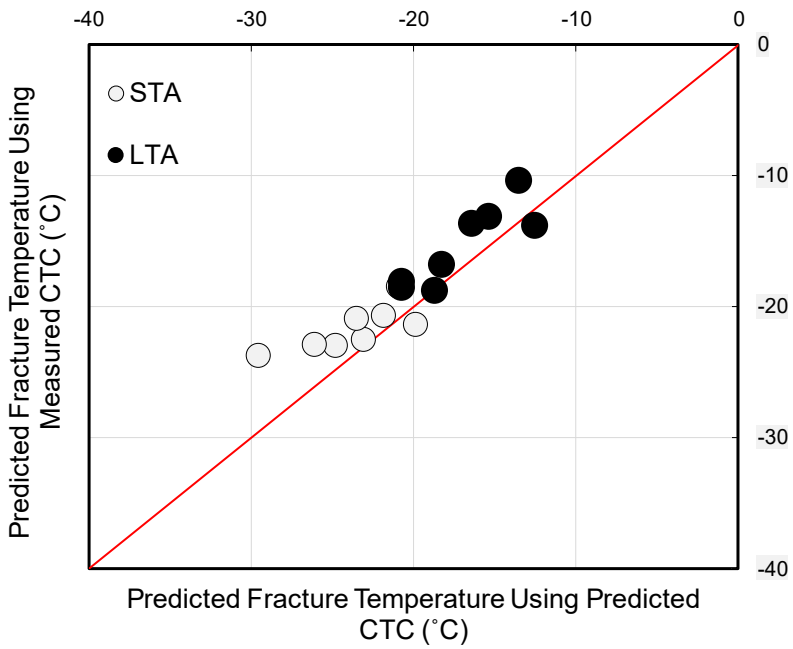

Figure 21. Graph. Comparison of predicted fracture temperatures for MnROAD mixtures using predicted and measured CTCs.[94]

The information presented in figure 20 can be investigated further by comparing the two cells in a pair. The MnROAD cells (and corresponding mixtures) are designed to evaluate various mix design factors for the RAP and RAS mixtures.[11,64] Table 12 categorizes the cells into eight pairs based on the difference between the two cells in a pair. For example, cells 16 and 17 in pair 1 are designed to assess the effect of RAP content on thermal cracking performance. Therefore, as shown in table 7Table 7. Properties of MnROAD mixtures., cell 16 contains the 20-percent RAP mixture whereas cell 17 contains the 10-percent RAP mixture. Also, the asphalt contents for the two cells are slightly different, 5.0 percent for cell 16 and 5.3 percent for cell 17. Because cell 17 uses less RAP and more asphalt binder, cell 17 would be expected to have better thermal cracking resistance than cell 16. All the pairs shown in table 12 are designed such that the ranking of thermal cracking performance between the two cells in each pair can be anticipated before testing using engineering intuition.

Table 12. MnROAD pairs defined for comparing mixture performance.

Pair	Cell	Reason
Pair 1	Cell 16	Difference in RAP contents
Pair 1	Cell 17	Difference in RAP contents
Pair 2	Cell 17	Difference in RAP and RAS contents
Pair 2	Cell 18	Difference in RAP and RAS contents
Pair 3	Cell 16	Difference in RAS contents
Pair 3	Cell 18	Difference in RAS contents
Pair 4	Cell 18	Difference in air void contents
Pair 4	Cell 19	Difference in air void contents

Pair	Cell	Reason
Pair 5	Cell 20	Difference in RAP contents
Pair 5	Cell 21	Difference in RAP contents
Pair 6	Cell 21	Limestone presence and difference in NMAS
Pair 6	Cell 22	Limestone presence and difference in NMAS
Pair 7	Cell 18	Difference in binder PG
Pair 7	Cell 21	Difference in binder PG
Pair 8	Cell 22	Difference in binder PG
Pair 8	Cell 23	Difference in binder PG

Figure 20 and table 12 present the following observations about the pairs of MnROAD cells:[11,64]

- Pair 1: Cell 17 has a lower RAP content and a higher binder content than cell 16. Therefore, cell 17 is expected to perform better than cell 16. However, the field condition survey results presented in figure 20 show the opposite trend, that is, worse performance for cell 17 compared to cell 16. Figure 20 also demonstrates that the predicted fracture temperatures for cell 17 at the STA and LTA conditions are close to those for cell 16. The reason for these opposite trends observed between engineering intuition and field performance is unknown. Visual observations of the field cores indicate delamination at the interface of two construction lifts, which may have affected the propagation of top-down thermal cracking and the number of transverse cracks presented in figure 20.

- Pair 2: The difference between cells 17 and 18 is the higher RAP content and lower RAS content in cell 18 than in cell 17. According to the prediction results and field observations, the higher RAS content in cell 17 compromises the lower RAP content and weakens the mixture's resistance to thermal loading.

- Pair 3: The effect of RAS content is shown in cells 16 and 18. The higher RAS content in cell 16 should diminish the low-temperature performance of the mixture. This expectation is compatible with the predictions and field results.

- Pair 4: The effect of air void content is shown in cells 18 and 19. Although the higher air void content in cell 18 makes the mixture more prone to cracking by weakening its microstructure, the induced thermal stress decreases as a result of the effect of the air void content on the mixture's stiffness. As a result, the microstructure and stiffness of the mixture are working against each other. The predicted fracture temperature indicates better performance for cell 19 than cell 18, which contradicts the trend shown in the field data.

- Pair 5: The comparative effect of higher RAP content and softer binder is shown in cells 20 and 21. Cell 20 has the higher RAP content and softer binder than cell 21. Based on the field results, cell 20 performed much better than cell 21. This observation is in line with the fracture temperatures predicted at the STA condition, which reflect a lower fracture temperature for cell 20 than cell 21. This finding suggests that the softer binder in cell 20 counterbalances its higher RAP content.

- Pair 6: The effects of NMAS value and aggregate type (limestone) are shown in cells 21 and 22. The higher NMAS of cell 21 weakens the microstructure of the mixture by increasing the stress concentration at the interface between the binder and aggregate. In addition, the limestone aggregate, which is used in cell 22, diminishes the performance of the mixture as well. The deteriorating effects of the larger NMAS and use of limestone aggregate are captured in the predicted fracture temperature of cell 22. The field data show the same trend as the predicted fracture temperature.

- Pair 7: The effect of binder LPG is shown in cells 18 and 21. Cell 21 has a lower PG, which intuitively indicates better performance. This expectation is captured in the predicted fracture temperatures where cell 21 shows a lower fracture temperature than cell 18. The field data do not follow this predicted trend. The field cores show that delamination occurred between the two lifts in cell 18. The delamination may have diverted the transverse cracking growth path from the vertical direction to the horizontal one.

- Pair 8: The effect of RAP content is shown in cells 22 and 23. Cell 22 has the higher RAP content and, as a result, exhibits greater stiffness compared with cell 23. The higher RAP content of cell 22 also incorporates a greater portion of aged material into the microstructure of the mixture. As a result, cell 23 is expected to exhibit better performance than cell 22. This expectation is confirmed by the predicted fracture temperatures and field data.

In summary, the trends observed for the predicted fracture temperatures match the field rankings in five out of eight pairs; the three exceptions are pair 1 (cells 16 and 17), pair 4 (cells 18 and 19), and pair 7 (cells 18 and 21). In these three pairs, engineering intuition supports the trends in the predicted fracture temperatures. The better-than-expected performance of cell 18 seems to be the reason for the unexpected trends in the field data.

Summary

This section describes a methodology to predict the fracture temperature in the TSRST that employs the DPSE failure criterion and the S-VECD model. The accuracy and applicability of the suggested prediction methodology were evaluated using eight MnROAD mixtures with different RAP and RAS contents, NMAS values, binder PGs, and aggregate types.[11,64] Dynamic modulus and cyclic fatigue tests were performed to characterize the DPSE failure criterion and the S-VECD model for all eight mixtures. Mixture CTCs were measured to characterize each mixture's thermal deformation at a wide range of temperatures. In general, the ranking of the predicted fracture temperatures using the material properties at the STA condition matches the ranking of the field-observed thermal cracking performance. Eight pairs of two mixtures were identified as pairs that would allow the evaluation of the effects of different mixture factors on thermal cracking. The trends from the predicted fracture temperatures match the field rankings in five out of the eight pairs and support engineering intuition for all eight pairs. In conclusion, the predicted TSRST fracture temperature using the DPSE failure criterion, the S-VECD model, and the CTC allows the thermal cracking predictions of asphalt mixtures with different RAP and RAS contents, NMAS values, binder PGs, and aggregate types. Moreover, the material properties required to use this predictive methodology can be obtained from the testing efforts

required for fatigue cracking, unifying and simplifying the testing effort needed for fatigue cracking (top-down and bottom-up) and thermal cracking.

FlexTC: A Thermal Cracking Analysis Framework for Asphalt Pavements

The evaluation of different thermal cracking prediction frameworks should be based on technical and practical perspectives. On the technical side, a framework should be able to keep track of the damage induced in a pavement during its service life. In addition, a framework should be able to capture the rate and temperature dependency of asphalt concrete. From a practical perspective, a workable framework should not require an excessive testing effort (and thus costs) for the material characterization program that would make the framework impractical.

This section introduces a new structural framework to predict the thermal cracking performance of asphalt pavements. The proposed framework, called FlexTC, employs the S-VECD model to characterize asphalt mixture behavior at low temperatures.[9] The use of the S-VECD model allows FlexTC to predict both fatigue cracking (top-down and bottom-up) and thermal cracking using a single set of test methods. The following sections provide a brief review of existing thermal cracking prediction models before describing the methodologies used in FlexTC.

Existing Thermal Cracking Prediction Models

Current frameworks for thermal cracking predictions can be categorized as either empirical or mechanistic.[36] Empirical models are regression equations based on observations of cracked field sections. These models involve the important parameters that affect the performance of asphalt sections subjected to thermal loading. For example, Fromm and Phang (1972) developed regression equations to express a thermal cracking index as a function of binder, aggregate, and base layer properties.[95] Fromm and Phang studied 33 pavement sections that were constructed in northern and southern Ontario, and their thermal cracking index was later used by the Ontario Department of Transportation to help determine the severity of observed transverse cracking.[37] Hass et al. (1987) also developed a regression equation to predict transverse crack spacing in airport asphalt pavement sections.[38] Their model uses pavement survey data and extensive laboratory test results. Hass et al. (1987) studied 26 pavement sections throughout Canada to develop their regression equation and determined that the important parameters that affect thermal cracking are the penetration-viscosity number, thickness of the asphalt layer, minimum temperature at the site, and the mixture CTC. Hass et al. (1987) also developed empirical-based formulas based on limited loading patterns specific to geographical regions and material and structural properties. However, the limitations of the databases for which these empirical-based formulas were developed makes the application of empirical methodology to other geographical regions or different pavements section layouts questionable. Moreover, empirical methods are unable to capture cracking at the fundamental level.

Researchers developed a thermal cracking performance model, referred to as TCModel, as part of SHRP to evaluate and eventually supplement PG binder specifications.[39] Later, TCModel was implemented into the Mechanistic-Empirical Pavement Design Guide software.[96] The goal of TCModel is to predict the amount (frequency) of thermal cracking in pavement sections as a function of time. TCModel consists of three modules: the thermal stress calculation, the crack propagation calculation, and the crack amount prediction. In the first module, the induced

thermal stress is calculated as a function of time. In the second module, crack propagation is calculated based on the amplitude of the stress intensity factor for each day and the crack depth is calculated based on Paris' law. The third module uses a calibration and transfer function to correlate crack depth to crack spacing. TCModel predictions are based on the tensile strength of the asphalt mixture and do not account for the quasi-brittle behavior of asphalt concrete that causes a relatively large fracture process zone (FPZ) that is formed ahead of the crack tip. However, the FPZ cannot be fully addressed by Paris' law. Furthermore, TCModel does not address the dependency of the asphalt mixture's strength, which is measured by indirect tension tests, on rate and temperature.

Another thermal cracking model was developed at the University of Illinois at Urbana-Champaign and introduced as the Illi-TC model.[97] The main improvement of Illi-TC over its predecessor, TCModel, is that Illi-TC employs the cohesive zone model (CZM) for crack propagation. The CZM can capture the mechanisms of crack propagation more accurately than TCModel. The Illi-TC also employs three modules:

- A pre-analysis module to reduce the computational costs and select the loading events, which are referred to as critical events, and impose stress that is more than 80 percent of the material strength.

- A crack propagation module that analyzes the pavement sections for ±12 h around the critical event.

- A crack amount module that transfers the calculated crack depth to crack spacing using a probabilistic function.

However, the CZM included in Illi-TC cannot account for the rate and temperature dependency of asphalt concrete. In addition, Illi-TC does not update the material strength, which is used in the preanalysis to select the critical events and is measured via indirect testing, based on the updated damage magnitude. If the effect of damage on material strength is considered in the analysis, then the number of critical events may increase significantly.

Researchers at the University of Nevada, Reno developed a comprehensive model called the thermal cracking analysis package (TCAP).[**Error! Reference source not found.**] TCAP includes four main modules for the prediction of the following conditions:

- Pavement temperature profile.
- Oxidative aging.
- Thermal stress.
- Thermal cracking events.

The pavement temperature module predicts the temperature distribution throughout the depth of the asphalt section and over time. The effect of oxidative aging in the second module is captured through the change in carbonyl level and is considered in the thermal stress calculation (the third module). The oxidative aging model developed at Texas A&M University is implemented in the TCAP software.[37] TCAP also can predict the carbonyl in asphalt binder at any depth within the asphalt layer over the analysis period. The mechanical properties of asphalt mixtures (i.e., linear

viscoelasticity, the CTC, and fracture) can be estimated as a function of the carbonyl level. The third module, thermal stress predictions, involves the analysis of one-dimensional viscoelastic rods that are assumed to be restrained at both ends and subjected to given temperature variations. The fourth module, the prediction of thermal cracking, is based on passing the threshold of the mixture aging-dependent parameter. This parameter, which is called crack initiation stress, is determined from uniaxial thermal stress-strain tests and is defined as the stress level at which the tangential stiffness of the mix that is measured during the test starts to decrease. TCAP also incorporates aging evolution in its framework, although TCAP does not consider cumulative damage. In addition, the fracture properties measured in uniaxial thermal stress-strain tests vary as a function of cooling rate and initial temperature, and considerable testing is required to obtain the whole range of fracture properties. The fracture properties are tested at a high cooling rate (i.e., −10 °C/h) in the uniaxial thermal stress-strain tests to facilitate the testing time, but the actual cooling rate in the field is much lower.[81]

Study Mixtures

Eight MnROAD mixtures shown in table 7 are used in this study.[11,64] In addition, three typical surface mixtures (RS 9.5B mixtures) used in North Carolina were used in this study to further verify the accuracy of the FlexTC framework.[9] Table 13 presents the RS9.5B mixtures and their sources and properties.

Table 13. Properties of RS9.5B mixtures.

Mixture ID	RAP (percent)	RAS (percent)	NMAS (mm)	AC (percent)	Binder Grade	Design Air Voids (percent)
RS 9.5B 0	0	0	9.5	6.6	PG 64-22	4
RS 9.5B 30	30	0	9.5	5.8	PG 58-28	4
RS 9.5B 50	50	0	9.5	5.2	PG 58-28	4

The input material properties needed to run FlexTC include dynamic modulus and phase angle master curves that are determined by dynamic modulus tests, the damage characteristic curve and DPSE failure criterion that are determined by AMPT cyclic fatigue tests, and the CTC of the asphalt mixture.[9] The NCHRP 09-54 aging models were used to change the material properties as a function of age.[17]

Methodology

Thermal Loading

Hourly air temperature variations can be viewed based on hourly, daily, monthly, seasonal, and yearly segments. The variation of each of these segments is dependent on different rates. Fourier transform can be used to study the rate for any of these time segments and therefore can help detect the relative importance of each segment. Figure 22 presents the magnitude of the Fourier transform of the surface temperature of a pavement constructed at MnROAD.[11,64] Four time segments are defined for each year:

- Segment 1 covers the daily thermal variation ranges from 0.041 Hz (= 1/24) to 1 Hz.

- Segment 2 covers the monthly thermal variation from 0.0012 Hz (= 1/720) to 0.041 Hz.
- Segment 3 covers the seasonal thermal variation ranges from 0.000463 Hz (= 1/2160) to 0.0012 Hz.
- Segment 4 covers the season-to-season variation and is expanded from 0.000114 Hz (= 1/8760) to 0.000463 Hz.

Figure 22 also shows that the greatest magnitude belongs to the daily segment, segment 1, which also has the highest frequency values (0.041 Hz to 1 Hz). Based on this observation and the fact that the asphalt mixture stiffness increases based on loading frequency, the thermal stress is calculated daily to capture the destructive effect of the air temperature variations.

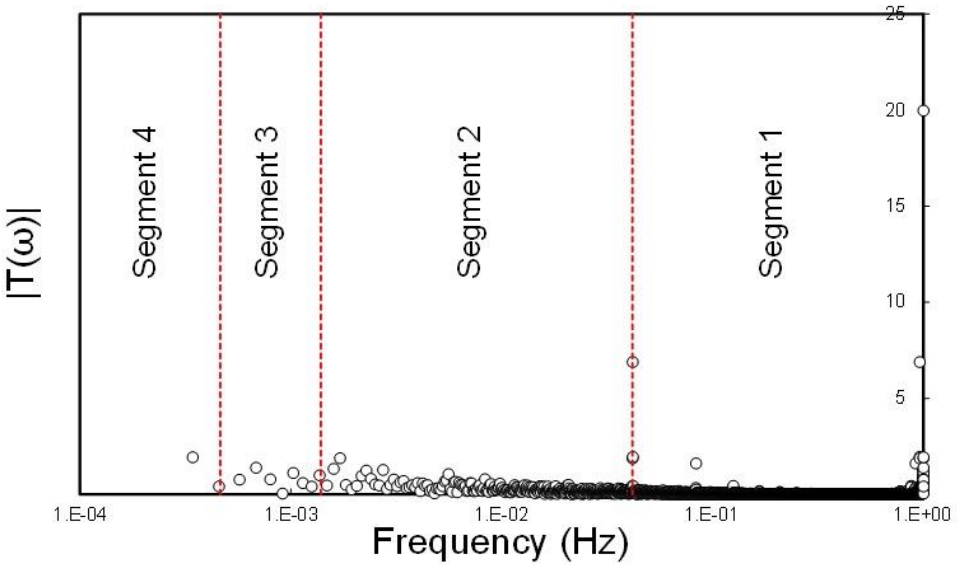

Source: FHWA.

Figure 22. Graph. Magnitude of Fourier transform of surface temperatures for a MnROAD pavement section.

Structural Analysis

The response of an asphalt pavement subjected to thermal loading can be determined by assuming that the pavement in both the traffic direction (longitudinal direction) and transverse direction (width direction) is long and wide enough that the plane-strain condition is applicable. Based on this observation, a pavement section can be decomposed as a series of independent uniaxial rods that are fixed at their ends.[37,96] Figure 23 presents the uniaxial rods that can be used to analyze the response of pavement sections.

Source: FHWA.

Figure 23. Illustration. Schematic view of sublayers assumed in FlexTC.

The pseudostrain for asphalt concrete can be expressed by equation 65.

$$\varepsilon^R(\xi) = \frac{1}{E_R} \times \int_0^{\xi} E(\xi - \tau) \frac{d\varepsilon}{d\tau} d\tau \tag{65}$$

Where:

ε^R= induced pseudostrain

ζ = reduced time at which the thermal stress response is desired.

τ = integration parameter.

E = relaxation modulus in terms of the Prony series.

ε = strain.

Equation 54 presents the Prony series representation of the relaxation modulus. The thermal strain term in equation 65 comes from the induced temperature variation. Thermal strain depends on the rate of the temperature variation, the temperature at which that rate occurs, and the CTC, as expressed by equation 66. FlexTC uses equation 57 to consider the variation of CTC as a function of temperature.(9)

$$\begin{aligned} &\varepsilon = CTC \times (T - T_0) \rightarrow \\ &\frac{d\varepsilon}{d\tau} = \frac{d}{d\tau}\left(CTC \times (T - T_0)\right) \rightarrow \\ &\frac{d\varepsilon}{d\tau} = \dot{\varepsilon_r} = CTC \times \frac{dT}{d\tau} = CTC \times a_T \times \frac{dT}{dt} \end{aligned} \tag{66}$$

Where:

T_0 = equilibrium temperature.

a_T = time-temperature shift factor value, and t is the time parameter.

The equilibrium temperature, T_0, is calculated based on equation 67.

$$T_0 = \frac{\int_0^{\xi_{day}} T d\xi}{\xi_{day}} \tag{67}$$

The a_T parameter can be calculated from equation 68.

$$a_T = \int_0^t \frac{d\zeta}{a_1 T^2(\zeta) + a_2 T(\zeta) + a_3} \tag{68}$$

Where:

a_1, a_2, a_3 = time-temperature shift factor coefficients.
ζ = time parameter.

Combining equation 65 and equation 66 expresses the relationship of the induced pseudostrain in the sublayers to the material properties and induced temperature variation, as shown in equation 69.

$$\varepsilon^R(t) = \frac{1}{E_R} \times \int_0^t E(t-\tau) \times \frac{d}{d\tau}\left(CTC \times \left(T - T_0\right)\right) d\tau \tag{69}$$

Each sublayer experiences some level of damage, and the magnitude of that damage must be included in the analysis framework. FlexTC uses S-VECD theory to account for the damage level in the stress calculation.[9] Equation 70 presents the damage characteristic curve that FlexTC uses in to keep track of damage.

$$C = 1 - C_{11} S^{C_{12}} \tag{70}$$

Where:

C = pseudostiffness and represents the material integrity.
S = internal damage parameter.
C_{11}, C_{12} = material parameters.

The pseudostiffness varies from 1 for the undamaged state to 0 for the failed state. The thermal stress can be expressed by equation 71.

$$\sigma(t) = C \times \varepsilon^R(t) \tag{71}$$

The evolution of the damage parameter as a function of thermal loading can be expressed by equation 72. Equation 72 gives a relationship that can be used to calculate the thermal stress by accounting for the current state of damage of the material.

$$\frac{dS}{dt} = \left(\frac{1}{2} \times C_{11} \times C_{12} \times S^{C_{12}-1} \right)^{\alpha} \left(\int_0^t E(t-\tau) \times CTC \times a_T \times \frac{dT}{d\tau} d\tau \right)^{2\alpha} \quad (72)$$

$$\alpha = \left(\frac{1}{m} \right) + 1 \quad (73)$$

Where:

α = damage evolution rate parameter.
m = maximum slope of the relaxation modulus in log-log scale.

Equation 72 should be solved at the end of each day to update the damage magnitude. Solving equation 69 in the time domain is a computationally expensive task. The Fourier transform technique is used to simplify the solution. Fourier transform is defined here as equation 74.

$$f(\omega) = \int_{-\infty}^{\infty} f(t) \times e^{-i\omega t} dt \quad (74)$$

Where:

f = Fourier transform of a generic function, f.
ω = temporal frequency.

Applying Fourier transform to equation 69 gives equation 75.

$$\varepsilon_R(\omega) = E^*(\omega) \times FT\left\{ CTC \times (T - T_0) \right\} \quad (75)$$

Where FT is Fourier transform.

FlexTC uses the DPSE failure criterion to detect failure for all the sublayers in the asphalt pavements.[9] DPSE is defined here as equation 60. In a 2020 journal article, Keshavarzi and Kim provide details about the DPSE failure criterion and its dependency on damage level.[82]

Finally, the thermal cracking performance of a pavement section is defined by the DF. The DF is defined as the ratio of the DPSE as a function of the current reduced strain rate to the maximum DPSE, which is defined based on the failure criterion. Figure 24 presents a sample calculation for defining the DF based on DPSE failure criterion methodology. In figure 24, d_1 and d_2 are the cumulative DPSE, from the intact state of the material to the current state, and the available capacity of the material to tolerate damage for the same reduced strain rate, respectively.

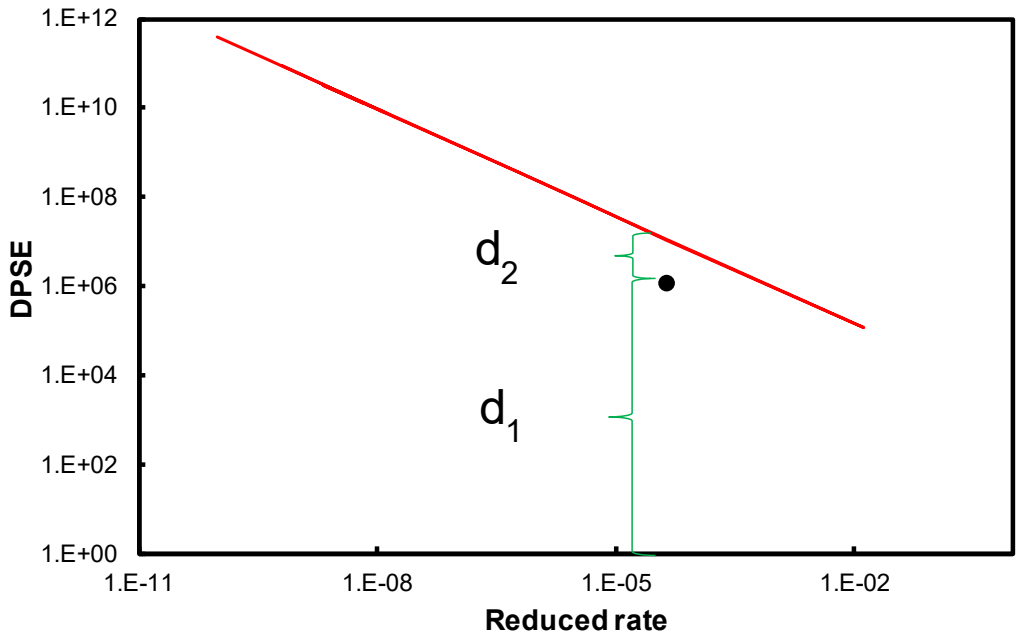

Source: FHWA.

Figure 24. Graph. Example for defining the damage factor based on the DPSE failure criterion.

Equation 76 expresses the proximity of each point in the pavement section to the failure envelope in terms of the DF.

$$DF = \frac{d_1}{d_1 + d_2} \tag{76}$$

With the definition of DF based on equation 76 in hand, the maximum experienced damage can be used to evaluate the effect of thermal loading on the pavement sections.

The Results section of this report presents thermal stress, thermal damage, reduced strain rate, and DPSE evolution. Figure 25 presents a schematic view of the implemented computational algorithm in FlexTC.[9]

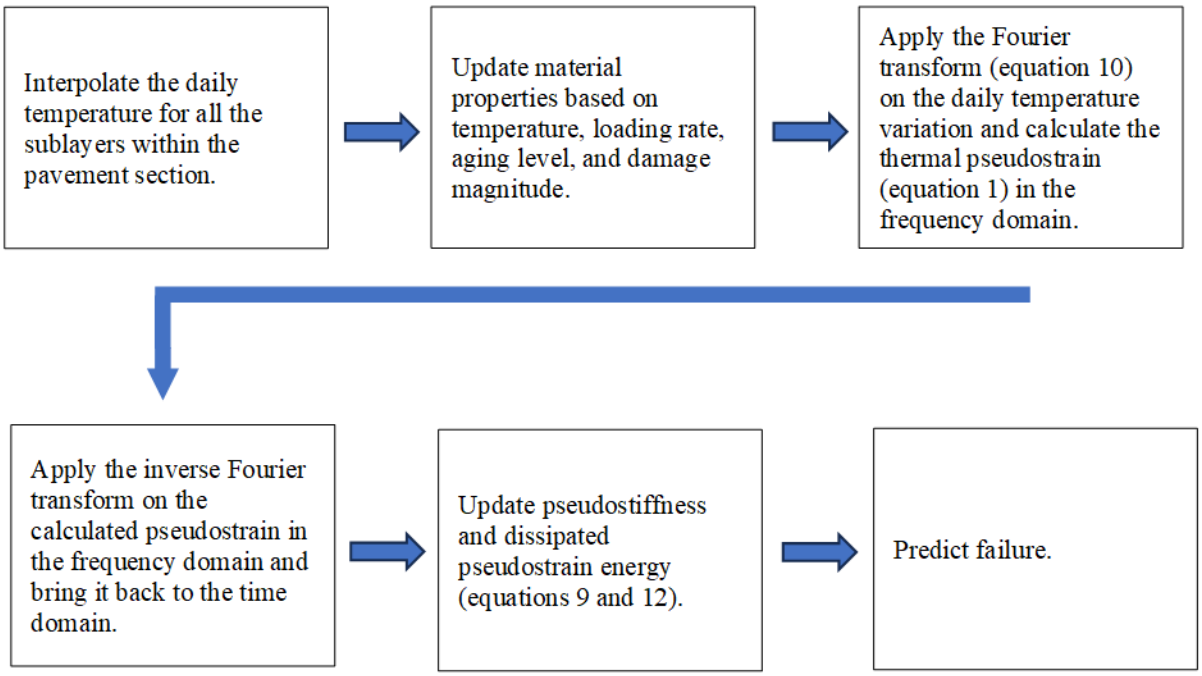

Source: FHWA.

Figure 25. Flowchart. Algorithm implemented in FlexTC for calculating pseudostrain, thermal stress, pseudostiffness, and dissipated pseudostrain energy, and detecting failure.

FlexTC Simulation Results

Figure 26 presents a schematic view of the structures of the pavement sections used in this study. The research team used the procedure described in the Methodology section to calculate the thermal stress and thermal damage, update the DPSE, detect failure, and calculate the DF. Figure 27 presents the induced thermal stress results at different pavement depths for one of the pavement sections that was constructed in North Carolina. Figure 27 shows that the thermal stress decreases as the pavement depth increases. This trend derives from the fact that lower layers of asphalt experience lower levels of temperature variation. Figure 28 presents the thermal damage in the same pavement section. As shown, the top surface experiences more damage (lower *C* value) than the lower layers. Figure 28-A shows that, at lower pavement depths, the *C* value increases and the material experiences less damage than nearer the surface. Figure 28-B presents the DPSE evolution and shows that less damage is experienced in the asphalt layers located at the bottom of the section compared to layers nearer the surface. This outcome is due to the fact that the top layers of an asphalt pavement section are exposed to air temperature variations and thus experience more damage than deeper layers.

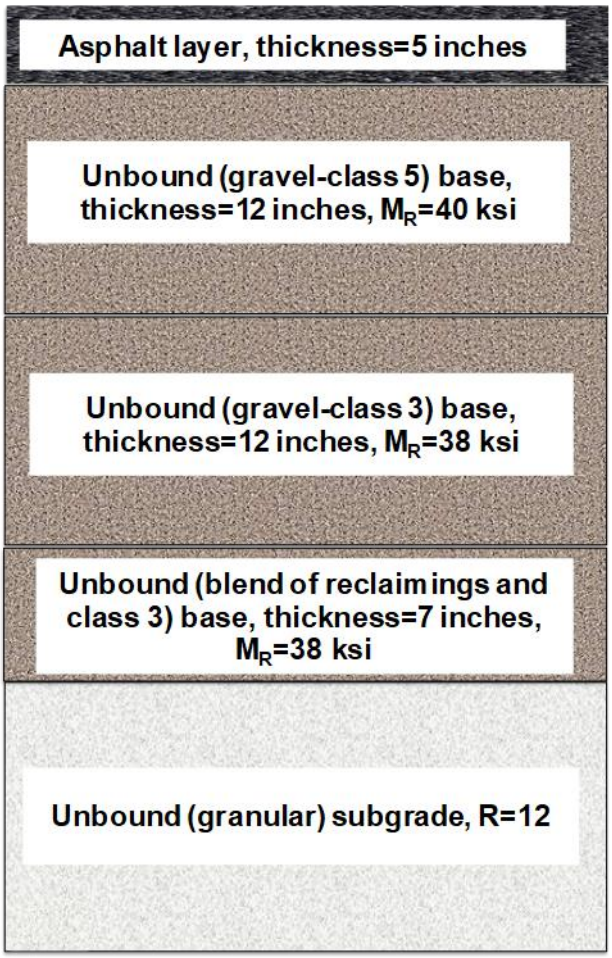

Source: FHWA.
M_R = resilient modulus; R = resistance value.

A. MnROAD sections.

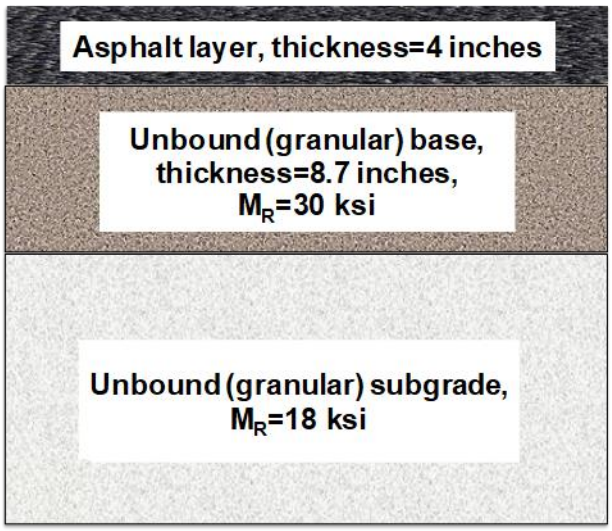

Source: FHWA.

B. North Carolina sections.

Figure 26. Illustrations. Layouts of study sections.

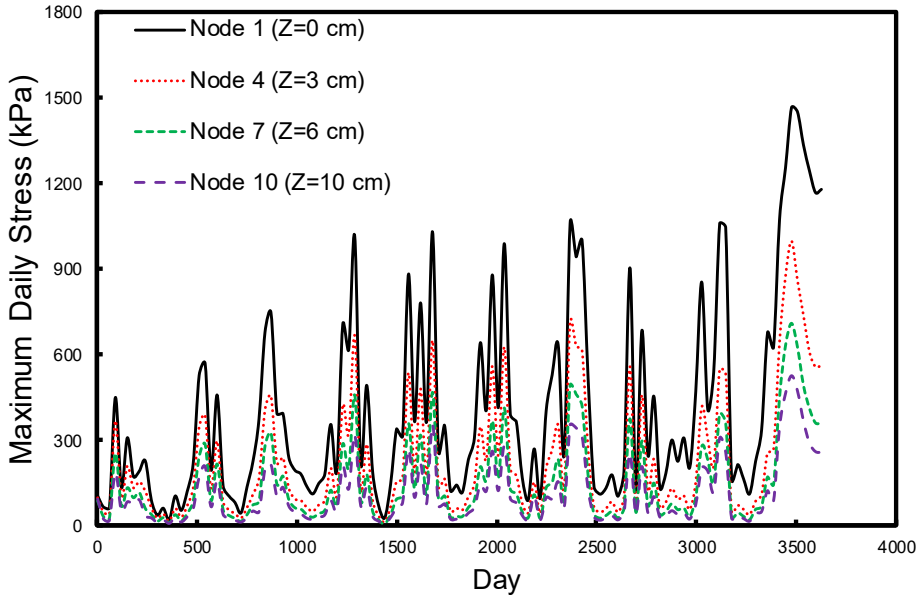

Source: FHWA.
1 cm = 0.4 inches; Z = depth in pavement.

Figure 27. Graph. Maximum induced daily thermal stress as a function of pavement depth and day for a synthetic section located in North Carolina (RS 9.5B 0-percent RAP).

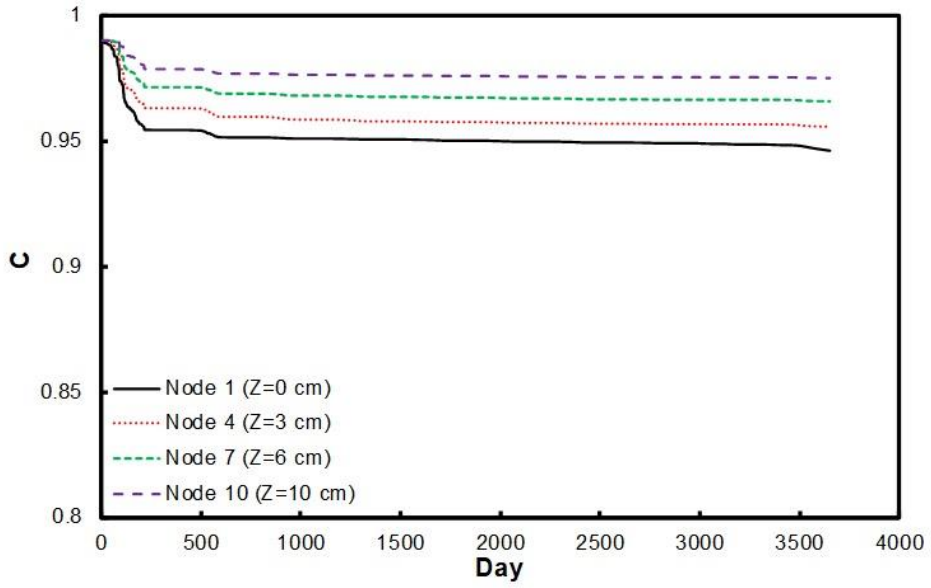

Source: FHWA.
1 cm = 0.4 inches.

A. Pseudostiffness (C) evolution versus time (day) for different nodes.

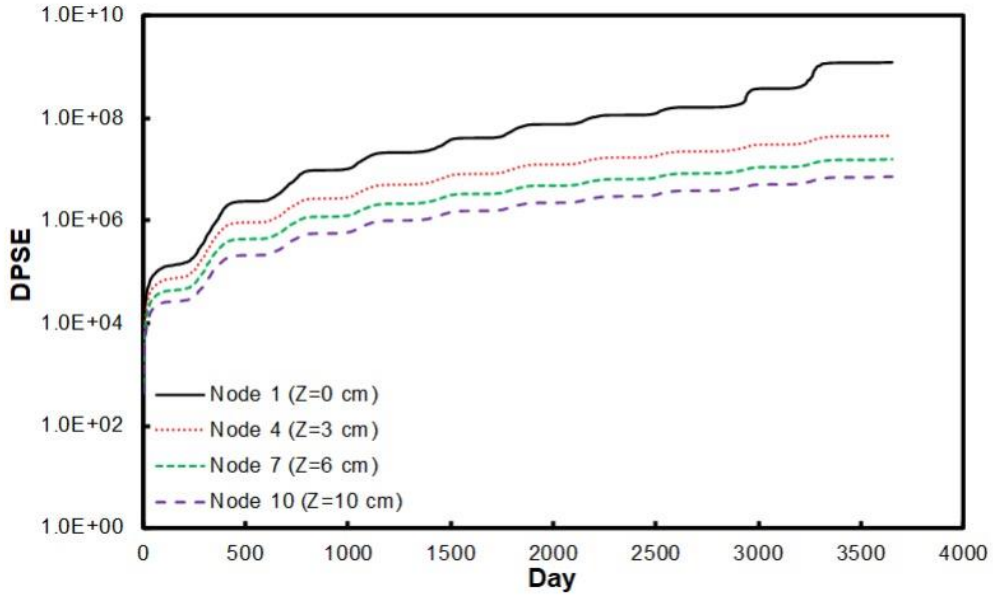

Source: FHWA.
1 cm = 0.4 inches.

B. DPSE evolution versus time (day) for different nodes in terms of pavement depth.

Figure 28. Graphs. Evolution of thermal damage-related parameters as a function of time and pavement depth for a pavement section constructed in North Carolina (RS 9.5B 0-percent RAP).

Figure 29 presents the daily thermal stress and temperature variations. Three regions can be defined in this figure:

- Region 1 corresponds to the beginning of the day when the air temperature and, correspondingly, the surface temperature drops gradually. As a result, the thermal stress increases and reaches its highest magnitude at 7 a.m.
- Region 2 corresponds to the time of day when the air temperature and surface temperature increase. As a result, the thermal stress starts to decrease.
- Region 3 corresponds to the end of the day when the pavement starts to cool down and the thermal stress begins to increase.

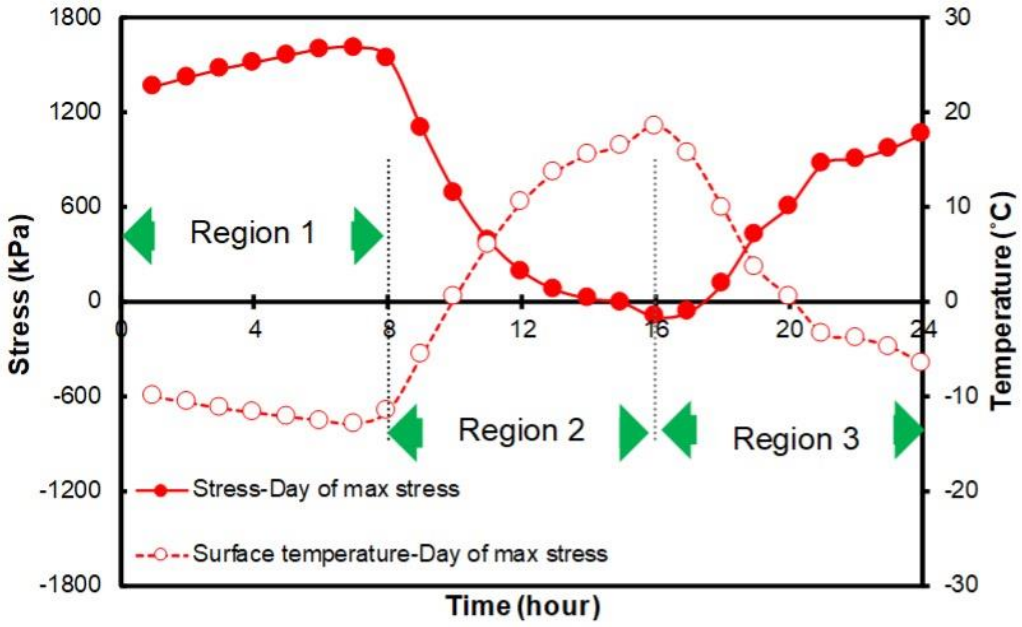

Source: FHWA.
1 kPa = 0.145 psi.

Figure 29. Graph. Thermal stress and temperature variations for the day at which maximum stress occurs at the pavement surface.

The induced thermal stress, defined as equation 71, depends on the reduced strain rate, defined in equation 66. For the sake of clarification, the day at which the maximum stress occurs and the history of the temperature and corresponding reduced strain rate for that day in addition to ±24 h of that day can provide clues for this phenomenon. Figure 30 presents the temperature and reduced strain rate for the day of maximum thermal stress and ±24 h of that day. As shown, three regions also are defined here. According to figure 30, the day during which the maximum thermal stress occurs also shows the maximum reduced strain rate and minimum temperature.

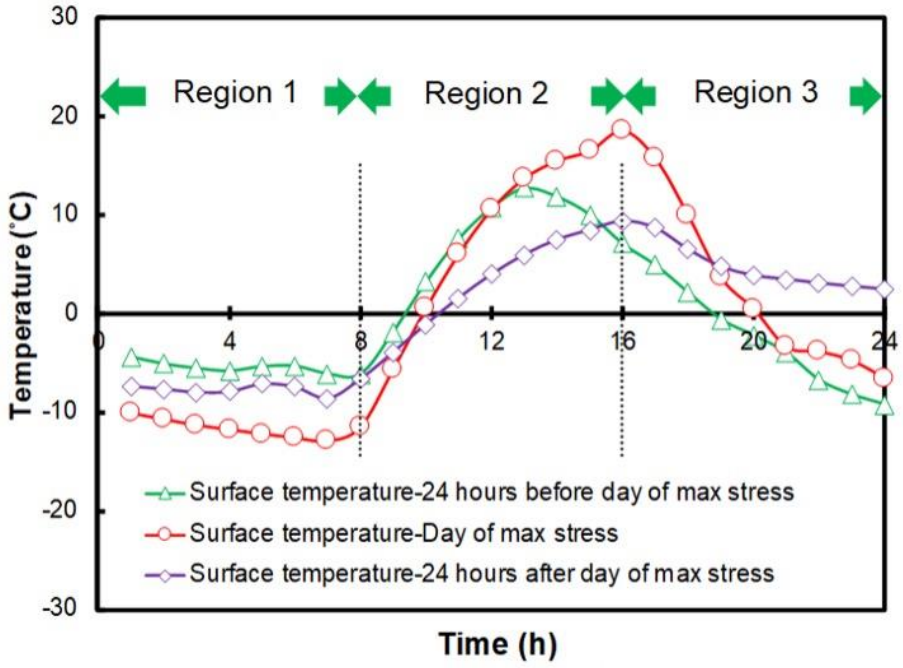

Source: FHWA.

A. Temperature distribution.

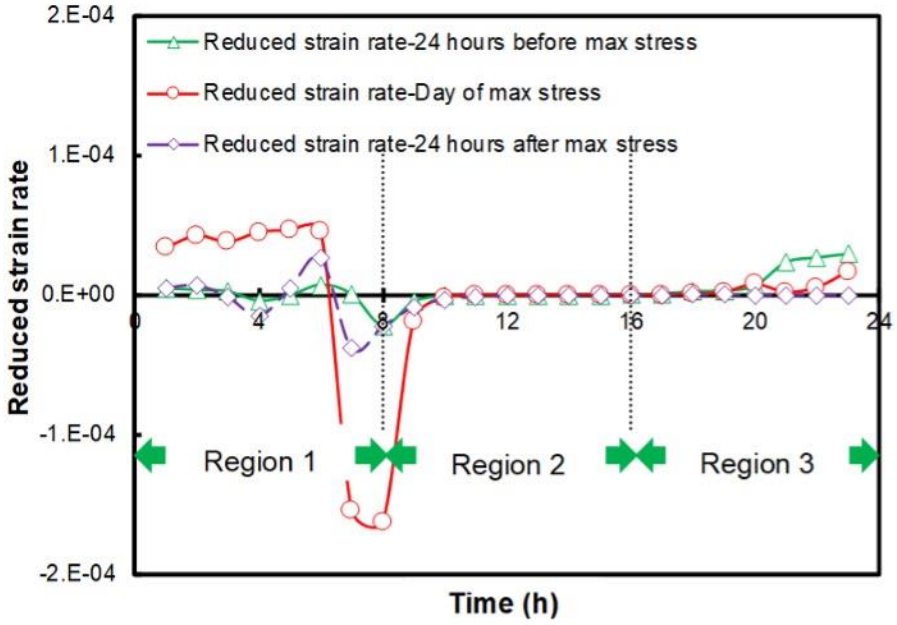

Source: FHWA.

B. Reduced strain rate.

Figure 30. Graphs. Temperature and reduced strain rate evolution as a function of time for the surface of the section and for the day of maximum thermal stress and ±24 h of that day.

Once the daily thermal stress variation and reduced strain rate are known, the DPSE can be calculated versus time. Once the DPSE, expressed as a function of reduced strain rate, passes the failure criterion, failure can be detected.

Figure 31 presents the maximum DF for each point in the MnROAD pavement sections as a function of depth.[11,64] The cells in the legend are arranged based on field performance, where cell 20 shows the best performance and cell 17 shows the worst.

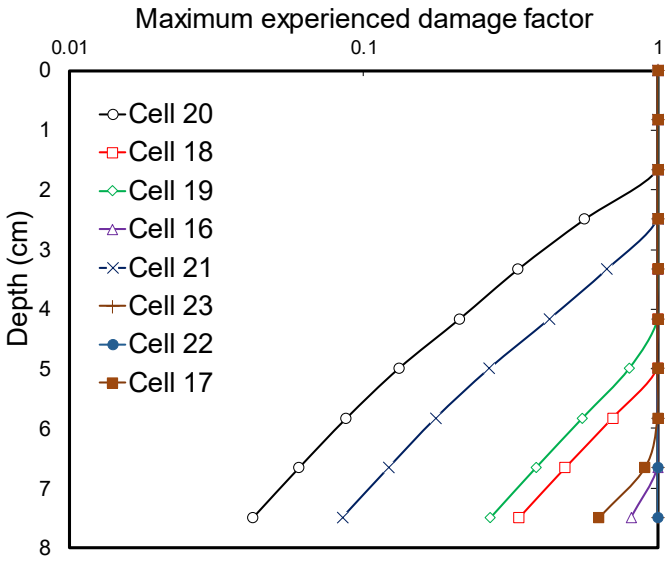

Source: FHWA.
1 cm = 0.4 inches.

Figure 31. Graph. Maximum experienced damage as a function of depth for eight cells constructed in phase III of the MnROAD test facility.

Figure 32 presents a comparison of the DFs of the three North Carolina synthetic pavement sections. As shown, the ranking based on the DF is compatible with the ranking for the predicted fracture temperatures for TSRST. Figure 33 presents the predicted fracture temperatures for the mixtures used in this study. As shown, aging had a significant effect on the predicted fracture temperatures of all the study asphalt mixtures.

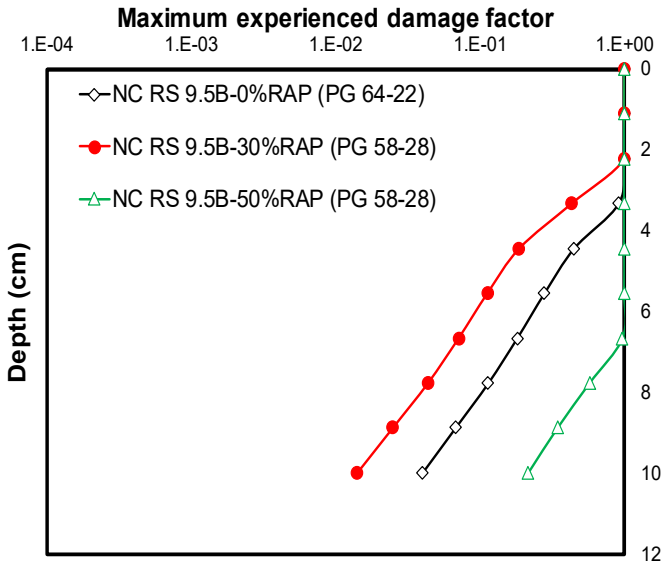

Source: FHWA.
1 cm = 0.4 inches.

Figure 32. Graph. Maximum experienced damage as a function of depth for three synthetic sections constructed in North Carolina.

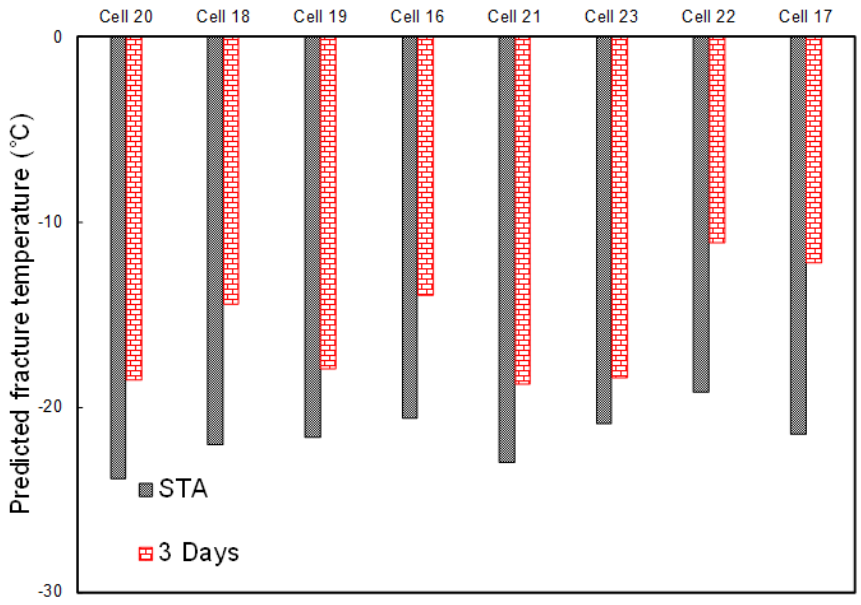

Source: FHWA.

A. MnROAD section's materials.

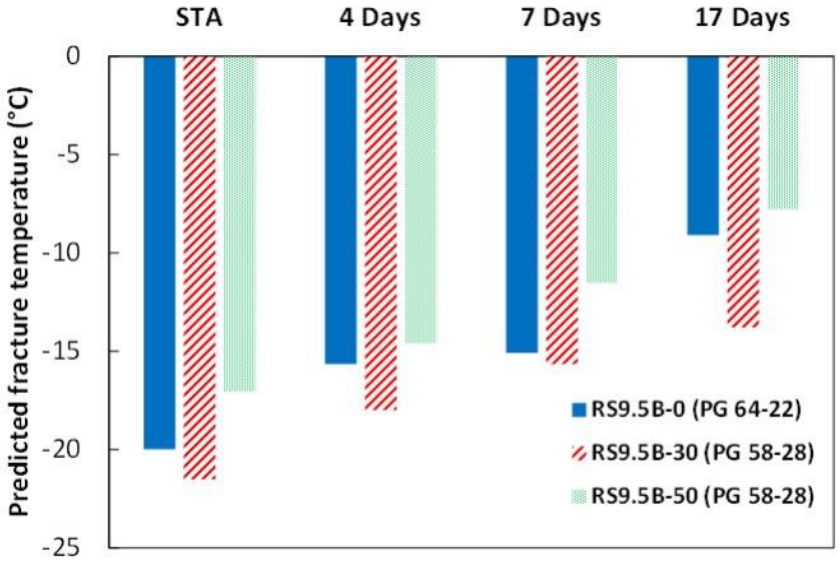

Source: FHWA.

B. North Carolina mixtures.

Figure 33. Graphs. Predicted fracture temperature for mixtures studied in this study.

Discussion of Results

A DF value of 1.0 represents failed or cracked material. As shown in figure 32, the NC RS 9.5B 0-percent RAP and NC RS 9.5B 30-percent RAP sections have the same predicted crack depth (around 2 cm deep) but the magnitudes of the DF are different for the points located below the crack. In addition, cells 20 and 21 in figure 32 have approximately the same depth of cracks but different DF distributions below the cracks. These two observations indicate that the DF is a more sensitive criterion for predicting the performance of asphalt sections subjected to thermal loading than crack depth.

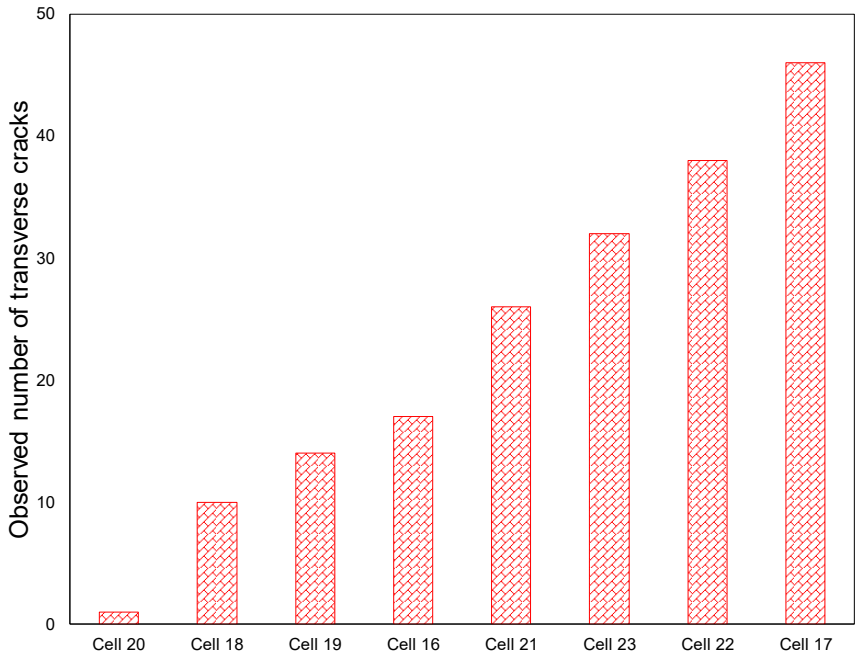

Source: FHWA.

Figure 34. Graph. Number of transverse cracks based on field survey data for MnROAD sections.

Figure 34 presents the observed field data for the MnROAD sections.[11,64] Figure 34 shows that cell 20 exhibited the best performance (fewest number of cracks) and cell 17 exhibited the worst performance (most cracks). The DF distribution shown in figure 31 suggests that cell 17 has a considerably higher DF at each sublayer compared to cell 20. Further verification can be made by pairing the MnROAD mixtures and comparing the rankings based on expectations derived from the volumetric properties (table 7 and table 13), field data (figure 34), predicted TSRST results (figure 33), and DFs (figure 31).

Table 14 presents the comparative study results for the MnROAD sections in which a tick mark indicates the better performance of the pair for these parameters.[11,64] Table 14 also shows that the rankings predicted by FlexTC match expectations for all the pairs.[9] Pair 1 consists of two mixtures that have different RAP contents. Cell 17 has the higher RAP content and, as expected, its performance suffered due to that higher RAP content. This expectation is not in line with the field ranking, but FlexTC was able to capture that discrepancy. The field cores indicated that cell 17 suffered from delamination at the interface of two construction lifts, even in the areas outside the wheel path. The presence of delamination may have slowed the propagation of transverse cracks and, as a result, cell 17 shows fewer transverse cracks. The TSRST ranking follows the FlexTC ranking. As shown in table 14, FlexTC can follow the field ranking, expected ranking, and TSRST ranking for pairs 2, 4, 5, and 6. Pair 3 was intended to be used to investigate the effects of air void content. Pair 3 is expected to exhibit better performance when the air void content is reduced, whereas the field data do not follow this expectation. In this case, the rankings obtained from TSRST and FlexTC match expectations. The field core data show that cell 18 experienced some delamination at the interface of two construction lifts for areas outside

the wheel path. The presence of delamination reduced the relative stiffness of the uncracked asphalt layer and hindered transverse cracking propagation.

Pair 8 was intended to be used to investigate the effects of the binder PG on the performance of the constructed section. Pair 8 is expected to exhibit better performance when the LPG is decreased from −22 (PG 64S-22 in cell 18) to −34 (PG 58H-34 in cell 21). In this case, whereas the FlexTC and TSRST rankings follow the expected trend, the field data do not.[9] As mentioned, cell 18 experienced delamination at the interface of construction lifts. The presence of delamination makes the comparison of the cells' performance difficult.

The reason (or reasons) that the field observations do not follow the expected trends for pairs 3 and 8 is unclear. Both pairs include cell 18. The better-than-expected performance of cell 18 seems to have affected the rankings of pairs 3 and 7. MnDOT will continue monitoring the performance of the MnROAD sections.[11,64] As more condition survey data become available, those data will be used to evaluate FlexTC's ability to predict the thermal cracking performance of asphalt pavements.[9]

Table 14. Comparisons of expected data, field survey data, predicted fracture temperatures, and FlexTC rankings for MnROAD pavement sections.

Pair Number	Target Cell	Expected	Field	TSRST	FlexTC
1	16	—	X	—	—
1	17	X	—	X	X
2	17	—	—	—	—
2	18	X	X	X	X
3	18	—	X	—	—
3	19	X	—	X	X
4	16	—	—	—	—
4	18	X	X	X	X
5	20	—	X	X	X
5	21	X	—	—	—
6	21	X	X	X	X
6	22	—	—	—	—
7	22	—	—	—	—
7	23	X	X	X	X
8	18	—	X	—	—
8	21	X	—	X	X

—No data.
X = Data available.

CHAPTER 3. ASPHALT MIXTURE PERFORMANCE TESTER INDEXES AND THRESHOLD VALUES

Development of a Fatigue Index Parameter, S_{app}, for Asphalt Mixes Using Viscoelastic Continuum Damage Theory

Fatigue cracking is one of the major distresses in asphalt pavements. Engineers have used many methods, from sophisticated numerical simulations to experience-based knowledge, to address fatigue cracking and deliver pavements that perform well. One strategy that is increasingly widespread is the use of a fatigue index parameter that identifies the cracking potential of asphalt mixtures independent of the pavement structure. The use of such an index allows pavement engineers to make quick and targeted decisions about mix design, mix acceptance, and mix QA specifications.

Fatigue cracking is the result of a combination of factors, such as the pavement's materials and structure, climate conditions, and traffic volume and load. Using asphalt mixtures that are reasonably resistant to fatigue is an effective way to help mitigate pavement cracking. The fatigue resistance of an asphalt mixture can be attributed to the quality of the material's components (asphalt binder, aggregate, etc.), the effectiveness of the mix design, and any variability in the production process. To ensure sufficient mixture fatigue resistance, pavement engineers have started to use cracking tests and associated fatigue cracking indexes to evaluate the fatigue resistance of asphalt mixtures.

Previous research has assigned value to this index-based approach and developed different protocols that use the overlay test, semicircular bending test, indirect tension test, beam fatigue test, and others.[98–105] Contractors can conduct these performance tests and use the corresponding parameters to evaluate the mixtures in their mix designs. State agencies can then use those test results (or their own results) to accept or reject the mixtures. However, a drawback of the current index-based approaches is that these approaches do not consider both material and structural factors, which means that these approaches cannot necessarily ensure that pavements will resist fatigue cracking. A truly effective fatigue index parameter would allow pavement engineers to:

- Estimate the cracking potential of a candidate asphalt mixture at the material level before the mixture's acceptance or deployment.
- Assure the quality of the mixture while the mixture is being produced.

In addition to the tests, another commonly used fatigue test is the direct tension cyclic fatigue test, which is performed using an AMPT and cylindrical specimens. AMPT cyclic fatigue test results are used to calibrate the coefficients in the S-VECD model. Unlike other methods and models that report only the cracking potential with pass or fail results at the test temperature and test conditions of interest, the S-VECD model allows the prediction of a mixture's fatigue damage evolution under any temperature and loading conditions based on a few AMPT cyclic fatigue tests at a single temperature.[106] In addition, the S-VECD model can be used to simulate the cracking evolution of pavement structures under real traffic loading and climate

conditions.[83,91] FHWA has adopted the AMPT cyclic fatigue test and the S-VECD model in the development of PRS.[107] Based on their combined efficacy, this study used both the direct tension cyclic fatigue test and the S-VECD model to develop a new fatigue index parameter that addresses both material and structural factors. Due to the fundamental nature of the S-VECD model, the model could be simplified even further to develop the proposed fatigue cracking index parameter, referred to as S_{app}, which represents the apparent damage capacity of a mixture. Unlike other indexes, this new index considers the effects of both material toughness and stiffness. The effectiveness of this S-VECD model-based approach is demonstrated using test results from 105 different asphalt mixtures with varied design factors. The results indicate that S_{app} can distinguish the fatigue resistance of asphalt mixtures with varied properties, including different binder contents, binder PGs, RAP contents, types of binder modifier, air void contents, aggregate gradations, and aging levels. The research team then used these results to propose a set of S_{app} threshold values to determine allowable traffic levels, which are provided at the end of this section.

This section is organized as follows:

- The theoretical background for the S-VECD model is discussed, followed by brief descriptions of the materials and test methods (dynamic modulus and direct tension cyclic fatigue tests) used in this study.

- The derivation of the S_{app} parameter that is based on S-VECD theory and the determination of its final form are explained in detail.

- The effects of the various mixture factors on the S_{app} parameter and a limited field verification study are provided, followed by suggested S_{app} threshold values for different traffic levels.

Theoretical Background

Schapery established the theories that form the basis of the S-VECD model in the 1980s.[108] Schapery first introduced the extended elastic-viscoelastic correspondence principle based on pseudo variables and later derived his work potential theory to develop a damage-based constitutive model. Later, Kim and Little and Kim et al. applied these principles to develop the VECD model that describes the fatigue damage evolution in asphalt mixtures.[107,109] Underwood, Baek, and Kim then derived a simplified version of the VECD model (i.e., the S-VECD model) and reconciled the various approximations made in previous VECD formulations.[106]

The S-VECD model characterizes changes in the constitutive relationship as fatigue damage accumulates in the tested material. The cumulative damage itself under external loading is characterized and can be predicted for different loading histories once the S-VECD model coefficients are known. Because the S-VECD model incorporates the t-TS principle and the pseudostrain energy concept, the model can describe the damage evolution under different modes of loading (i.e., control-strain, control-stress, monotonic, or mixed-mode loading) at different temperatures. Equation 77 presents the governing damage evolution law.

$$\frac{\partial S}{\partial t} = \left(-\frac{\partial W^R}{\partial S} \right)^{\alpha}$$

(77)

Where:

t = reduced time after applying the t-TS principle.
α = a material constant calculated from the maximum slope of the relaxation modulus in log-log scale.
W^R = pseudostrain energy.
S = internal state variable.

The pseudostrain energy is a function of pseudostrain and pseudostiffness. According to S-VECD theory, as the material enters the quasi-static cyclic status, the pseudostrain at each loading cycle can be simplified, as shown in equation 78.

$$\varepsilon^R = \left| E^* \right| \cdot \varepsilon$$

(78)

Where $|E^*|$ is dynamic modulus of the mixture at the loading temperature and frequency of interest.

The constitutive relationship of the material is presented in equation 79.

$$\varepsilon^R = \frac{\sigma}{C}$$

(79)

Where:

C = pseudostiffness that indicates the status of the material from its intact state to failure.
σ = stress in kPa.

The pseudostiffness value starts at one and decreases as the damage increases. Using this constitutive relationship, the pseudostrain energy can be expressed as equation 80.

$$W^R = \frac{1}{2} C \left(\varepsilon^R \right)^2$$

(80)

The relationship between pseudostiffness and the internal state variable, S, which quantifies the cumulative damage, is termed the damage characteristic curve. The damage characteristic curve is unique for each material and can be characterized using a power function, as shown in equation 70. Using these principles, the S-VECD model can predict the damage evolution and mechanical responses (i.e., stress and strain) in the material under fatigue loading.

Wang and Kim developed a failure criterion for the S-VECD model.[110] This failure criterion uses one variable, D^R, which is the average reduction in material integrity up to failure, to determine the number of load cycles at which a macro-crack forms in the material. The mathematical expression is presented as equation 81.

$$D^R = \frac{\int_0^{N_f} (1-C)\, dN}{N_f} = \frac{\text{sum}(1-C)}{N_f} \tag{81}$$

Where N_f is number of load cycles at failure.

The value of D^R is also material-specific whereby a higher value indicates the material's greater resistance to damage.

In Wang and Kim's work, the failure of an asphalt mixture is defined by the drop in phase angle.[110] However, further investigations of cyclic fatigue test results from multiple agencies revealed that using the phase angle drop as the failure definition could lead to an inaccurate determination of the failure in some cases. The drop in modulus value multiplied by the number of load cycles ($|E^*|$ x N) as the cyclic loading continues is a more stable way of determining the material's failure. Also, the number of cycles to failure using the $|E^*|$ x N approach results in slightly fewer load cycles to failure (N_f) than the N_f determined by the drop in phase angle. However, the effect of this difference on the S_{app} values is insignificant.

Materials

A major challenge of validating a fatigue cracking index parameter is finding experimental data that will confirm the parameter. For such a validation, mixtures with a range of index parameter values should be placed in pavements with the same or similar structures and traffic and climatic conditions, as pavement fatigue performance is dependent on the mixture and the structural and external conditions. Some researchers have followed this path but found that the number of mixtures that can be used reliably is relatively small or constrained to a specific agency or jurisdiction.[111,112]

Here, a slightly different approach is taken where 105 different mixtures from the United States, South Korea, and Canada were evaluated using the S_{app} index parameter. (See references 11, 21–23, and 64.) Table 15 presents the sources and characteristics of the study mixtures. Details regarding each set of mixtures are presented and discussed where their S_{app} values are reported later in this study. As indicated by table 1, some of these mixtures already had been used in well-designed tests with systematically varied parameters. These change factors include binder content, binder PG, RAP content, type of binder modifier, air void content, aggregate gradation, and aging level. These 105 mixtures have been able to provide important indications regarding the reasonableness of S_{app} in terms of changes in mixture constitution and composition. Engineering experience shows that certain mixture composition changes are associated with corresponding changes in fatigue performance; for example, an increase in binder content or RAP content can lead to good and poor fatigue resistance, respectively. Other mixtures do not have systematic changes associated with them. However, in these cases, the mixtures have been

designed using standard protocols of a State or Provincial transportation agency. These agencies' mix design practices already target some implicit performance goals, for example, designating an acceptable traffic level for which that mixture can be used. Therefore, these mixtures also provide valuable evidence regarding the reasonableness of the S_{app} index parameter.

Table 15. Materials used in the development and validation of the S_{app} parameter.

Source	Total	Conventional [a]	PMA	WMA	RAP≥ 40 percent	Binder PG	NMAS (mm)	Gradation Type	Remarks
AL (surface)	6	0	2	3 [b]	2 [b]	67-22, 76-22	9.5, 12.5	Fine OGFC	National Center for Asphalt Technology (NCAT) test track mixtures, 2009 cycle, includes 1 polymer-modified OGFC mixture
AL (bottom)	5	1	0	3 [b]	2 [b]	67-22	19	Fine	NCAT test track mixtures, 2009 cycle
AL (aged)	4	0	0	0	4	67-22	19	Fine	50-percent RAP mixtures at different aging levels
Canada (surface)	8	3	0	3	2	58-28, 58-34	16	Fine	Mixtures used in Manitoba test road
Canada (base)	4	1	0	3	0	58-28	16	Fine	Mixtures used in Manitoba test road
VA-ALF	7	3	2	0	2	58-28, 64-22, 70-22, 70-28, 76-28	12.5	Coarse	ALF mixtures used in 2003 and 2013 tests
VA-PEMD	10	10	0	0	0	64-22	12.5	Coarse	Mixtures designed for different volumetric properties
NH	9	6	0	0	3	58-28, 64-28	12.5	Fine	Mixtures used in Northeast RAP study with various percent RAP, percent binder, and binder grades
Korea	2	1	1	0	0	64-22, 76-22	19	Fine	Surface mixtures from S. Korea test road
NC (aged)	4	4	0	0	0	58-28 (64-22 Pay Grade)	9.5	Fine	Surface mixtures at different aging levels

Source	Total	Conventional [a]	PMA	WMA	RAP≥ 40 percent	Binder PG	NMAS (mm)	Gradation Type	Remarks
NC	7	6	1	0	0	64-22, 70-22, 76-22	9.5, 19, 25	Fine	Mixtures commonly used in North Carolina
NC-PEMD	9	9	0	0	0	58-28 (64-22 Pay Grade)	9.5	Fine	Mixtures with different volumetric properties
ME-QA	10	0	10	0	0	64E-28	12.5	Fine	Mixtures sampled from actual paving project for quality assurance
ME	4	4	0	0	0	64-28	12.5	Fine	Mixtures with different binder contents
GA	16	14	2	0	0	64-22, 67-22, 76-22	9.5, 12.5, 19, 25	Fine, Coarse	Paving mixtures commonly used in Georgia
Total	105	62	18	12	15	—	—	—	—

—No data.

[a] Conventional mixtures without polymer or WMA additives.

[b] One mixture from each row of the NCAT mixtures is a WMA mixture with high RAP content. This mixture is shown in both the WMA and high RAP columns.

AL = Alabama; VA = Virginia; NH = New Hampshire; ME = Maine; GA = Georgia; OGFC = open-graded friction course; ALF = FHWA's Accelerated Load Facility; PEMD = performance-engineered mix design.

Test Methods: Dynamic Modulus and Direct Tension Cyclic Fatigue Tests

The dynamic modulus tests were performed using an AMPT in axial compression, load-controlled mode. Two sizes of cylindrical specimens were fabricated for these tests:

- 100 mm in diameter and 150 mm in height for all tests (except those that used the NC aged, NC, NC-PEMD, ME, and ME-QA mixtures listed in table 15).
- 38 mm in diameter and 110 mm in height for the aging study.

The research team followed the procedure in AASHTO PP 99 to fabricate the 38-mm diameter specimens.(90) All the test specimens were cored and cut from Superpave gyratory-compacted samples that were 150 mm in diameter and 180 mm in height. The research team tested the 100-mm diameter specimens following the protocol given in AASHTO T 378/R 84 and tested the 38-mm diameter specimens according to AASHTO TP 132.(89,113) The team conducted tests for all mixtures at 4 °C, 20 °C, and 40 °C. The tests were conducted at 25 Hz, 10 Hz, 5 Hz, 1 Hz, 0.5 Hz, and 0.1 Hz as specified in AASHTO T 378/R 84 and at 10 Hz, 1 Hz, and 0.1 Hz as specified in AASHTO TP 132. A trial-and-error process determined load levels so that the resulting strain amplitudes were between 50 and 70 microstrain to prevent damage to the specimens. The research team imported test results to the FlexMAT program and processed those results to calculate the dynamic modulus and phase angle values and to develop the dynamic modulus master curves and t-TS factors.(5)

The team performed the direct tension cyclic fatigue tests in control actuator displacement mode loading the protocols specified in AASHTO T 400 for the 100-mm diameter specimens and AASHTO TP 133 for the 38-mm diameter specimens.(93,114) The heights of the 100-mm diameter and 38-mm diameter specimens were 130 mm and 110 mm, respectively. All the cyclic tests were performed at the frequency of 10 Hz using three to four crosshead displacement amplitudes to cover a range of cycles to failure. The resulting on-specimen strain levels at the beginning of each test varied from 300 microstrain to 800 microstrain. These tests were conducted at the average temperature of the high and low PGs that were determined using LTPPBind Online for the project of interest minus 3 °C.(12) The fatigue life of the specimens was determined by observing the drop in phase angle. The research team imported the test results to FlexMAT and processed those results to calculate the S_{app} values.(5)

Derivation of the S_{app} Index Parameter Using Simplified Viscoelastic Continuum Damage Theory

Identifying Important Factors for Modeling Fatigue Damage

The research team developed the S_{app} parameter to account for two main factors that affect the cracking potential of an asphalt mixture: the modulus and the toughness (i.e., the ability of a material to absorb energy without fracturing). Under the same load amplitude, a material with a higher modulus value yields a lower strain value than a material with a lower modulus value. If the other properties (for example, toughness) are similar in the two materials, then the lower strain value in the material with the higher modulus value would yield a longer fatigue life. When two materials with different toughness values are subjected to the same strain level, the

tougher material would have a longer fatigue life than the less tough material. Many engineering materials with poor cracking resistance either have a high modulus value with a low level of toughness or a low modulus value with a high level of toughness. Therefore, an appropriate fatigue cracking index parameter must be able to address the effects of both modulus and toughness on fatigue cracking.

In the S-VECD model, the modulus effect can be captured by the position of the damage characteristic curve, i.e., the *C* versus *S* curve. When the pseudostiffness, *C*, and damage, *S*, are plotted against each other, the damage characteristic curves for mixtures with high modulus values usually appear higher on the plot than curves for mixtures with low modulus values. In addition, with D^R indicating a parametric estimate of the toughness of the material, for mixtures with the same modulus value, the longer-lasting mixture will have a higher D^R value, which indicates that the material is more resistant to failure.[110]

Figure 35 presents an example of these modeling concepts using two asphalt mixtures subjected to cyclic fatigue tests. These two mixtures are the New Hampshire (NH) mixtures presented in table 15 and both consist of the same components, except that the NH6440-opt mixture contains 40-percent RAP and a binder content that is 0.5 percent less than the volumetric design optimum content and the NH6420-opt mixture has 20-percent RAP and asphalt binder at the volumetric design optimum content.

Figure 35-A presents two observations. First, the damage characteristic curves of the NH6420-opt mixture tested at two different strain levels collapse well, demonstrating the strain-level independence of the damage characteristic curve, which is a strength of the S-VECD model. Second, the damage characteristic curve of the NH6440-opt mixture is positioned higher than that of the NH6420-opt mixture, which is related to the fact that the modulus value of the NH6440-opt mixture is higher than that of the NH6420-opt mixture (1,253 MPa versus 1,018 MPa at 9 °C and 10 Hz). That is, the material's modulus affects the position of the damage characteristic curve, and therefore, the fatigue cracking resistance cannot be assessed using the position of the damage characteristic curve only. Figure 35-B illustrates this point.

In figure 35-B, the NH6420-opt mixture has a higher D^R value than the NH6440-opt mixture. Figure 35-B shows the pseudostiffness response of these two mixtures when the mixtures are subjected to 1,500 microstrain in machine actuator displacement mode and the pseudostiffness response of the NH6420-opt mixture when the mixture is subjected to 1,200 microstrain. Comparing the two 1,500 microstrain cases, even though the pseudostiffness value of the NH6440-opt mixture is higher at the beginning, because of its lower D^R value, its pseudostiffness undergoes a reduction earlier than the NH6420-opt mixture (at 11,000 cycles versus at 18,000 cycles). As for the NH6420-opt mixture, its higher D^R value allows the pseudostiffness to remain at a low level without failure.

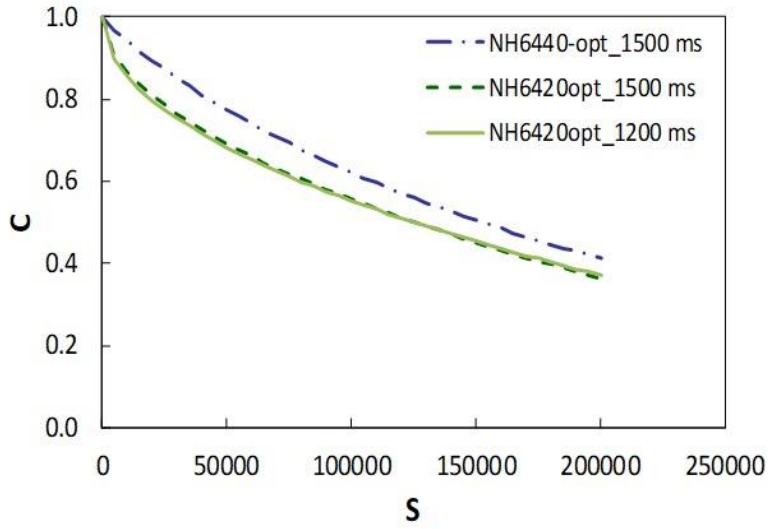

A. Damage characteristic curves for NH6440-opt and NH6420-opt mixtures.

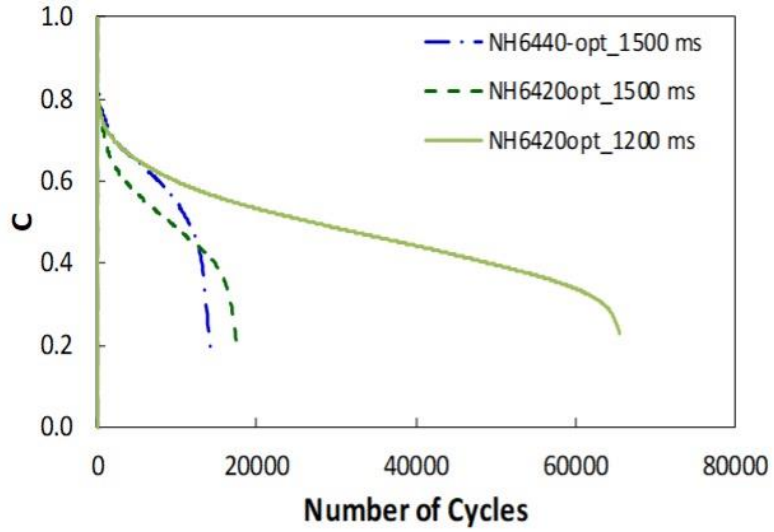

B. *C* versus *N* curves for the two mixtures at different strain levels in cyclic fatigue tests.

Figure 35. Graphs. Damage characteristic curves for NH6440-opt and NH6420-opt mixtures and *C* versus *N* curves for the two mixtures at different strain levels in cyclic fatigue tests.[(115)]

This failure mechanism can be observed under another loading situation as well. Under the condition where NH6420-opt is loaded with an initial strain level of 1,200 microstrain in machine actuator displacement mode, as the number of cycles increases, the pseudostiffness

starts to decrease, similar to the NH6440-opt mixture at 1,500 microstrain loading. However, the NH6420-opt mixture was able to maintain its integrity for a considerable number of cycles as the pseudostiffness changed from 0.6 to 0.4.

Another important point to be made regarding the fatigue behavior of asphalt concrete is that a mixture with a high modulus value does not necessarily ensure a longer fatigue life under a certain load; similarly, a D^R value alone cannot necessarily determine the fatigue life of a material. Figure 36 presents two mixtures with similar D^R values but different modulus values. The two mixtures are the Alabama (AL) (bottom) mixtures that are presented in table 15 for the control section (S9) and the high RAP section (N10) used in the NCAT Test Track 2009 Research Cycle study.[116] These control and RAP mixtures are designated as C3 and R3 in the figure, respectively. The R3 mixture contains the same components as the C3 mixture but with 50-percent RAP. A higher modulus value was found for the R3 mixture in the dynamic modulus laboratory tests compared to the C3 mixture, and similar D^R values were reported from the cyclic fatigue tests. The laboratory test results suggest that the R3 mixture might have better fatigue resistance than the C3 mixture under similar loading conditions. Also, in the field, more bottom-up cracking was observed in the control section than in the RAP section.[116]

In summary, stiffness and toughness are both important material properties that contribute to the ability of a mixture to resist fatigue failure. Therefore, these properties should be reflected in an effective fatigue index parameter.

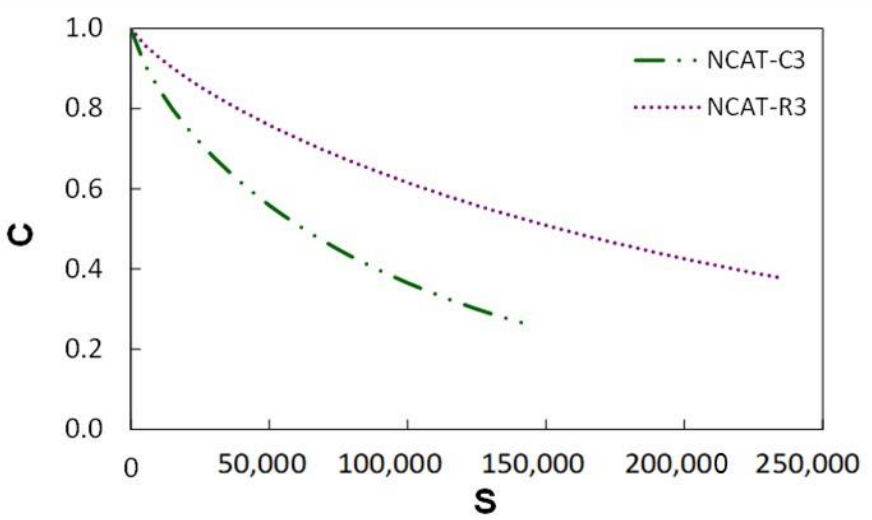

Figure 36. Graph. Damage characteristic curves for NCAT C3 (control) and NCAT R3 (50-percent RAP) bottom-layer mixtures.[115]

Developing the New S_{app} Index Parameter

S-VECD theory is based on the evolution of pseudostrain energy. The pseudostrain energy accumulates at each load cycle until the material fails when cyclic loading is applied. As damage

grows, the material loses its capacity to store the pseudostrain energy. The difference between the energy that could be stored at the undamaged state under the corresponding load strain amplitude ($\varepsilon_{0,ta}^{R}$) and the current stored maximum pseudostrain energy has been defined as the total released pseudostrain energy, W_C^R , at each cycle.(106) Equation 82 expresses the total released pseudostrain energy concept.

$$W_C^R = \frac{1}{2}(1-C)\left(\varepsilon_{0,ta}^R\right)^2 \tag{82}$$

Where $\varepsilon_{0,ta}^{R}$ is pseudostrain amplitude for the duration of the stress in tension.

Combining equation 77 and equation 80, the following equation 83 can be obtained.

$$dS = \left[-\frac{dC}{dS}\right]^{\alpha}\left[\frac{1}{2}\left(\varepsilon^R\right)^2\right]^{\alpha} dt \tag{83}$$

If the damage characteristic curve is modeled using the power function, as shown in equation 70, substitution of the damage function into equation 83 results in equation 84.

$$S^{\alpha} dS = \left[\frac{1}{2}C_{12}\left(1-C\right)\left(\varepsilon^R\right)^2\right]^{\alpha} dt \tag{84}$$

Integrating both sides of equation 84 results in the computation of *S*, as shown in equation 85 or equation 86.

$$S^{\alpha+1} = (\alpha+1){C_{12}}^{\alpha}\int_0^t\left[\frac{1}{2}(1-C)\left(\varepsilon_{0,ta}^R\right)^2\right]^{\alpha} dt \tag{85}$$

$$S^{\alpha+1} = (\alpha+1){C_{12}}^{\alpha}\int_0^t\left(W_C^R\right)^{\alpha} dt \tag{86}$$

In equation 85 and equation 86, α and C_{12} are constants within a test; thus, *S* is related directly to the total released pseudostrain energy during the test. Therefore, using *S*, which represents the released energy that has accumulated to the current cycle, as part of the developed index parameter is reasonable.

The overall basis for the developed S_{app} parameter is the damage characteristic curve. The position of the curve indicates the modulus of an asphalt mixture. The effect of the D^R value also can be reflected by introducing the variable C_{avg}, which is the average pseudostiffness value

during a fatigue test. The value of C_{avg} is calculated from equation 87, and the D^R value is mathematically equal to the value of 1- C_{avg}.

$$C_{avg} = \frac{\int_0^{N_f} CdN}{N_f} \tag{87}$$

Greater resistance to damage is indicated by a low average pseudostiffness value, which physically can be understood in the following way. Greater resistance to damage typically leads to later failure of the material. As the number of load cycles increases, the pseudostiffness decreases and remains at a low level and, as a result, the average pseudostiffness value, C_{avg}, also remains low throughout the mixture's entire fatigue life.

With C_{avg} located on the damage characteristic curve, the corresponding S value, when C is equal to C_{avg}, can be defined as representative fatigue damage, designated as S_{rep}. This definition stems from the observation that the internal state variable, S, represents the accumulated damage in the material. Figure 37 presents schematics of the C_{avg} and S_{rep} concepts. Using the variable, S_{rep}, the fatigue resistance of different mixtures can be ranked. In this study, the NH6420-opt mixture exhibits greater fatigue resistance than the NH6440-opt mixture due to its D^R value, and the R3 mixture ranks higher than the C3 mixture because of its high modulus value. Equation 88 or equation 89 are the formulas that are used to compute the S_{rep} value.

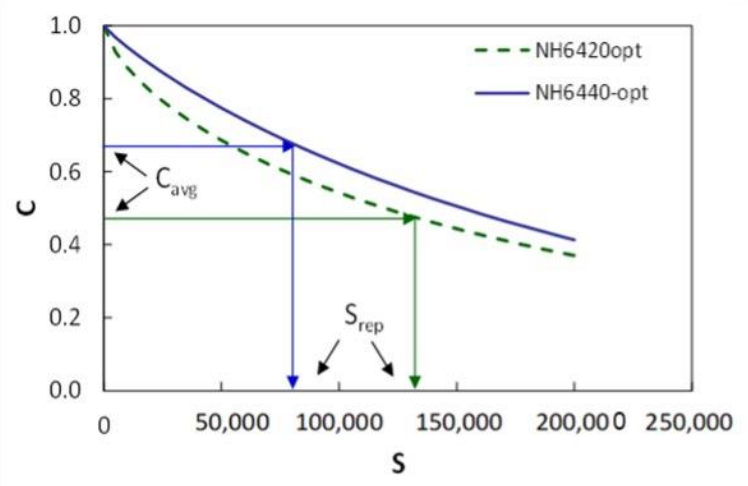

A. NH6420-opt and NH6440-opt mixtures.

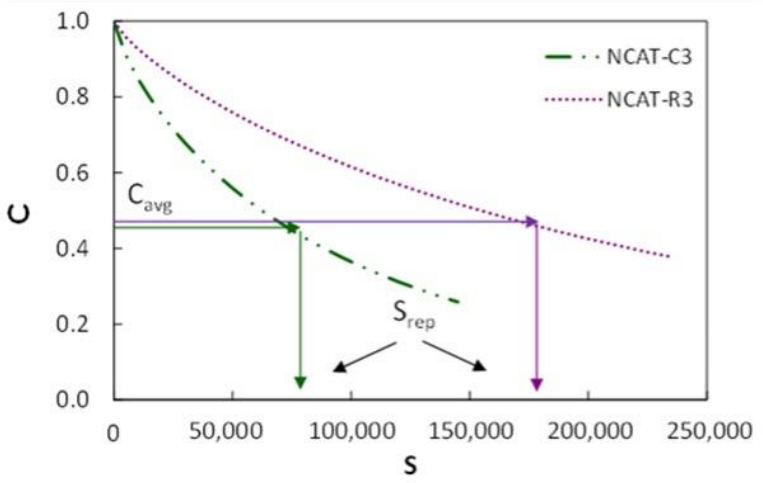

B. NCAT-C3 and NCAT-R3 mixtures.

Figure 37. Graphs. Schematics for C_{avg} and S_{rep} with damage characteristic curves.[115]

$$S_{rep} = \left(\frac{a_T^{\frac{C_{12}}{\alpha+1}}}{C_{11}} \left(1 - C_{avg}\right) \right)^{\frac{1}{C_{12}}} \tag{88}$$

$$S_{rep} = \left(\frac{a_T^{\frac{C_{12}}{\alpha+1}}}{C_{11}} D^R \right)^{\frac{1}{C_{12}}} \tag{89}$$

Where a_T is t-TS factor.

The shift factor should be computed at the reference temperature, which is the average of the climate binder PG minus 3 °C. By considering the reference temperature in the calculation, the S_{rep} parameter accounts for the effect of climate on the fatigue behavior of the mixture.

The S value starts to increase from zero as damage is introduced and evolves. As mentioned, the failure of the material should be considered in any fatigue index parameter. The researchers initially assessed whether S_{rep} could be used directly as the new index. The S_{rep} value uses the failure criterion, D^R, in the calculation and is mathematically equal to the S value when the corresponding pseudostiffness, C, is equal to ($1-D^R$). These formulas are presented in equation 88 and equation 89. The coefficients in equation 88 and equation 89 are constants in the damage characteristic curve and the failure criterion, and those coefficients are independent of mode of loading.[110] Therefore, in principle, the index, S_{rep}, is capable of evaluating materials under

different loading scenarios. The following paragraphs present a detailed rationale for using S_{rep}, with control-strain loading mode conditions as an example.

When the material reaches the steady state condition, equation 83 can be expanded to become equation 90.

$$dS = \left[C_{11}C_{12}S^{C_{12}-1}\right]^{\alpha}\left(\frac{1}{2}\left(\varepsilon^{R}\right)\right)^{2}\cdot\frac{K_1}{f_R}dN \tag{90}$$

Where:

K_1 = loading shape factor that accounts for the effective loading time in tension of a load cycle.

f_R = reduced frequency.[110]

Equation 90 presents the algorithm that is used to predict damage growth within a cyclic loading path with known material properties.

In steady-state control-strain mode, ε^R and K_1 can be simplified as constants. Thus, if integrations are applied on both sides of equation 90, equation 91 can be obtained.

$$\int_0^S S^{(1-C_{12})\alpha}dS = \int_0^N \frac{\left(\frac{1}{2}\left(\varepsilon^{R}\right)^{2}\right)^{\alpha}}{f_R}\left[C_{11}C_{12}\right]^{\alpha}K_1 dN \tag{91}$$

Through algebraic and integral manipulations, equation 92 and equation 93 then can be derived.

$$S^{1-\alpha C_{12}+a} = \left[\frac{1}{2}C_{11}C_{12}\left(\varepsilon^{R}\right)^{2}\right]^{\alpha}\cdot\left(1-\alpha C_{12}+\alpha\right)\cdot\frac{K_1}{f_R}\cdot N \tag{92}$$

$$N = \left(\frac{f_R}{\left(1-\alpha C_{12}+\alpha\right)\left[\frac{1}{2}C_{11}C_{12}\left(\varepsilon^{R}\right)^{2}\right]^{\alpha}K_1}\right)S^{1-\alpha C_{12}+\alpha} \tag{93}$$

At the reference temperature, the t-TS factor is equal to one, and the number of cycles when S is equal to S_{rep} can be obtained by substituting equation 88 into equation 93 to derive equation 94.

$$N_{S_{rep}} = \left(D^R\right)^{\frac{1-\alpha C_{12}+\alpha}{C_{12}}} \left(\frac{1}{C_{11}}\right)^{\frac{1-\alpha C_{12}+\alpha}{C_{12}}} \left(\frac{f_R \cdot 2^{\alpha}}{\left(1-\alpha C_{12}+\alpha\right)\left(C_{11}C_{12}\right)^{\alpha}\left(\varepsilon^R\right)^{2\alpha} K_1}\right) \tag{94}$$

Where N_{Srep} is number of cycles when S is equal to S_{rep}.

On the other hand, when the material is loaded until failure in control-strain mode, part of the right side of equation 81 can be expressed as shown in equation 95.

$$sum\left(1-C\right) = \int_0^{N_f} \left(1-C\right) dN = \int_0^{N_f} C_{11} S^{C_{12}} dN \tag{95}$$

Where N_f is number of cycles to failure.

If equation 92 is substituted into equation 95 and integration is performed on the right side of the equation, equation 96 is obtained.

$$sum\left(1-C\right) = \left(\frac{f_R \cdot 2^{\alpha}}{\left(1-\alpha C_{12}+\alpha\right)\left(C_{11}C_{12}\right)^{\alpha}\left(\varepsilon^R\right)^{2\alpha} K_1}\right)^{-\frac{C_{12}}{p}} \frac{C_{11}}{\frac{C_{12}}{p}+1} N_f^{\frac{C_{12}}{p}+1} \tag{96}$$

Where $p = 1-\alpha C_{12}+\alpha$.

If this equation is combined with equation 81, then the number of cycles to failure in control-strain mode can be obtained, as shown in equation 97.

$$N_f = \left(D^R\right)^{\frac{1-\alpha C_{12}+\alpha}{C_{12}}} \left(\frac{C_{12}+1-\alpha C_{12}+\alpha}{C_{11}\cdot\left(1-\alpha C_{12}+\alpha\right)}\right)^{\frac{1-\alpha C_{12}+\alpha}{C_{12}}} \left(\frac{f_R \cdot 2^{\alpha}}{\left(1-\alpha C_{12}+\alpha\right)\left(C_{11}C_{12}\right)^{\alpha}\left(\varepsilon^R\right)^{2\alpha} K_1}\right) \tag{97}$$

Combining equation 94 and equation 97, equation 98 is derived.

$$N_f = \left(\frac{1}{m}+1\right)^m \times N_{S_{rep}} \tag{98}$$

Where m is material constant equal to p/C_{12}.

Equation 98 shows that, under control-strain loading mode, the number of cycles when S is equal to S_{rep} is proportional to the number of cycles to failure. Therefore, S_{rep} is an adequate parameter

to evaluate the material's fatigue resistance under this mode of loading. Similar but more complicated derivations can be performed for other modes of loading; however, due to the limited space, those derivations are not presented in this section.

Modifying and Finalizing the S_{app} Index

This study first used the S_{rep} parameter as an index to evaluate the 105 asphalt mixtures in the NCSU database. The S_{rep} parameter was able to rank most of the mixtures according to expected performance based on engineering judgment, field performance data, and structural numerical simulation results. Figure 38 presents an example that provides the S_{rep} values of mixtures with various RAP contents and binder contents. This series of mixtures, which includes the two mixtures (NH mixtures with 20-percent and 40-percent RAP) discussed earlier, contains the same PG 64-28 binder from New Hampshire but has different RAP contents and binder contents. The first two mixtures, NH6420-opt and NH6420-opt, were fabricated with 20-percent RAP but with binder contents at the volumetric optimum and 0.5 percent less than the optimum, respectively. The last three mixtures, NH6440-opt, NH6440-opt, and NH6440+opt, contain 40-percent RAP and 0.5 percent less than the binder content volumetric optimum, the volumetric optimum, and 0.5 percent more than the volumetric optimum content, respectively. Table 15 presents details regarding these mixtures. Figure 38 shows that, for the mixtures with the same RAP contents, as the binder content increases, the S_{rep} value increases. However, the effects of RAP content on the S_{rep} value are not clear in figure 38, as the increase in RAP content from 20 percent to 40 percent in the NH mixtures with 0.5 percent less than the binder content volumetric optimum increases the S_{rep} value whereas the opposite trend is found in the NH mixtures with the volumetric optimum.

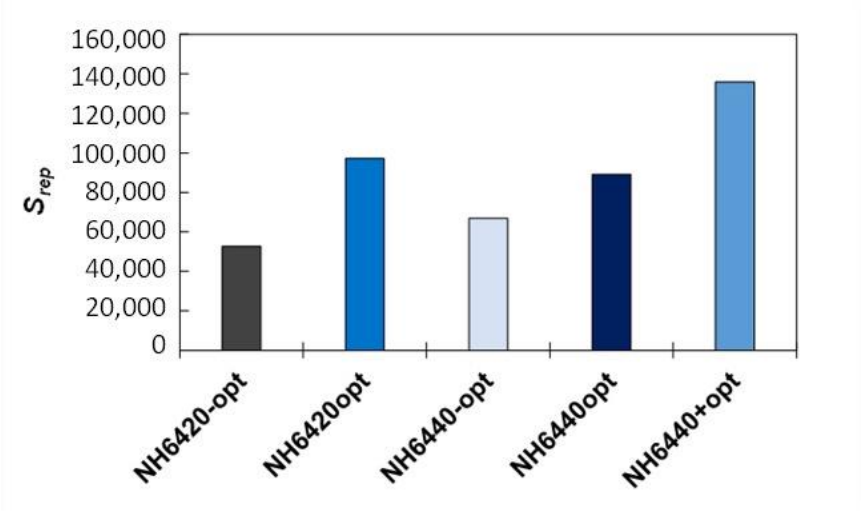

Figure 38. Graph. S_{rep} values of mixtures with various RAP contents and binder contents.[(115)]

In addition, the S_{rep} parameter did not reflect the expected fatigue resistance of LTA mixtures. Figure 39 presents an example of such cases. In this example, the NCAT mixture with 50-percent RAP was STA at 135 °C for 4 h and then LTA in the oven at 95 ℃ for 7 d (AL1), 11 d (AL2), and 21 d (AL3), respectively.[116] Figure 39-A shows that the S_{rep} values indicate that the most LTA mixture (AL3) would exhibit the most fatigue resistance, which is opposite to the general understanding of the effect of aging on the fatigue resistance of asphalt mixtures. Careful investigation of the effects of different variables in equation 88 on the S_{rep} value revealed that this opposite trend is due to the increase in modulus as the mixture is aged, which is shown in figure 39-B.

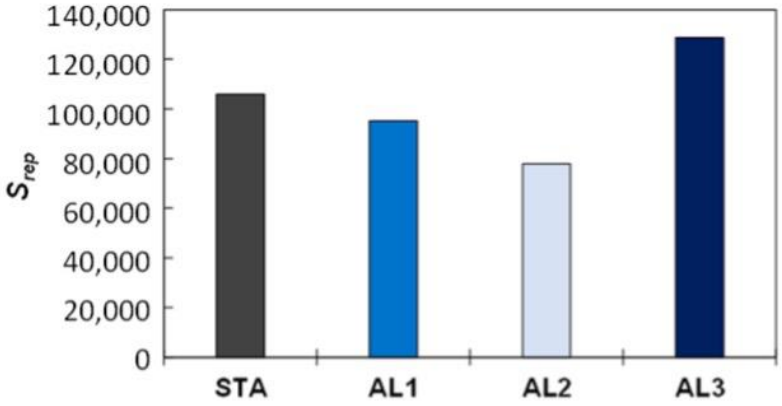

A. S_{rep}.

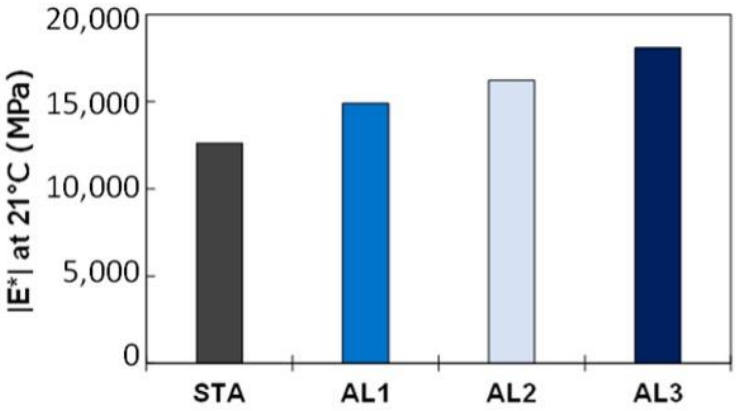

1 MPa = 145.04 psi.

B. $|E^*|$ at 21 °C.

Figure 39. Graphs. Material properties of NCAT mixtures with 50-percent RAP oven aged for 0 d, 7 d, 11 d, and 21 d, respectively.[115]

After reviewing the damage behavior and modulus values of the mixtures that resulted from the S_{rep} parameter's failure to reflect knowledge-based performance expectations, the researchers made a semiempirical modification that relates to the modulus. Following this modification, the new parameter was termed damage capacity and designated as S_{app}. Equations 99 and 100 show the definition of S_{app} with the dynamic modulus ($|E^*|$) in GPa and kPa, respectively. As shown in equation 99, the mixture dynamic modulus value at 10 Hz and the reference temperature were introduced as part of the modification. Here, a power term that is equal to the value of $\alpha/4$ is applied, as the $|E^*|$ value is implicitly included in the computation of pseudostrain in S-VECD theory and pseudostrain is always associated with a power term that is related to α. In addition, the term 1/10,000 is applied so that the computed S_{app} value is within the range of 0 to 50 for convenience. Equation 100 is derived from equation 99, using the dynamic modulus value in kPa.

$$S_{app} = \frac{1}{10,000} \frac{S_{rep}}{\left|E^*\right|^{\frac{\alpha}{4}}} \tag{99}$$

Where $|E^*|$ is material dynamic modulus value at 10 Hz and reference temperature in GPa.

$$S_{app} = 1,000^{\frac{\alpha}{2}-1} \frac{S_{rep}}{\left|E^*\right|^{\frac{\alpha}{4}}} \tag{100}$$

Where $|E^*|$ is material dynamic modulus value at 10 Hz and reference temperature in kPa.

Equation 101 is the finalized formula used to calculate the S_{app} value of an asphalt mixture using the dynamic modulus in kPa.

$$S_{app} = 1,000^{\frac{\alpha}{2}-1} \frac{a_T^{\frac{1}{\alpha+1}} \left(\frac{D^R}{C_{11}}\right)^{\frac{1}{C_{12}}}}{\left|E^*\right|^{\frac{\alpha}{4}}} \tag{101}$$

Effects of Mixture Factors on S_{app}

This study applied the S_{app} parameter to evaluate the effects of changes in various mixture factors on the fatigue resistance of the 105 asphalt mixtures presented in table 1. Table 16 shows the factors investigated, the increasing and decreasing trends of the S_{app} values as a function of the direction of the individual factors, and the mixtures that were used to find these trends. The following subsections provide details about the mixtures used for individual mixture factors and the trends that are summarized in table 16.

Table 16. Materials used in the development and validation of S_{app}.

Factor	Direction	S_{app}	Mixture Used
Binder content	Increase	Increase	ME, NC-PEMD, VA-PEMD, NH
Aging level	Increase	Decrease	AL (aged), NC (aged)
RAP content	Increase	Decrease	NH, MIT (surface), AL (surface), AL (bottom), VA-ALF
Gradation	Coarser	Decrease	NC-PEMD, VA-PEMD
Air void content	Increase	Decrease	NC-PEMD, VA-PEMD, ME-QA
Binder grade	Lower	Increase	NH, MIT (surface), VA-ALF, GA
Binder modifier	Addition	Increase	VA-ALF, KEC, NC

KEC = Korea Expressway Corporation.

Effects of RAP Content, Binder Content, and Binder Grade

Figure 40 presents the first set of mixes tested, i.e., four mixtures from Manitoba, Canada, designated as the MIT (Manitoba Infrastructure and Transportation) RAP mixes.[22,83,84] These four mixtures were designed to have the same components and gradations but different RAP contents: 0 percent (control), 15 percent, 50 percent, and 50 percent with a soft binder. Figure 40 also presents the corresponding S_{app} values of the four MIT mixtures. The S_{app} values indicate that the fatigue resistance decreases as the RAP content is increased and that the soft binder in the high RAP mixture helps to improve its fatigue resistance.

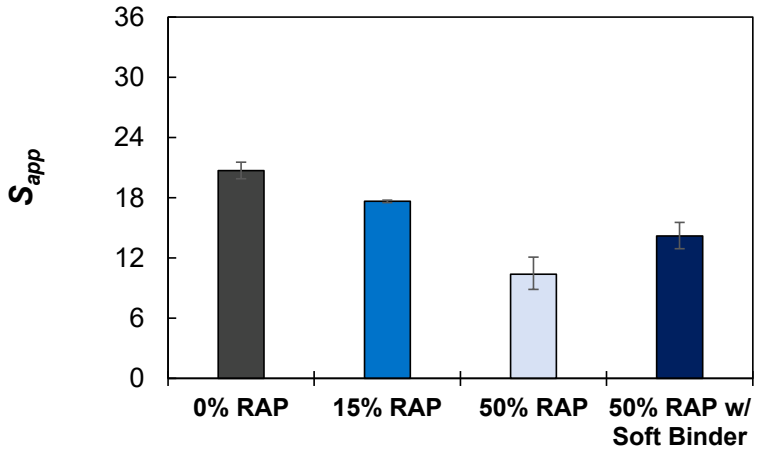

Figure 40. Graph. Evaluation of effects of RAP content and soft binder using S_{app}: MIT-RAP mixtures.[115]

Another study to evaluate RAP mixtures in the northeastern United States is referred to as the NE (New England) RAP study.[117] Nine mixtures from New Hampshire were tested in that study. The mixtures contained different RAP contents, binders with different PGs, and different binder contents. Table 17 presents detailed information about these mixtures and figure 41 presents the computed S_{app} values. The S_{app} values indicate the following:

- As the RAP content is increased among the mixtures with PG 64-28 binder, a general trend of decreasing fatigue resistance can be observed.

- As the binder content is increased when using the same binder and RAP content, the fatigue resistance increases.

These results also suggest that the mixture with PG 58-28 binder and 20-percent RAP (NH5820-opt) has greater cracking resistance than the binder with 40-percent RAP (NH5840-opt). This finding may be due to the use of soft and insufficient binder in the former.

Table 17. Mixture properties used in NE RAP study.

Mix ID	Binder PG	RAP (percent)	Binder Content
NH5820−opt	PG 58-28	20	Optimum − 0.5 percent
NH5840−opt	PG 58-28	40	Optimum − 0.5 percent
NH6400−opt	PG 64-28	0	Optimum − 0.5 percent
NH6400opt	PG 64-28	0	Optimum
NH6420−opt	PG 64-28	20	Optimum − 0.5 percent
NH6420−opt	PG 64-28	20	Optimum
NH6440−opt	PG 64-28	40	Optimum − 0.5 percent
NH6440−opt	PG 64-28	40	Optimum
NH6440+opt	PG 64-28	40	Optimum + 0.5 percent

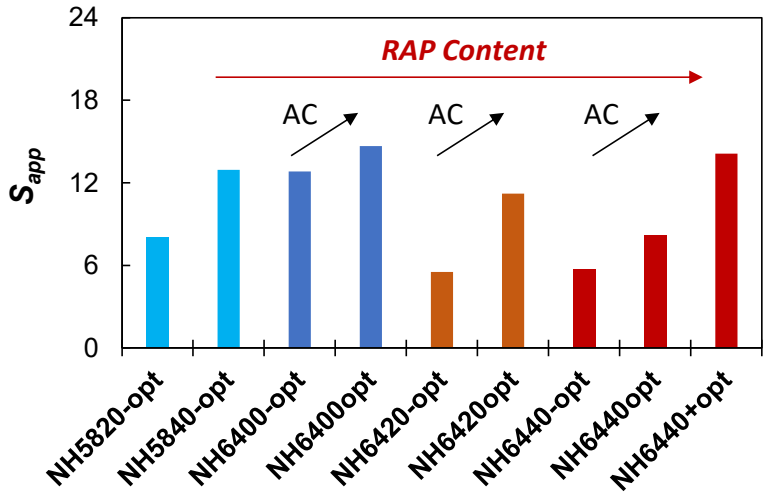

Figure 41. Graph. S_{app} values of mixtures used in the NE RAP study.[115]

MaineDOT conducted a mix design study in 2017 and early 2018.[118] The study researchers performed cyclic fatigue tests using a single mixture but with four binder contents: 0.5 percent less than the original Superpave optimum binder content (considered the optimum), optimum asphalt content, 0.5 percent more than the optimum, and 1 percent more than the optimum. Except for the binder contents, the other mixture properties, such as gradation and air void content, were controlled. The researchers then computed the S_{app} values for the four different conditions. Figure 42 presents the results and shows that, as the binder content increases, the fatigue resistance increases, as suggested by the S_{app} fatigue index values.

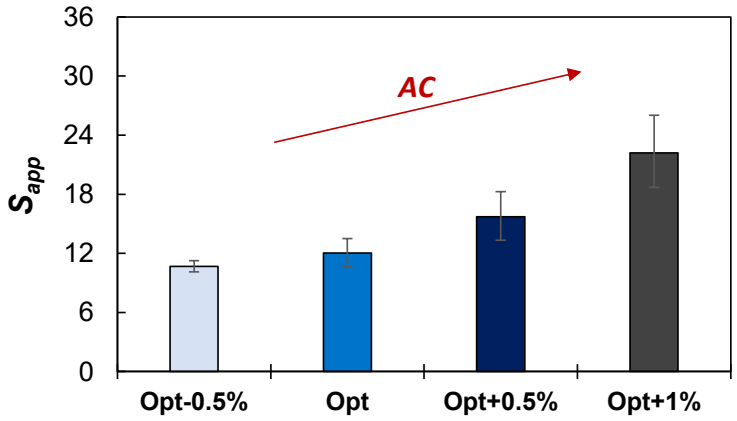

Figure 42. Graph. Change in S_{app} values as binder content increases.[115]

Effects of Different Mixture Types

The S_{app} parameter also was applied to compare the fatigue resistance of different types of mixtures, for example, WMA mixtures versus HMA mixtures. Guo evaluated mixtures from the NCAT test track (Research Cycle 2009) by testing six surface mixtures sampled from sections S8, S9, S10, S11, N10, and N11.[21,119] The six test mixtures included a control mix, WMA with Ingevity™ Evotherm® additive, WMA with foaming technology, an open-graded friction course (OGFC) mixture, a mixture with 50-percent RAP, and WMA mixed with 50-percent RAP.[120] For this study, these six mixtures are designated as Control, Evotherm, Foam, OGFC, High RAP, and WMA-RAP, respectively. Figure 43 presents the S_{app} values of these mixtures. The OGFC mixture, as an open-graded surface mix, shows the least cracking resistance. Not surprisingly, in the field, that OGFC section showed a considerable amount of top-down cracking.[116,119] Among the remaining five mixes, the WMA mixtures, i.e., Evotherm and Foam, are shown to exhibit slightly less cracking resistance than the Control mix but are believed to perform better than the High RAP and RAP-WMA mixes. The RAP-WMA mixture shows better fatigue resistance than the High RAP mixture, which is consistent with engineering judgment. Except for the OGFC section results, the field test results were not used in this study, because the focus is on evaluations at the material level. In the field, the mixtures had been placed on top of two asphalt layers in thick asphalt pavements. Thus, the field results should be affected significantly by the properties of the mixtures underneath these asphalt layers and the pavement structure, where in the OGFC section, the observed top-down cracking can be attributed to the properties of the surface mix.

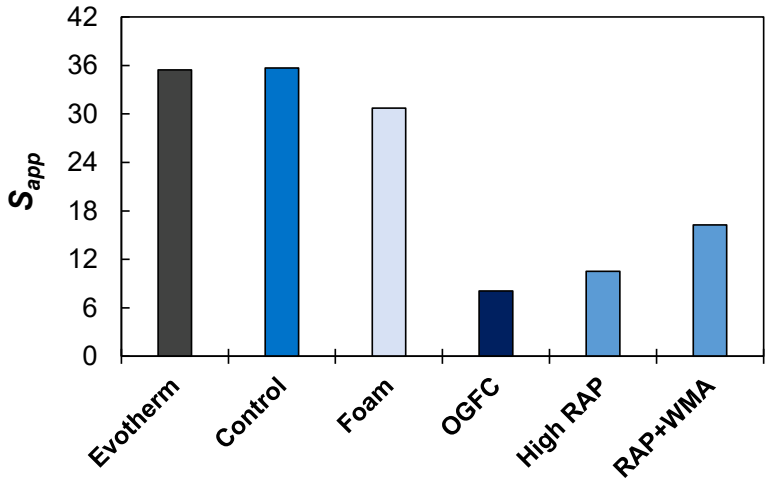

Figure 43. Graph. S_{app} values of NCAT mixtures.[115]

Effects of Aggregate Gradation, Binder Content, and Air Void Content

BMD has become popular among pavement researchers. Two similar studies that involve BMD have been conducted, one at FHWA's Turner-Fairbank Highway Research Center and the other at NCSU. In each of these two studies, the researchers fabricated mixtures using the same

materials but with different volumetric conditions. To vary the volumetric parameters, three gradations were first determined using the Bailey method to ensure differences in the VMA. The researchers then fabricated asphalt samples with different binder contents and air void contents at each gradation to vary the VFA and density parameters. As a result, 21 conditions for a 12.5-mm mixture were used for the FHWA study tests. Later, in the second study, FHWA's experimental design was repeated and simplified to nine conditions, and the tests were performed using a 9.5-mm mixture. Li and Gibson (2016) and Wang et al. (2019) provide detailed information about the experimental design and volumetric information.[121,122]

Figure 44 presents the S_{app} values that were calculated from the cyclic fatigue tests of the FHWA PEMD specimens and the second PEMD specimens with different volumetric conditions. Figure 44-A shows the S_{app} index values for the nine volumetric conditions used in the FHWA PEMD study. The nine conditions are three gradations, three binder contents at each gradation, and the air void contents for the nine conditions that were controlled at the same level (7 percent ±0.5 percent). In the figure, the mixtures are designated using the format G*x*-AC*y*, where *x* indicates the gradation type and *y* indicates the binder content and percentage.

Figure 44-B shows the S_{app} index values of the nine mixtures with various gradations, binder contents, and air void contents that were used in the second PEMD study. Table 18. Volumetric conditions used in second PEMD study and volumetrics at number of design gyrations. lists the design parameters of the nine conditions used in these mixtures. The mixtures are designated as C*x*-yz, where *x* indicates the gradation type, *y* indicates the percentage of air voids during the mix design, i.e., the number of design gyrations (N_{des}), and *z* represents the percentage of air voids of the test specimens. The *x* value for each gradation is equal to the percentage of the aggregate coarse loose unit weight that is used in the Bailey method. The S_{app} values indicate that, in both studies, as the gradation becomes coarser, a decreasing trend in fatigue resistance can be observed. When the gradation and air void contents are controlled, the higher binder percentages appear to improve the cracking resistance of the mixtures. In the second PEMD study, as the air void content increases, the fatigue resistance of the mixture generally decreases. However, in both studies, unexpected trends in the S_{app} values can be observed for the conditions with the coarsest gradations. This discrepancy is believed to be caused by difficulties in mix compaction due to the coarse gradation and low binder contents.

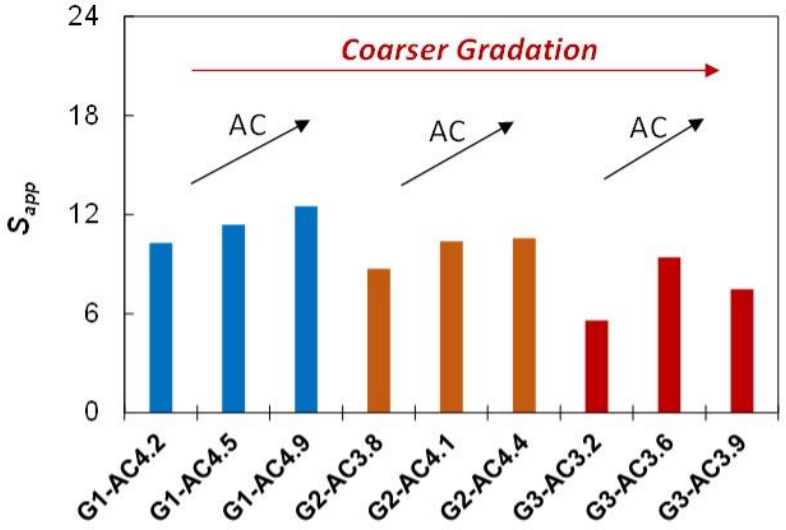

A. FHWA PEMD study.

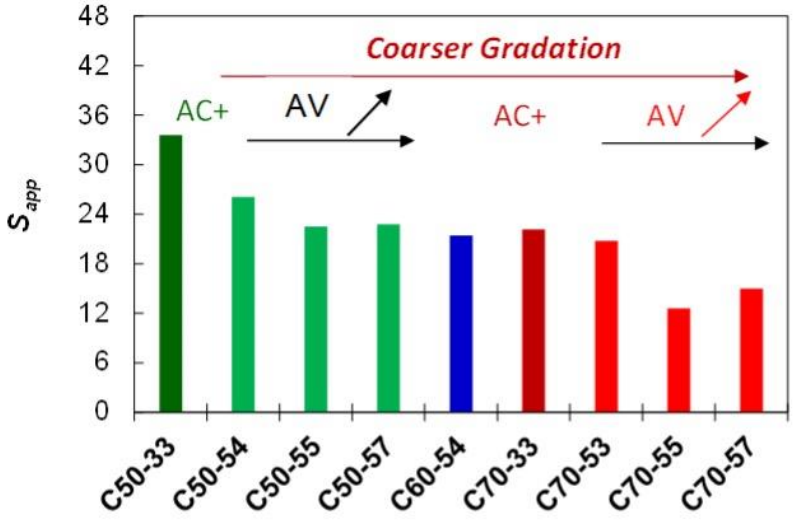

B. Second PEMD study.

Figure 44. Graphs. S_{app} values of study mixtures with different mix design volumetric conditions.[(115)]

Table 18. Volumetric conditions used in second PEMD study and volumetrics at number of design gyrations.

Gradation	ID	VMA	AC (percent)	VFA	Air Void (percent)
CUW 70	C70-33	15.3	6.0	80.4	3.0
CUW 70	C70-53	15.7	5.3	68.1	5.0
CUW 70	C70-55	15.7	5.3	68.1	5.0
CUW 70	C70-57	15.7	5.3	68.1	5.0
CUW 60	C60-44	16.3	5.8	71.2	4.7
CUW 50	C50-33	17.4	7.0	82.8	3.0
CUW 50	C50-54	17.2	6.1	70.9	5.0
CUW 50	C50-55	17.2	6.1	70.9	5.0
CUW 50	C50-57	17.2	6.1	70.9	5.0

CUW = chosen unit weight and represents percent coarse aggregate loose unit weight in the Bailey method.[123]

Effects of Oven Aging on Mixtures

This study used two sets of oven-aged mixtures as examples to validate the effectiveness of the S_{app} index parameter for evaluating fatigue properties. Figure 45-A and figure 45-B show the computed S_{app} values of the aged materials for a North Carolina mixture, NC RS9.5B, and an Alabama NCAT mixture, respectively.[21] The four aging levels are designated as STA and three LTA levels: AL1, AL2, and AL3. To achieve the LTA levels for the first set of mixtures, following short-term aging, the NC RS9.5B loose mixtures were oven-conditioned at 95 °C for 2 (AL1), 4 (AL2), and 7 (AL3) d, respectively, and then compacted. The other set of mixtures, the NCAT mixtures, contained 50-percent RAP. Four aging levels were used to test the Alabama NCAT mixtures (similar to the first set of oven-aged North Carolina mixtures). The oven-aging durations for the three LTA levels were 5 d, 11 d, and 21 d, respectively. A previous aging study showed that these NCAT mixtures simulated aging oxidation after 3.7 yr, 8.2 yr, and 15.7 yr at 0.25-inch depth in the climate of Anniston, AL.[124] According to the S_{app} index parameter, the NCAT mixture that contained 50-percent RAP showed less fatigue resistance than the NC 9.5-mm mixture. For both mixtures, as the aging level increased, the fatigue resistance decreased dramatically.

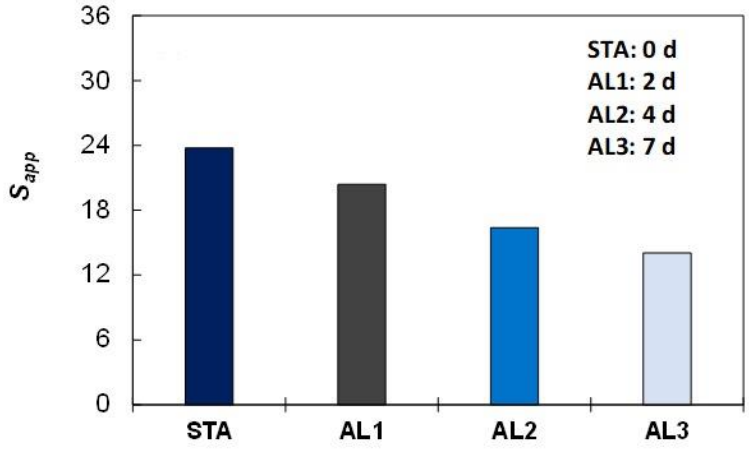

A. NC RS9.5B mixture.

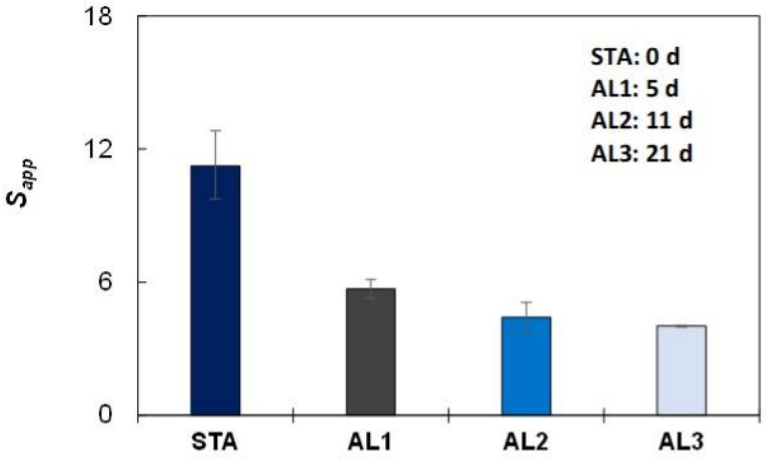

B. NCAT mixture with 50-percent RAP.

Figure 45. Graphs. S_{app} values of oven-aged mixtures.[115]

Limited Field Verification of S_{app}

The mixtures used in the FHWA ALF study were evaluated as part of this study.[121,125] Figure 46-A presents the S_{app} values of the FHWA ALF mixtures. The four mixtures were tested by FHWA, and the S_{app} values were calculated by the research team. The four mixtures—no RAP (control), RAP with 40 percent ABR, RAP with 20 percent ABR, and RAS with 20 percent ABR—were used in lane 1, lane 5, lane 6, and lane 7, respectively. As shown, the mixtures from lane 1, lane 5, and lane 6 used the same PG 64-22 binder, where the mixture from lane 7 used PG 58-28 binder. Based on the S_{app} values, the lane 1 mixture shows the highest cracking

resistance, followed by the lane 6 mixture. The mixtures from lane 5 and lane 7 have more cracking potential than the other two mixes. These observations based on the S_{app} index have been validated by field test results, which are presented in figure 46-B and figure 46-C.

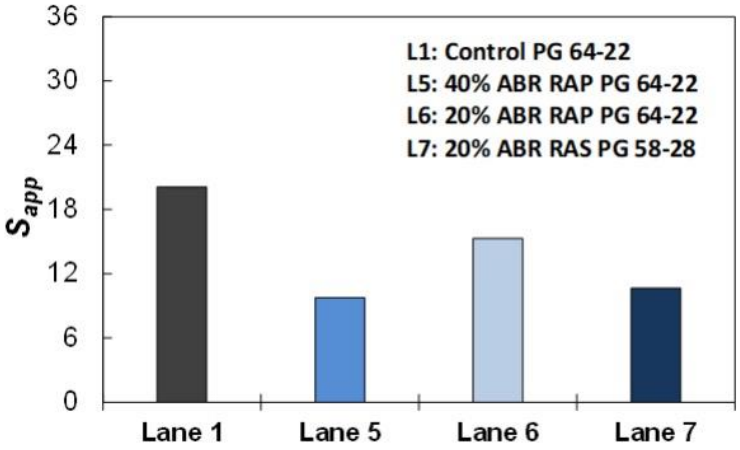

A. S_{app} values.

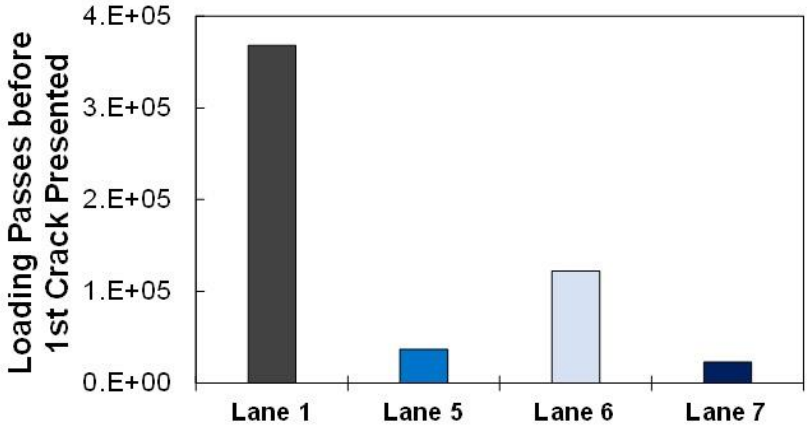

B. Loading passes before the first crack appears.

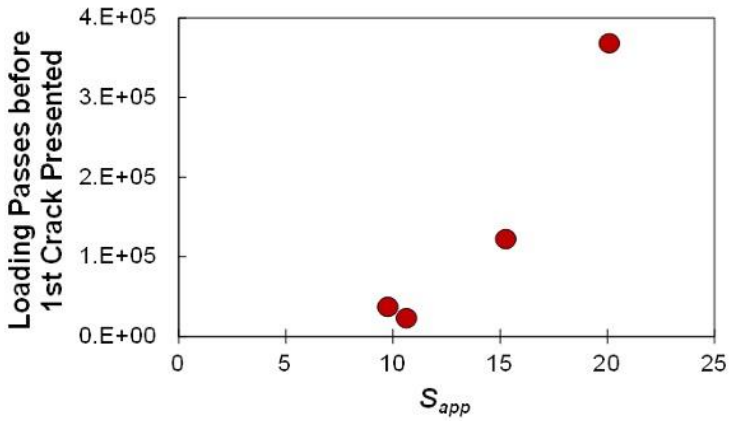

C. Comparison between S_{app} values and field performance.

Figure 46. Graphs. S_{app} values and field performance of ALF-RAP mixtures.[115]

This study applied the S_{app} index parameter to evaluate the effects of the different types of binder modification that were used in the FHWA ALF study mixtures.[126] Two of the mixtures were composed of modified binder and the third mixture, without modified binder, served as the control mix. The two mixtures with modified binders contained crumb rubber terminal blend (CR-TB) and styrene-butadiene-styrene (SBS), respectively. Figure 47-A presents the S_{app} values of these mixtures. The results suggest that the two mixtures with modified binders would exhibit better cracking resistance than the control mixture. Moreover, among the three mixtures, the SBS-modified mixture should perform the best in terms of fatigue cracking resistance. These predictions that are based on the S_{app} index parameter have been verified by field test results, as shown in figure 47-B and figure 47-C. The percentage of cracking area that was measured from the pavements is plotted against the S_{app} values in figure 47-C, which shows an expected inverse relationship.

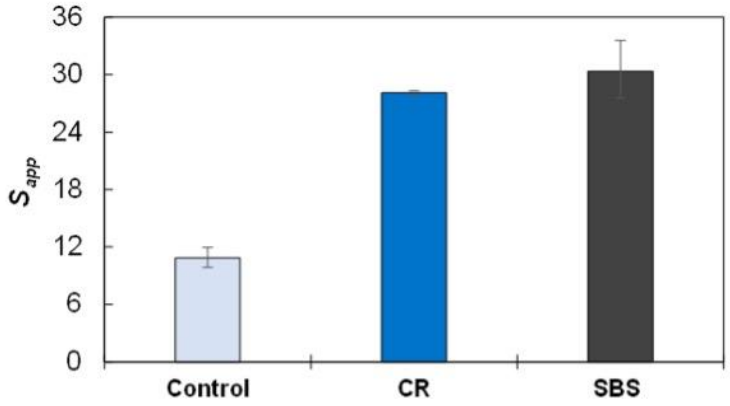

A. S_{app} values of mixtures.

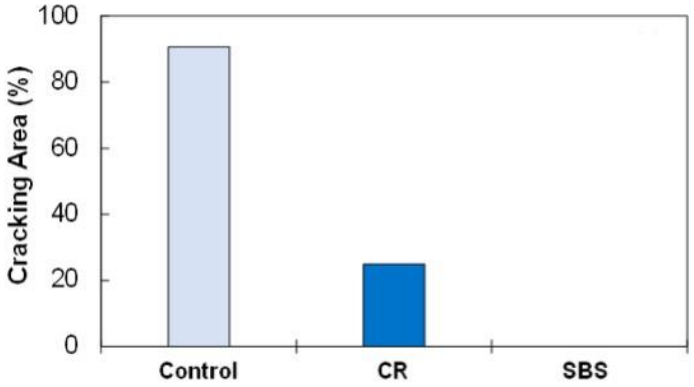

B. Percentage of cracking at each test lane.

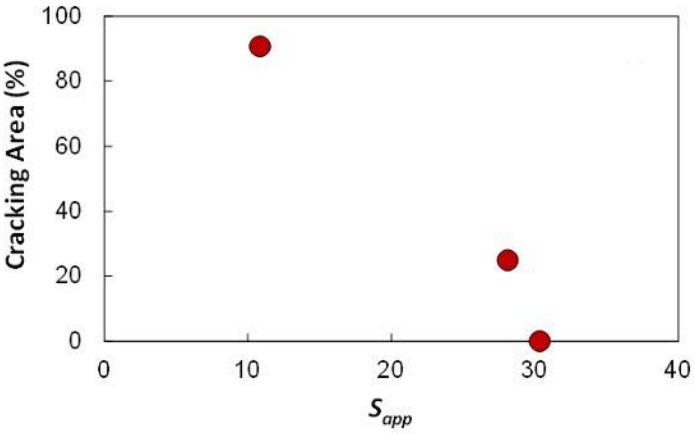

C. Comparison between index values and field cracking measurements.

Figure 47. Graphs. S_{app} values of FHWA ALF study mixtures with modified binders and their field performance.[(115)]

Suggested S_{app} Thresholds for Traffic Levels

One of the benefits of the new index parameter, S_{app}, is that State agencies can use the parameter for mix design, mix acceptance, QA, and so forth. Table 19. Recommended threshold values of Sapp parameter at different traffic level. presents the recommended S_{app} threshold values to help agency personnel complete these tasks. The threshold values represent requirements for the mixtures' fatigue resistance when the mixtures are categorized according to allowable traffic levels, presented in table 19. recommended threshold values of sapp parameter at different traffic level. as equivalent single-axle loads (ESALs). The S_{app} threshold values shown in table 19. recommended threshold values of sapp parameter at different traffic level. were determined using the S_{app} values obtained for the 105 mixtures presented in table 19. recommended threshold

values of sapp parameter at different traffic level.; figure 48 shows the S_{app} values of all the mixtures and the threshold values. These threshold values were determined by comparing the mixtures' S_{app} values with the information gathered from State highway agencies and accelerated pavement testing facilities, which includes information regarding pavement performance observed at test tracks, test roads, and in-service pavements, allowable traffic levels used in agencies' mix designs, general performance feedback from State highway agencies, and numerical pavement performance simulation results. For example, the mixtures in the NC mixture set in figure 48-C are regular paving materials typically used in North Carolina. The mixtures with the letter D in the designations usually contain modified binder and were designed initially for more than 30 million ESALs (MESALs). The mixtures with C were designed for 3 to 30 MESALs and B indicates 0.3 to 3 MESALs. In addition, during the full-scale accelerated loading tests that were conducted at the NCAT test track, fatigue cracking was not observed on the pavement sections for 10 MESALs during the first 2-yr research cycle, except for the OGFC section.[21] Alligator cracking started to present on the other five sections during the second research cycle. The S_{app} values and their corresponding traffic levels shown in figure 48-A indicate agreement with the field observations. Another benefit of the S_{app} index is that, although the threshold values presented in table 19. recommended threshold values of sapp parameter at different traffic level. were determined from a wide range of mixtures, those threshold values can be further refined for local materials and conditions.

Table 19. Recommended threshold values of Sapp parameter at different traffic level.

Traffic (MESALs)	S_{app} Limits	Tier	Designation
Less than 10	$S_{app} > 8$	Standard	S
Between 10 and 30	$S_{app} > 24$	Heavy	H
Greater than 30	$S_{app} > 30$	Very heavy	V
Greater than 30 and slow traffic	$S_{app} > 36$	Extremely heavy	E

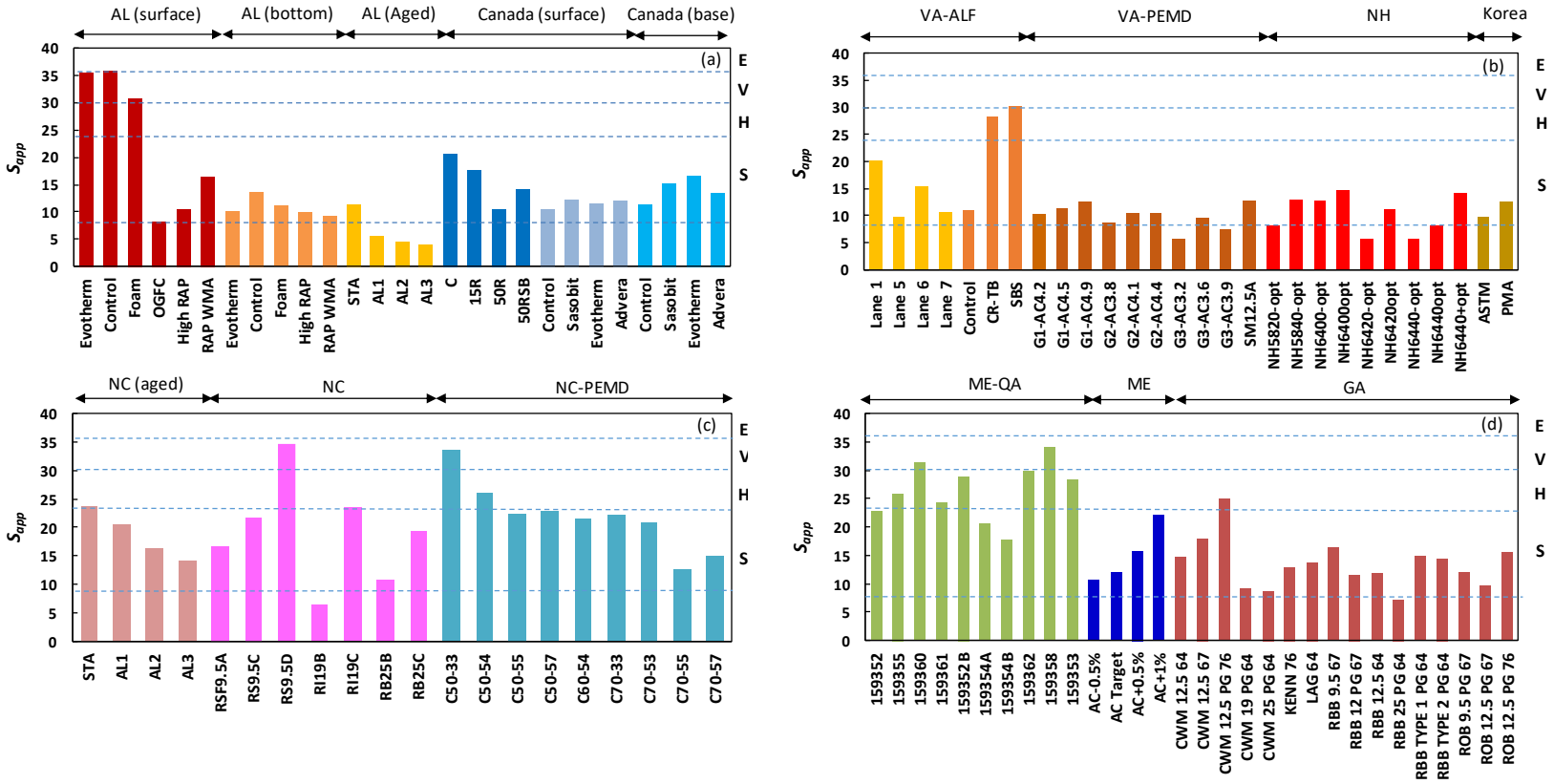

Figure 48. Graph. Allowable traffic levels of mixtures based on S_{app} index parameter.[115]

Table 19 does not provide the threshold values for the surface mixtures and intermediate and bottom layer mixtures separately. However, during the development of the S_{app} parameter, researchers evaluated these two types of mixtures separately using different pavement structures. In general, the intermediate and bottom layer mixtures had lower D^R values but higher modulus values than the surface mixtures, and the intermediate and bottom layer mixtures had been placed at the bottom of thicker pavements. As a result of the combination of the differences in material properties and loading conditions, the threshold values for the surface, intermediate, and base layer mixtures are recommended to be the same. For example, part of this study simulated the performance of pavement structures with different mixtures and compared the results with the corresponding S_{app} values. For the surface materials, the mixtures were placed in a 100-mm single asphalt layer on top of an aggregate base and subgrade. For the intermediate and base layer materials, the mixtures were placed in a 75-mm asphalt layer below a 51-mm surface layer and on top of an aggregate base and subgrade. The surface layer in the dual layer system used the same mixture, but the bottom layer material was varied. For both types of structures and mixtures, local climate conditions and 1 MESALs were applied for a 5-yr simulation period. The researchers performed the simulations using the FlexPAVE program, which applies the layered viscoelastic finite element method and S-VECD model for the damage calculations.[6,110] The percentage of pavement damage, referred to as %Damage, was determined for the layer in which the target mixture was utilized.

Figure 49 presents an example of the surface and bottom layer mixtures used in the Canada MIT project. The relationships between the S_{app} values and the predicted percent damage in the pavement layers for the surface mixtures and bottom layer mixtures can both be described by one linear function. Based on this observation, one set of threshold values can be given for the surface mixtures and for the intermediate and bottom-layer mixtures.

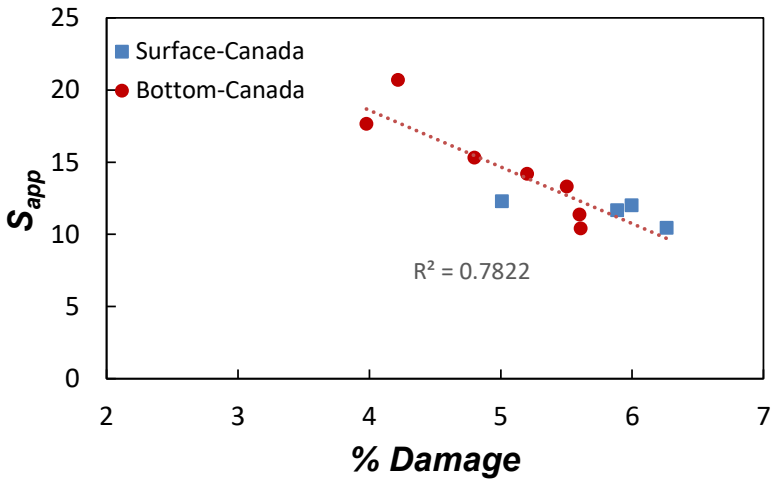

Figure 49. Graph. S_{app} values versus predicted percent damage in layers where target mixtures were utilized.[115]

Summary

This section presents the development and implementation of a new fatigue index parameter, referred to as S_{app}. The major strength of the S_{app} parameter is that the parameter considers the effects of both the material's modulus and toughness on fatigue failure. In this study, the S_{app} index parameter was applied to evaluate 105 asphalt mixtures with a wide range of mixture factors and from different climate regions. The results demonstrate the S_{app} parameter's sensitivity to mixture factors (e.g., aggregate gradation, binder content, RAP content, binder grade, and type of binder modifier), compaction, and aging and its ability to predict the effects of these variables on fatigue cracking performance and to confirm engineering expectations. Furthermore, the evaluation results agree well with limited field observations. Finally, threshold values for the S_{app} parameter are provided to determine allowable traffic levels for the study mixtures.

The S_{app} index parameter's main strength is that the parameter has been derived from the S-VECD model, which is used to describe the stress-strain behavior of an asphalt mixture for a wide range of loading and temperature conditions. As a result, the threshold values of the S_{app} parameter remain the same for different climatic regions and the S_{app} parameter thus can be determined at the effective temperature for the project of interest. In addition, the test results that are generated to determine the S_{app} value for a given mixture can be used in FlexPAVE for long-term pavement performance predictions.[6] Moreover, State agencies and contractors can use the S_{app} parameter for mix design, mix acceptance, and QA purposes. Lastly, the parameter can be employed in the development of PRS.

The research team is currently conducting a ruggedness and interlaboratory study of the AMPT cyclic fatigue test protocol (AASHTO TP 133).[93] That study is collecting cyclic fatigue test data from multiple organizations and developing metrics to determine any variability in the cyclic fatigue test results. When the data become available from that study and the statistical analysis is complete, the variability of the S_{app} parameter can be defined and mixtures with different levels of fatigue resistance can be differentiated more accurately. Also, as engineers become more familiar with the S_{app} parameter in future, more field data will be collected and used to verify the S_{app} index and calibrate the threshold values for the materials, climatic conditions, traffic volumes, and specifications that are specific to individual States and regions.

DEVELOPMENT OF A RUTTING INDEX PARAMETER BASED ON THE STRESS SWEEP RUTTING TEST AND PERMANENT STRAIN SHIFT MODEL

Index parameters for evaluating the performance of asphalt mixtures have become a common and important component of making informed pavement material decisions. These index parameters are quick indicators of asphalt mixture performance and thus are widely used in the asphalt paving industry. This section presents a new rutting index parameter to assess the rutting resistance of asphalt mixtures using the stress sweep rutting (SSR) test and the permanent strain shift model. The developed parameter, referred to as the RSI, is novel in that the parameter integrates material testing and structural simulations. To develop the RSI, the research team selected and evaluated more than 70 different mixtures that exhibit a wide variety of performance and were sourced from different geographical locations. The results show that the RSI can capture the effects of different mix design factors, such as RAP content, binder content,

and volumetric properties. Furthermore, a set of RSI threshold values is provided for different allowable traffic levels in terms of rutting. As engineers become familiar with the RSI, the RSI threshold values can be adjusted according to local experience. Agencies can also employ the RSI as a tool for BMD and QA purposes whereby agencies will be able to accept or reject a mixture based on RSI thresholds.

Asphalt pavements constitute one of the largest infrastructure systems in the world. Rutting (permanent deformation) is one of the most concerning pavement distresses for engineers and the pavement industry. Several tests have been developed and used in asphalt pavement studies to evaluate the resistance of asphalt mixtures to rutting. The most well-known tests include the following tests:

- The Marshall stability test (AASHTO T 245).[127]
- The Superpave shear tester (SST) test (AASHTO T 320).[128]
- The Hamburg wheel-tracking (HWT) test (AASHTO T 324) and other wheel-tracking tests such as the French rutting test (EN 12697-22) and the asphalt pavement analyzer (APA) test (AASHTO T 340).[129–131]
- The triaxial repeated load permanent deformation (TRLPD) test (AASHTO T 378).[113]
- The incremental repeated load permanent deformation (iRLPD) test (AASHTO TP 116).[132]
- The triaxial stress sweep (TSS) test.[36]

Broadly, these tests can be characterized as fully empirical (the Marshall stability test), simulative (the wheel-tracking tests), or representative of a stress state (the SST, TRLPD, iRLPD, and TSS tests). Each test shares similarities in that the test is performed, typically at a fixed temperature or a temperature that represents the location where the mixture will be placed, and some parameter is extracted from the test itself and reported.

Agencies tend to gravitate toward one of these tests based on either known performance correlations determined through parametric studies or engineering experience, simplicity, compatibility with the agency's existing expertise and equipment, or a combination of these factors. In addition, different agencies have implemented tests and indexes differently. For example, the HWT test, which is one of the most common tests, produces rutting by rolling a 705-N (158-lb) steel wheel on the surface of two asphalt specimens. In the AASHTO T 324 standard version of the HWT test, the specimens are submerged in a temperature-controlled water bath and the loading stops after 20,000 passes.[129] At this point, the rut depth caused by the steel wheels is recorded (AASHTO T 324). For most agencies, the rut depth after 20,000 cycles of loading at 50 °C is the index threshold for the test. However, no consensus exists on the rut depth threshold after 20,000 cycles, and all States and agencies have their own rules based on their location and climatic conditions.[133] For example, in Louisiana, maximum rut depths of 6 mm and 10 mm at 20,000 passes for high and medium traffic levels, respectively, were established.[134] In Illinois, the number of wheel passes needed to produce a

rut depth of 12.5 mm is the criterion used to accept or reject the mixture, and this threshold changes based on the high-temperature PG of the asphalt binder used.(105) These examples are only two examples related to the HWT test, as other agencies also differ in their precise testing implementation.

Table 20. Summary of common rutting performance tests. provides a summary of some of the common tests and index parameters currently being used by different agencies to evaluate rutting. As noted, different States use different threshold values to evaluate the rutting performance of asphalt mixtures in the lab and to accept or reject the proposed mix design.

Table 20. Summary of common rutting performance tests.

Test	AASHTO Standard	Specimen Height × Diameter (mm)	Loading Conditions	Temp.	Performance Prediction Model	Index
Marshall Stability	T 245(127)	63.5 × 100	Monotonic at a rate of 50 mm/min diametrically	60 °C	No	Maximum load
HWT	T 324(129)	60 × 150	Rolling a 705-N steel wheel at 52 passes/min	[1]50 °C	No	Rut depth stripping inflection point
APA	T 340(131)	75 × 150	Rolling a 445-N wheel over an air hose	High-temp. PG	No	Rut depth
TRLPD	T 378(113)	150 × 100	Repeated haversine axial compressive load pulse of 0.1 s every 1.0 s	[2]Effective temp.	Yes	Flow number
iRLPD	TP 116(132)	150 × 100	Repeated haversine axial compressive load pulse of 0.1 s every 1.0 s while varying the applied vertical stress	[3]Effective temp.	Yes	Minimum strain rate

[1]The temperature is not specified in the AASHTO standard; 50 °C is recommended by Tex-242-F.
[2]The effective temperature is based on critical depth and mean annual air temperature data.
[3]The effective temperature is based on degree-days and depth from the surface.

The RSI aids pavement engineers in determining whether a given mixture is likely to exhibit sufficient permanent deformation resistance or to help them select among multiple material alternatives for the given climatic conditions. The following sections discuss the test method and supporting model that form the basis of the RSI and then describe how the RSI is applied to more than 70 mixtures to determine its reasonableness and establish initial target threshold values.

Background of Stress Sweep Rutting Test

The developed RSI parameter is based ultimately on the outcomes of SSR tests. The initial motivation for the SSR test emerged through NCHRP 09-19, which showed that asphalt mixtures, when subjected to deviatoric axial loads in a confined state, exhibit sensitivity to load level, loading history, and temperature.(134) Subsequent work confirmed these findings and showed that the amount of rest time between load repetitions could also influence permanent

strain accumulation.[135,136] Asphalt mixtures in pavement structures seem to have a similar dependence on loading, temperature, and rest time and, as a result, these findings have been used to define material models of varying complexity and applicability. For example, the SSR test, like several other tests, is designed to calibrate a mechanistic-empirical model that describes an asphalt mixture's permanent strain behavior as a function of temperature, stress, and loading time. The permanent deformation model that the SSR test supports is referred to as the shift model and has been implemented into a finite element program, FlexPAVE, that calculates the permanent deformation of asphalt pavement under different traffic loading and climatic conditions over a multidecade period.[6]

The shift model is based on the concept of time-temperature-stress superposition where the equivalency of these three factors is considered through the horizontal translation of cycle-wise permanent strain accumulation curves at these different conditions. The strain curve that is created following the horizontal shift is the permanent strain master curve and the amount of translation is defined as the shift factor. This approach is conceptually the same as that taken to derive the dynamic modulus master curve and its predictions using the shift function.

The report by Kim et al. (2020) provides details regarding the calibration process, but, in short, the overall SSR test consists of four tests at two different temperatures (i.e., the test at each temperature is replicated).[107] The first temperature (T_L) is a relatively low temperature and represents the average air temperature and the second temperature (T_H) is a relatively high temperature and represents summertime temperatures. The actual temperatures used in the test are indexed to the climate conditions of the location where the mixture will be used. The load profile consists of repeated haversine loading with a 0.4-s pulse time and either a 1.6-s (at T_L) or 3.2-s (at T_H) rest period. The specimen is confined at a pressure of 70 kPa (10 psi). The deviatoric stress increases from 482 kPa, 689 kPa, and 896 kPa (70 psi, 100 psi, and 130 psi) at T_L, but the changed sequence of 689 kPa, 482 kPa, and 896 kPa (100 psi, 70 psi, and 130 psi) is used at T_H. Once testing is finished, the four test results are used to characterize the shift model. The final form of this process is presented as equations 102 to 107. Details regarding the SSR test, sample fabrication, and analysis of the test results can be found elsewhere (AASHTO TP 134).[26]

$$\varepsilon_{vp} = \frac{\varepsilon_0 N_{red}}{\left(N_I + N_{red}\right)^{\beta}} \tag{102}$$

$$N_{red} = A \times N\left(\xi_p\right)^{p_1} \left(\frac{\sigma_v}{P_a}\right)^{D} \tag{103}$$

$$A = 10^{p_2} \times 10^{-0.877 * D} \tag{104}$$

$$a_{\xi_p} = p_1 \log\left(\xi_p\right) + p_2 \tag{105}$$

$$a_{\sigma_v} = D \times (\log(\sigma_v / P_a) - 0.877) \tag{106}$$

$$D = d_1 \times T + d_2 \tag{107}$$

Where:

ε_{vp} = viscoplastic strain (permanent strain).
ε_0, N_1, β = coefficients of the incremental model.
N = number of cycles for a certain loading condition.
ξ_p = reduced load time.
$a_{\xi p}$ = the reduced load time shift factor.
σ_v = vertical stress, kPa.
P_a = atmospheric pressure, kPa.
$a_{\sigma v}$ = vertical stress shift factor.
D = vertical stress shift factor coefficient.
T = test temperature, °C.
d_1, d_2, p_1, p_2 = linear regression coefficients.

Table 21. General SSR test information. provides a comparative summary of the general test information for both rutting tests performed in this study. The total time estimates provided in table 21. general ssr test information. do not include the time required to prepare and compact the mixture because that time depends on whether the mixture is prepared from component materials (e.g., a mix design case) or from plant-produced materials (e.g., a QA case). Also, the total testing time calculation assumes that the test specimens are preconditioned sufficiently in the external chamber before the low-temperature tests. The total testing time required for the four SSR tests (two at the low temperature and two at the high temperature) for a single mixture is 540 min. The SSR test results can be input to the pavement performance prediction software, FlexPAVE, to simulate the mixture's rutting performance in a pavement structure under moving loads and varying environmental conditions.(6) This integration between the SSR test and FlexPAVE is highly beneficial because the method can be used in mixture design, pavement design, and PRS and thus bridge these important components in pavement engineering using the same principles.

Table 21. General SSR test information.

Information	Description	Estimation
Test equipment	AMPT	—
External chamber	Yes	—
Minimum required test specimens	4	7,500 g (per specimen)
Specimen geometry	Cylindrical (100-mm diameter and 150-mm height)	—
Test temperature	Low and high temperatures	—
Test specimen fabrication process	Coring and cutting	60 min
Air void measurement	SSD[a] method (AASHTO T 166)(137)	30 min
Conditioning time	—	60 min (per specimen)
Temperature transition	Low to high temperature	90 min
Number of tests	2 tests at each of low and high temperatures	LT: 20 min, HT: 40 min (per specimen)
Total time[b]	—	540 min
Pavement performance simulation	Yes	FlexMAT, FlexPAVE

—No data.
[a]Saturated surface dry.
[b]Total Time includes coring, cutting, air void measurements, temperature conditioning, and testing times.

Materials

This study used 72 asphalt mixtures from several different climate regions. These mixtures include surface, intermediate, and base layers and contain different aggregate types, binder contents, volumetrics, and gradations. Many of these mixtures also contain RAP, WMA additives, or PMA. Table 22. Materials information for surface layers. presents information for the surface layer materials and table 23. materials information for intermediate and base layers. presents information for the intermediate and base layer materials. Additional information about these mixtures can be found elsewhere.(107)

Table 22. Materials information for surface layers.

Project, Location	Label	NMAS (mm)	Binder Grade	Air Voids (percent)	RAP Content (percent)	Binder Modification
NCAT, AL, USA	NCAT-C1	9.5	PG 76-22	4.3	—	SBS
NCAT, AL, USA	NCAT-O1	9.5	PG 76-22	18.3	—	SBS
NCAT, AL, USA	NCAT-FW1	9.5	PG 76-22	4.9	—	Foam
NCAT, AL, USA	NCAT-AW1	9.5	PG 76-22	3.9	—	Advera
NCAT, AL, USA	NCAT-R1	9.5	PG 67-22	4.7	50	—
NCAT, AL, USA	NCAT-RW1	9.5	PG 67-22	5.0	50	Foam
KEC, South Korea	ASTM	19	PG 64-22	5.9	—	—
KEC, South Korea	PMA	19	PG 76-22	5.9	—	SBS
NCSU – PEMD, NC, USA	RS9.5B	9.5	PG 64-22	4.2	20	—
NCSU – PEMD, NC, USA	C50-33	9.5	PG 64-22	3.3	20	—

Project, Location	Label	NMAS (mm)	Binder Grade	Air Voids (percent)	RAP Content (percent)	Binder Modification
NCSU – PEMD, NC, USA	C50-54	9.5	PG 64-22	4.1	20	—
NCSU – PEMD, NC, USA	C50-55	9.5	PG 64-22	5.5	20	—
NCSU – PEMD, NC, USA	C50-57	9.5	PG 64-22	7.1	20	—
NCSU – PEMD, NC, USA	C70-33	9.5	PG 64-22	3.0	20	—
NCSU – PEMD, NC, USA	C70-53	9.5	PG 64-22	3.2	20	—
NCSU – PEMD, NC, USA	C70-55	9.5	PG 64-22	4.9	20	—
NCSU – PEMD, NC, USA	C70-57	9.5	PG 64-22	6.9	20	—
New ALF, Washington DC, USA	L1	12.5	PG 64-22	4.2	—	—
New ALF, Washington DC, USA	L5	12.5	PG 64-22	4.1	40	—
New ALF, Washington DC, USA	L6	12.5	PG 64-22	4.0	20	—
New ALF, Washington DC, USA	L7	12.5	PG 58-28	4.2	20 RAS	—
New ALF, Washington DC, USA	L8	12.5	PG 58-28	4.3	40	—
MaineDOT, ME, USA	159352	12.5	PG 64E-28	7.2	20	Polymer
MaineDOT, ME, USA	159352B	12.5	PG 64E-28	3.1	20	Polymer
MaineDOT, ME, USA	159353	12.5	PG 64E-28	4.4	20	Polymer
MaineDOT, ME, USA	159354A	12.5	PG 64E-28	4.9	20	Polymer
MaineDOT, ME, USA	159354B	12.5	PG 64E-28	5.8	20	Polymer
MaineDOT, ME, USA	159355	12.5	PG 64E-28	2.2	20	Polymer
MaineDOT, ME, USA	159358	12.5	PG 64E-28	4.6	20	Polymer
MaineDOT, ME, USA	159360	12.5	PG 64E-28	2.4	20	Polymer
MaineDOT, ME, USA	159361	12.5	PG 64E-28	7.6	20	Polymer
MaineDOT, ME, USA	159362	12.5	PG 64E-28	5.8	20	Polymer
MaineDOT, Mix Design, ME, USA	Low (AC-0.5 percent)	12.5	PG64-28	4.7	20	—

Project, Location	Label	NMAS (mm)	Binder Grade	Air Voids (percent)	RAP Content (percent)	Binder Modification
MaineDOT, Mix Design, ME, USA	Aim (AC-Target)	12.5	PG64-28	4.7	20	—
MaineDOT, Mix Design, ME, USA	Mid (AC+0.5 percent)	12.5	PG64-28	4.7	20	—
MaineDOT, Mix Design, ME, USA	High (AC+1 percent)	12.5	PG64-28	4.7	20	—
Old ALF (FHWA), Washington, DC, USA	Control	12.5	PG 70-22	4.1	—	—
Old ALF (FHWA), Washington, DC, USA	CR-TB	12.5	PG 70-28	4.3	—	Crumb Rubber
Old ALF (FHWA), Washington, DC, USA	SBS	12.5	PG 70-28	4.2	—	SBS
NCDOT, NC, USA	RS9.5B	9.5	PG 64-22	5.6	30	Foam
NCDOT, NC, USA	RS9.5C	9.5	PG 70-22	5.4	25	—
MIT, Manitoba, Canada	C1	16	PG 58-28	3.9	—	—
MIT, Manitoba, Canada	S1	16	PG 58-28	3.2	—	Sasobit
MIT, Manitoba, Canada	E1	16	PG 58-28	3.8	—	Evotherm
MIT, Manitoba, Canada	A1	16	PG 58-28	3.0	—	Advera
MIT, Manitoba, Canada	Control	16	PG 58-28	5.4	—	—
MIT, Manitoba, Canada	15R	16	PG 58-28	5.2	15	—
MIT, Manitoba, Canada	50R	16	PG 58-28	5.9	50	—
MIT, Manitoba, Canada	50RSB	16	PG 52-34	5.7	50	—

—No data.
SBS = styrene-butadiene-styrene; NCDOT = North Carolina Department of Transportation.

Table 23. Materials information for intermediate and base layers.

Project, Location	Label	NMAS (mm)	Binder Grade	Air Voids (percent)	RAP Content (percent)	Binder Modification
NCAT, AL, USA	NCAT-C2	19	PG 76-22	6.1	—	SBS
NCAT, AL, USA	NCAT-C3	19	PG 67-22	7.4	—	—
NCAT, AL, USA	NCAT-O2	19	PG 76-22	5.1	—	SBS
NCAT, AL, USA	NCAT-O3	19	PG 67-22	8.3	—	—
NCAT, AL, USA	NCAT-FW2	19	PG 76-22	6.0	—	Foam
NCAT, AL, USA	NCAT-FW3	19	PG 67-22	7.7	—	Foam
NCAT, AL, USA	NCAT-AW2	19	PG 76-22	6.2	—	Advera
NCAT, AL, USA	NCAT-AW3	19	PG 67-22	6.1	—	Advera
NCAT, AL, USA	NCAT-R2	19	PG 67-22	6.1	50	—
NCAT, AL, USA	NCAT-R3	19	PG 67-22	5.0	50	—
NCAT, AL, USA	NCAT-RW2	19	PG 67-22	5.8	50	—
NCAT, AL, USA	NCAT-RW3	19	PG 67-22	5.8	50	—
KEC, South Korea	BB1	40	PG 64-22	6.0	—	—

Project, Location	Label	NMAS (mm)	Binder Grade	Air Voids (percent)	RAP Content (percent)	Binder Modification
KEC, South Korea	BB3	25	PG 64-22	8.0	—	—
KEC, South Korea	BB5	25	PG 64-22	9.9	—	—
MIT, Manitoba, Canada	C2	16	PG 58-28	4.8	35	—
MIT, Manitoba, Canada	S2	16	PG 58-28	4.9	35	Sasobit
MIT, Manitoba, Canada	E2	16	PG 58-28	5.4	35	Evotherm
MIT, Manitoba, Canada	A2	16	PG 58-28	5.4	35	Advera
NCDOT, NC, USA	RB25C	25	PG 64-22	5.5	20	—
NCDOT, NC, USA	RI19B	19	PG 64-22	5.4	20	—
NCDOT, NC, USA	RI19C	19	PG 64-22	5.6	30	—

—No data.

Using Stress Sweep Rutting Test Results to Define the Rutting Index Parameter

The SSR test characterizes a mixture's behavior, which can be input to structural analysis. This study considered two candidates for the SSR test-based rutting index parameter. The first candidate is the permanent strain that is predicted using the shift model under repeated haversine loading (0.1-s pulse and 0.9-s rest) at a fixed temperature and stress level. The second candidate is a performance simulation of a standard pavement structure under a realistic load level and thermal history.

Permanent Strain Under Repeated Loading

The permanent strain at 12,000 cycles at a reference temperature under TRLPD test conditions can be predicted based on the shift model. For this simulation, the pulse time, vertical applied stress, and temperature are fixed. Therefore, in the shift model, parameters ξ_p, σ_V, and T each have a constant value. Rearranging the functions with this constraint leads to equations 102 and 108 where all the SSR test parameters (ε_0, N_I, β, d_1, d_2, p_1, and p_2) are known once the SSR tests and characterization process have been completed.

$$N_{red} = 10^{p_2} \times 10^{-0.877 \times (d_1 \times T + d_2)} \times N\left(\xi_p\right)^{p_1} \left(\frac{\sigma_v}{P_a}\right)^{d_1 \times T + d_2} \quad (108)$$

The research team used the NCAT test track materials to demonstrate the benefits and limitations of this approach because some of the field performance data of those materials already had been measured.[116] For the evaluation process, the research team made predictions based on two vertical applied stress levels (482 kPa and 689 kPa) and two temperatures (30 °C and 50 °C). The loading time for all simulations was 0.1 s with a 0.9-s rest period. The team calculated the permanent strain after 12,000 cycles for each mixture and used that result as the index threshold value. In this study, the permanent strain was designated as ε_{TRLPD}. The ε_{TRLPD} was calculated for different mixtures and compared to the field results.

Figure 50 shows the permanent deformation behavior of the different surface layers in the NCAT project.[116] As shown, the shift model can predict the permanent strain behavior and differentiate, or rank, the mixtures (table 24. rankings based on permanent deformation predictions for different surface layers in the ncat project.). However, the rankings vary based on the temperature and loading conditions. Therefore, using a single loading condition to evaluate the asphalt mixtures is efficient, but may not best represent the mixture's behavior. Note that the field performance is a consequence of rutting across all layers of the system, and so direct comparisons of the field performance and these rankings are not possible. This study measured the total rut depth. To find the rut depth in each layer, the research team used FlexPAVE to simulate the pavement structure and predict the rut depth for each asphalt layer within the pavement section.[6] Knowing the total rut depth and the rut depth for each layer, the research team could calculate the contributing percentage of each asphalt layer. Therefore, based on the rutting percentage of each layer obtained from FlexPAVE and knowing the measured total rut depth, the rut depth for each layer could be estimated.

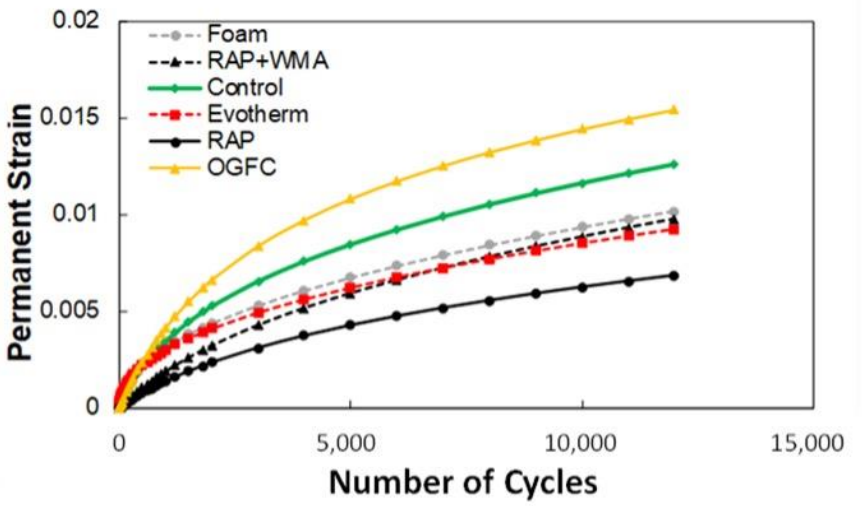

A. 482 kPa and 30 °C.

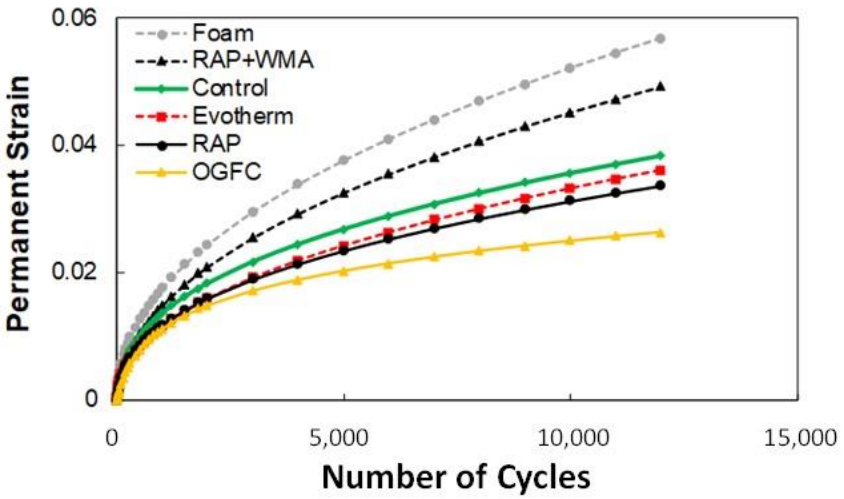

B. 482 kPa and 54 ℃.

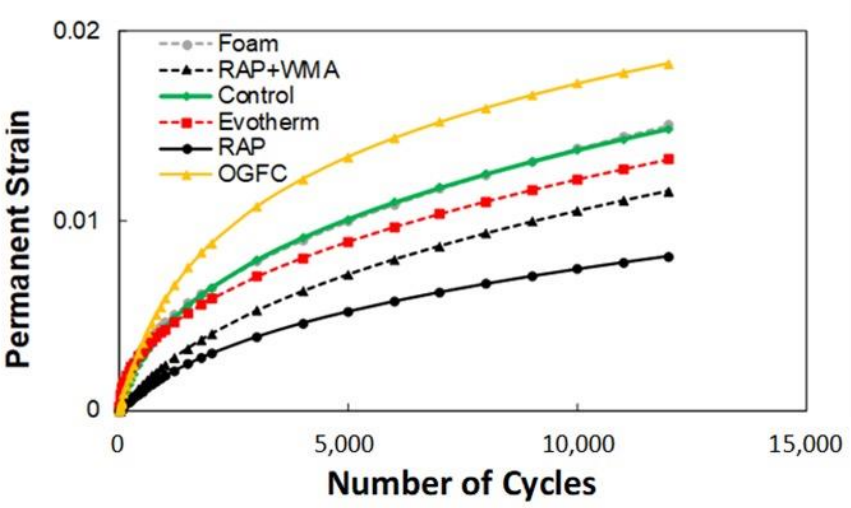

C. 689 kPa and 30 ℃.

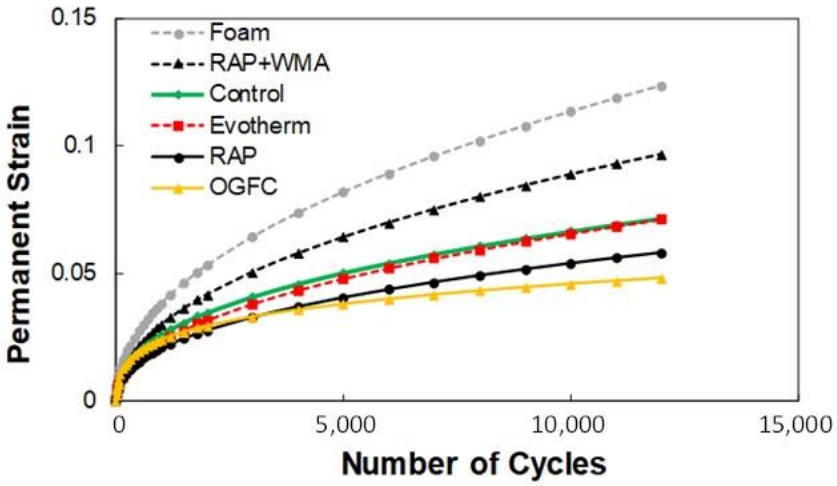

D. 689 kPa and 54 °C.

Figure 50. Graphs. Permanent strain predictions using triaxial repeated loading under different vertical stress and temperature conditions.(138)

Table 24. Rankings based on permanent deformation predictions for different surface layers in the NCAT project.

Section	Label	54 °C 689 kPa	54 °C 482 kPa	30 °C 689 kPa	30 °C 482 kPa	Field[b]
Evotherm	NCAT-AW1	4	4	4	5	1
RAP+WMA	NCAT-RW1	2	2	5	4	2
Foam	NCAT-FW1	1	1	2	3	3
Control	NCAT-C1	3	3	3	2	4
OGFC	NCAT-O1	6	6	1	1	5
RAP	NCAT-R1	5	5	6	6	6

[a]A higher number in the rankings indicates more permanent deformation.
[b]The field rankings were estimated based on the total rut depth for each section.

Pavement Performance Simulations

Pavement performance prediction software, such as FlexPAVE, can simulate the stress distribution in a pavement structure and consider the interactive effects of climate, load, and subsurface conditions.(6,83,107) A comparison of simulation results and field measurements indicates that the shift model can predict rut depths in the field well. Figure 51 presents a comparison of the rut depth measurements and FlexPAVE predictions for the NCAT project.(116) For this project, the research team input the as-constructed pavement structure to FlexPAVE along with the climate data from Auburn, AL (the NCAT's location), the backcalculated base and subgrade modulus values at the test track, the shift model parameters determined from the SSR test, and the dynamic modulus value for each material. FlexPAVE then used data obtained from the EICM to predict the pavement temperatures and eventually the rutting in the asphalt mixture layers.(13) Figure 52 presents the predictions of rut depths for different projects for

different climatic conditions and different structures. Details can be found elsewhere.[83,107] For each project, FlexPAVE could predict the rut depth knowing the design traffic, pavement structure, and location of the project. In figure 52, the *y*-axis shows the measured total rut depth and the *x*-axis indicates the rut depth in the asphalt layer. The basis for this comparison comes from forensic investigations into these projects that found that the base and subgrade rutting was negligible compared to the rutting in the asphalt concrete layer.

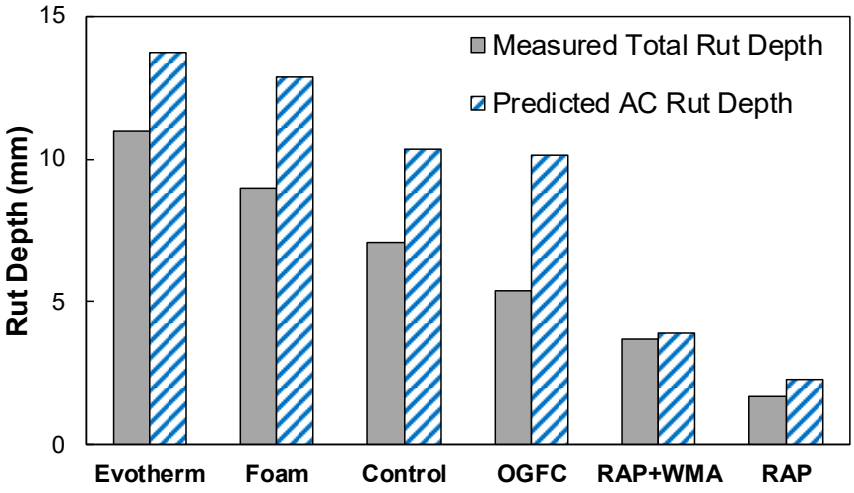

Figure 51. Graph. Comparison of rut depth measurements and FlexPAVE predictions for the NCAT project.[138]

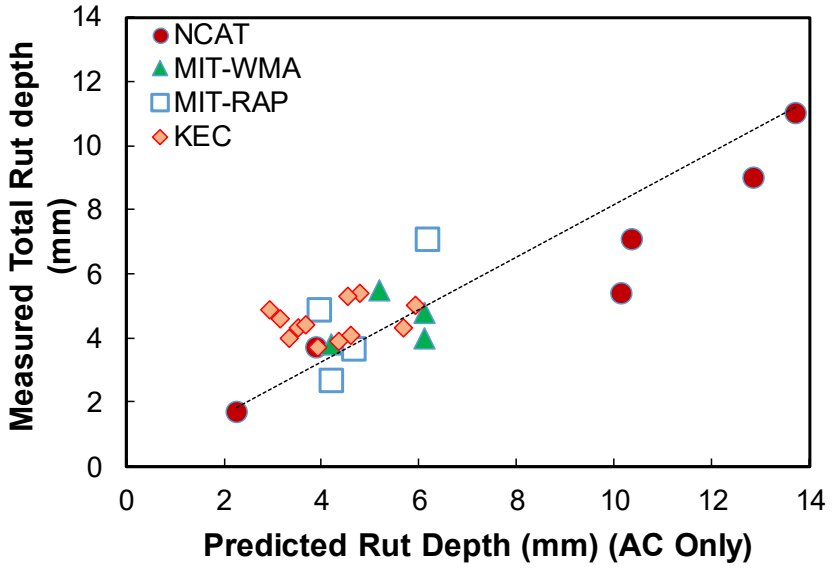

1 mm = 0.04 inches.

Figure 52. Graph. Comparison of rut depth measurements and FlexPAVE predictions for different projects.[138]

Given the positive results obtained from the structural simulations, the second candidate for the rutting index parameter also involved FlexPAVE.[6] However, some issues affected the direct adoption of FlexPAVE in the same way FlexPAVE was used for the field sections. This limitation is inherent to the way an index parameter is used to support decision-making; mixtures are often designed, verified, and approved for use separately from the pavement design process. Thus, the pavement structure and exact location are not known for situations when the index parameter would be needed. However, to conduct pavement simulations, a structure is needed. This study approached this dilemma by assuming a standardized structure for carrying out the performance simulations and defining the RSI parameter. The research team investigated multiple factors to quantify the sensitivity of different structural parameters to the predicted asphalt layer rut depth and to determine the proper structure. The following parameters were considered and are discussed separately in the following subsections:

- Asphalt layer thickness.
- Aggregate base and subgrade modulus values.
- Aggregate base thickness.
- Layer thicknesses for different mixture categories.

Asphalt Layer Thickness

To determine the effect of asphalt layer thickness, the research team predicted rutting using the material properties from several of the mixtures identified in table 22. materials information for surface layers. and table 23. materials information for intermediate and base layers. with 10-cm and 15-cm asphalt layer thicknesses. Based on these simulations, the research team calculated the average permanent strain, defined as the ratio of rut depth to asphalt thickness.

Figure 53 shows a strong correlation between the average permanent strain levels obtained for both surface layer thicknesses. Therefore, the asphalt layer thickness does not affect the ranking of the different mixtures, and the index parameter can be defined based on the 10-cm thickness.

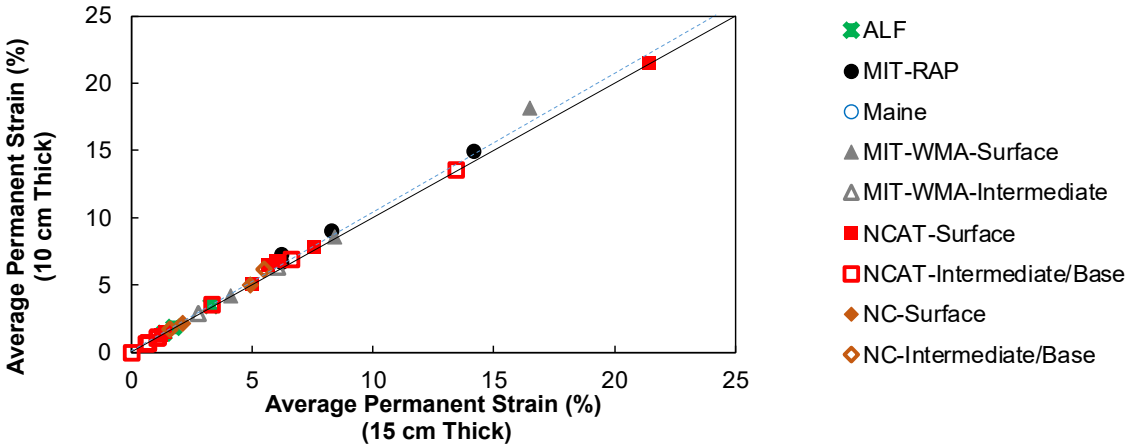

1 cm = 0.4 inches.

Figure 53. Graph. Predicted rut depths using 10-cm and 15-cm surface layer thicknesses.[138]

Aggregate Base and Subgrade Moduli

The moduli of the base and subgrade have a great impact on the total rut depth of a pavement. To ascertain the effects of the moduli and the thicknesses of the base and subgrade on pavement rut depth, the research team simulated the rutting in different projects using different base and subgrade modulus values. Figure 54-A shows the total rut depths obtained from a structure that consists of 10 cm of asphalt mixture and 20 cm of aggregate base. In this study, two typical base modulus values were defined for the aggregate base, 100 MPa and 300 MPa, the weak and strong bases, respectively. The same concept was utilized for the subgrade modulus with values of 30 MPa and 80 MPa (weak and strong, respectively). As expected, the pavement with the weak base and subgrade exhibited the most permanent deformation, where the pavement with the strong base and subgrade exhibited the least permanent strain. However, when the research team examined only the asphalt layer rutting, as illustrated in figure 54-B, the permanent deformation in that layer did not notably change with different base and subgrade modulus values. The team repeated this test using different asphalt mixtures and in all the cases the difference between the asphalt layer's rut depth at the end of the design life for the cases where both the base and subgrade were weak and where both were strong was less than 5 percent. In summary, although the base and subgrade moduli have a significant effect on overall pavement rut depth, the moduli of the base and subgrade do not specifically affect the rut depth in the asphalt layer.

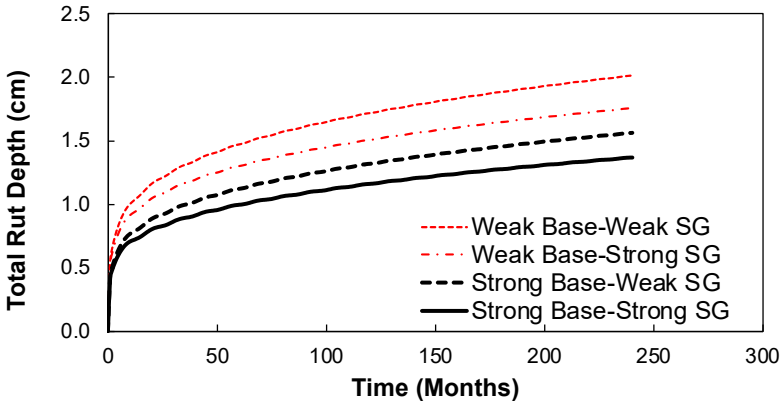

A. Total rut depths.

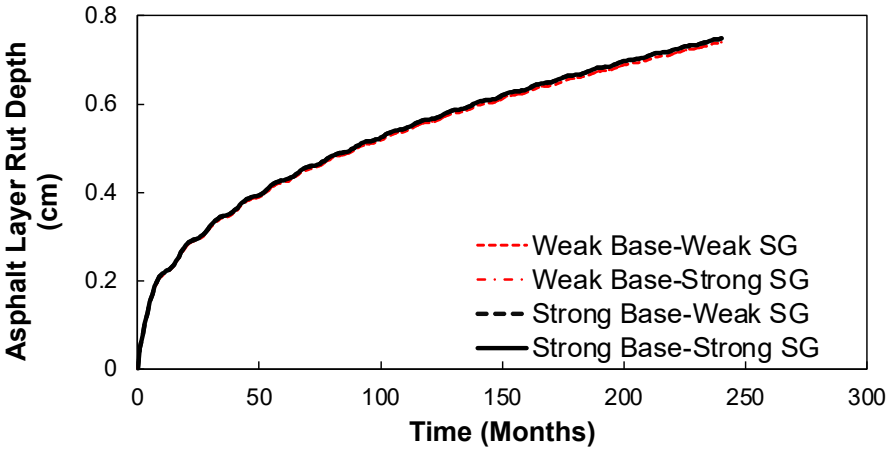

B. Surface layer rut depths.

Figure 54. Graphs. Total rut depths and surface layer rut depths using different base and subgrade modulus values.[138]

Aggregate Base Thickness

The research team investigated the effects of the base layer thickness via simulations of a structure with the asphalt layer thickness of 10 cm, a base layer with a modulus of 206 MPa, a subgrade with a modulus of 69 MPa, and a base thicknesses of 10 cm, 20 cm, 30 cm, or 40 cm. Figure 55-A and figure 55-B show the predicted asphalt layer rut depth values and total pavement rut depth values for each of these simulations, respectively. Increasing the base thickness did not change either the asphalt layer rut depths or the total rut depths. The permanent deformation information currently used in FlexPAVE to predict rutting in an aggregate base is the same as that used in Pavement ME, which is known to demonstrate no sensitivity to base thickness.[6,18,139] Therefore, these results are not surprising.

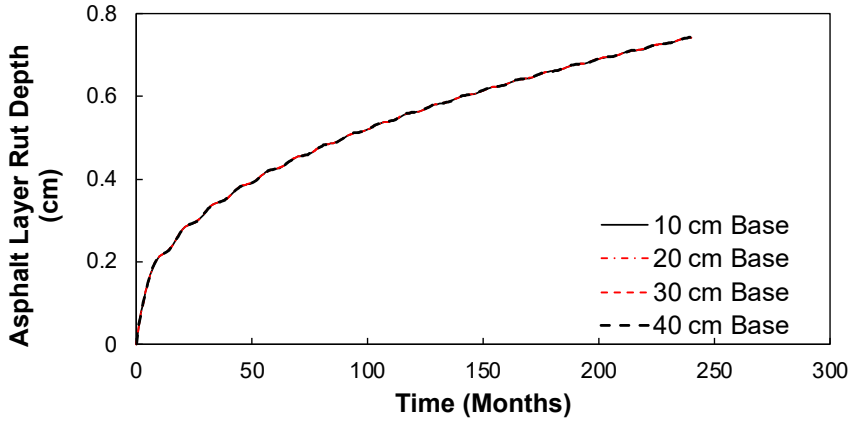

A. Surface asphalt layer rut depths.

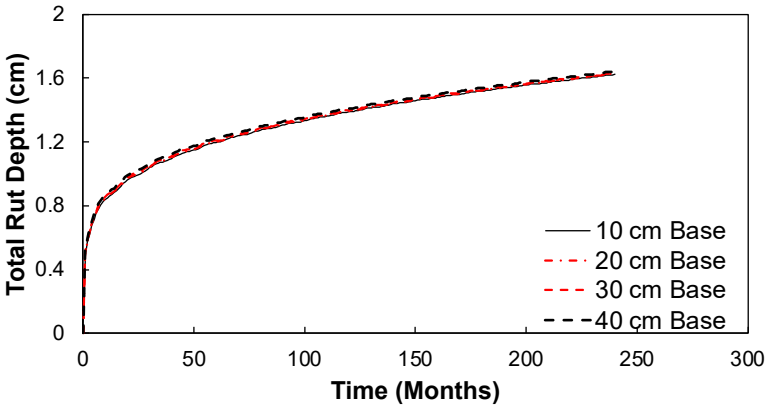

B. Total rut depths.

Figure 55. Graphs. Surface asphalt layer rut depths and total rut depths using different base layer thicknesses.(138)

Layer Thicknesses for Different Mixture Categories

Rutting accumulation is a function of temperature, stress level, and loading time, which all change with depth. As a result, surface course mixtures experience conditions in a pavement structure that are different than those of mixtures that are placed deeper into the pavement structure. Within the RSI parameter framework, the exact structure in which a mixture will be used is unknown, but the framework presumes that the basic mixture category (surface, intermediate or binder, or base) is known. The approach the research team took for the RSI parameter development was to consider these basic mixture categories when computing the index, and thus to consider the depth and, by extension, the surface thickness of the asphalt layer to use for evaluating the intermediate or binder and base mixtures. Evaluating the asphalt mixture under its in-service loading and temperature conditions is critical. For example, the base layer is not subjected to the same loading conditions as the surface layer. The upper layers experience different temperatures and stress levels in comparison to the lower layers. Therefore, based on the application of different mixtures, different structures should be considered. By studying typical mixtures used in North Carolina and other locations, the research team divided the mixture types for asphalt pavements into three categories: surface, intermediate, and base layers.(140) For the mixtures used in the intermediate layers, the chosen surface layer thickness was 7.5 cm (3 inches). For the mixtures used in the base layer, the surface and intermediate layer thicknesses were chosen as 7.5 cm for each layer. Based on the four parameters of standard structures for evaluating the surface, intermediate or binder, and base mixtures discussed in the previous subsections, figure 56 shows the standard structures that the research team ultimately used to determine the RSI parameter.

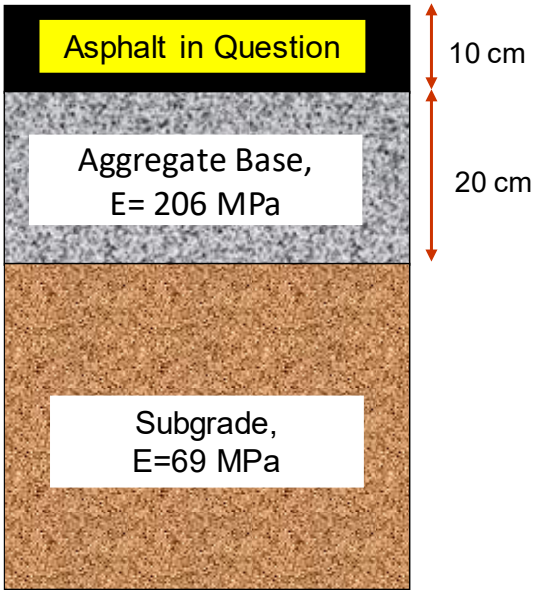

1 MPa = 145.04 psi.

A. Surface layer.

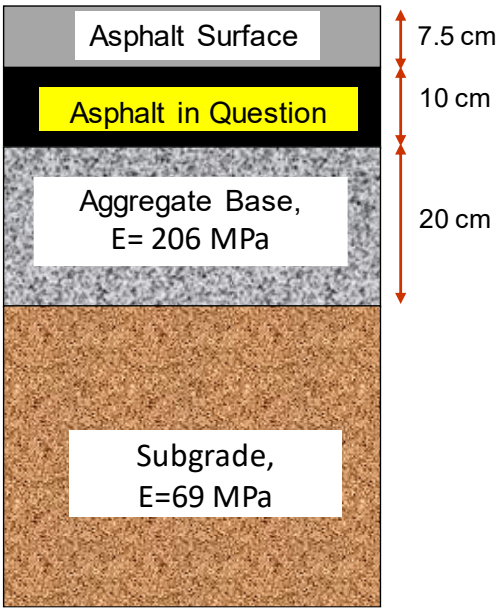

B. Intermediate layer.

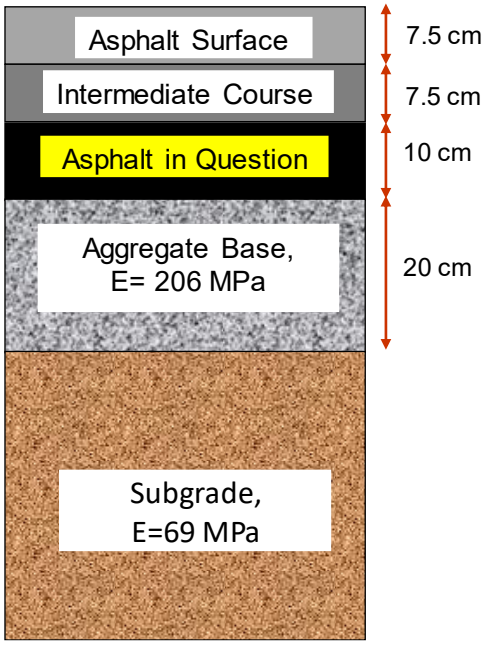

C. Base layer.

Figure 56. Illustrations. Pavement structures used to determine the RSI parameter.[138]

Rutting Strain Index

Permanent deformation in asphalt mixtures is a function of temperature, stress level, and loading time, which all change with pavement depth. The approach the research team took to develop the RSI parameter was to consider these factors using FlexPAVE to compute the average permanent strain.[6] FlexPAVE is a three-dimensional finite element program that predicts the fatigue cracking and rutting performance of asphalt pavements under moving loads using realistic temperature changes generated by the EICM.[13] In the RSI calculation framework and to calculate the average permanent strain, FlexPAVE uses a set of three standard structures (for the surface, intermediate, and base course mixtures, respectively) and standard 18-kip single-axle loads. The stress levels in these structures are calculated using FlexPAVE and then used as fixed inputs for the average permanent strain calculations. The FlexPAVE algorithm with the fixed stress values is implemented in FlexMAT.[5] The following section describes the investigation into the feasibility of simplifying the FlexPAVE algorithm and implementing the simplified algorithm in FlexMAT.

Simplifying the FlexPAVE Algorithm

One of FlexPAVE's advantages is the ability to perform analysis under different traffic, loading, and climatic conditions.[6] Moreover, FlexPAVE simulations accurately match field performance. The limitation of FlexPAVE is the simulation time, which is not a significant problem in some

FlexPAVE applications but is considered a limitation for the RSI calculations. The most significant portion of the FlexPAVE rutting analysis runtime (95 percent of the total runtime) is consumed by calculating the structural responses (stress and strain) in the pavement system. This response modeling involves calculating the stress and strain throughout the pavement structure for the three following predefined analysis time segments:

- Segment 1: 5 a.m. to 12 p.m.
- Segment 2: 12 p.m. to 7 p.m.
- Segment 3: 7 p.m. to 5 a.m.

The temperature profiles for each of these segments is first determined for each month of the simulation and then fed into the structural analysis model along with the linear viscoelastic properties of the asphalt mixture, elastic modulus values of the base and subgrade, and the external loading configuration. The stress and strain levels are then computed at the nodal points throughout the structure and used with the shift model to compute the permanent strain and, ultimately, rutting.

Because FlexPAVE is a general-purpose structural analysis platform, FlexPAVE needs the flexibility to analyze any structural configuration.[6] However, because the RSI parameter uses a set of three fixed structures, full FlexPAVE simulations may not be needed to compute the RSI. In this scenario, the structural responses could be prepopulated into a database, which would reduce the runtime substantially. The research team investigated this possibility by performing simulations with different mixtures and climate conditions using the structures shown in figure 56. For each mixture evaluated and for each structure, the vertical stress (the structural response used in the shift model to compute pavement rutting) was first calculated at different depths using FlexPAVE. In these simulations, the climate conditions chosen were consistent with the mixture being evaluated. Seven climate conditions and 35 mixtures were considered. Among the 35 mixtures, the three cases with the widest range of variation in vertical stress were selected.

Figure 57-A and figure 57-B present the vertical stress values for the third segment of January and the second segment of June, respectively, for those three cases. The third segment of January and the second segment of June show the most extreme cases of low and high temperatures, respectively. The research team selected these two conditions as an example in figure 57, but other segments and months also were examined to confirm that this scenario is representative. Figure 57-A and figure 57-B both show that the vertical stress variation increases through the pavement depth and that the most variability is evident at the bottom of the surface layer (depth of 10 cm). This variability can be as much as 35 percent at the bottom of the asphalt layer. However, the impact of these differences on the computed asphalt rut depth is relatively small.

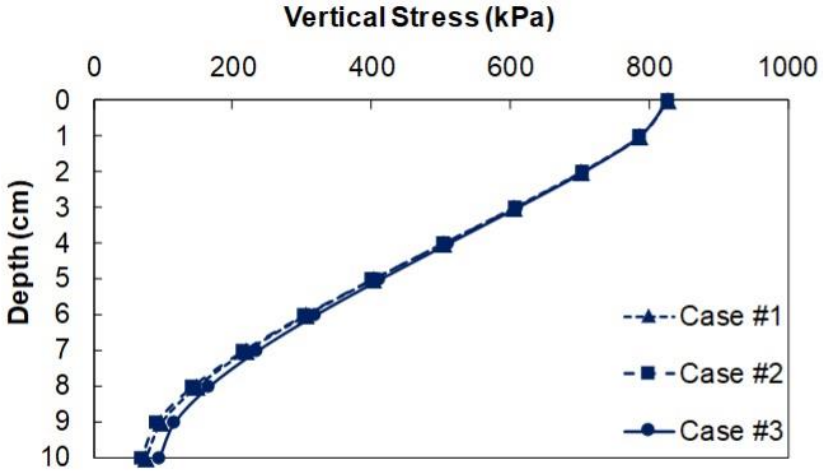

A. January, third segment (7 p.m. to 5 a.m.).

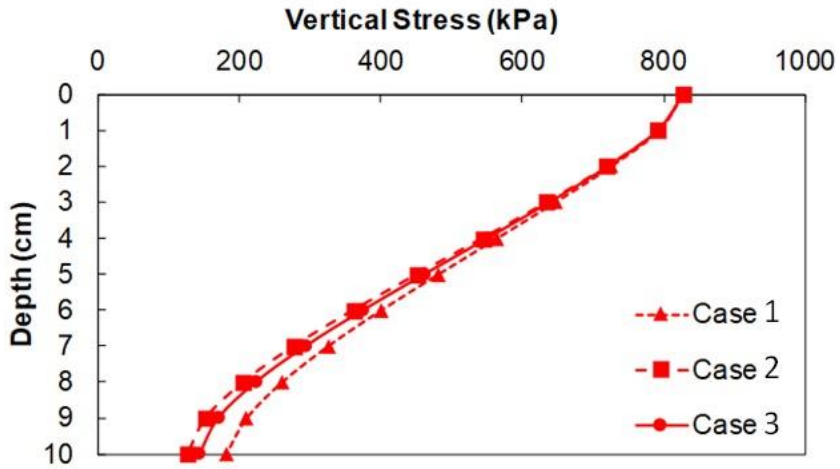

B. June, second segment (12 p.m. to 7 p.m.).

Figure 57. Graphs. Vertical stress through pavement depth for different cases of stress variation.[(138)]

For this part of the study, the research team selected 35 mixtures from different locations and calculated the rut depth for each layer using three different cases of stress variation throughout the pavement depth (cases 1, 2, and 3, respectively). Figure 58 shows that the predicted rut depth in the asphalt layer is based on the three different cases of stress variation. The results show that the rut depth at the end of 20 yr did not change significantly (less than 5 percent) within each layer. The research team established a database of stress responses that reflects the variations by segment and month and used this database to determine the RSI.

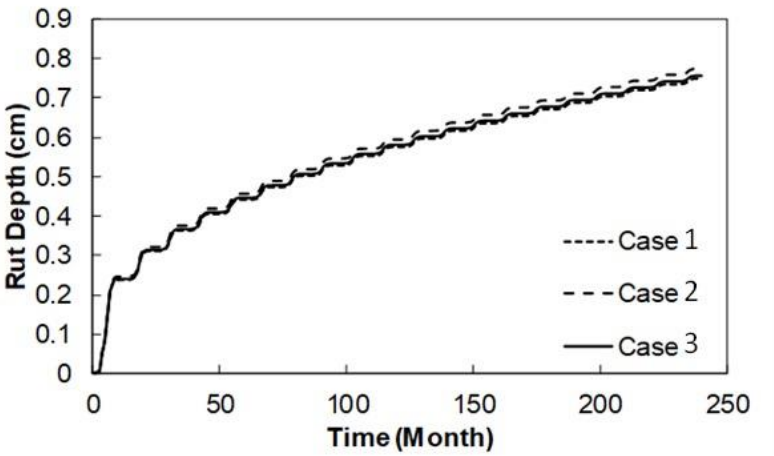

Figure 58. Graph. Predicted rut depths using a single mixture for three cases of stress variation.[138]

Defining the Rutting Strain Index

To determine a proper rutting index parameter, the average permanent strain at the end of the 20-yr pavement service life (240 mo) was considered. Then a fixed threshold value for all the mixture categories (surface, intermediate, and base layers) was needed for each traffic level. Although the different layers experience different loading and in-service temperature conditions, these effects can be captured by selecting different structures and selecting the same threshold value for the different categories of asphalt mixtures. This study subjected the pavement to 30 MESALs with the design speed of 96 km/h (60 mph) and the average permanent strain was calculated for 20 design yr. Figure 59 shows an example of the average permanent strain behavior over the service life of the pavement. In this figure, the RSI is defined as the average permanent strain at the end of 20 yr.

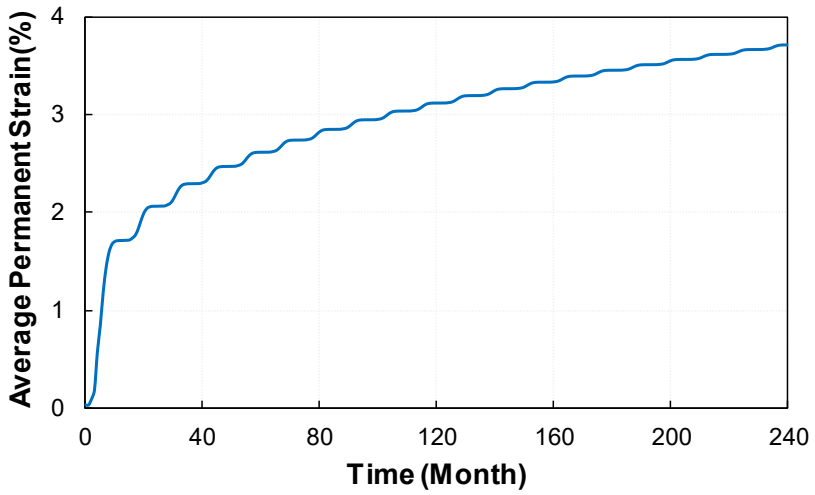

Figure 59. Graph. Average permanent strain in the asphalt layer during pavement life.[138]

Figure 60 presents a flowchart that describes the process to find the RSI parameter. In brief, the first four gyratory-compacted specimens are fabricated for the given mixture. SSR tests are performed using the four test specimens (two at T_H and two at T_L), and the test results are input to FlexMAT along with the location of the project and the type of layer where the mixture will be used to determine the RSI value.[5]

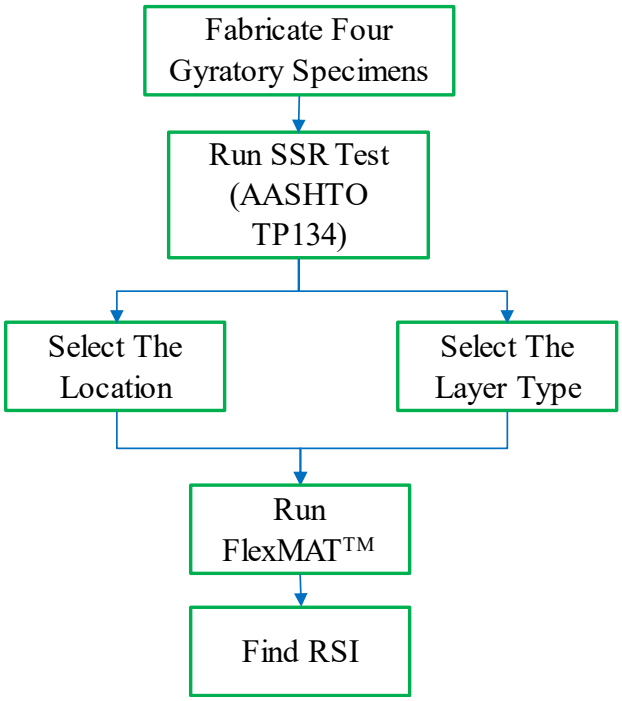

Figure 60. Flowchart. Process to find the RSI parameter.[138]

Recommended Traffic Level Designations for Rutting Strain Index

No clear mechanistic definition for the acceptable level of permanent strain is available, but usually, total rutting is used as this criterion. Therefore, this study investigated the acceptable level of permanent strain empirically. The research team used a data-driven decision process based on engineering experience and the measured behavior of 72 mixtures from different projects to select the most appropriate threshold values. Figure 61 presents the RSI values for the different mixtures listed in table 22. materials information for surface layers. and table 23. materials information for intermediate and base layers..

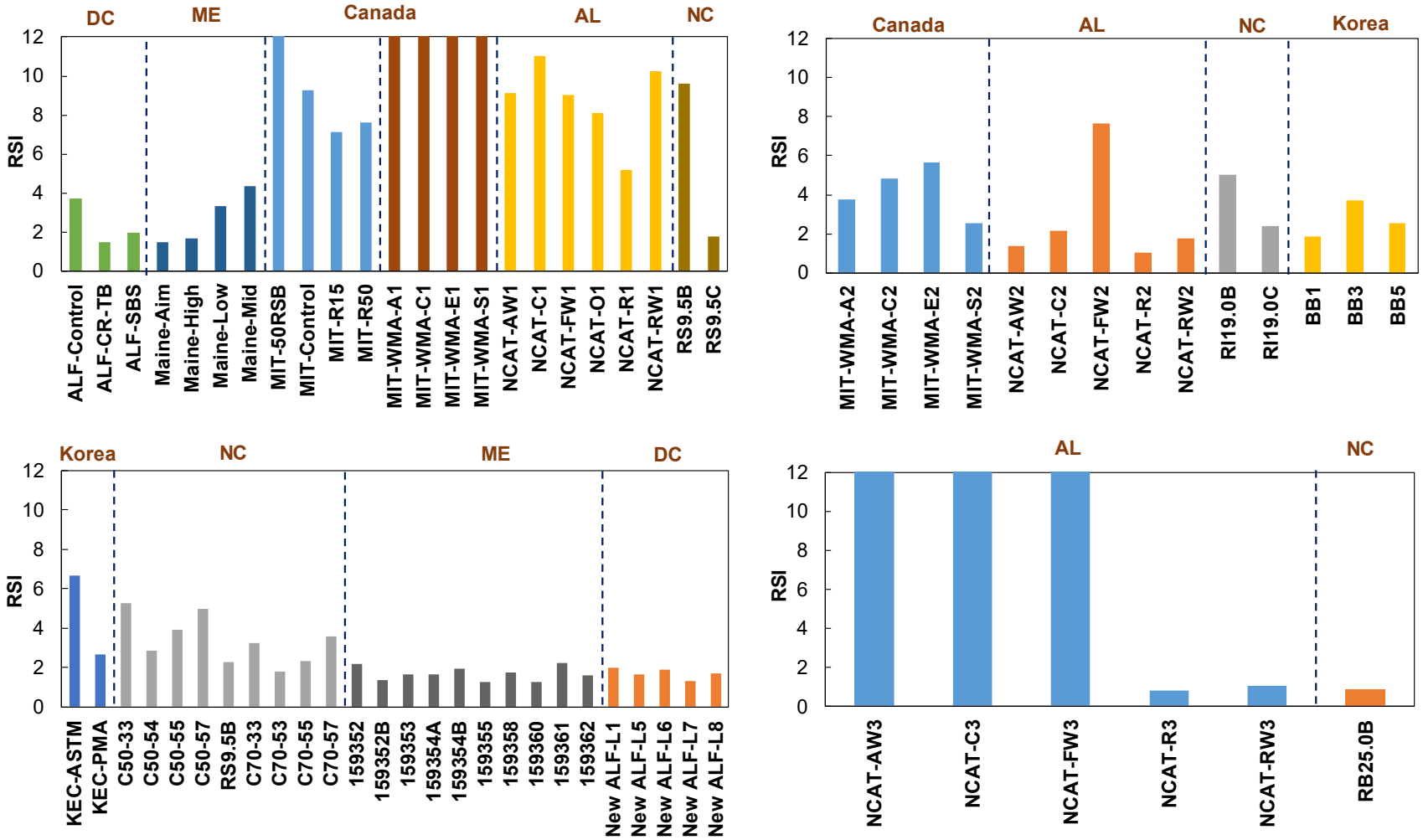

Figure 61. Graph. RSI values for different mixtures.[138]

Table 25. Recommended threshold values of RSI at different traffic levels. presents the RSI limits that are tied to the four traffic designations of standard, heavy, very heavy, and extremely heavy traffic tiers used to categorize the different levels of traffic. These threshold limits were chosen based on engineering expectations and design traffic.

Table 25. Recommended threshold values of RSI at different traffic levels.

Traffic Level (MESALs)	RSI Limits	Tier	Designation
Less than 10	RSI < 12	Standard	S
Between 10 and 30	RSI < 4	Heavy	H
Greater than 30	RSI < 2	Very heavy	V
Greater than 30 and slow traffic	RSI < 1	Extremely heavy	E

The research team applied the threshold values shown in table 25. recommended threshold values of rsi at different traffic levels. to the mixtures shown in figure 61 to determine the allowable traffic designations for these mixtures. Table 26. RSI values and rutting allowable traffic designations for the study mixtures. provides a summary of the results. The allowable traffic determined by the RSI is for rutting specifically and does not represent allowable traffic for all types of distress. For example, in the Maine DOT shadow project, the binder used in the mixtures is PG 64E-28. The PG of 64 is too high for climate conditions in Maine. This high PG binder was used specifically to address durability issues in Maine. Therefore, the rutting allowable traffic designation for those mixtures is mostly V (very heavy). In these cases, rutting is not the dominant distress during the pavement's service life; cracking is the driving distress.

Table 26. RSI values and rutting allowable traffic designations for the study mixtures.

Project	Mix ID	RSI	Traffic Designation
ALF	Control	3.7	H
ALF	CR-TB	1.5	V
ALF	SBS	2.0	V
Maine	Aim	1.7	V
Maine	High	4.3	S
Maine	Low	1.5	V
Maine	Mid	3.3	H
MIT	50RSB	15.7	ND
MIT	Control	9.3	S
MIT	15R	7.1	S
MIT	50R	7.6	S
MIT-WMA	A1	21.5	ND
MIT-WMA	A2	3.8	H
MIT-WMA	C1	24.8	ND
MIT-WMA	C2	4.8	S
MIT-WMA	E1	34.3	ND
MIT-WMA	E2	5.6	S
MIT-WMA	S1	28.3	ND

Project	Mix ID	RSI	Traffic Designation
MIT-WMA	S2	2.5	H
NCAT	AW1	9.1	S
NCAT	AW2	1.3	V
NCAT	AW3	29.2	ND
NCAT	C1	11.0	S
NCAT	C2	2.2	H
NCAT	C3	18.2	ND
NCAT	NCAT-FW1	9.0	S
NCAT	NCAT-FW2	7.6	S
NCAT	NCAT-FW3	20.6	ND
NCAT	NCAT-O1	8.1	S
NCAT	NCAT-O2	3.4	H
NCAT	NCAT-O3	16.9	ND
NCAT	NCAT-R1	5.2	S
NCAT	NCAT-R2	1.0	V
NCAT	NCAT-R3	0.8	E
NCAT	NCAT-RW1	10.2	S
NCAT	NCAT-RW2	1.7	V
NCAT	NCAT-RW3	1.0	V
NC	RB25.0B	0.9	E
NC	RI19.0B	5.0	S
NC	RI19.0C	2.4	H
NC	RS9.5B	9.6	S
NC	RS9.5C	1.8	V
KEC	ASTM	6.7	S
KEC	BB1	1.9	V
KEC	BB3	3.7	H
KEC	BB5	2.6	H
KEC	PMA	2.6	H
NC-PEMD	RS9.5B	2.3	H
NC-PEMD	C50-57	5.0	S
NC-PEMD	C50-54	2.9	H
NC-PEMD	C70-33	3.2	H
NC-PEMD	C50-55	3.9	H
NC-PEMD	C70-53	1.8	V
NC-PEMD	C70-55	2.3	H
NC-PEMD	C70-57	3.6	H
NC-PEMD	C50-33	5.3	S
Maine-Shadow	159352	2.2	H
Maine-Shadow	159352B	1.4	V

Project	Mix ID	RSI	Traffic Designation
Maine-Shadow	159353	1.6	V
Maine-Shadow	159354A	1.7	V
Maine-Shadow	159354B	2.0	V
Maine-Shadow	159355	1.3	V
Maine-Shadow	159358	1.8	V
Maine-Shadow	159360	1.3	V
Maine-Shadow	159361	2.2	H
Maine-Shadow	159362	1.6	V
NEW-ALF	L1	2.0	V
NEW-ALF	L5	1.6	V
NEW-ALF	L6	1.9	V
NEW-ALF	L7	1.3	V
NEW-ALF	L8	1.7	V

The research team believes that some mixtures that have passed current rutting criteria thresholds based on empirical tests may fail under the RSI criterion due to the sensitivity of the RSI parameter to changes in mixture factors. Table 26. RSI values and rutting allowable traffic designations for the study mixtures. shows that several mixtures have RSI values greater than 12 and were assigned the allowable traffic designation of ND, meaning no designation. According to the RSI threshold values presented in table 25. recommended threshold values of rsi at different traffic levels., these mixtures cannot be assigned the lowest allowable traffic designation of S. However, if State highway agency personnel believe, based on their local experience, that those mixtures should pass, then those State highway agency personnel can calibrate the RSI threshold values accordingly.

Effects of Mixture Variables on Allowable Traffic for Rutting

The RSI results obtained for the mixtures listed in figure 61 can be examined more closely to evaluate the overall reasonableness of the RSI with respect to factors that are known to contribute to more or less rutting. For these purposes, the effects of air void content, binder content, and RAP content and binder grade were systematically examined and are discussed in the following sections. Several examples in the literature suggest that increases in air void content, binder content, and RAP content have consistent effects on rutting performance where notably higher asphalt contents, higher air void contents, and lower RAP contents correspond to higher rutting levels.[141–143]

Effects of Air Void Content on Rutting Strain Index

The effects of air void content can be found by analyzing data from the North Carolina State University—Performance-Engineered Mix Design (NCSU-PEMD) study. The mixtures of interest from that study are C50-54, C50-55, and C50-57. Each mixture uses the same 9.5-mm NMAS gradation and PG 64-22 binder. These three mixtures were compacted to three different air void contents of 4.1 percent, 5.5 percent, and 7.1 percent, respectively. Figure 62 shows the

effects of the different in-place air void contents on the RSI. As the in-place air void content increases, the RSI value increases, which matches expectations.

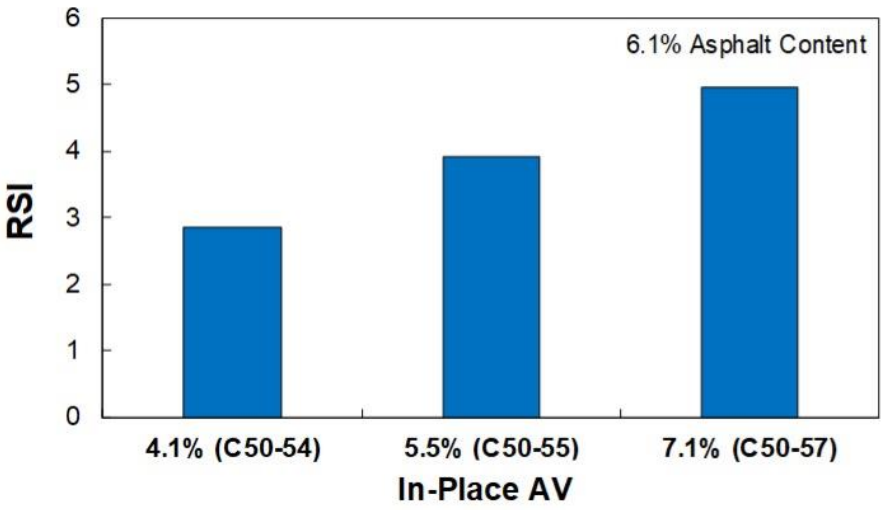

AV = air void.

Figure 62. Graph. Effects of in-place AV content on RSI.[138]

Effects of Binder Content on Rutting Strain Index

Mixture data from the MaineDOT project were used to investigate the effects of binder content on the RSI. To generate these data, MaineDOT performed a mix design study using a single mixture but varied the asphalt content in 0.5-percent increments. Figure 63 shows that the RSI value increases as the asphalt content increases. This trend is expected based on engineering intuition that purports that a higher asphalt content leads to a softer mixture and less rutting resistance.

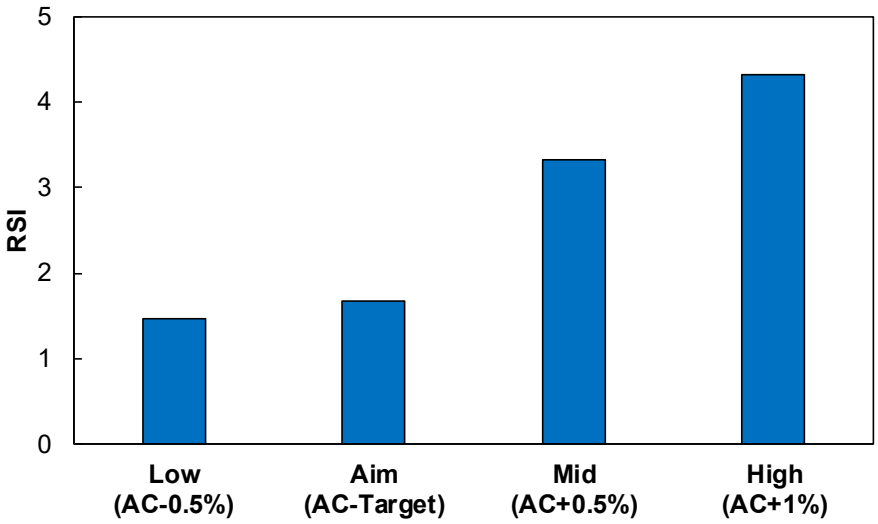

Figure 63. Graph. Effects of binder content on RSI.[138]

Effects of RAP Content and Binder Grade on Rutting Strain Index

Data from the MIT-RAP project and the new FHWA ALF project (new ALF) were used to study the effect of RAP content on the RSI. The MIT-RAP project tested four different mixtures with different RAP contents and binders. In that study, the RAP content was changed systematically from 0 percent to 15 percent to 50 percent. Then a soft binder was used for the 50-percent RAP mixture to investigate the effects of using a soft binder for high RAP content mixtures. Figure 64 shows the RSI values for these four mixtures. As expected, the RSI value of the 15-percent RAP mixture is lower than that of the control mixture; however, a further increase in the RAP content from 15 percent to 50 percent did not affect the RSI value significantly. The slight increase in the RSI value for the 50-percent RAP mixture compared to that of the 15-percent RAP mixture could be due to specimen-to-specimen and test-to-test variabilities.

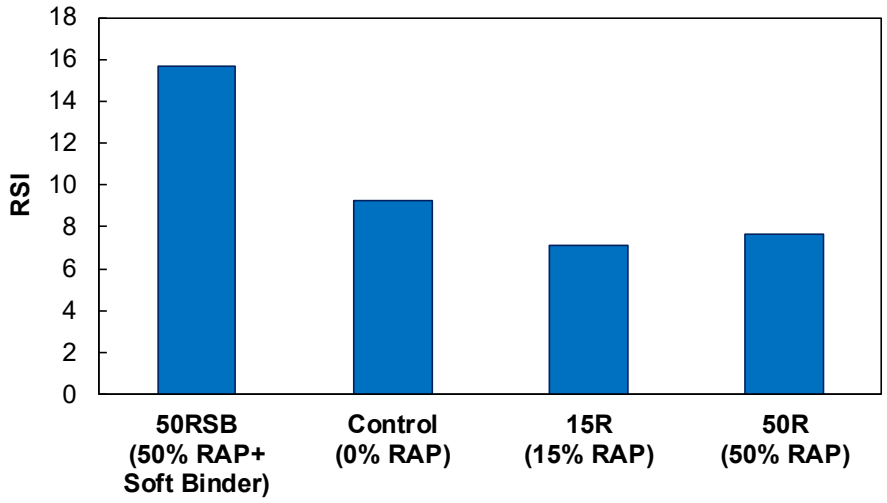

Figure 64. Graph. Effects of RAP content on the RSI (MIT-RAP project).[138]

FHWA's new ALF project evaluated the rutting resistance of five mixtures via SSR tests. Figure 65 presents the RSI values for the five mixtures tested in this project. As the RAP content increases, the RSI values decrease, which again is in line with engineering intuition. In this study, the mixtures in lanes 1, 6, and 5 had the same binder PG, but different RAP contents. Lane 1 has the highest RSI value. The lane 5 and lane 8 mixtures had the same RAP content, but different binder types. Lane 8, with the softer binder, has a higher RSI value than lane 5, as expected. Comparing lane 6 and lane 7, the mixtures had the same binder type, but lane 7 contained 20-percent RAS, which are known to cause a stiffer mixture than RAP. Therefore, the RSI value decreased. All these predictions are in line with engineering intuition and verify that using the RSI concept can capture the effects of RAP, RAS, and binder type well.

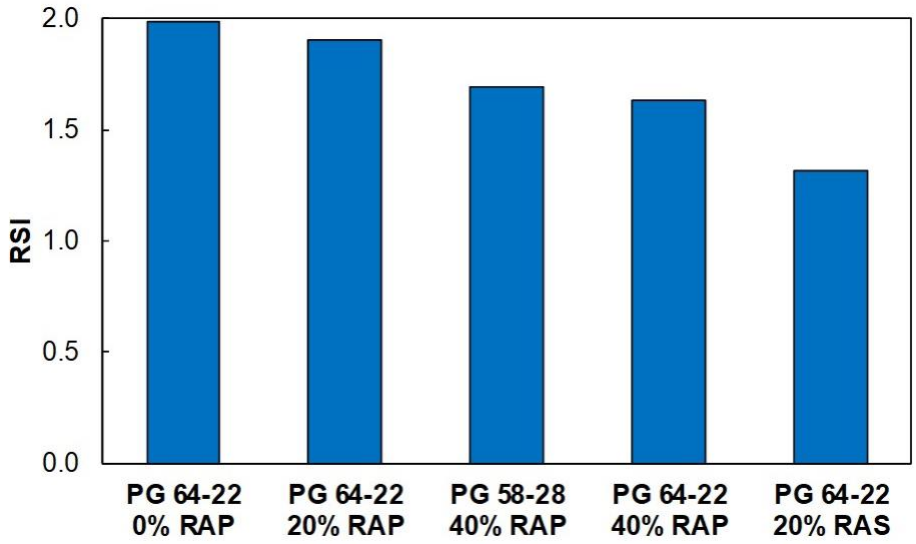

Figure 65. Graph. Effects of RAP and RAS content and binder type on RSI (new ALF project).[138]

Application of Rutting Strain Index in Index-Based Balanced Mix Design

The performance of an asphalt mixture depends on several factors, including aggregate gradation, design air void content, binder content, aggregate properties, and binder properties. These factors have a significant impact on mixture performance and should be reflected during the mix design process. AMPT BMD is now an important component of asphalt mixture PRS. In the AMPT BMD research conducted at NCSU and FHWA, cracking and rutting are the most important distresses that should be considered as factors in BMD. With regard to cracking, the S_{app} parameter can capture the effects of volumetric properties, RAP content, and binder content using different mixture types.[115] With regard to rutting, which is the focus of this section, the RSI can be used as an index. These two indexes, S_{app} and the RSI, can be employed as inputs for index-based BMD.

Summary

This section presents the development and implementation of a new rutting index parameter, referred to as the RSI. The RSI is based on the permanent deformation shift model that can be characterized by the SSR test and indicates the rutting resistance of an asphalt mixture more realistically than other index parameters. Other index parameters and empirical test methods for rutting rely on the response of the material under a single load and temperature condition. This snapshot approach to the determination of the rutting resistance of a mixture can be misleading, as demonstrated in the Permanent Strain under Repeated Loading section. The RSI parameter is determined from FlexPAVE mechanistic pavement analysis that incorporates the effects of realistic loading and climatic conditions on the mixture at various depths in the pavement.[6] This determination is performed in the Microsoft® Excel®-based FlexMAT program by incorporating major functions in FlexPAVE into FlexMAT.[5,6,24] The basic concept behind the

RSI parameter provides a mechanistically sound and realistic way to determine the rutting resistance of asphalt mixtures.

This study evaluated 72 asphalt mixtures with a wide range of mixture factors and from different climatic regions for the RSI parameter. The results show that the RSI can capture the effects of different mix design factors, such as RAP content, binder content, and volumetric properties. Furthermore, a set of RSI threshold values is proposed for different allowable traffic levels in terms of rutting. As engineers become familiar with the RSI, the RSI threshold values can be adjusted according to local experience and conditions The RSI also can be employed by agencies as a tool for BMD and QA purposes where agencies will be able to accept or reject a mixture based on RSI thresholds.

In short, the benefits of the developed RSI include the RSI's ability to determine the rutting resistance of asphalt mixtures using realistic moving loads and climatic conditions of the location where the mixture would be used, its sensitivity to various mix design factors, and its threshold values for different traffic levels that have been determined from a large number of mixtures with a wide range of compositions and from different climatic regions. These strengths make the RSI an excellent rutting index for BMD and QA to improve highway infrastructure.

CHAPTER 4. DEVELOPMENT OF FLEXMAT VERSION 2.1

FlexMAT's role is to simplify the analysis procedure for tested mixtures, thereby generating the required coefficients for the mechanistic-empiric simulations that may take place in FlexPAVE and performance predictions in PASSFlex.[5–7] The models calibrated in FlexMAT have strong mechanistic foundations but may seem complex to users who are not accustomed to them due to the models' several coefficients and convoluted equations. To ensure the development of a tool that pavement engineers can use without the need for deeper theoretical understanding of the models and to provide a simpler step between lab tests and simulations, FlexMAT is under constant development through the combined effort of FHWA and the research team. The current FlexMAT version under review for public release, FlexMAT 2.1, is the basis for the work described here.

This section briefly discusses the models and concepts used in FlexMAT so that these models and concepts will be familiar to the reader and user when these models and concepts are mentioned later in the discussion of the PASSFlex framework.[5,7] However, understanding the models is not a priority for using FlexMAT. In fact, FlexMAT is most valuable when the user is not fully versed in the entirety of the conceptual modeling because the simple selection of AMPT outputs through FlexMAT will provide the characterization needed for the most basic form of mixture evaluation in this framework.

FlexMAT is a spreadsheet-like program, hosted under Microsoft Excel.[5,24] Most of the procedures and calculations of FlexMAT are made in the background through Microsoft Visual Basic for Applications® (VBA).[144] FlexMAT's VBA code is not accessible to the user to avoid unintended modifications that could change a fundamental feature of the calibrated models.

The two different FlexMAT programs are:

- FlexMAT Cracking, where the dynamic modulus, fatigue cracking, CTCs, and aging models are calibrated and the cracking index and the apparent damage capacity (S_{app}) can be calculated.[15]

- FlexMAT Rutting, where the rutting model is calibrated and the permanent deformation index, RSI, can be calculated.[16]

Figure 66 presents a flowchart of FlexMAT.[5]

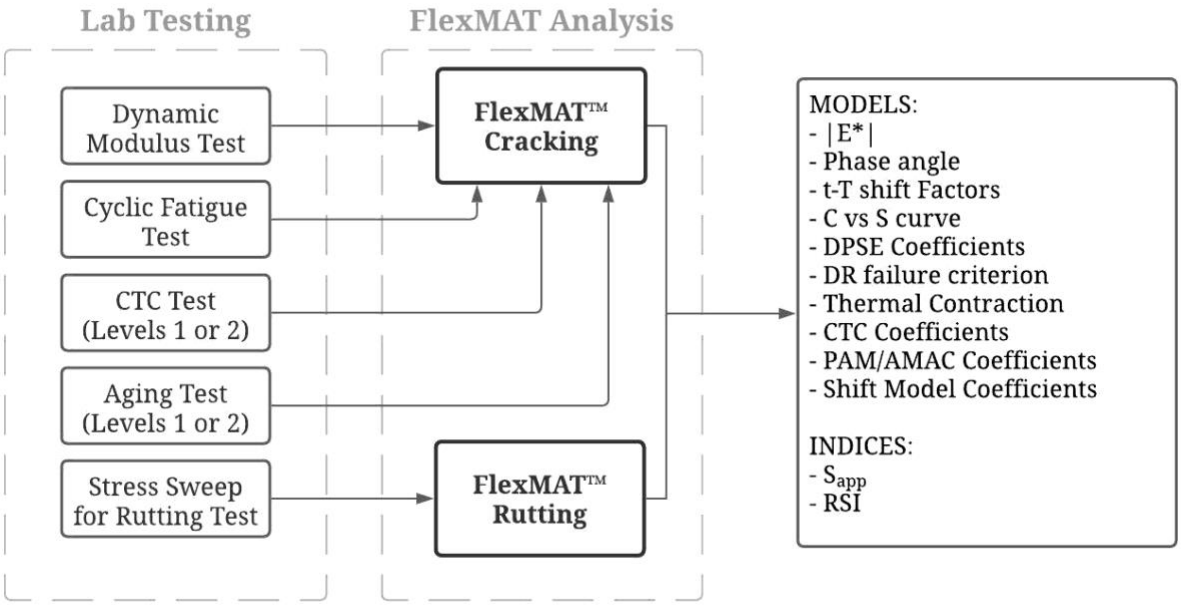

Source: FHWA.

Figure 66. Flowchart FlexMAT flow overview.

Although FlexMAT is treated as a single software program for overall workflow understanding, FlexMAT is composed of two separate spreadsheets based on different needs.[5] The climatic database needed for RSI calculations originally was planned to be included within FlexMAT Rutting's spreadsheet, which would cause that spreadsheet to become a much larger file than FlexMAT Cracking.[15,16] The research team decided it was best to leave FlexMAT Cracking and FlexMAT Rutting as separate files to avoid the problems associated with big files in FlexMAT Cracking and isolate them into FlexMAT Rutting, as the climatic database was used only in FlexMAT Rutting.

In this approach, FlexMAT Cracking is responsible for most of the models that are related to material characterization, i.e., cyclic fatigue, CTC analysis (levels 2 and 3), and aging analyses (all levels) are all based on the dynamic modulus characterization.[15] The first model to be characterized in FlexMAT Cracking is 2S2P1D, which is the current implemented dynamic modulus model in FlexMAT Cracking v. 2.1. The exception is level 1 CTC analysis, where the CTCs were measured in the lab and the calibrated coefficients are the actual inputs; therefore, the calibrated dynamic modulus model is not necessary, as opposed to levels 2 and 3.

The following sections provide a summary of each of the analysis modules in FlexMAT.[5]

Dynamic Modulus

Dynamic modulus characterization is normally the first analysis carried out in FlexMAT Cracking, and the expected inputs are the folders that contain AMPT dynamic modulus test data. To start the analysis, the user must select the number of specimens tested in the lab, shown in the "Input Data" screen using a drop-down list in cell B3, as shown in figure 67. Clicking "Load and Analyze Dynamic Modulus Data" will start the specimen selection and, once all the specimens have been selected, the analysis will begin automatically.

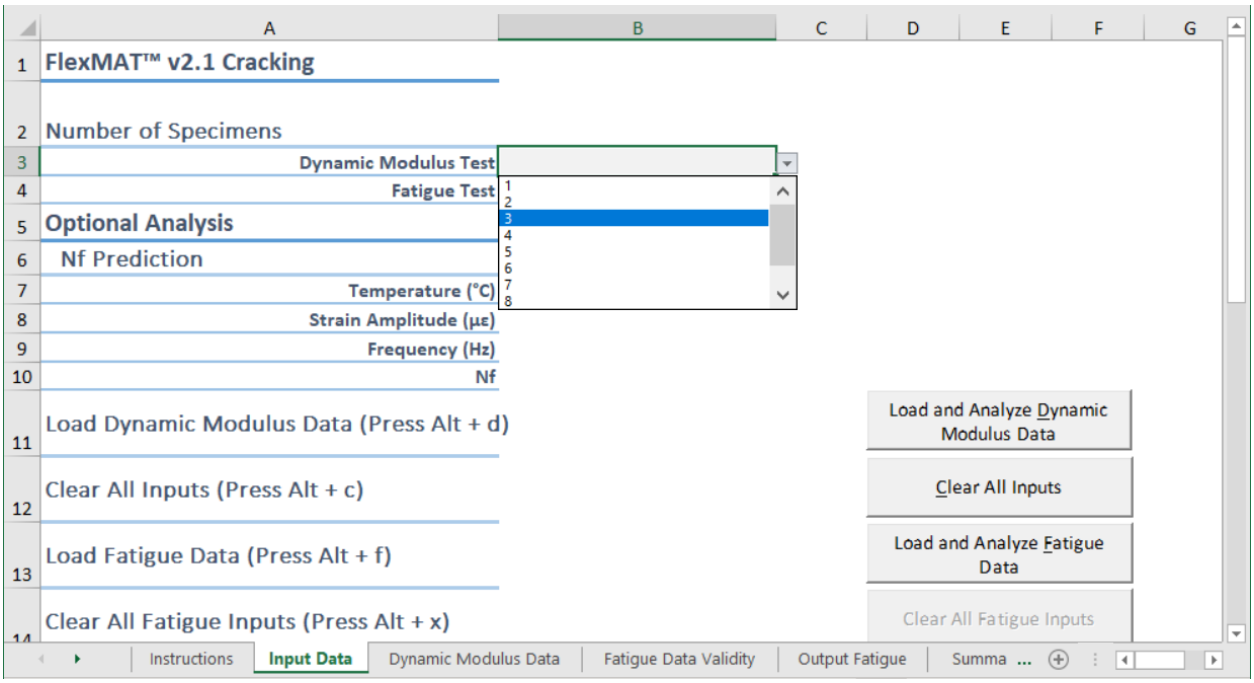

Source: FHWA.

Figure 67. Screenshot. FlexMAT Cracking version 2.1 dynamic modulus input screen.

The "Dynamic Modulus Data" dynamic modulus screen provides details about the characterization procedure presented in figure 68, where the coefficients for the outputs are given. The following three main outputs from the dynamic modulus analysis are:

- 2S2P1D coefficients, given in cells E6 through E12.
- t-TS shift factors, given in cells B4 through B6.
- Damage evolution rate factor, α, in cell B13.

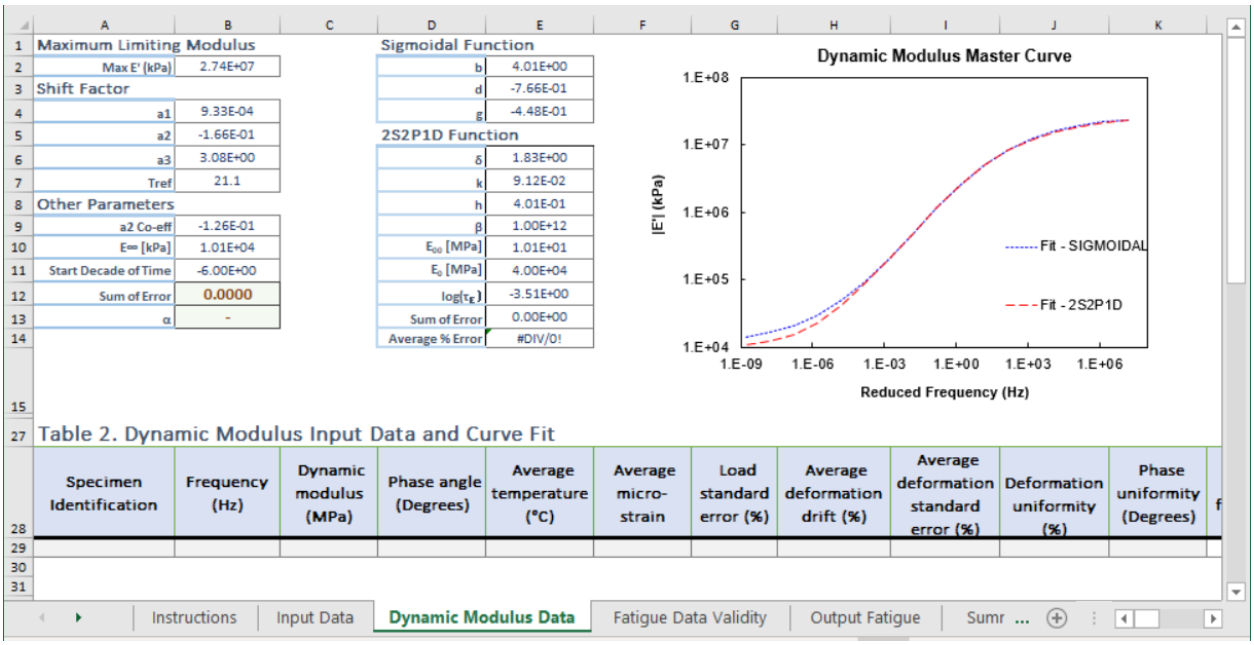

Source: FHWA.

Figure 68. Screenshot. FlexMAT dynamic modulus data screen.

The 2S2P1D model presented by Olard and Di Benedetto is the model adopted for dynamic modulus characterization and follows equations 109 to 114.[74]

$$E'_1 = (E_0 - E_{00})\left[1 + \delta(2\pi f \tau_E)^{-\kappa}\cos\left(\frac{k\pi}{2}\right) + (2\pi f \tau_E)^{-h}\cos\left(\frac{h\pi}{2}\right)\right] \quad (109)$$

$$E'_2 = (E_0 - E_{00})\left[\delta(2\pi f \tau_E)^{-\kappa}\sin\left(\frac{k\pi}{2}\right) + (2\pi f \tau_E)^{-h}\sin\left(\frac{h\pi}{2}\right) + (2\pi f \tau_E \beta)^{-1}\right] \quad (110)$$

$$DEN = \left(\frac{E'_1}{(E_0 - E_{00})}\right)^2 + \left(\frac{E'_2}{(E_0 - E_{00})}\right)^2 \quad (111)$$

$$\mathrm{Re}(E^*) = E_{00} + \frac{E'_1}{DEN} \quad (112)$$

$$\mathrm{Im}(E^*) = \frac{E'_2}{DEN} \quad (113)$$

$$|E^*| = \sqrt{\left[\mathrm{Re}(E^*)\right]^2 + \left[\mathrm{Im}(E^*)\right]^2} \quad (114)$$

Where:

E_{00} = minimum storage modulus value (kPa).
E_0 = maximum storage modulus value (kPa).
κ, δ, h, β, τ_E = fitting coefficients.
f = loading frequency (Hz).
E^* = complex modulus (kPa).

To calibrate the coefficients of the 2S2P1D function, a specific fitting method was developed to overcome the initial value dependency reported by Mangiafico et al. 2019. The following steps are taken to fit the 2S2P1D model in FlexMAT:[5]

- Step 1. Fit the experimental storage modulus data to the sigmoidal function. Through minimization of the square logarithmic error between the experimental data in the tested reduced frequency range and the predicted storage modulus using the sigmoidal function, calibrate the coefficients of equations 115 and 116 in a single Solver minimization using the initial values for the fitting coefficients given in table 27. initial values for sigmoidal experimental fitting procedure..

Table 27. Initial values for sigmoidal experimental fitting procedure.

Fitting Coefficient	Initial Value
Max (*E'*)	25.106
b	4
d	−1.5
g	−0.5
c1	0.005
c2	−0.15

$$\log\left(E'\left(f_R\right)\right) = b + \frac{\log(\max \mathrm{E'}) - b}{1 + e^{d + g\log\left(f_R\right)}} \quad (115)$$

$$f_R = f \cdot 10^{c_1 T^2 + \left(c_2 - 2c_1 T_{ref}\right)T + \left(c_1 {T_{ref}}^2 - c_2 T_{ref}\right)} \quad (116)$$

Where:

E' = storage modulus (kPa).
f_R = reduced frequency (Hz).
max E', b, d, g = sigmoidal function's fitting coefficients.
c_1, c_2 = fitting coefficients.
f = loading frequency (Hz).
T_{ref} = dynamic modulus' reference temperature (°C).

T = temperature (°C).

- Step 2. Select the reduced frequency range. The implemented selection of the reduced frequency range creates a vector of 21 values separated in decades from 10^{-15} to 10^{5}.

- Step 3. Determine the initial values for 2S2P1D fitting. Before fitting the actual experimental data to the 2S2P1D model, determine the initial values for the 2S2P1D model by matching the 2S2P1D function to the sigmoidal function calibrated in step 1 at each frequency in the vector of frequencies created in step 2. Table 28. Initial values for 2S2P1D sigmoidal fitting. presents the initial values required for this error minimization and table 29. 2s2p1d sigmoidal fitting constraints. presents the coefficients constraints.

Table 28. Initial values for 2S2P1D sigmoidal fitting.

Fitting Coefficient	Initial Value
δ	2.5
κ	0.1
h	0.5
β	10^{12}
E_{00}	$10^{(b\_sigmoidal\ -\ 3)}$
E_0	40,000
$log(\tau_E)$	−3

Table 29. 2S2P1D sigmoidal fitting constraints.

Fitting Coefficient	Constraint
δ	≥ 0 ≥ 20
κ	≥ 0 ≤ 1 $\leq h$
h	≥ 0 ≤ 1
β	$=10^{12}$
E_{00}	$=10^{(b\_sigmoidal\ -\ 3)}$
E_0	=40,000
$log(\tau_E)$	≥ -10 ≤ 10

- Step 4. Determine the 2S2P1D coefficients. This final step uses the actual experimental data in the reduced frequency (same as in step 1) to calculate errors using the 2S2P1D model. For each coefficient error, the minimization algorithm uses the initial values

obtained from the fitting procedure in step 3. Table 30. 2S2P1D experimental fitting constraints. shows the constraints.

Table 30. 2S2P1D experimental fitting constraints.

Fitting Coefficient	Constraint
δ	≥ 0 ≤ 20
κ	≥ 0 ≤ 1 $\leq h \geq$
h	≥ 0 ≤ 1
β	$=10^{12}$
E_{00}	$=10^{(b\_sigmoidal\ -\ 3)}$
E_0	$=40{,}000$
$log(\tau_E)$	≥ -10 ≤ 10

The dynamic modulus master curve is defined based on the experimental data. To calculate the t-TS factor coefficients, equations 117 to 120 are used with the reference temperature of 21.1 °C.

$$a_T = 10^{\left(a_1 T^2 + a_2 T + a_3\right)} \tag{117}$$

$$a_1 = c_1 \tag{118}$$

$$a_2 = c_2 - 2c_1 T_{ref} \tag{119}$$

$$a_3 = c_1 T_{ref}^2 - c_2 T_{ref} \tag{120}$$

Where:

a_T = time-temperature superposition shift-factor.
T_{ref} = dynamic modulus reference temperature (°C).
c_1, c_2 = fitting coefficients.
T = temperature (°C).
a_1, a_2, a_3 = shift-factor coefficients.

Finally, the damage evolution rate parameter (α) is calculated through equation 73.

Cyclic Fatigue

To characterize fatigue cracking properties in FlexMAT, cyclic fatigue data from the AMPT and dynamic modulus characterization are needed.(5) Once the dynamic modulus analysis is complete, the number of cyclic fatigue specimens tested is needed, as shown in the "Input Data" screen, cell B4, as shown in figure 69. After selecting the number of specimens, the analysis procedure will start once the "Load and Analyze Fatigue Data" button is clicked, which starts the specimen data selection and automatically runs the analysis procedure once all the specimens have been selected.

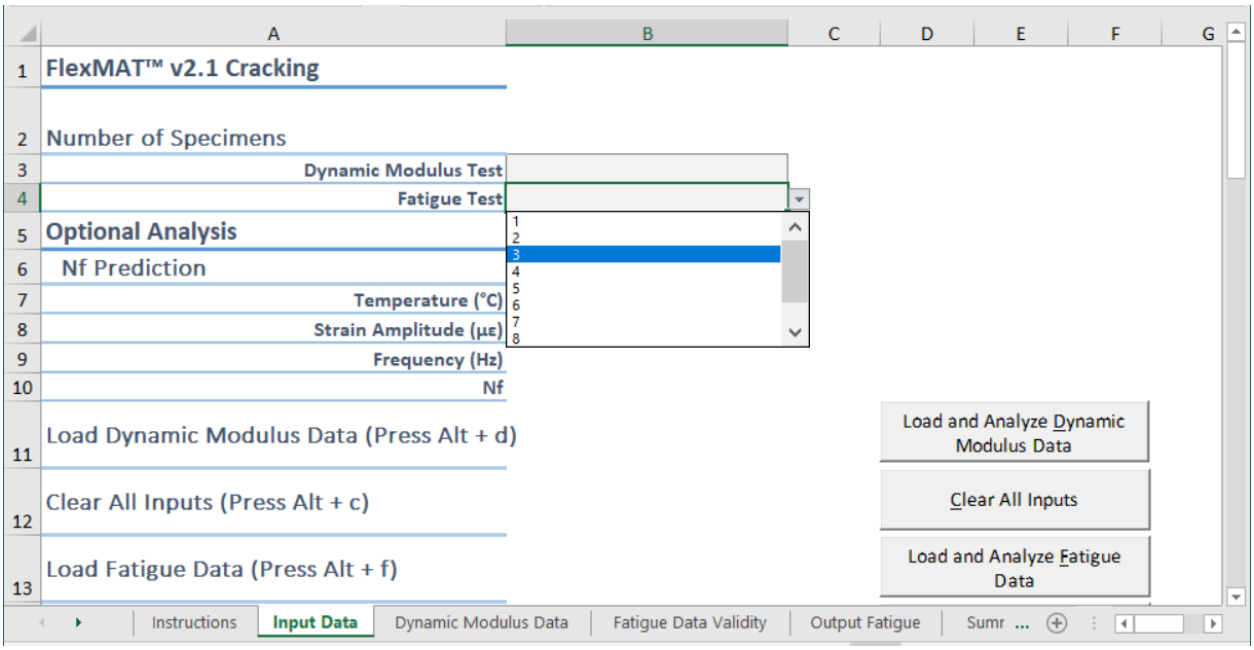

Source: FHWA.

Figure 69. Screenshot. FlexMAT Cracking version 2.1 cyclic fatigue input screen.

The S-VECD model is used for damage characterizations. Details about the theoretical background of the S-VECD model are outside the scope of this report, but the work of Underwood et al. provides a deeper understanding of the model.(106)

The following four outputs of interest from this analysis are:

- Damage characteristic curve characterization (C versus S curve).
- Failure criterion (D^R).
- DPSE characterization.
- S_{app}.

Details regarding the characterizations are presented in the "Output Fatigue" screen in figure 70.

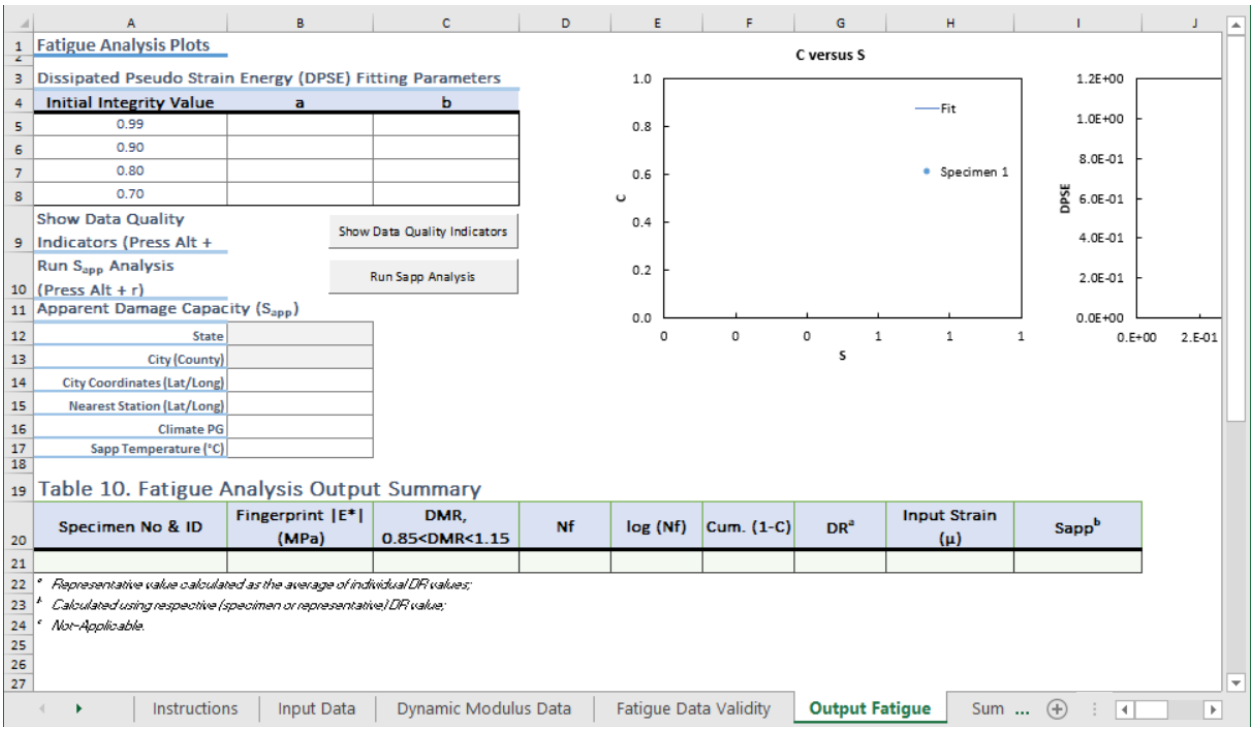

Source: FHWA.

Figure 70. Screenshot. FlexMAT cyclic fatigue model overview screen.

The "Output Fatigue" tab presents three important plots:

- "C versus S," which contains the material representative damage characteristic curve, with individual curves and fitted representative behavior for the tested material.
- "DPSE versus Reduced Strain Rate," with the DPSE as a function of reduced strain rate for four conditions of initial integrity.
- "Cumulative (1-C) versus N_f," with the plot of the failure criterion (D^R) points for each specimen.

These plots and the cyclic fatigue characterization procedure can be organized in the following steps:

- Step 1. Calculate individual *C* versus *S* curves. In this initial step, each input specimen data point is analyzed independently, and a *C* versus *S* curve is calculated for each of the specimens following standard procedures (AASHTO TP 107-18, PP 99-19, and TP 133-19).[(90,93,114)] This information will be used in the calculations in the following steps.
- Step 2. Calculate a representative *C* versus *S* curve. Fit equation 70 by using the individual *C* versus *S* curves calculated in step 1. However, depending on the individual specimens' testing characteristics, a different number of *C*(*S*) points can be calculated for each curve. To avoid biasing the representative curve toward tests that have more

calculated points than others, a filtering process is applied taking the nearest lower calculated *C* value for each 5000 incremental step in the *S* parameter. Figure 71 depicts this filtering process, which is designed to even out the weight of each specimen in the final representative *C* versus *S* curve and in the C_{11} and C_{12} coefficients.

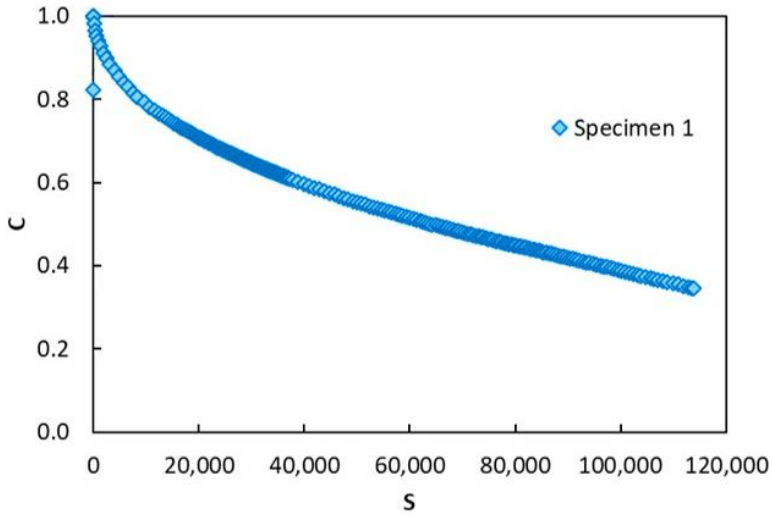

Source: FHWA.

A. Before representative fitting filtering.

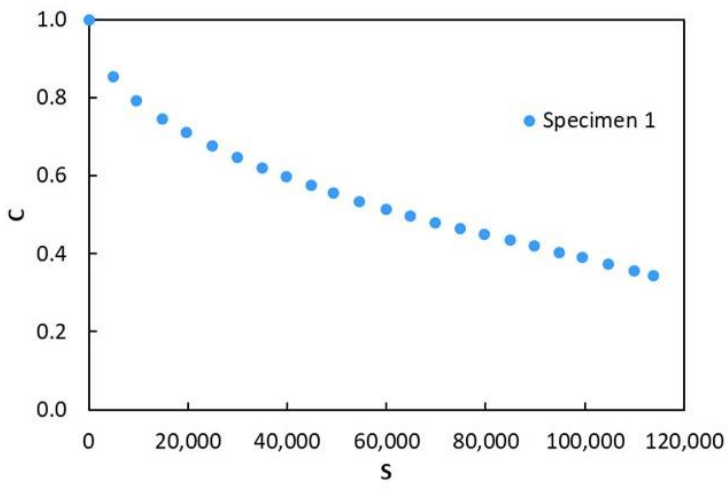

Source: FHWA.

B. After representative fitting filtering.

Figure 71. Graphs. *C* versus *S* curve.

- Step 3. Calculate the DR failure criterion. To calculate DR, the currently implemented failure criterion of FlexMAT, the failure point of the specimen needs to be determined.[5,110] The current specimen failure definition uses the number of cycles to failure (N_f) whereby the value of the applied peak-to-peak stress multiplied by the cycle number reaches its local maximum. Figure 72 illustrates this point.

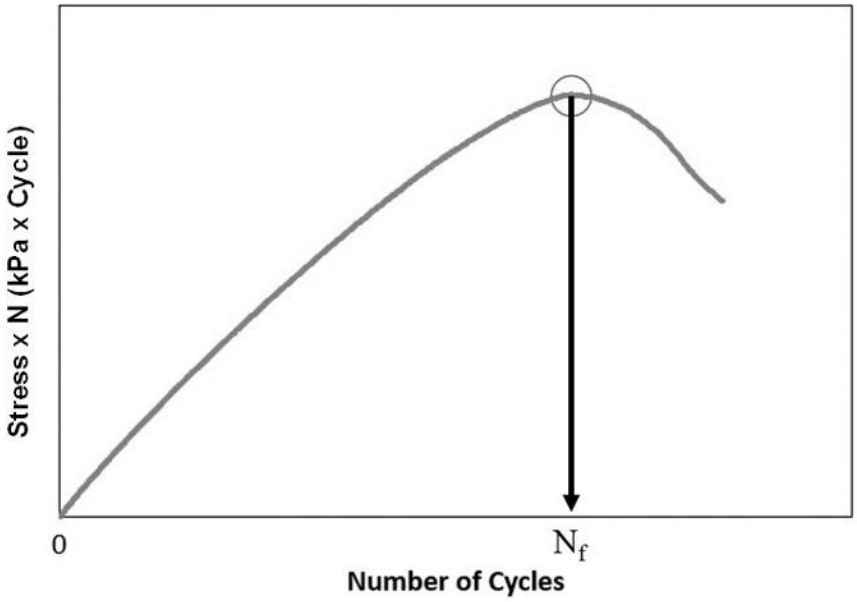

Source: FHWA.

Figure 72. Graph. Failure cycle determination.

Once N_f is determined for each specimen, D^R is determined by equation 121 for each individual specimen and by equation 122 as the mix representative value (Wang 2017).[110]

$$D_i^R = \frac{\int_0^{N_{f,i}} \left(1 - C(N)_i\right) dN}{N_{f,i}} \tag{121}$$

$$D^R = \sum_{i=1}^{M} \frac{D_i^R}{M} \tag{122}$$

Where:

$C(N)_i$ = integrity at cycle N for the ith specimen.
$N_{f,i}$ = cycle number of failure for the ith specimen.
M = the number of specimens tested.

- Step 4. Characterize the DPSE reduced strain rate. To calculate the DPSE as a function of the reduced strain rate for a given initial material integrity, a monotonic tensile test is simulated using the damage characteristic curve coefficients and a Prony series representation of the dynamic modulus to obtain the relaxation modulus of the mixture. The following steps describe this process:

- Step 4.1. Determine the reduced strain rate vector in which the DPSE values are calculated in the simulated strain-controlled monotonic test. For FlexMAT, the reduced strain rate vector contains 20 different values, starting at 4.10^{-6} s^{-1} and constant increments up to 5.10^{-3} s^{-1}.[5] Equation 123 represents the strain input of the simulated monotonic test.

$$\varepsilon = k\xi \tag{123}$$

Where:

ε = input strain.
k = strain rate (s^{-1}).
ξ = reduced time.

- Step 4.2. Calculate pseudostrain using equation 65 and the Prony series for relaxation modulus given in equation 125.

$$\varepsilon^R(\xi) = \frac{1}{E_R}\int_0^{\xi} E(\xi-\tau)\frac{d\varepsilon}{d\tau}d\tau \tag{124}$$

$$E(\xi) = E_\infty + \sum_{i=1}^{17} E_i e^{\frac{-\xi}{\rho_i}} \tag{125}$$

Where:

ε^R = pseudostrain.
E_R = reference modulus (kPa).
ξ = reduced time (s).
ε = input strain.
$d\tau$ = differential of time (s).
$E(\xi)$ = relaxation modulus (kPa).
E_∞, E_i = Prony coefficients (kPa).
ρ_i = Prony coefficients (s).

- Step 4.3. Solve the ordinary differential equation in equation 126 to find damage (S) as a function of time for the given condition.

$$\frac{dS}{d\xi} = \left(-\frac{1}{2}\frac{dC}{dS}\left(\varepsilon^R\right)^2 \right)^{\alpha} \tag{126}$$

Where:
S = damage.
ξ = reduced time (s).
C = material integrity, equation 70.
ε^R = pseudostrain.
α = damage evolution rate parameter, equation 73.

To solve this ordinary differential equation, an initial value for material integrity is required. Four values are used in current version of FlexMAT to characterize the DPSE behavior.[5] These values are C0 = 0.99, C0 = 0.90, C0 = 0.80, and C0 = 0.70.

- Step 4.4. Determine the point of maximum stress using equation 127.

$$\sigma\left(\xi\right) = C\left(\xi\right)\varepsilon^R\left(\xi\right) \tag{127}$$

Where:
σ = stress (kPa).
C = material integrity.
ε^R = pseudostrain.

- Step 4.5. Calculate the DPSE using equation 128 for each strain rate defined in step 4.1 and for each initial integrity defined in step 4.3.

$$DPSE = \int_0^{\xi_{max}} \left(\varepsilon^R\left(\xi\right)\right)^2 \left(1 - C\left(\xi\right)\right) d\xi \tag{128}$$

Where:
$DPSE$ = dissipated pseudostrain energy.
ξ_{max} = reduced time for peak-stress (s).
ε^R = pseudostrain.
C = integrity.

- Step 4.6. Fit the results of equation 128 for the same initial integrity into a power-law function in the format of equation 129.

$$DPSE = a\left(k\right)^{b} \tag{129}$$

Where:

DPSE = dissipated pseudostrain energy.
a, *b* = fitting coefficients.
k = reduced strain rate (s^{-1}).

Figure 73 presents an example of typical DPSE characterization results in FlexMAT.[5]

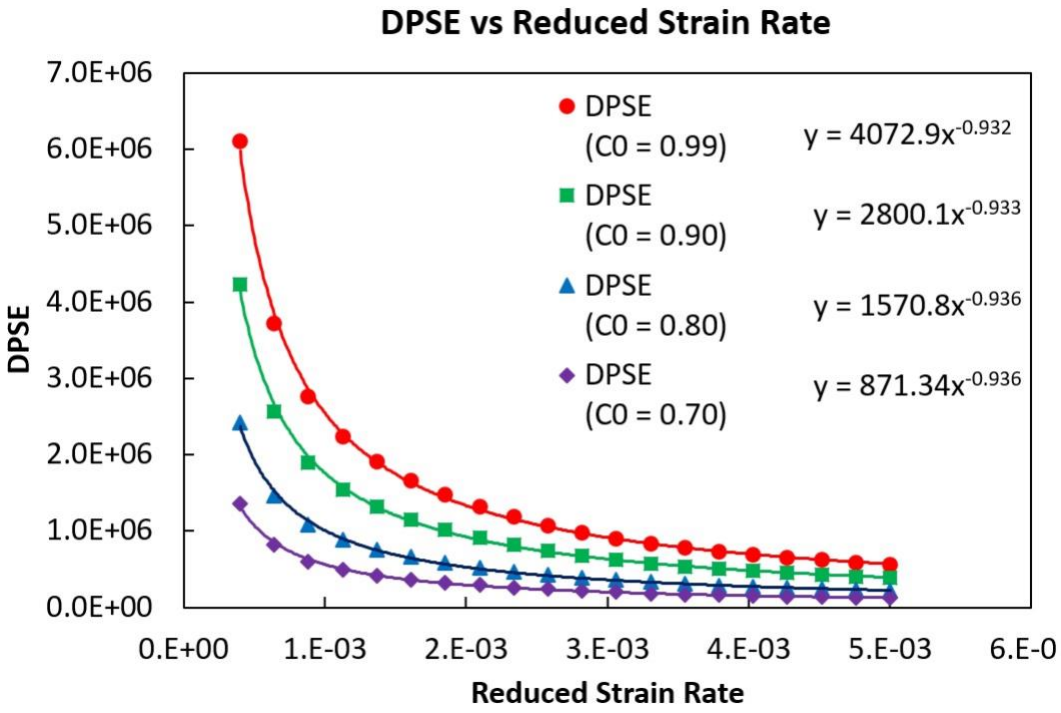

Source: FHWA.

Figure 73. Graph. Typical DPSE characterization in FlexMAT.

- Step 5. Calculate S_{app} using equation 130.

$$S_{app} = 1{,}000^{\frac{\alpha}{2}-1} \frac{a_T^{\frac{1}{\alpha+1}} \left(\frac{D^R}{C_{11}} \right)^{\frac{1}{C_{12}}}}{\left| E^* \right|_{LVE}^{\frac{\alpha}{4}}}$$

(130)

Where:

S_{app} = apparent damage capacity.
a_T = shift-factor for project location temperature.
C_{11}, C_{12} = damage characteristic curve fitting coefficients, equation 70.
D^R = failure criterion, equation 122.
α = damage evolution rate parameter, equation 73.
$|E^*|_{LVE}$ = dynamic modulus at target temperature and 10 Hz (kPa).

Further details regarding the S_{app} development and calculation can be found in the literature, but note that S_{app} is not a material property, but rather an index that evaluates the material's fatigue resistance given a certain climatic condition.(115) To calculate S_{app} in FlexMAT, the user must input a selection of State/City (in the United States) on cells B12 and B13 on the screen shown in figure 70 and, on its background, FlexMAT determines the target temperature for the S_{app} calculations.(5) An alternative input method for S_{app}'s temperature is through the direct climatic PG by selecting the alternative "Other" in the state selection field (cell B12). The S_{app} temperature is calculated using equation 131.

$$T_{S_{app}} = \frac{T_H + T_L}{2} - 3$$

(131)

Where:

T_{Sapp} = S_{app} calculation temperature (°C).
T_H = high climatic PG temperature (°C).
T_L = low climatic PG temperature (°C).

Use the "Fatigue Data Validity" screen in figure 74 to verify individual specimen details about the described calculations. Selection the specimen in cell B1. The following four plots are available on this screen:

- "Dynamic Modulus and Failure Definition" for stiffness behavior and failure definition verification.
- "Applied Stress" for applied stress during the test evolution.
- "Peak to Peak Strain" for LVDT behavior verification.
- "*C* versus *S*" for the individual damage characteristic curve of the selected specimen.

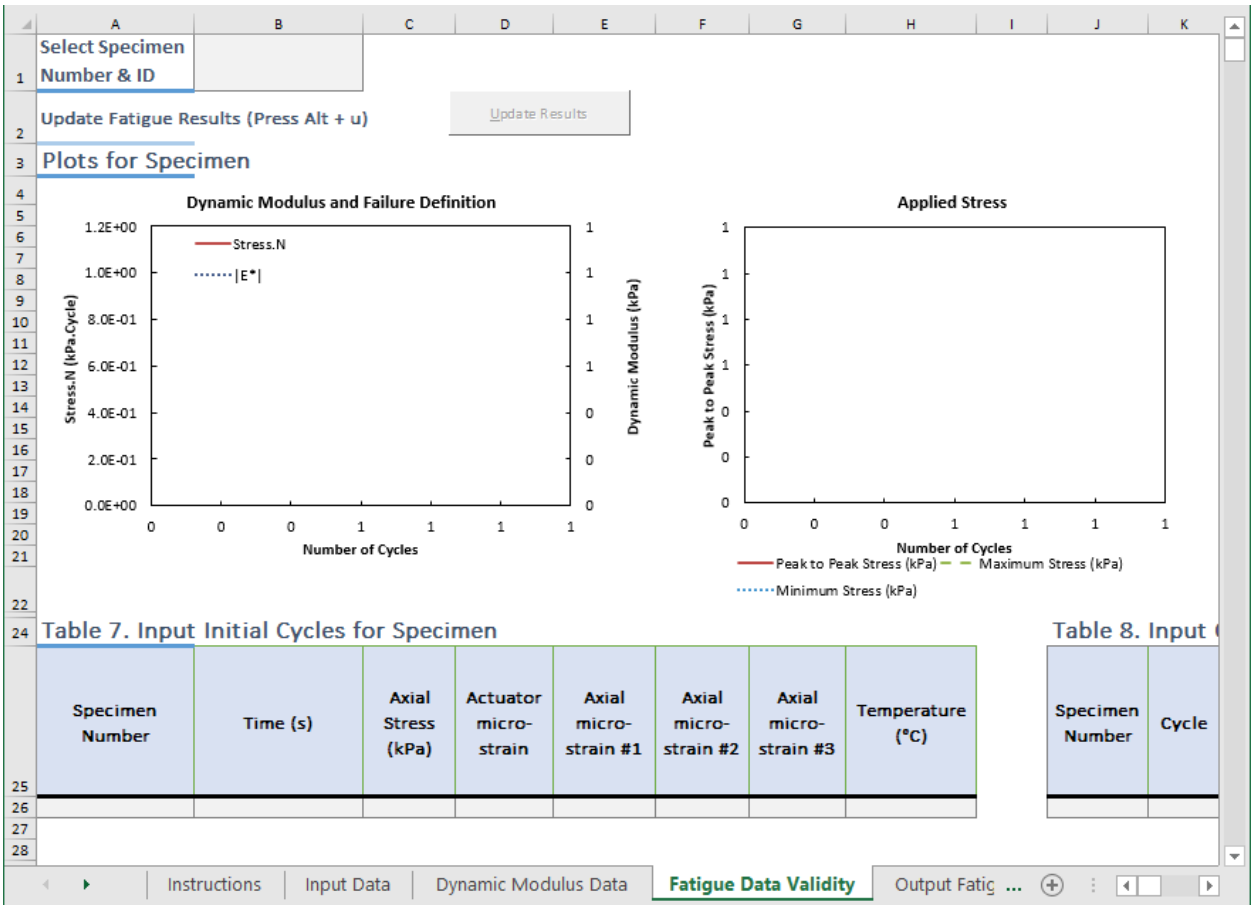

Source: FHWA.

Figure 74. Screenshot. FlexMAT screen for cyclic fatigue validity of individual specimens.

After all the calculations are completed, users can identify possible problems with the data using a set of data quality indicators. The indicators follow Bonaquist (2008) based on the calculation of the following information:[(145)]

- Fingerprint's average load standard error.
- Fingerprint's deformation standard error.
- Fingerprint's deformation uniformity.
- Fingerprint phase uniformity.
- Cyclic fatigue average deformation standard error.

The limits adopted for these parameters are given in table 31. data quality indicator validity range., based on AASHTO T 378-17.[(113)]

Table 31. Data quality indicator validity range.

Data Quality Indicator	Validity Range
Load standard error	≤10 percent
Deformation standard error	≤10 percent
Deformation uniformity	≤30 percent
Phase deformity	≤3 degrees

To enable the individual specimen data quality indicator verification "Data Quality Indicators" screen in figure 75, click the "Show Data Quality Indicators" button. This screen enables the visual verification of the proportional integral derivative (PID) tuning quality, plotting the measured actuator strain and the command strain as a function of time in the "PID Tuning Quality" graph. Select the specimens in the list in cell B4.

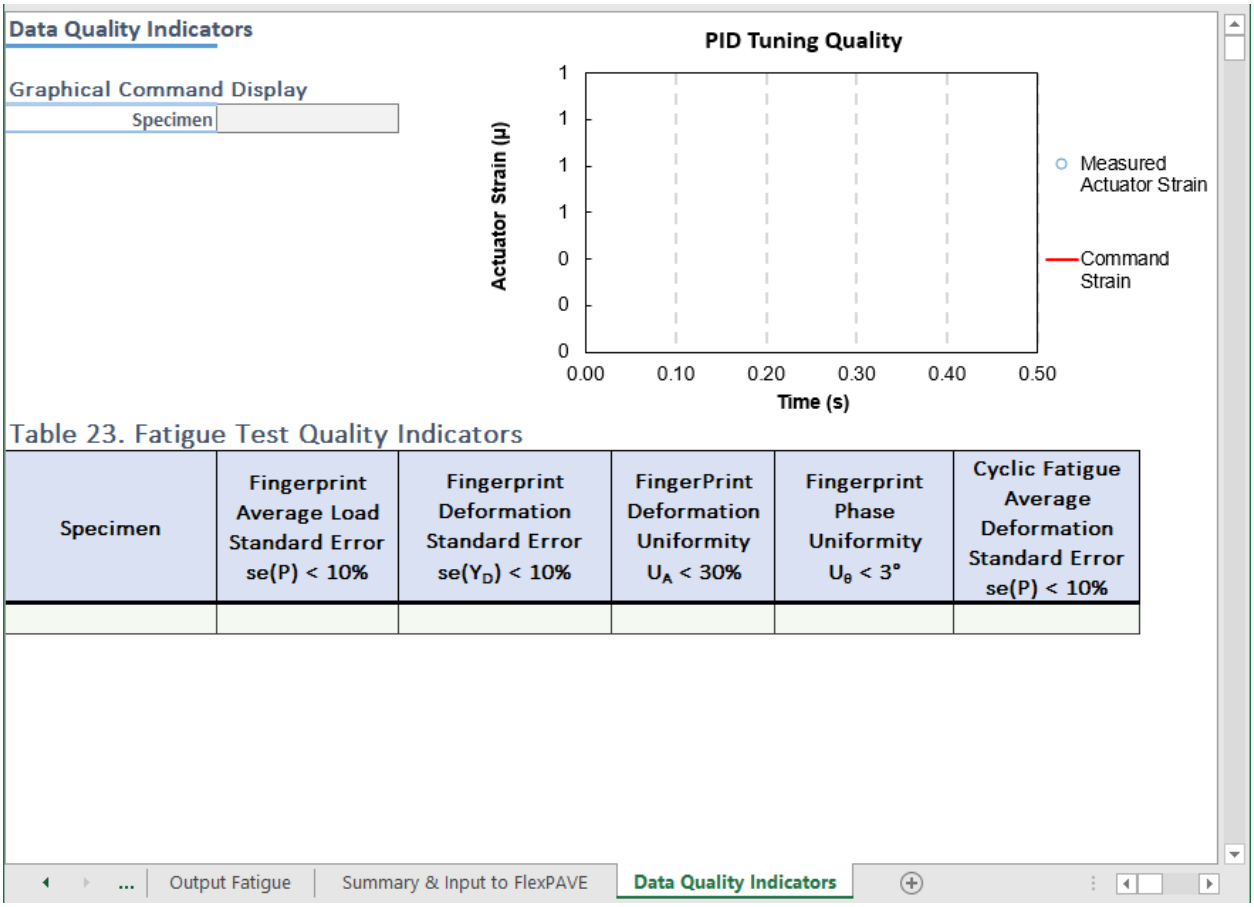

Source: FHWA.

Figure 75. Screenshot. FlexMAT "Data Quality Indicators" screen.

Coefficient of Thermal Contraction

The CTC is one of the parameters that require a hierarchical input selection in multiple-level alternatives. The level is selected in the "Input Data" screen in figure 76 using the list in cell B20.

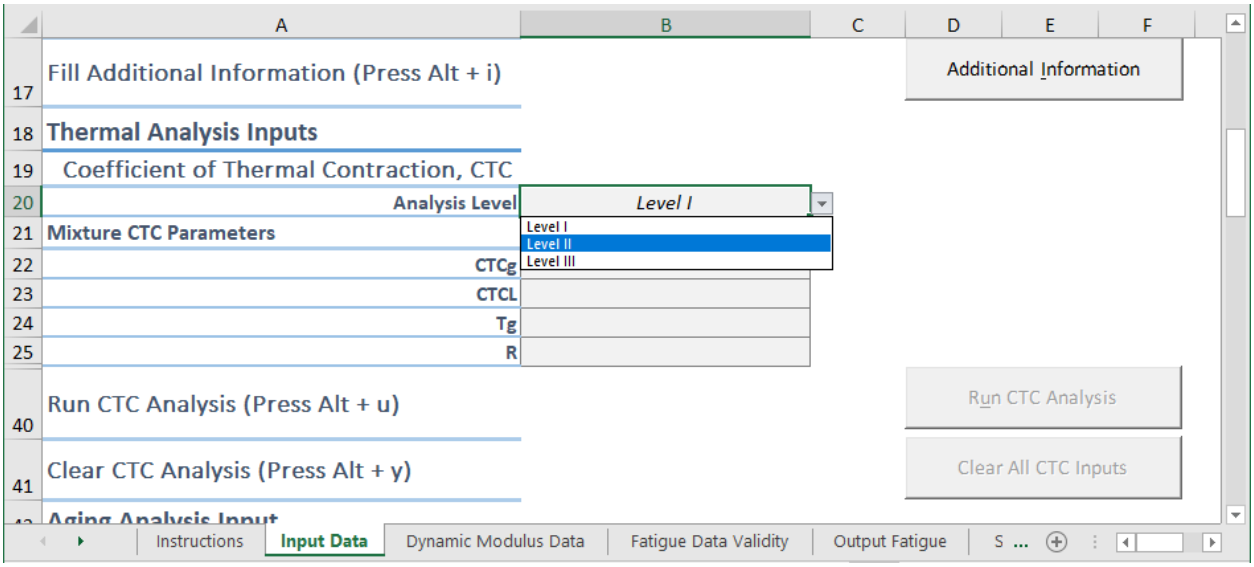

Source: FHWA.

Figure 76. Screenshot. FlexMAT CTC input screen.

The basic objective of the CTC analysis is to calibrate the CTC model given by equation 57.

The work of Keshavarzi (2019) describes in detail the three different levels used to calibrate the CTC properties, which are summarized as follows:[(65)]

- Level 1 assumes direct measurements of the mixture's CTC. The coefficients are obtained by a method of the user's discretion, outside of FlexMAT, and therefore do not require any calculation in FlexMAT.[(5)] Inputting the calibrated coefficients in level 1, however, will transfer them to the "Mixture Summary" tab to make them available for further propagation in the expected format for the PASSFlex system.[(7)]

- Level 2 estimates the CTC of the mixture by using the VMA of the mixture, aggregate bulk specific gravity (G_{sb}), CTC of the mineral aggregate in the mixture, and thermo-volumetric calibrated model of the binder (CTC_g, CTC_L, T_g, and R of binder used).

The following steps summarize the procedure:

- Step 1. Estimate the Prony coefficients of the binder using the 2S2P1D model fitted coefficients of the mixture. This model will be used to estimate the relaxation modulus of the binder in step 2.

- Step 2. Calculate the CTC of the mixture using equations 40 and 41 and equations 132 and 133. The relaxation modulus of the aggregate is considered constant with respect to time as a material-dependent property and is normally a tabulated value, whereas the relaxation modulus for the binder is calculated using the Prony coefficients calibrated in step 1.

$$A_{agg} = \left(1 - \frac{VMA}{100}\right)^{\frac{2}{3}} \tag{132}$$

$$A_{bind} = \left(\frac{VMA}{100}\right)^{\frac{2}{3}} \tag{133}$$

Where:

CTC = the coefficient of thermal contraction ($°C^{-1}$).
E = the relaxation modulus.
VMA = voids in mineral aggregate.
G_{sb} = bulk specific gravity.

- Step 3. Fit the CTC model given in equation 57 to the predicted evolution of the CTC of the mixture in step 2. Figure 77 presents an example of the simulation in the level 2 analysis of FlexMAT.[5]

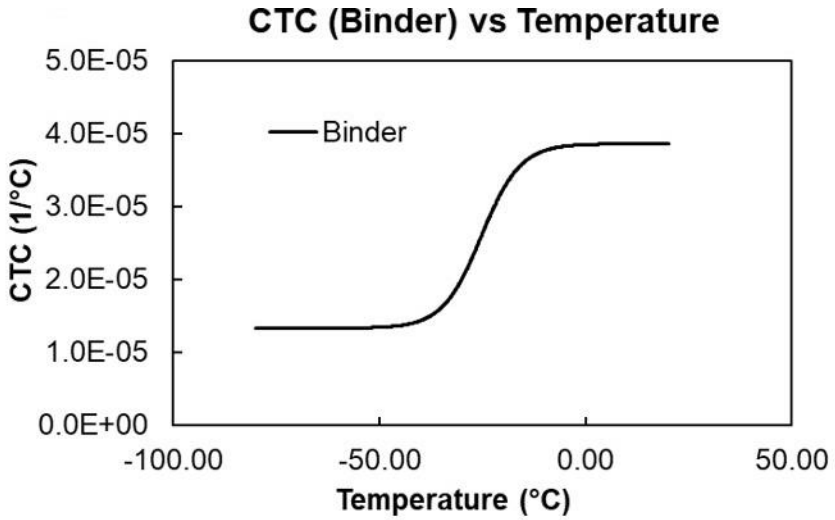

Source: FHWA. FlexMAT generated chart.

A. Binder CTC behavior.

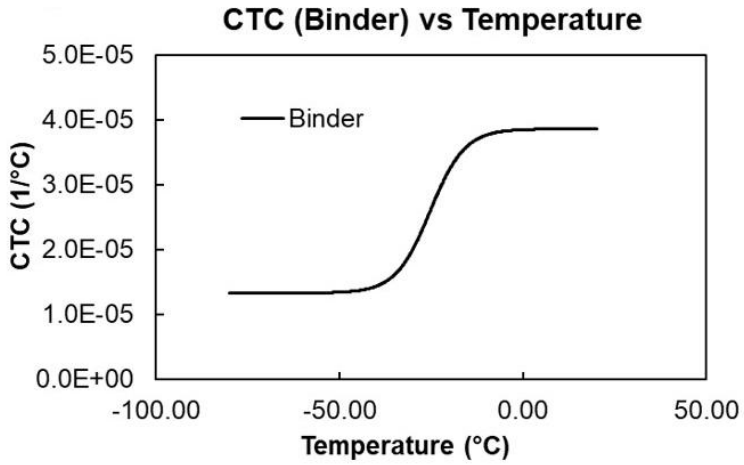

Source: FHWA. FlexMAT generated chart.

B. Predicted mixture CTC behavior estimated from input properties.

Figure 77. Graphs. Level 2 CTC analysis in FlexMAT.

When the analysis is complete, the user will be redirected to the "CTC Level 2" screen where the details of the procedure can be verified using the graphs shown in figure 77 with the fitted model.

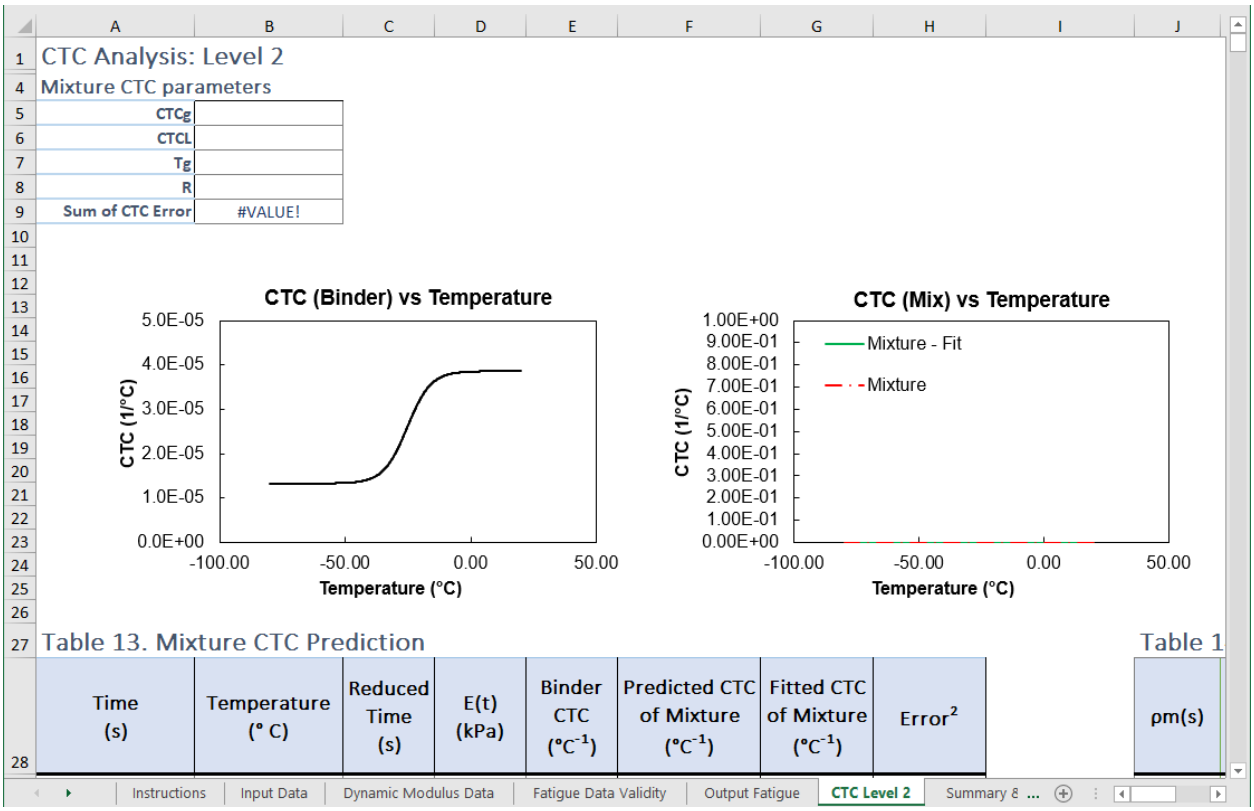

Source: FHWA.

Figure 78. Screenshot. FlexMAT "CTC Analysis: Level 2" model overview screen.

Level 3 has a similar approach to level 2, except instead of using the measured binder CTC coefficients as inputs, these inputs are estimated using the low-temperature PG of the binder. The inputs for this level are the VMA, G_{sb}, CTC of the aggregate, and low-temperature PG of the binder.

The CTC behavior of the binder is approximated by assuming the constants given in table 32. constant values for ctc parameters in level 3 analysis..

Table 32. Constant values for CTC parameters in level 3 analysis.

CTC Model Coefficient	Estimated Value
CTC_g	0.003
CTC_L	0.006
R	6
T_g	−40 °C for low PG = −40 −25 °C for −34 ≤ low PG ≤−22

When the analysis is complete, the user is redirected to the "CTC Analysis: Level 3" screen where the results of the fitting procedure, shown in figure 79, can be used for visual verification of the fitting validity and assumed CTC behavior.

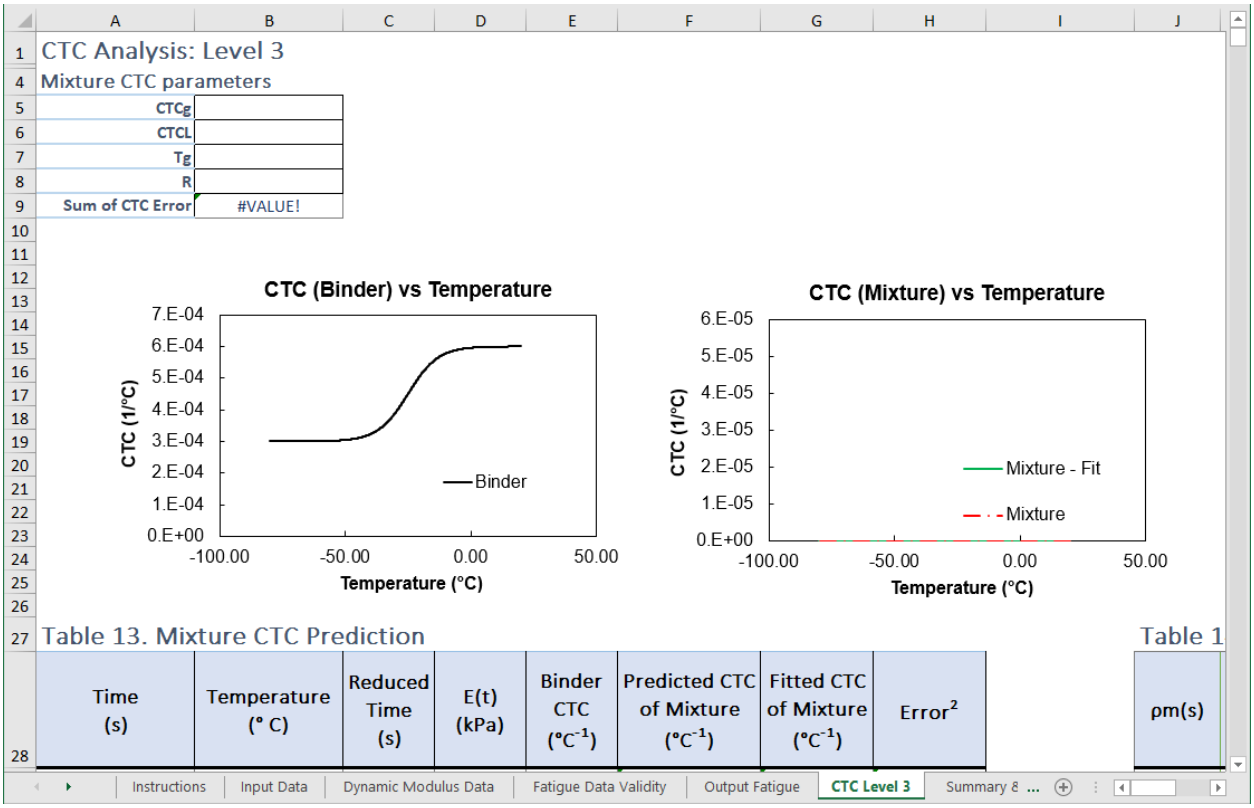

Source: FHWA.

Figure 79. Screenshot. FlexMAT "CTC Analysis: Level 3" model overview screen.

Aging

The aging analysis in FlexMAT, similar to the CTC analysis, also presents a hierarchical structure of input.[5] Three input levels can be used to calibrate the aging models, as shown in figure 80. These levels have different experimental procedures and analysis demands, but their final goal is to provide the calibrated coefficients used in the PAM and the AMAC model. These models and procedures are a product of NCHRP 09-54.[17]

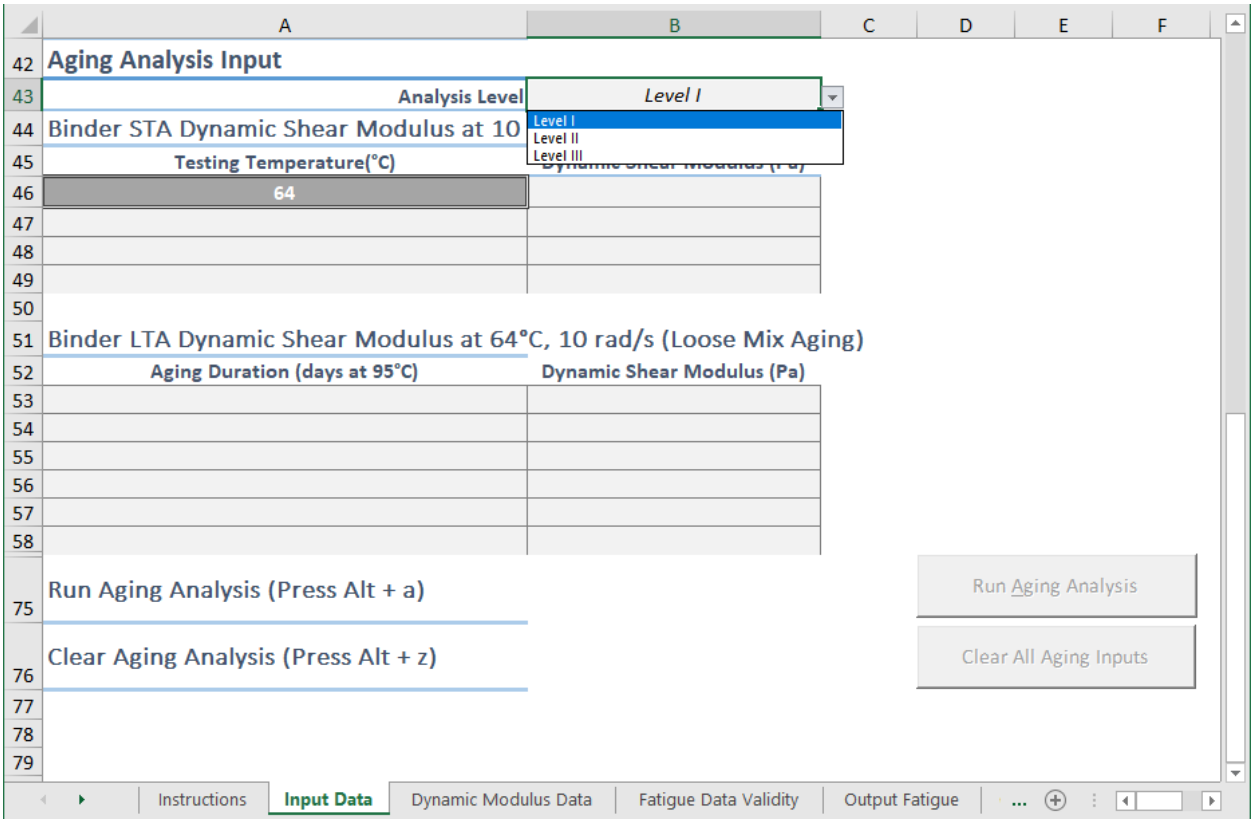

Source: FHWA.

Figure 80. Screenshot. FlexMAT "Aging Analysis Input" screen.

Ultimately, the goal of the aging analysis calibration is to output the following three parameters:

- The aging susceptibility parameter (M).
- The binder's log($|G^*|$) at STA conditions, at 64 °C, tested at 10 rad/s.
- The time aging parameter (c).

Each level uses a different approach to determine these three parameters.

Level 1 is the most accurate method for determining the aging analysis output, but level 1 is also the most intensive in terms of laboratory work. The background calculations in FlexMAT are based on the following steps:[5]

- Step 1. Calculate the t-TS factors for a reference temperature of 64 °C. For this step, the same procedure described for the characterization of dynamic modulus is used, in which a combination of the sigmoidal function and the shifting of the reduced frequencies is used in the fitting procedure (see equations 115 and 116).

- Step 2. With the shift factor function calibrated, calculate the time aging parameter (c) as the slope of the linear regression through the origin of the logarithmic value of the shift factor at the tested temperatures and the logarithmic difference between measured $|G^*|$ at the test temperature and $|G^*|$ at the reference temperature (64 °C). Figure 81 illustrates this step.

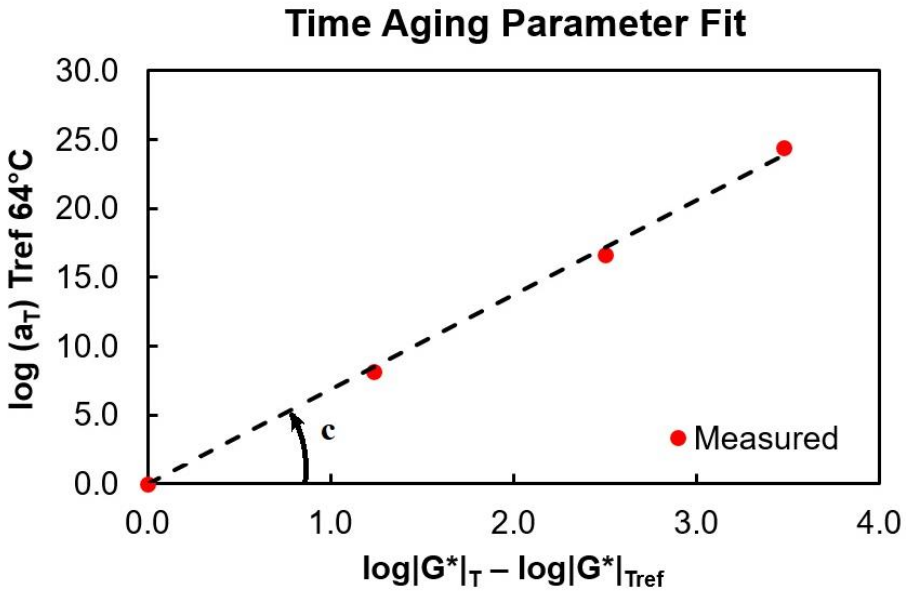

Source: FHWA. FlexMAT generated chart.

Figure 81. Graph. Time aging parameter determination example.

- Step 3. Fit the aging susceptibility parameter using the experimental data of the tested binder with at least 3 d. The model calibrated for finding M is given in equation 134 and is referred to as the kinetics model.

$$\log\left(\left|G^*\right|_t\right) = \log\left(\left|G^*\right|_0\right) + M\left[\left(1-\frac{k_c}{k_f}\right)\left(1-e^{-k_f t}\right)+k_c t\right] \quad (134)$$

$$k_c = 3.68 \times 10^7 \times e^{\left(\frac{-62.21}{0.008314 \times T}\right)} \quad (135)$$

$$k_f = 1.25 \times 10^3 \times e^{\left(\frac{-95.04}{0.008314 \times T}\right)} \quad (136)$$

Where:

$|G^*|_t$ = aged dynamic shear modulus at time t (kPa).
$|G^*|_0$ = dynamic shear modulus at STA condition (kPa).
M = aging susceptibility parameter.
t = time (days).
T = temperature (K).

Figure 82 presents an example of the fitting of M.

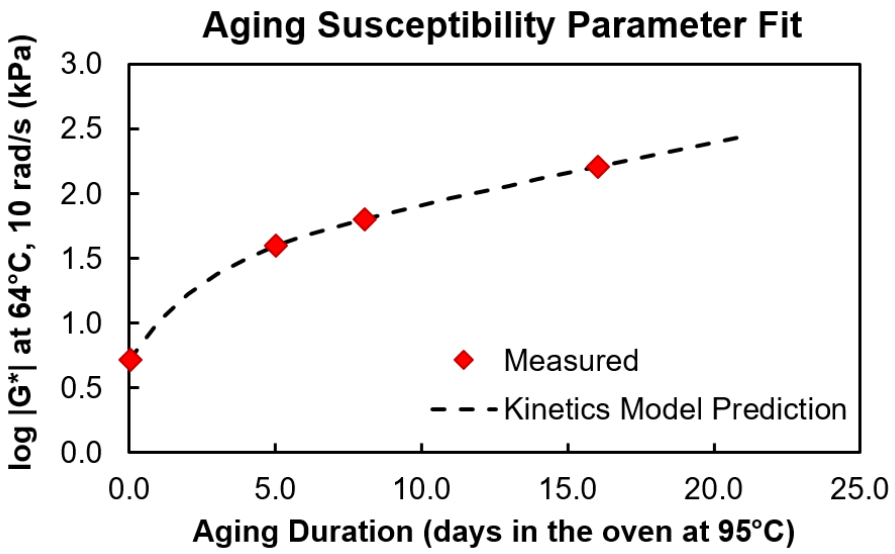

Source: FHWA. FlexMAT generated chart.

Figure 82. Graph. Aging susceptibility parameter fit in level 1 analysis.

Once the analysis procedure is complete, the active screen is redirected to the "Aging Analysis: Level 1" screen in figure 83 where details of the characterization procedure can be verified.

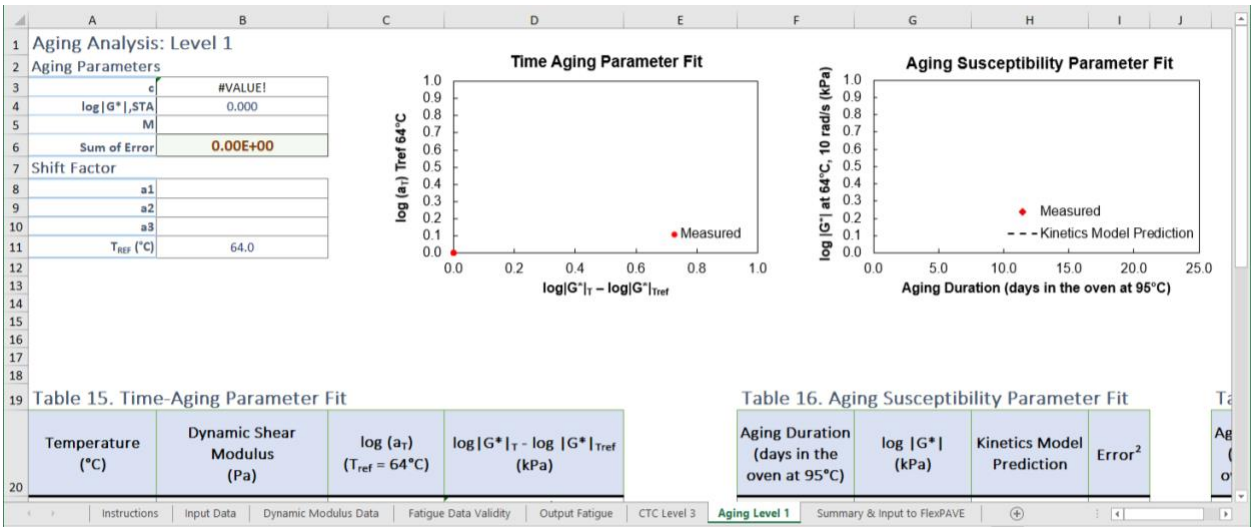

Source: FHWA.

Figure 83. Screenshot. FlexMAT "Aging Analysis: Level 1" model overview screen.

Level 2 is a balanced approach in terms of performance accuracy and lab effort. Level 2 requires RTFO aging and 40 h (double) of PAV aging of the binder before modulus testing the mixture's virgin binder. This level requires an additional step if the mixture contains any RAP. The steps in this level's characterization are as follows:

- Step 1. Follow the same instructions as step 1 of level 1. Calibrate the shift factors at a reference temperature of 64 °C.

- Step 2. Follow the same instructions as step 2 of level 1. Calculate *c* by fitting a linear curve to the shift factor behavior as a function of the binder's shear modulus difference using the reference temperature of 64 °C. If the mixture contains any RAP, however, *c* is no longer a fitted parameter and is considered a constant with the value of 1.710.

- Step 3: Follow similar instructions to step 3 of level 1, except use short-term aging (0 d) and PAV (2 d) and double PAV (6 d) aging of the binder for fitting *M*. The prediction of aging durations longer than double PAV aging is given in equation 137. Figure 84 presents the prediction of the modulus for the fitting procedure for 10, 14, and 18 d beyond the actual measured points.

$$\log\left(\left|G^*\right|_t\right) = \log\left(\left|G^*\right|_{2\times PAV}\right)(1.0264)^{t-6} \tag{137}$$

Where:

$|G^*|_t$ = aged dynamic shear modulus at time t (kPa).
$|G^*|_{2xPAV}$ = aged dynamic shear modulus after double PAV procedure (kPa).
t = time (days) for $t > 6$ d.

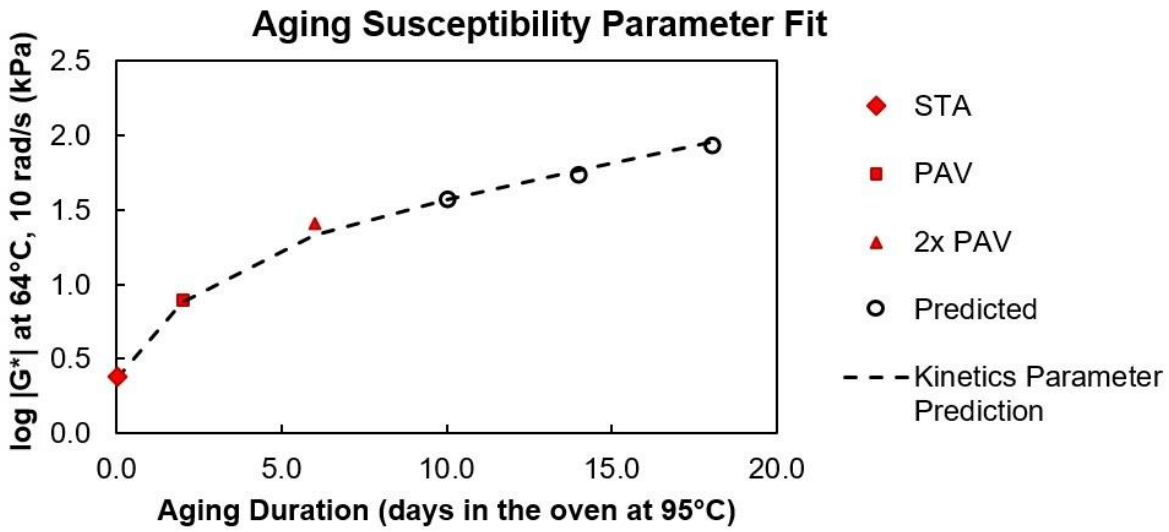

Source: FHWA. FlexMAT generated chart.

Figure 84. Graph. Aging susceptibility parameter fit in level 2.

Figure 85 shows the "Aging Analysis: Level 2" screen for no RAP and the calibrated models.

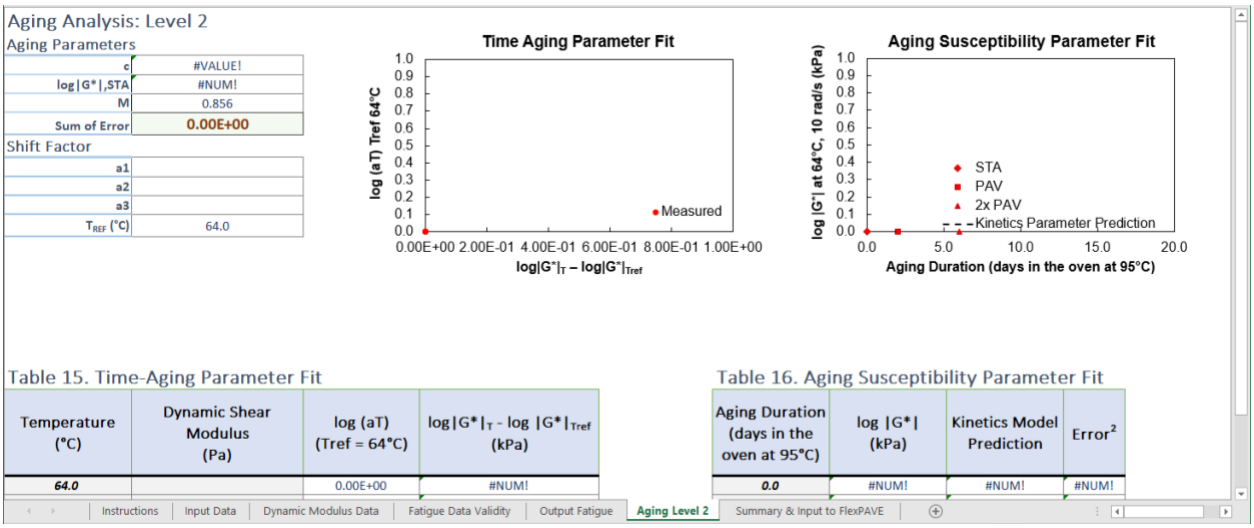

Source: FHWA.

Figure 85. Screenshot. FlexMAT "Aging Analysis: Level 2" (no RAP) model overview screen.

This step requires an adjustment for mixes with RAP whereby the described procedure up to this point used to calibrate the *M* parameter for the virgin binder is used for the adjustments in the RAP portions, given in equations 138 through 141. When the analysis with RAP content is complete, the "Aging Analysis: Level 2 (with RAP)" screen is activated, as shown in figure 86.

$$\log\left(\left|G^*\right|_{STA,RAP}\right)=0.0217\left(e^{0.0514\times HPG_{RAP}}\right)$$

(138)

$$M_{RAP}=\frac{0.94}{1+\left(\frac{HPG_{RAP}}{82.68}\right)^{7.96}}$$

(139)

$$\log\left(\left|G^*\right|_{STA,mix}\right)=\left(1-RBR\right)\log\left(\left|G^*\right|_{STA,bind}\right)+RBR\times\log\left(\left|G^*\right|_{STA,RAP}\right)$$

(140)

$$M_{mix}=\left(1-RBR\right)M_{bind}+RBR\times M_{RAP}$$

(141)

Where:

$|G^*|_{STA,RAP}$ = aged dynamic shear modulus of the RAP binder at STA condition (kPa).
$|G^*|_{STA,bind}$ = aged dynamic shear modulus of the virgin binder at STA condition (kPa).
$|G^*|_{STA,mix}$ = aged dynamic shear modulus of the mix's binder at STA condition (kPa).
HPG_{RAP} = RAP binder HPG.
M_{RAP} = aging susceptibility parameter of RAP binder.
M_{bind} = aging susceptibility parameter of virgin binder.
M_{mix} = aging susceptibility parameter of the mix's binder.
RBR = reclaimed binder ratio.

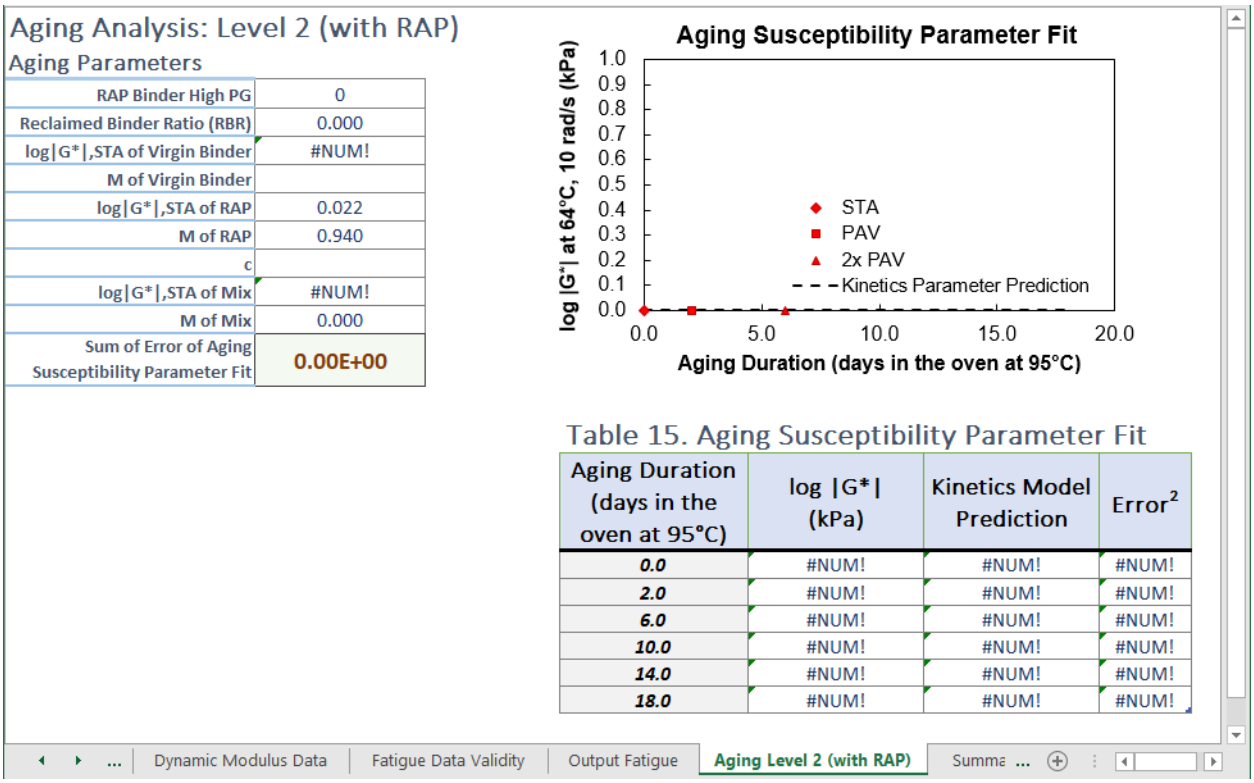

Source: FHWA.

Figure 86. Screenshot. FlexMAT "Aging Analysis: Level 2 (with RAP)" model overview screen.

Level 3 is the simplest level of the aging framework in FlexMAT and does not require any laboratory effort.(5) Although the accuracy of this method is restricted, level 3 may become an attractive approach for agencies or contractors that do not have resources for accurate aging behavior predictions and the lab characterization associated with such work. This level 3 approach uses the following steps:

- Step 1. Assume the time aging parameter, c, is constant, regardless of the presence of RAP in the mixture.

- Step 2. Calculate the aging susceptibility parameter, M, of the mixture using equation 141 where M_{RAP} is calculated using equation 139 and M_{bind} is calculated using equation 142.

$$M_{bind} = \frac{0.94}{1+\left(\frac{HPG_{bind}}{82.68}\right)^{7.96}} \quad (142)$$

Where:

HPG_{bind} = virgin binder HPG.

M_{bind} = aging susceptibility parameter of the virgin binder.

- Step 3. Calculate the dynamic shear modulus of the mixture's binder at the STA condition using equation 140, where the dynamic shear modulus of the RAP's binder can be obtained through equation 138 and the virgin binder's dynamic shear modulus at STA condition through equation 143.

$$\log\left(\left|G^*\right|_{STA,bind}\right) = 0.0217\left(e^{0.0514\times HPG_{bind}}\right) \quad (143)$$

Where:

$|G^*|_{STA,bind}$ = aged dynamic shear modulus of the virgin binder at STA condition (kPa).
HPG_{bind} = virgin binder's HPG.

Without RAP in the mixture, the reclaimed binder content is zero, and the prediction for the mix characteristics becomes the virgin binder's prediction.

Permanent Deformation

To initialize FlexMAT analysis of permanent deformation, the user must select the number of specimens tested at each temperature by choosing one of the available numbers from the list in cells B3 and B4 of the data input screen in figure 87.[5] After the number of specimens is selected, select the overarching folder in which the data files are stored by clicking the "Load High Temperature Data" button for specimens tested at high temperatures or the "Load Low Temperature Data" button for specimens tested at low temperatures. These buttons are displayed once the number of specimens is selected.

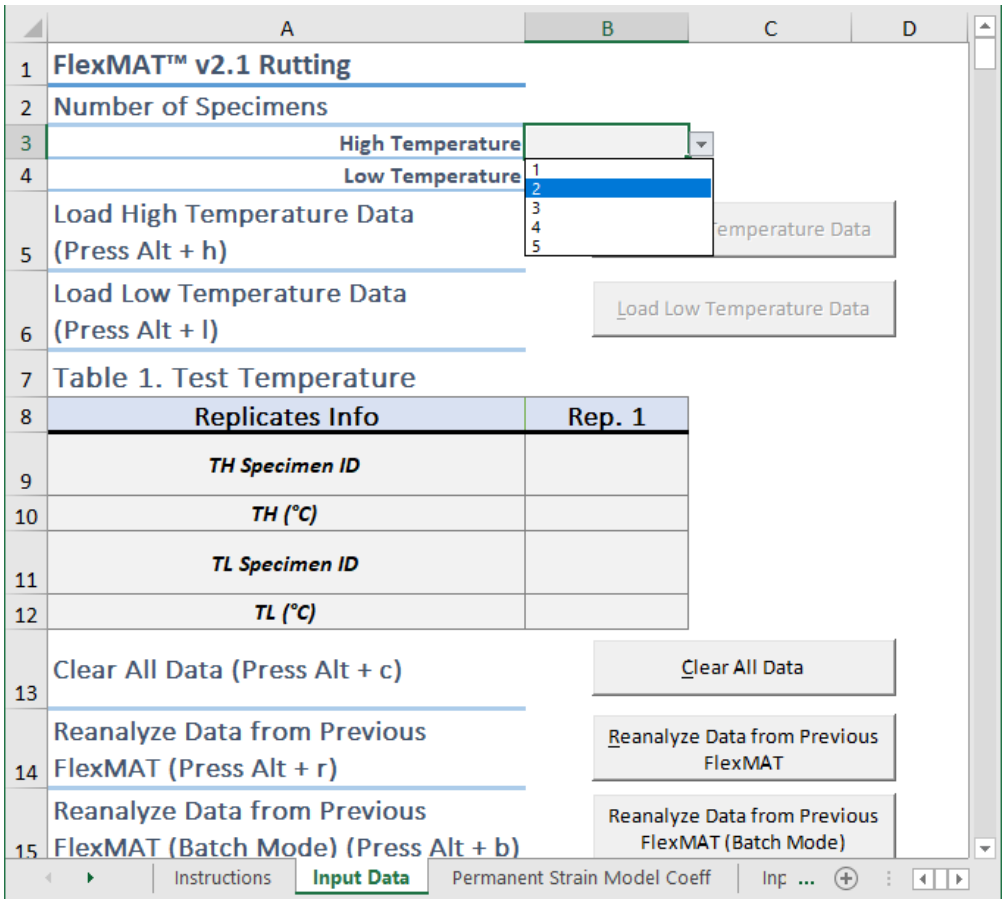

Source: FHWA.

Figure 87. Screenshot. "FlexMAT™ v2.1 Rutting" SSR input screen.

The order of selection of the files is not relevant to the results, but the analysis procedure will initialize once both temperature levels are selected. Two graphs are presented in the "Input Data" screen:

- "Permanent Strain, High Temperature," which shows the vertical permanent strain accumulation during the cycle evolution of the SSR test for high temperature testing.
- "Permanent Strain, Low Temperature," which shows the vertical permanent strain accumulation during the cycle evolution of the SSR test for low temperature testing.

These graphs are updated once the data are input into FlexMAT using individual specimen information.[5] Selecting data for either of the temperatures also updates the information in the "Table 1. Test Temperature" table for the corresponding temperature data that have been added with the individual specimen test temperature and given specimen identification (if present) during testing.

The permanent deformation model used for rutting characterization is the shift model, presented by Kim and Kim.[146] The shift model uses a combination of two test temperatures (high and low) and three loading levels (high, intermediate, and low) to predict the material's behavior under

varying conditions of stress, loading time, and temperature. The shift model characterized in FlexMAT is given by equations 102 to 107.[5] Even though the parameters in these equations are numerous, only eight coefficients, ε_0, N_1, β, p_1, p_2, d_1, d_2 and T_{ref}, are sufficient for the shift model characterization; these coefficients are the coefficient outputs from FlexMAT Rutting.

The idea behind the shift model is the application of shift factors for temperature and load levels so that an equivalent number of cycles in the reference condition can be calculated. Equation 144 is a simplification of equation 103 and reflects this concept, presenting a combined shift factor for the conditions.

$$N_{red} = N \times 10^{a_{tot}} \tag{144}$$

Where:

N_{red} = reduced number of cycles at reference loading conditions.
N = physical number of cycles of a certain loading condition.
a_{tot} = shift factor for selected stress and temperature conditions.

Details concerning the calculations and fitting of the shift model can be found in the "Permanent Strain Model Coeff" screen in figure 88, which is automatically activated once the analysis is complete. The "Permanent Strain Model Coeff" screen is a busy screen, with multiple tables used in the fitting and calculations that are necessary in the shift model calibration. The shift model coefficients, although present on this screen, are also given in a summarized fashion in the "Input to FlexPAVE" screen for simplicity of reading.[6] Typically, the most important information that is uniquely given in this screen is the "Measured Vs Predicted Permanent Strain" graph, which provides the average specimen permanent deformation behavior at each temperature and the respective calibrated shift model prediction.

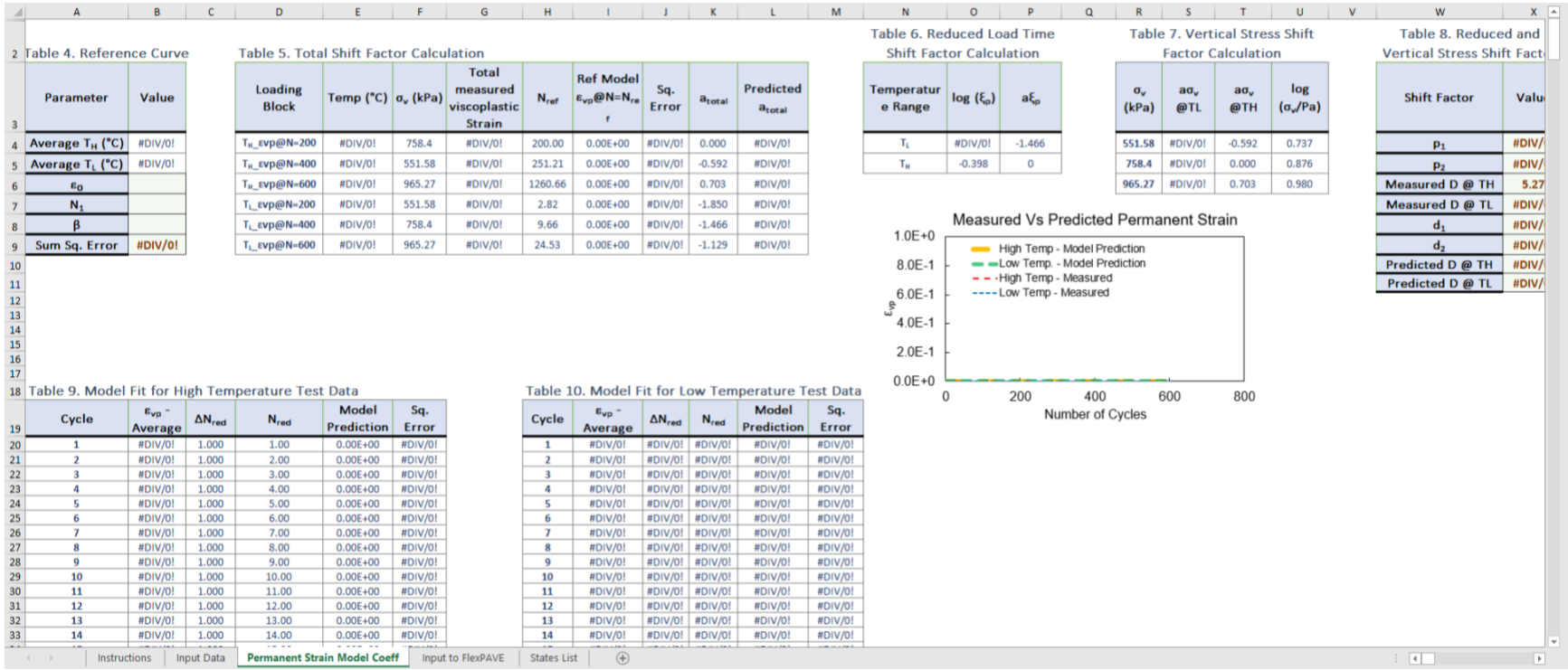

Source: FHWA.

Figure 88. Screenshot. FlexMAT shift model overview screen.

The calculation of the shift model coefficients based on the elements shown on the screen involves the following steps:

- Step 1. Calculate the reference temperature (T_{ref}) as the average of the temperatures tested for the high temperature determination, T_H.

- Step 2. Calculate the best fitting values for ε_0, N_1, and β of equation 103 by minimizing the cumulative squared error between the observed vertical permanent strain (averaged between specimens for each cycle) and predicted vertical permanent strain values using equation 145 for high temperature determination and initial 200 cycles (intermediate stress level) of the test.

$$Error^2 = \sum_{i=1}^{200} \left(\varepsilon_{vp,i} - \hat{\varepsilon}_{vp,i} \right)^2 \tag{145}$$

Where:

$\varepsilon_{vp,i}$ = observed vertical permanent strain.
$\hat{\varepsilon}_{vp,i}$ = predicted vertical permanent strain.

The minimization technique applied is the standard "GRG Non-Linear" of the Microsoft Excel Solver application, which uses the default configuration of the 2016 version.(24) The initial values adopted for the fitting procedure are in table 33**Error! Reference source not found.**. This condition, which uses the high temperature level and intermediate stress level, will be treated as the reference condition for the shift model in the following calculations.

Table 33. Initial values for vertical permanent strain fitting procedure.

Fitting Coefficients	Initial Value
ε_0	0.002
N_1	2
β	0.75

- Step 3. Calculate the last reduced cycle, N_{red}, for the other stress levels and temperature using the same standard Microsoft Excel Solver configuration to reduce the squared error between the observed and predicted vertical permanent strain for the cycles and temperature levels given in table 34 and using the initial values provided in the "Initial Value" column and fitting N_{red} of equation 102 using the previously calibrated ε_0, N_1, and β.(24)

Table 34. Initial values for reduced cycles fitting procedure.

Cycle (*N*)	Temperature Level	Initial Value for Last Reduced Cycle
400	High	100
600	High	100
200	Low	0.5
400	Low	0.1
600	Low	0.1

The objective function of step 2 takes the cumulative squared error described in equation 145. In step 3, the objective function takes the squared error of a single point, which is the last cycle of each stress level. For the reference condition (high temperature level and intermediate stress), N_{red} is 200.

- Step 4. Calculate the shift factor for each stress condition at both temperatures using equation 146.

$$a_{\sigma y,n} = \begin{cases} \log\left(\frac{N_{red,n}}{200}\right), \text{ for n = 1} \\ \log\left(\frac{N_{red,n} - N_{red,n-1}}{200}\right), \text{for n = 2 or 3} \end{cases} \quad (146)$$

Where:

$a_{\sigma v}$ = vertical stress shift factor.
N_{red} = reduced number of cycles at reference loading conditions.
n = stress level for selected temperature level.

- Step 5. Calculate the reduced load time shift factors and reduced load times for each temperature level, given by equations 147 and 148, respectively.

$$a_{\xi_p} = a_{\sigma_y,\text{intermediate}} \quad (147)$$

$$\xi_p = \frac{0.4}{10^{\left(0.000642\times\left(T^2 - T_H{}^2\right) + 0.15649\times\left(T - T_H\right)\right)}} \quad (148)$$

Where:

$a_{\xi p}$ = reduced load time shift factor.
$a_{\sigma v,\ intermediate}$ = vertical stress shift factor for the intermediate stress condition.
ξ_p = reduced load time.
T = tested temperature of interest (°C).
T_H = tested high temperature (°C).

If the temperature of interest is the tested high temperature, $a_{\xi p}$ and $a_{\sigma v}$ are 0, and ξ_p becomes 0.4 s, which is the pulse time, then the reference condition is verified. For details regarding pulse and rest periods, see Kim and Kim.[146].

- Step 6 calculates p_1 and p_2 using equation 105 and d_1 and d_2 using equation 107, given the shift factors calculated in step 5, for each temperature.

All the parameters needed for the calibration of the shift model are determined and summarized in the "Input to FlexPAVE" screen.

Like S_{app} for FlexMAT Cracking, the RSI is the index output for FlexMAT Rutting.[15,16,138] The RSI is an alternative output of FlexMAT in the sense that RSI is not a material property.[5] However, as an index, RSI provides valuable information to evaluate the characterized mix's performance given the climatic condition and predefined structural position of the mix (i.e., surface, intermediate, or base layer). The RSI is defined as the simulated average permanent strain for 20 yr of traffic with 30 MESALs applied and a design speed of 96 km/h. For details regarding RSI calculations, see Ghanbari et al.[138]

Calculating the RSI via FlexMAT requires the definition of three inputs:

- "State" in cell B20 will update the available list of cities for selection in cell B21.
- "City" in cell B21 will be used to determine the temperature profile for the RSI calculation.
- "Layer Type" in cell B22 will be used to determine the stress profile in the RSI calculation.[5]

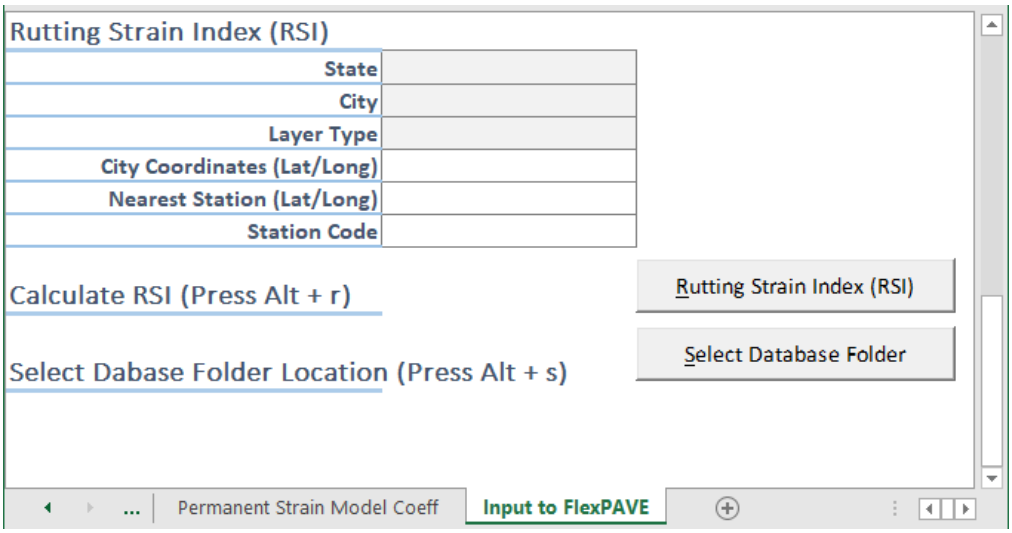

Source: FHWA.

Figure 89. Screenshot. FlexMAT RSI calculation inputs screen.

Temperature is known to be a commanding factor of pavement stiffness, so to calculate RSI values and incorporate realistic climatic conditions, FlexMAT uses a summarized database of temperature profiles with 2,798 stations throughout the United States.[5] The summarized climatic data include the estimated temperature for every 1-inch depth of a generic asphalt concrete structure up to 10 inches thick. These characteristics were estimated using MERRA2 station information gathered from LTPP Bind™ and the EICM.[12–14] The final summary file for each station contains historical temperature information (in Fahrenheit) for each depth of the pavement for 20 yr (January 1996 to December 2015). To reduce the size of the database, each depth has a reported temperature that is averaged monthly and averaged again into three segments: 7 p.m. to 5 a.m., 5 a.m. to 12 p.m., and 12 p.m. to 7 p.m.

Figure 90 presents a screenshot of one of the summary files. Each row contains the monthly average temperature (in degrees Fahrenheit) data for one segment and for each of the evaluated depths.

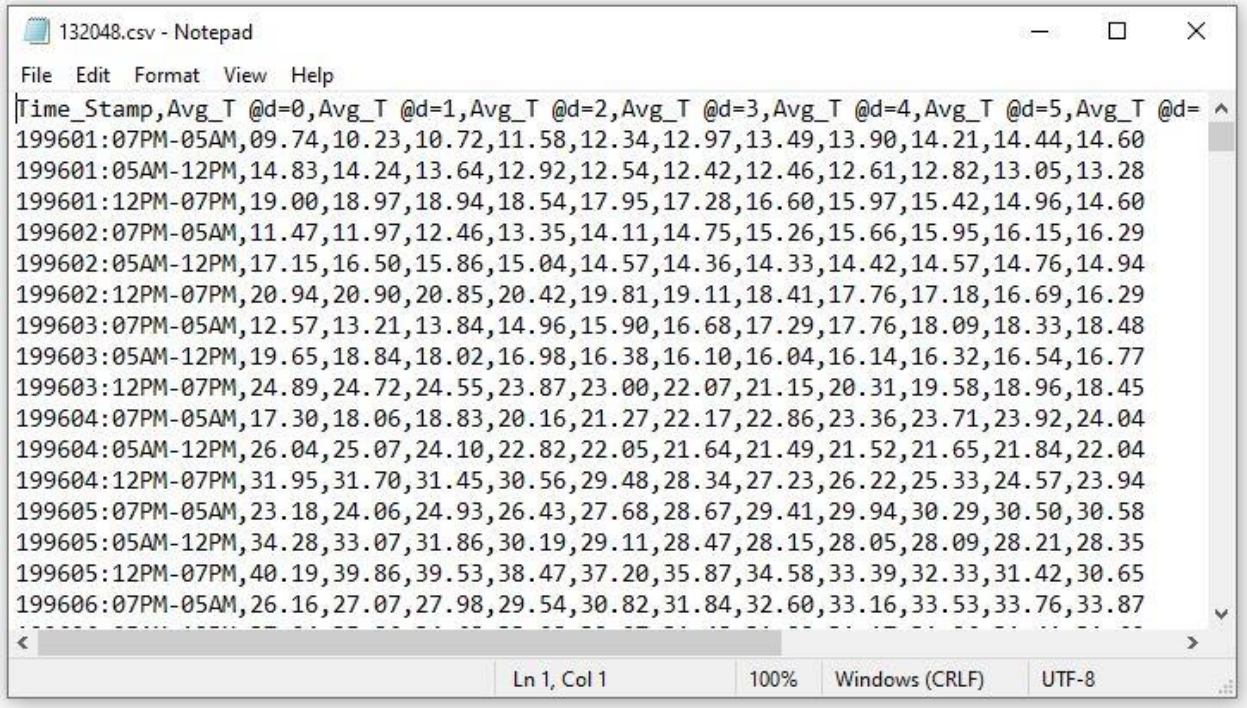

Source: FHWA.

Figure 90. Screenshot. Temperature database file sample for RSI calculations.

When all the required inputs are present, click the "Rutting Strain Index (RSI)" button on the "Input to FlexPAVE" screen to initialize the RSI calculation. Once completed, the RSI calculation normally takes only a few seconds to activate the "Rutting Index Parameter" screen in figure 91. The calculated RSI value is displayed in cell B5.

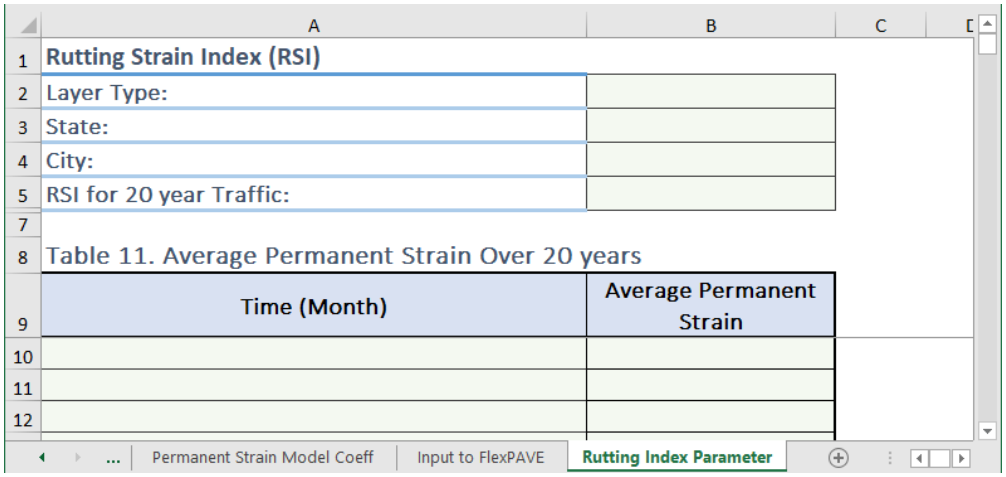

Source: FHWA.

Figure 91. Screenshot. FlexMAT "Rutting Strain Index (RSI)" calculation screen.

FlexMAT Outputs

FlexMAT Cracking and FlexMAT Rutting have dedicated tabs, "Summary and Input to FlexPAVE" and "Input to FlexPAVE", respectively, for summarizing all the calibrated coefficients.[15,16] Table 35 presents a compilation of the coefficients calibrated in FlexMAT Cracking, with the source of calibration, type of characterization location in the summary tab, and adopted symbols.

Table 35. Summary of characterized coefficients in FlexMAT Cracking.

Analysis Source	Characterization	Location	Number of Coefficients	Coefficients
Dynamic modulus test	Time-temperature superposition	Cells B9–B12	4	T_{ref}, a_1, a_2, a_3
Dynamic modulus test	2S2P1D	Cells B15–B21	7	δ, k, h, β, E_{00}, E_0, $\log(\tau_E)$
Dynamic modulus test	Prony series	Cells A25–B41	34	T_i, E_i (i = 1, 2, 3, … , 17)
Dynamic modulus test	Damage evolution rate factor	Cell E15	1	α
Cyclic fatigue test	Damage characteristic curve	Cells E15 and E16	2	C_{11}, C_{12}
Cyclic fatigue test	Failure criterion	Cell E20	1	D^R
*Output fatigue tab	Damage capacity index	Cell E22	1	S_{app}
Cyclic fatigue test	Dissipated pseudostrain energy	Cell E34–F37	8	a_i, b_i (i = 1, 2, 3, 4)
CTC analysis	CTC model	Cell E24–E27	4	CTC_g, CTC_L, T_g, R
Aging analysis	PAM and AMAC	Cell E29–E31	3	c, $\log\|G^*\|_{STA}$, M

*Calculation is dependent on user-defined inputs during FlexMAT analysis using the "Output Fatigue" screen.

The information presented in table 35 is found in FlexMAT Cracking in the "Summary and Input to FlexPAVE" screen in figure 92.[15]

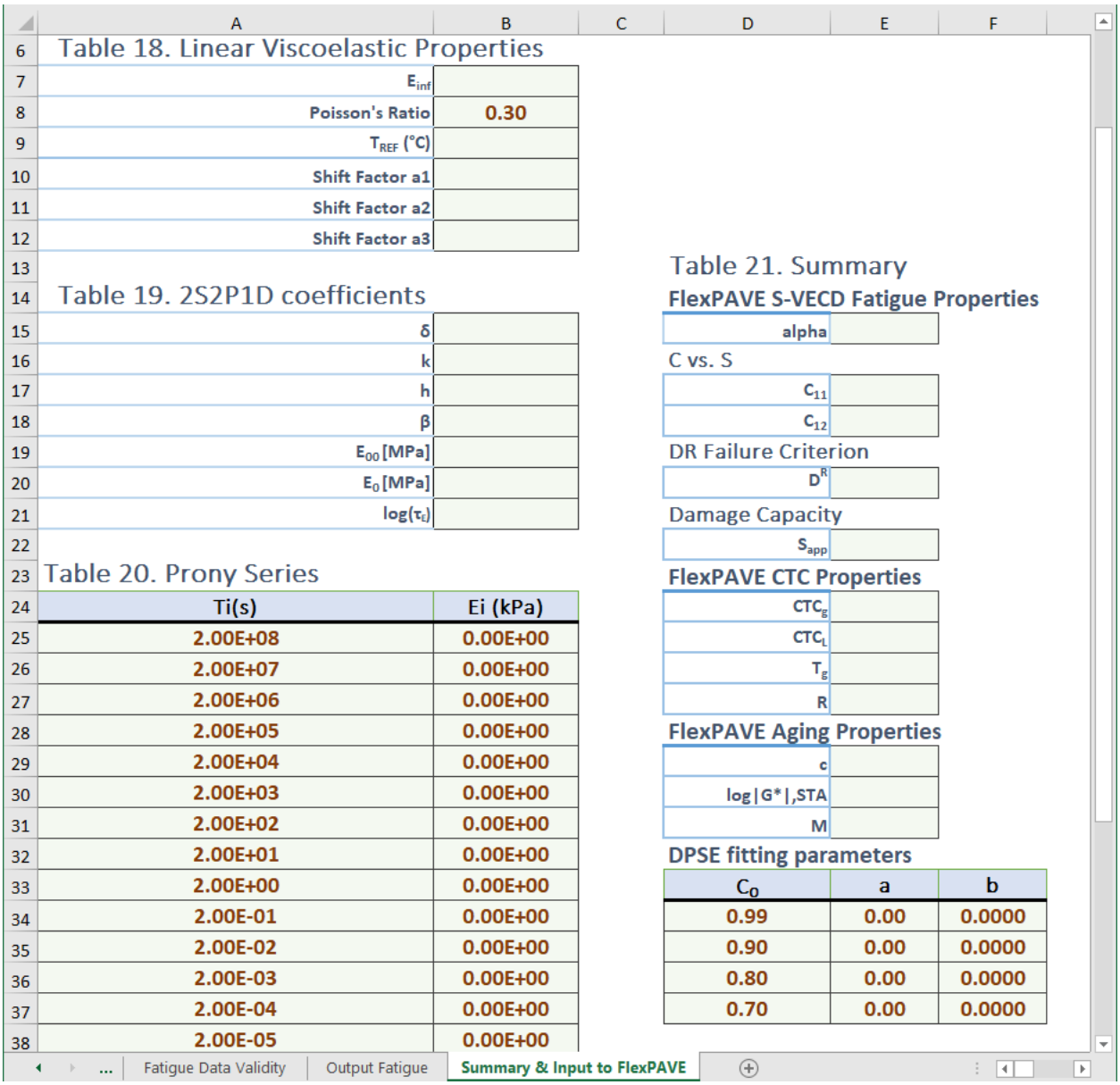

Source: FHWA.

Figure 92. Screenshot. FlexMAT Cracking coefficients summary screen.

Table 36 presents a compilation of the coefficients calibrated in FlexMAT Rutting, with the calibration source, characterization type, location in the summary tab, number of coefficients, and adopted symbols.[16]

Table 36. Summary of characterized coefficients in FlexMAT Rutting.

Analysis Source	Characterization	Location	Number of Coefficients	Coefficients
SSR test	Shift model	Cells B4, B5, B6, B9, B10, B13, B14 and B16	8	ε_0, N_1, β, p_1, p_2, d_1, d_2, T_{ref}
*Input to FlexPAVE tab	RSI	"Rutting Index Parameter" tab, Cell B5	1	RSI

*Calculation is dependent on user-defined inputs during FlexMAT analysis on the "Input to FlexPAVE" screen.

The information described in Table 36 is found in FlexMAT Cracking on the "Summary and Input to FlexPAVE" screen in figure 93.[15]

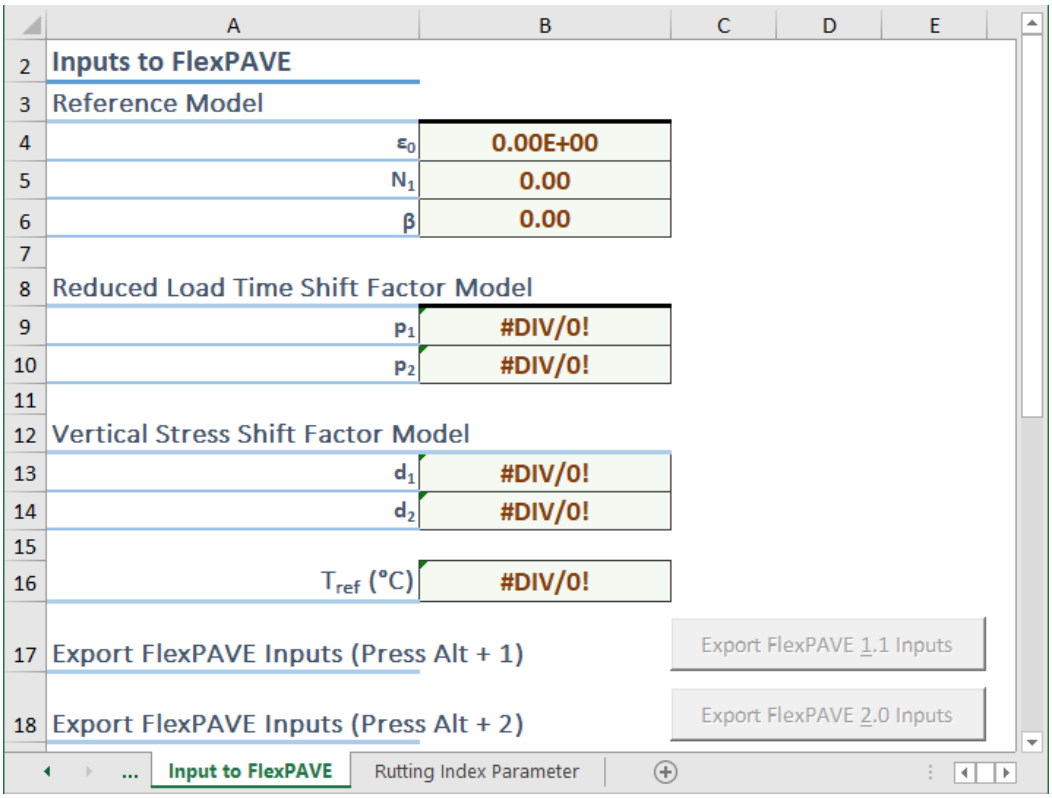

Source: FHWA.

Figure 93. Screenshot. FlexMAT Rutting coefficients summary screen.

Note the two unavailable "Export FlexPAVE 1.1 Inputs" and "Export FlexPAVE 2.0 Inputs" buttons in figure 93. These buttons are also present in the FlexMAT Cracking summary tab.[15] These buttons export a file that is compatible with FlexPAVE software, contains the existing index values, and becomes available when the characterizations are complete.[6]

One previously unmentioned feature of FlexMAT Cracking is the "Table 22. Dynamic Modulus" table, which is in the "Summary and Input to FlexPAVE" tab.[15] The user can generate a table with a selection of frequencies and temperatures to obtain the dynamic modulus value of the

characterized mixture calculated using the 2S2P1D model calibrated for the given conditions. This table was created for compatibility with AASHTOWare™ Pavement ME Design software, which takes as input a table in a similar format for dynamic modulus property input. Figure 94 presents an overview of this utility.[18]

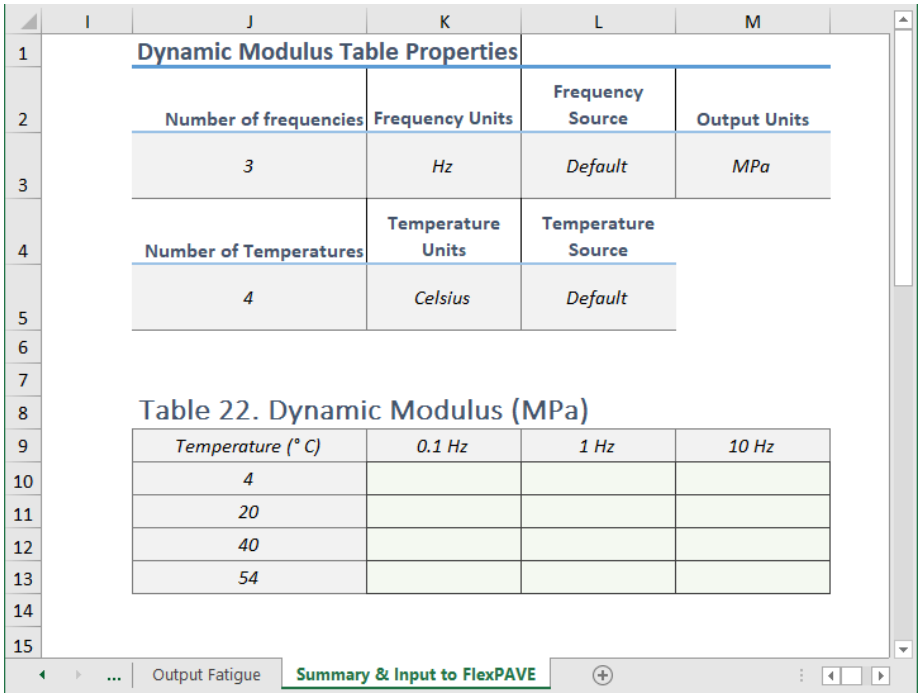

Source: FHWA.

Figure 94. Screenshot. FlexMAT Cracking dynamic modulus calculation table.

This table can be customized by modifying the selection of the cells J3 to M3 and J5 to L5 in six possible ways:

- Use cell J3 to select any number of frequencies between three and six and automatically adjust the table to the selected number, adding or removing frequencies as needed.
- Use cell J5 to select between three and eight temperatures.
- Use cell K3 to select a frequency unit, “Hz” or “rad/s.”
- Use cell K5 to select the temperature unit, “Celsius” or “Fahrenheit.”
- Use cells L3 and L5 to select default values for frequencies or temperatures or to enable user-defined values that the user can modify.
- Use cell M3 to modify the dynamic modulus’ output unit, MPa or psi.

CHAPTER 5. STRUCTURAL MODEL ADVANCEMENT

DEVELOPMENT OF PRELIMINARY TRANSFER FUNCTIONS FOR PERFORMANCE PREDICTIONS IN FLEXPAVE VERSION 1.1

Mechanistic-empirical design and PRS are state-of-the-art tools for designing pavements and determining incentives/disincentives for paving contracts. These methods require the reliable prediction of pavement performance throughout the pavement's design life. One such prediction program is FlexPAVE, which applies three-dimensional viscoelastic finite element analysis with moving loads to calculate the pavement's mechanical responses (stress and strain) under prescribed loading, environmental and climatic, and structural conditions.[6] The direct tension cyclic fatigue test and the S-VECD model are employed to address fatigue cracking and the SSR test and the permanent strain shift model are used to address rutting.[72,147,148] Several studies have shown that the predicted FlexPAVE results match field observations in terms of ranking the cracking and rutting severity of field sections. (See references 122 and 149–151.) However, to produce pavement designs or to determine incentives and disincentives for PRS, ranking the performance of the materials and pavement sections is not enough h. Accurate predictions of pavement distress over time are needed.

With regard to fatigue damage, a fatigue transfer function is needed to convert the computed cross sectional damaged area (i.e., the damage level) to the cracked area on the pavement surface. With regard to rut depth, a rutting transfer function is needed to calibrate the predicted rut depths. In this section, preliminary transfer functions for the predicted fatigue damage and rut depths are developed using four sets of field measurement data obtained from test sections in the United States, Canada, and South Korea that include interstate highways and an accelerated testing facility. (See references 11, 21–23, and 64.) Good agreement between the predicted performance and field observations was found after the calibration of FlexPAVE.[6]

Two major challenges are involved in accurately predicting a pavement distress as a function of time. The first is differences in the loading and environmental conditions between laboratory testing and field testing. This factor is particularly important in the case of rutting where the principal stress rotation and variations in overall stress state occur due to the passing wheel load but are not considered directly in laboratory tests and modeling. The other challenge is specific to fatigue cracking predictions. The fatigue damage used in FlexPAVE is calculated based on the pavement's cross section, i.e., the x-z plane of the pavement structure where z is the depth, y is the travel direction, and x is transverse to the travel direction.[6] However, in the field, fatigue performance is measured from visible cracking on the pavement surface, i.e., the x-y plane. The approach that has been taken in pavement engineering practice to overcome this limitation is to employ so-called transfer functions that are empirical calibration functions introduced as the final step in the distress prediction process. The definition of the transfer function used in FlexPAVE is similar to that used in the Pavement ME Design software.[18] In Pavement ME, the transfer function converts the computed damage level at a critical point in the pavement's cross section to the percentage of the cracked area on the pavement surface.[152] The transfer function used for rutting in Pavement ME also corrects for the imprecise stress state and loading rate considerations with depth, and this correction factor is applied to the mechanistic model predictions of permanent strain in the various layers.

The preliminary transfer functions for fatigue cracking and rut depth predictions are developed using 39 pavement sections from 4 field projects: 5 sections from the NCAT test track in Alabama (data are from the NCAT's 2009 research cycle), 14 sections from the 2016 MnROAD project in Minnesota, 4 sections from the MIT test road in Manitoba, Canada, and 16 sections from the Korean Expressway Corporation (KEC) test road in Yeoju, South Korea. (See references 11, 21–23, and 64.)

Performance Predictions Using FlexPAVE

The FlexPAVE prediction model follows four basic steps.[6] First, the user collects and inputs the required material, structural, and climatic data. FlexPAVE then calculates the pavement's mechanical responses, i.e., the stress and strain, using the three-dimensional finite element method under the load of moving tires. The program divides each pavement layer, including asphalt layers, unbound aggregate layers, and subgrade layers, into ten sublayers to perform the finite element analysis. Fast-Fourier transform is used in this step to accelerate the computation. Next, the calculated responses are used in the fatigue damage and rut depth prediction models. The S-VECD model is used to compute the damage in the asphalt layers. The damage evolution at each time interval from the beginning of the simulation until the end of the design period can be calculated using given traffic loads and estimated traffic volumes. To take the on-site climate conditions into account, the program is integrated with a pavement temperature database that is prepopulated from simulations that utilize hourly climatic data (temperature, precipitation, wind speed, and percentage of sunshine) in the EICM.[13] Temperature variations throughout the year are taken into account by dividing the analysis into months. Variations throughout the day are determined by dividing the monthly temperatures into one of three periods: morning-to-midday, midday-to-evening, and evening-to-morning. The periods at the same times of each day within a month are combined into a segment, and each month is considered a life stage. Thus, a 20-yr simulation contains 240 life stages (12 × 20) and each of these life stages has three separate temperature profiles that are considered for the pavement response and damage predictions.[147,150]

For fatigue cracking, the S-VECD model coefficients for the asphalt mixtures also need to be input to complete the fatigue damage prediction. These coefficients are obtained from dynamic modulus tests and cyclic fatigue tests performed using an AMPT in the laboratory. The dynamic modulus test uses either AASHTO T 378 for 100-mm × 150-mm specimens or AASHTO TP 132 for 38-mm × 110-mm specimens and the cyclic fatigue test uses either AASHTO TP 107 for 100-mm × 130-mm specimens or AASHTO TP 133 for 38-mm × 110-mm specimens. The percentage of damage, (%Damage), is computed as the ratio of the damaged area to the total effective area, as presented in equation 149.

$$\%\,Damage = \frac{\sum_{i=1}^{M} \left(Damage\ Factor \right)_i \times A_i}{\sum_{i=1}^{M} A_i} \tag{149}$$

Where:

i = nodal point number in the finite element mesh.
M = total number of nodal points in the finite element mesh.
A_i = area represented by nodal point i in the finite element mesh.
$\sum Ai$ = total effective area.
Damage Factor = computed amount of damage at the nodal point (1 is fully damaged and 0 is no damage).

Fatigue damage contours can be plotted at each life stage; figure 95-A provides an example. Damage values in this figure are calculated from one minus pseudostiffness, *C*. The damage contours shown in figure 95-A indicates the damage at the top and bottom of the pavement is one, i.e., complete failure with *C* equals to zero. The large bulb of damage in a half-oval shape propagates from the top until approximately one third of the asphalt layer thickness from the pavement surface. The other damage bulb in a half-oval shape propagates from the bottom of the pavement until the same location, creating damage contours in an hourglass shape. The total effective area used in FlexPAVE is formed by two overlapping triangles to form the reference cross sectional area within which the level of damage is calculated.[6,150] The top inverted triangle has a 170-cm wide base that is located at the top of the surface layer and a vertex that is located at the bottom of the bottom asphalt layer. The 120-cm wide base of the second triangle is located at the bottom of the bottom asphalt layer and its vertex is positioned at the surface layer. Figure 95-B shows this area schematically. The transfer function converts the obtained %Damage in the asphalt layer cross section to the measurable percentage of cracking, %Cracking, on the pavement surface. A previous study has shown that the FlexPAVE program yields significantly higher accuracy in fatigue performance predictions than the AASHTOWare Pavement ME Design software.[6,18,103]

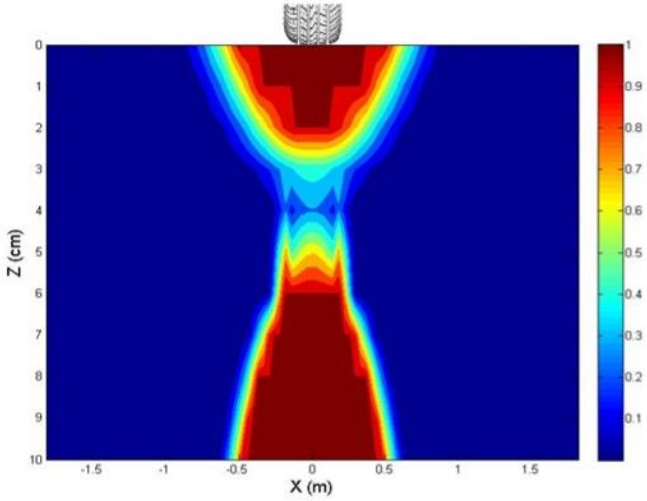

1 m = 40 inches.

A. Damage contours.

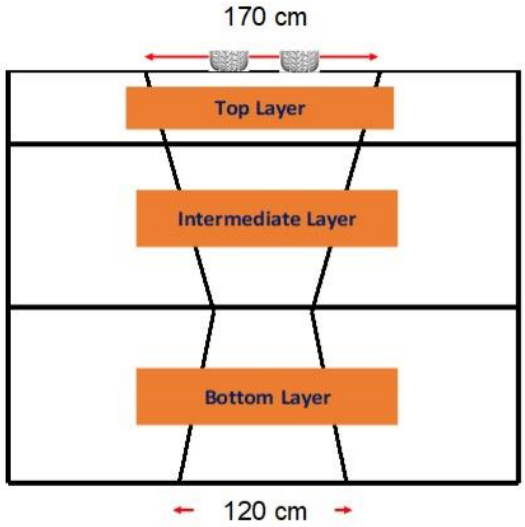

B. Total effective area used for %Damage calculations.

Figure 95. Illustrations. Predicted fatigue damage in asphalt layer cross section.[153]

The mechanical responses computed for each segment also are used in the rut depth predictions in FlexPAVE.[6] The permanent deformation shift model is applied for the predictions. The shift model considers the effects of vertical stress and temperature on permanent strain development. The shift model coefficients are calibrated using SSR tests and the AMPT (AASHTO TP 134).[26] The SSR test is conducted at two temperatures and, at each temperature, three levels

of deviatoric stress (482.6 kPa, 689.5 kPa, and 896.3 kPa) are applied to the specimen with a confining pressure of 68.9 kPa. One of the advantages of the shift model is that the shift model can account for different loading conditions. Once the model coefficients are calibrated, the model can predict the permanent strain under various load levels and at different temperatures. To calculate rut depths in asphalt layers using FlexPAVE, each layer in the pavement structure is divided into 10 sublayers. The software then uses the shift model to compute the permanent deformation at each nodal point based on the obtained pavement responses and the climate data for each segment. With regard to the permanent strain that is contributed from the unbound layers, FlexPAVE applies the same mechanistic-empirical model used in the original Pavement ME program.[6,18,152] The permanent strain in the model is a function of the resilient modulus, the California bearing ratio of the unbound material, and the groundwater table. After the permanent strain levels are calculated, the permanent deformation in each sublayer can be determined by multiplying the permanent strain by the thickness of each sublayer. The total permanent deformation (rut depth) is the summation of the permanent deformation of each sublayer. With the current version of FlexPAVE, each 20-yr simulation takes about 20 to 40 min, depending on the number of viscoelastic layers in the structure and the performance of the user's computer.

Field Sections

Korea Expressway Corporation Test Road

The KEC test road in South Korea was built to evaluate the effects of different materials and structures on pavement performance.[23] Figure 96-A presents the structural layouts of the pavement sections. As shown, the pavement sections are designed to include systematic variations in materials and structures. Two dense-graded materials are used in the surface layer. The NMAS of the two mixtures is 19 mm. The mixture designated as PMA uses a PG 76-22 polymer-modified asphalt (PMA) binder with SBS and the mixture designated as ASTM contains standard PG 64-22 binder. The sections with the PMA mixture as the surface mixture are designated with −2 in figure 96-A. One intermediate layer material (BB5) and two asphalt concrete base layer mixtures (BB1 and BB3) are also included in the study. The three mixture types, i.e., BB5, BB1, and BB3, are coarse-graded mixtures with the NMAS of 40 mm and 25 mm for the base and intermediate layer mixtures, respectively. The binder grade for these three mixtures is PG 64-22. In these KEC pavement sections, the total asphalt thickness varies from 12 cm (4.7 inches) for the sections with no asphalt base (the aggregate base course, or ABC) pavements to 40 cm (15.7 inches) for the sections with an asphalt base. The material properties for these mixtures can be found elsewhere.[103,150] Due to the nature of this study and the data collection efforts, field performance data for all the KEC sections were only available after 5 yr of loading.[154] During this time, traffic levels on the test road were estimated to be 1.68 MESALs). Figure 96-A presents all the 24 KEC test road sections; however, only 16 have available field data.

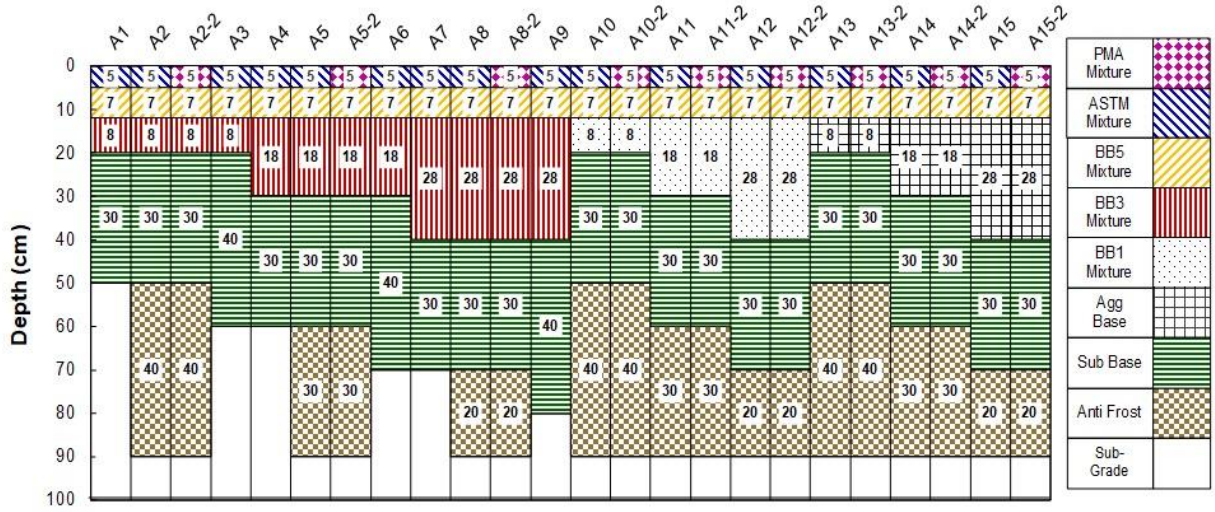

Note: The numbers in the figures indicate the thickness (cm) of the layers.

A. KEC test road.

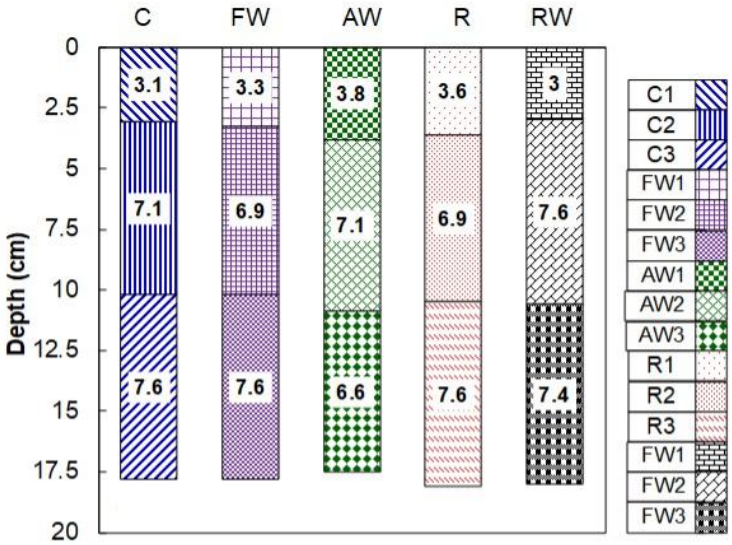

Note: The numbers in the figures indicate the thickness (cm) of the layers.

B. NCAT test track.

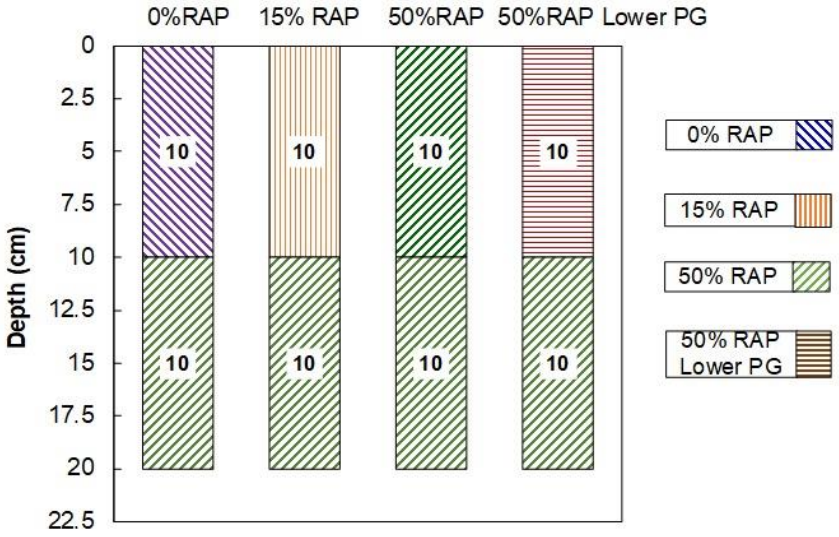

Note: The numbers in the figures indicate the thickness (cm) of the layers.

C. MIT-RAP test road.

Figure 96. Graphs. Layout of pavement test sections.[153]

National Center for Asphalt Technology Test Track

Figure 96-B presents the pavement structures of the five NCAT test track sections (S9, S10, S11, N10, and N11 from the 2009 research cycle).[21] Unlike the KEC sections, the pavement thickness of the NCAT test track is fixed at 18 cm (7 inches). Each section contains three asphalt layers, and different types of asphalt mixtures are used in the sections to evaluate the effects of the materials on pavement performance, as presented in table 37. These sections have undergone accelerated loading that has been continued through two research cycles without any pavement preservation efforts. The total traffic volume is about twenty MESALs for the two research cycles.

Table 37. Mixtures used in NCAT test sections.

Section ID	Track Section ID	Mix ID	Binder PG	NMAS (mm)	Modifier and Additive	RAP (percent)	Remarks
C	S9	C1	76-22	9.5	SBS	0	Control
C	S9	C2	76-22	19	SBS	0	Control
C	S9	C3	67-22	19	NA	0	Control
FW	S10	FW1	76-22	9.5	Foam	0	WMA−Foaming
FW	S10	FW2	76-22	19	Foam	0	WMA-Foaming
FW	S10	FW3	67-22	19	Foam	0	WMA-Foaming
AW	S11	AW1	76-22	9.5	Evotherm	0	WMA-Additive

Section ID	Track Section ID	Mix ID	Binder PG	NMAS (mm)	Modifier and Additive	RAP (percent)	Remarks
AW	S11	AW2	76-22	19	Evotherm	0	WMA-Additive
AW	S11	AW3	67-22	19	Evotherm	0	WMA-Additive
R	N10	R1	67-22	9.5	NA	50	High RAP
R	N10	R2	67-22	19	NA	50	High RAP
R	N10	R3	67-22	19	NA	50	High RAP
RW	N11	RW1	67-22	9.5	NA	50	WMA+High RAP
RW	N11	RW2	67-22	19	NA	50	WMA+High RAP
RW	N11	RW3	67-22	19	NA	50	WMA+High RAP

NA = not applicable.

MIT-RAP Test Road

The MIT-RAP test road was constructed in Manitoba, Canada, in 2009.[22] This 1.3-km (0.8-mi) test road is divided into four sections in the northbound direction, and each section is paved with a different type of surface asphalt mixture. Two 152-m (500-ft) intervals were monitored in each section after the road was opened to traffic. Each pavement section contains two 10-cm layers. The first layer of each section respectively contains four 16-mm NMAS mixtures with different RAP contents: 0 percent, 15 percent, 50 percent, and 50 percent. One of the four mixtures has a high RAP content and was produced using soft binder (PG 58-34) whereas the binder used in the other three mixtures is PG 58-28. The four mixtures in this section are designated as 0-percent RAP, 15-percent RAP, 50-percent RAP, and 50-percent RAP with soft binder. The second layer material, the 50-percent RAP mixture, is the same for all four sections. However, the design traffic volume is low. The design ESALs are only 3 million over 20 yr for these 20-cm (8-inch) asphalt pavement test sections. A field survey was conducted in 2017, 8 yr after construction.

MnROAD Test Road

MnROAD is a pavement test road operated by the Minnesota Department of Transportation and is composed of various materials and pavement structures.[11,64] In 2016, cell 16 to cell 23 of MnROAD were reconstructed using different materials to evaluate the low-temperature thermal cracking potential of these materials. The mixtures were placed in the same structure but in different cells. The pavement structure is a 12.7-cm (5-inch) single-layer asphalt pavement with a 78-cm aggregate base on top of clay soil. Table 38 presents the mixture information for these MnROAD cells. The test road is part of Interstate I-94 (mainline) and the driving lane and passing lane are monitored separately. Therefore, 14 sections with field distress data could be used in this study (the material properties of cell 21 were not available). By the time the field performance was reported, the driving lane had been subjected to about 1.7 MESALs and the passing lane had undergone 0.4 MESALs.

Table 38. Mixture information for MnROAD cells.

Cell	Binder	Polymer-Modified	RAP (percent)	Description
16	PG 64S-22	No	30	High temperature mix
17	PG 64S-22	No	<20	High temperature mix
18	PG 64S-22	No	<20	High temperature mix
19	PG 64S-22	No	<20	High temperature mix + low in-place air voids
20	PG 52S-34	No	>30	Soft binder
22	PG 58H-34	Yes	<20	Typical low temperature mix + limestone
23	PG 70E-34	Yes	<15	HiMA mix

Quantification of Distress in the Field

According to the Distress Identification Manual developed from the LTPP program, fatigue cracking is defined as interconnected cracks that are due to repeated traffic loading in the wheel paths.[155] The fatigue cracking area used in this study is the sum of the reported fatigue cracking area and the area affected by longitudinal cracking in the wheel paths. The area affected by longitudinal cracking is calculated as the product of the length of the crack and the affected range (0.3 m or 1 ft), as suggested by Jackson and Puccinelli.[156] In FlexPAVE, the predicted fatigue cracking is reported as %Cracking, which is the ratio of the sum of the fatigue cracking area to the total lane area.[6] A few sections have patched sections, most of which are in the KEC project and occurred during the early stage of pavement life. In these cases, the patched area was added to the fatigue cracking area if the patching was in the wheel paths. The performance data for those sections after the first year of maintenance were not used in the calibration of the %Cracking predictions. With regard to the NCAT test sections, the amount of cracking measured by the NCAT is reported in three separate categories for each pavement section: right wheel path (RWP), left wheel path (LWP), and the percentage of the cracked area within a lane, which is obtained either by calculating the length of simple cracks and multiplying by 1 ft or by directly calculating the area affected by complex cracking; this study adopted this latter calculation method.[21,157] This method for reporting distress in the NCAT sections is consistent with the reporting for other field test sections. With regard to rut depths measured in the field, only the total rut depth in the wheel paths is reported, and no trench cut data were available to calibrate separately the predictions of permanent deformation in the asphalt layers and unbound layers.

Development of Fatigue Transfer Function for FlexPAVE

Figure 97-A and figure 97-B present the %Cracking measured in the field and %Damage predicted from FlexPAVE for the field sections, respectively.[6] Based on these figures, the magnitudes of the measured %Cracking and the predicted %Damage differ, and the trend in the ranking of the predictions among the different sections mostly follows the trend for measurements in the field and engineering judgment. For example, the ranking of the NCAT sections in the predictions is the same as the ranking for %Cracking in the field.[21] As for the KEC sections, the thinner pavements (A13–A15-2) show more damage in the predictions than observed in the field, and the pavements with thicker asphalt layers (A7–A12-2) show little damage, as expected. In addition, small values for the measured %Cracking and predicted

%Damage are evident for the MIT-RAP sections. The relatively good agreement among the rankings and the differences in the magnitudes of %Cracking and %Damage indicate that a proper transfer function should be able to convert %Damage to %Cracking.

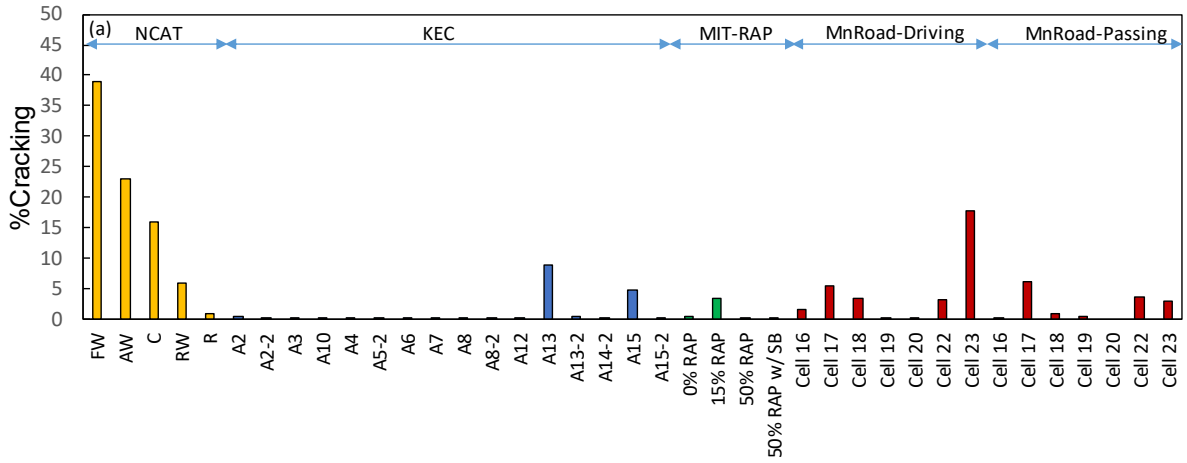

A. Field measurements.

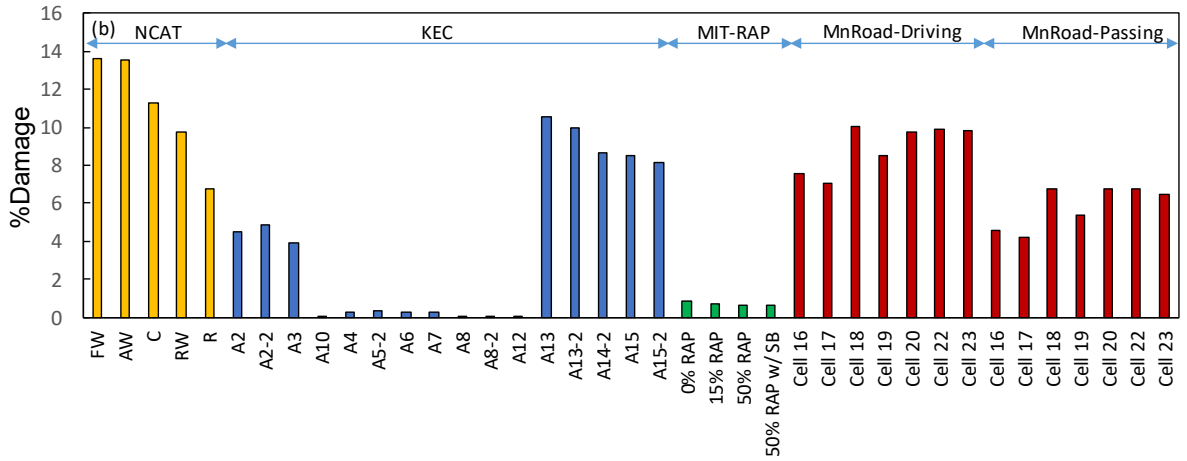

B. FlexPAVE predictions.

Figure 97. Graphs. Measured %Cracking and predicted %Damage.[153]

Figure 98-A and figure 98-B present the predicted %Damage and the measured %Cracking for the different pavement projects plotted together for different %Damage value ranges, 0 percent to 40 percent and 0 percent to 20 percent, respectively. The following observations can be made based on these two figures:

- An overall trend is evident between %Damage and %Cracking. As %Damage increases, %Cracking increases as well.

- When %Damage is lower than 10 percent, the corresponding %Cracking increases slowly and usually remains less than 5 percent. When the predicted %Damage is more than 10 percent, the %Cracking increases dramatically.

- The data have a limited range. The maximum measured %Cracking is 40 percent and the predicted %Damage values are all less than15 percent.

- Within the range of the available data in the current study, the overall relationship between %Damage and %Cracking appears to follow an exponential-type or power-type function.

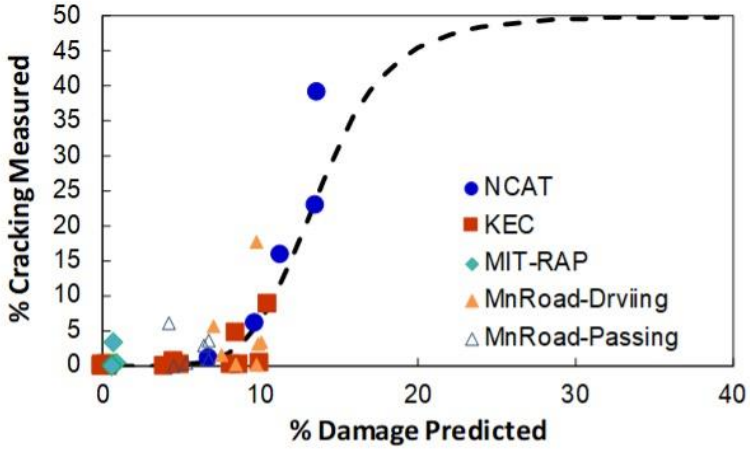

A. Range of %Damage is 0 percent to 40 percent.

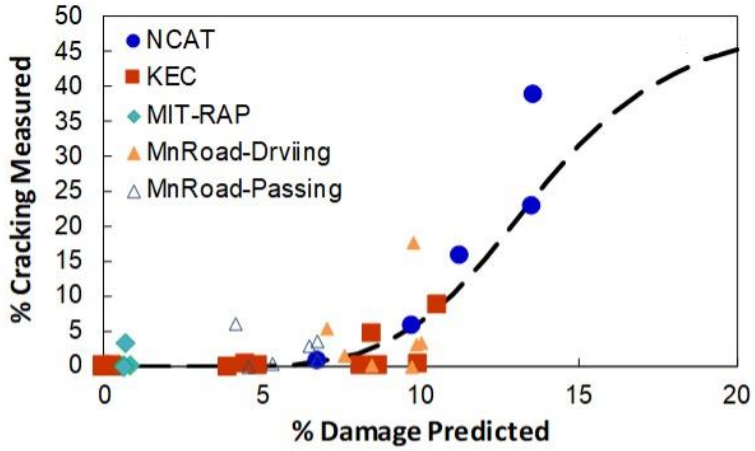

B. Range of %Damage is 0 percent to 20 percent.

Figure 98. Graphs. Preliminary fatigue transfer function.[153]

The last observation made in the previous list presents a challenge for the transfer function calibration process. Even if either a power-form function or an exponential-type function can represent the data well, neither is a good candidate for the fatigue cracking transfer function because the %Cracking for the surface of the pavement cannot exceed a certain value. Based on the quantification protocol for fatigue distress, %Cracking is the ratio of the fatigue cracking area over the whole lane area. If fatigue cracks are assumed to be throughout the lane in the longitudinal direction and each wheel path is 1-m (3-ft) wide, then the maximum %Cracking is 50 percent (= 3 × 2/12, where 12 is the width of a lane in feet). Engineering judgment also would suggest that after %Cracking has accumulated to a certain level, the cracking growth will slow down. However, this trend cannot be observed due to the limited data for the field measurements. The reason the measured %Cracking is not more than 20 percent (except for the NCAT test road, which is an accelerated test track) is that these test roads are usually under routine maintenance.[21] The limitation in the measured data is another challenge in the development of a fatigue transfer function. Given the limited field data, some assumptions based on engineering judgment had to be made to develop a viable transfer function. An S-shaped curve or sigmoidal function was considered to be suitable for this scenario and is also consistent with the transfer function used in Pavement ME.[18,152] Based on these observations and assumptions, the function shown in equation 150 was proposed for the fatigue cracking transfer function.

$$\%Cracking = \frac{50}{1 + C_{f1} e^{\left[C_{f2}\left(\log C_{f3} - \log \%Damage\right)\right]}} \quad (150)$$

Where C_{f1}, C_{f2}, C_{f3} are calibration factors and values are 0.342, 13.97, and 16.38, respectively.

Figure 99-A through figure 99-D present the calibrated prediction results after the fatigue transfer function was applied for the four test road sections. Figure 99-A shows that, after calibration, the predictions provide values that are similar to the measurements for the NCAT sections, except for the FW section.[21] As for the KEC sections shown in figure 99-B, the ABC pavements with thin asphalt layers (A13–A15) have high predicted %Cracking values and the full-depth pavements (A2–A12) show little fatigue cracking. This trend is consistent with the field observations. Figure 99-C indicates that FlexPAVE predicts almost no cracking for the MIT-RAP sections.[6] Given the low traffic volume in the MIT-RAP project and the low observed %Cracking, this result is considered acceptable. The offset between the measurements and the predictions will not affect decision making when FlexPAVE is used in pavement design or for QA because the overall amount of fatigue cracking is low. For the MnROAD sections shown in figure 99-D, a general matching trend can be observed between the predictions and the measurements because the transfer function was able to convert the predictions to the same magnitude as the measurements.[11,64]

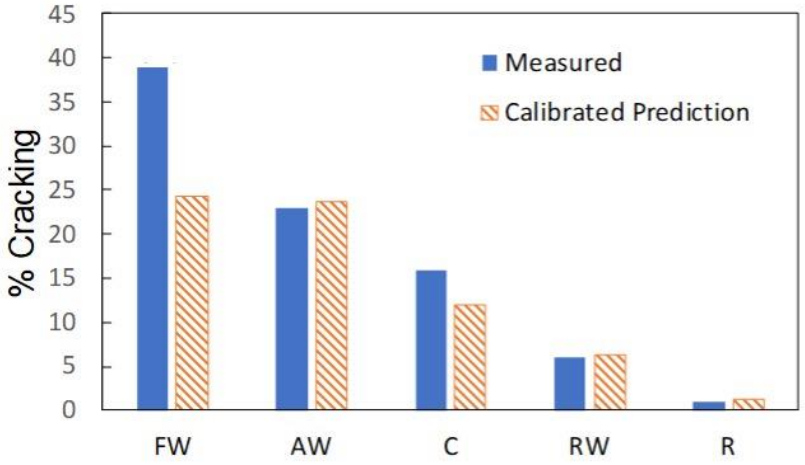

A. NCAT test track.

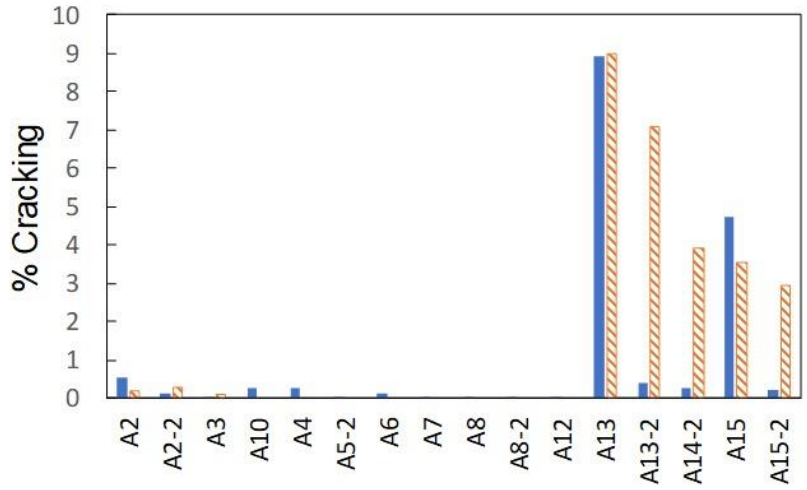

B. KEC test road.

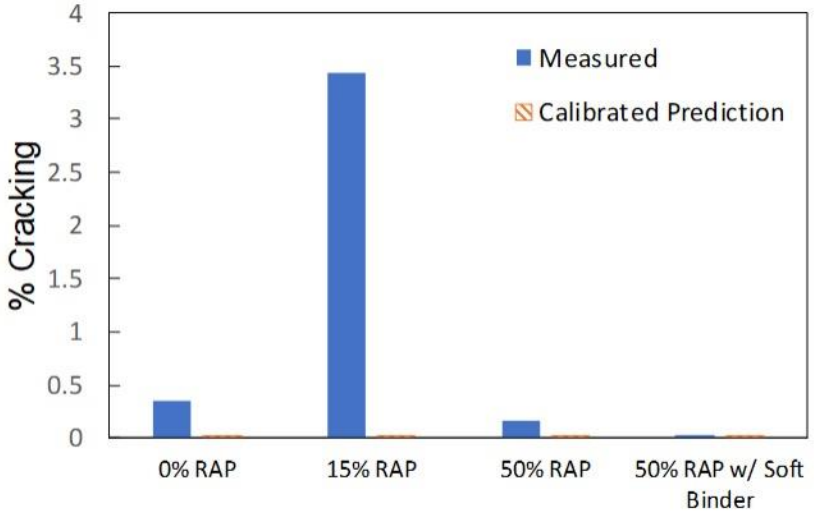

C. MIT-RAP test road.

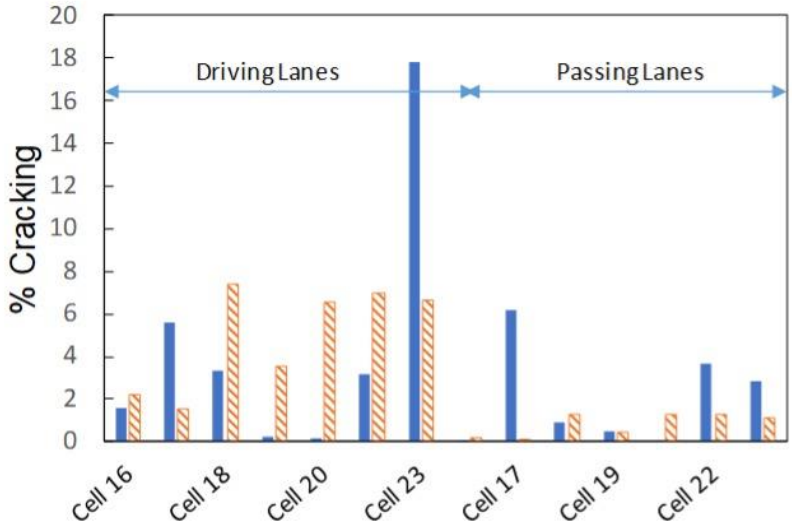

D. MnROAD sections.

Figure 99. Graphs. Predicted versus measured %Cracking for pavement sections after application of fatigue transfer function.[11,64,153]

Development of Rutting Transfer Function for FlexPAVE

The same sections used to calibrate the fatigue cracking transfer function were used to calibrate the proposed rutting transfer function, except for the MnROAD project because laboratory test data for the MnROAD materials were not available.[11,64] Figure 100 presents the measured total rut depths and predicted asphalt layer rut depths. Good agreement can be observed between the predictions and measurements in the comparison, even before calibration. Because the unbound materials' permanent deformation model from NCHRP 01-53 has not been fully vetted at the time of this report writing, this study used only the predicted rut depths in the asphalt layers in its results. In this study, most of the test sections (the exceptions being a few KEC sections) have thick asphalt pavements and, because the vertical stress in the aggregate base decreases with depth, the permanent deformation of the aggregate base layer is negligible. Therefore, most of the permanent deformation comes from the asphalt layers. This phenomenon may be one of the possible reasons for the good agreement between the asphalt layer rut depth predictions and field measurements. The proposed rutting transfer function can be employed for thick asphalt pavements. A transfer function for thin asphalt layers can be developed once the mechanical permanent deformation model for unbound layers becomes available from NCHRP 01-53. The rutting transfer function is presented in equation 151.

$$RD = C_r \cdot RD_{AC} \tag{151}$$

Where:

RD = total rut depth after calibration, mm.
RD_{AC} = predicted rut depth in the asphalt layers, mm.
C_r = calibration coefficients and equals 0.8165.

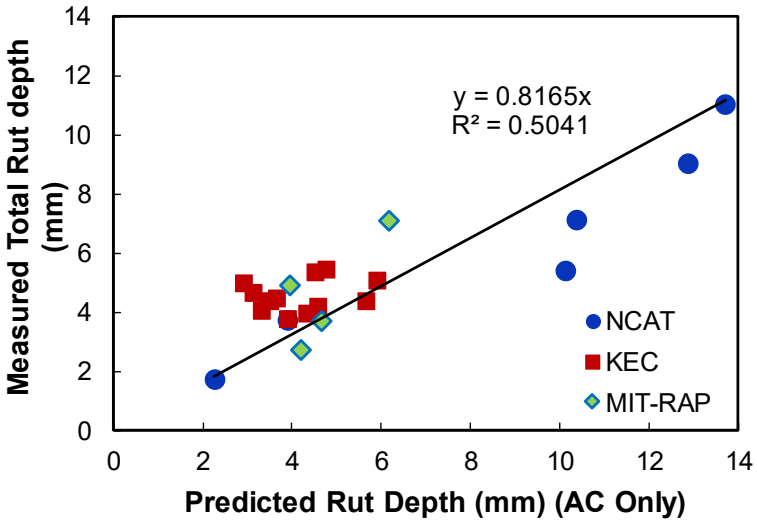

1 mm = 0.04 inches.

Figure 100. Graph. Predicted rut depths versus measured total rut depths.[153]

Summary

In this study, preliminary transfer functions to be used in FlexPAVE were developed for fatigue cracking and rut depth predictions.[6] Thirty-nine pavement sections at the NCAT test track, KEC test road, MIT-RAP test road, and MnROAD were used for the calibrations. (See references 11, 21–23, and 64.) A sigmodal function was adopted as the fatigue transfer function to convert %Damage in the asphalt layer cross section to %Cracking on the pavement surface. A simple calibration coefficient (close to 1) was used to calibrate the rut depth predictions in FlexPAVE. The prediction results after calibration show good agreement with the field measurements.

Future Work

Limited field data were used in the development of the preliminary fatigue and rutting transfer functions for FlexPAVE.[6] As a result, a few assumptions based on engineering judgment had to be made. In the future, more pavement sections, including a number of LTPP sections, will be added to the calibration program, and full transfer functions will be developed. To take full advantage of the LTPP InfoPave database, a predictive equation to predict the material modulus and fatigue and rutting properties will be developed based on the massive amount of test data collected by the research team.[158] The asphalt material properties of the asphalt mixtures in the LTPP sections will be predicted and used in the FlexPAVE performance predictions. In addition, the reliability of the developed transfer function will be evaluated using statistical methods as more pavement sections are involved in the calibration effort.

DEVELOPMENT OF FLEXPAVE VERSION 2.0

FlexPAVE is a state-of-the-art pavement performance analysis software program that utilizes the S-VECD model and the permanent strain shift model for cracking and rutting simulations, respectively.[6] FlexPAVE predicts the pavement performance under moving loads and using realistic climatic conditions that are predicted by the EICM.[13] Updates from the research efforts presented in this report have been incorporated into FlexPAVE version 2.0.

FlexPAVE version 2.0 allows the user to predict fatigue cracking, thermal cracking, and rutting with aging effects.[6] The same test methods are used to predict both fatigue cracking and thermal cracking. The major strength of FlexPAVE is not only that FlexPAVE uses realistic loading and climatic conditions but also that its material characterization methods are much simpler than other mechanistic-empirical asphalt pavement analysis methodologies. The research team performed preliminary tests of the program, which resulted in the alpha version of the program.

In the following sections, the algorithms for the finite element analysis and the graphical user interface (GUI) implemented in FlexPAVE version 2.0 are described.[6]

FlexPAVE 2.0 Engine

FlexPAVE 2.0 utilizes the Fourier Finite Element (FFE) method, developed by Eslaminia and Guddati, for pavement performance modeling.[6,147] Two key ideas underly FlexPAVE 2.0:

- Structural analysis combining an analytical (Fourier) approach and discretization using finite elements.[147]

- Pavement performance modeling using segmentation and extrapolation.

FFE achieves accurate stress analysis under moving vehicular load by considering full 3D deformation, but at a an extremely small fraction of the computational cost of full 3D finite element analysis, which several assumptions valid for pavement simulations make possible. The main idea behind this method is to perform Fourier analysis in the direction of traffic and in time, and use finite elements in the cross section, hence the name FFE method.

The FFE stress analysis approach is combined with extrapolation techniques discussed later in the section, and the pavement material models developed at NCSU and EICM to provide robust estimation of pavement performance under millions of load repetitions.[13]

Outline of the Approach

Considering the evolution of a pavement over its life, there are three time scales associated with its behavior. Traffic loading and resulting stresses vary in the order of second(s), temperature and thermal stresses vary in the order of hours, while pavement damage and rutting evolve in the order of months. The pavement damage and rutting level can be assumed to be constant when performing the stress analysis under traffic and thermal loads. Furthermore, when performing stress analysis for traffic load applied within a few seconds, the temperature and thermal stresses in the pavement can also be assumed to be constant. This concept has been utilized in developing pavement performance modeling using the finite element method during an earlier project with FHWA, and outlined later in the section. Using this approach, the effect of millions of cycles of traffic load on a pavement can be simulated with the help of a few hundred independent stress analyses at different levels of damage and rutting and at different temperatures and associated thermal stresses.

Essentially, the basic building block for pavement performance modeling is to perform stress analysis under single cycle of traffic load at a given temperature, with altered material properties due to damage. In this report, the research team proposes a stress analysis technique that performs fully 3D analysis under moving load by combining Fourier analysis and finite element method in an efficient manner. The FFE method is the proposed stress analysis procedure based on the following observations and approximations:

- The pavement can be approximated as straight and infinite in the direction of the traffic, which is appropriate because the length of the pavement segment and the radius of curvature for curved pavements are both large compared to the other dimensions (the width and the depth of the pavement and the footprint size of the tire).

- The pavement damage distributions are largely invariant in the direction of traffic. The damage profile can be assumed to be prismatic with all the geometric variation occurring within the cross section of the pavement. Obviously, this approximation fails in some advanced stages of pavement failure, where there may be macro cracks that are perpendicular to the direction of traffic. Full three-dimensional finite element method is warranted in such situations.

- The traffic load can be idealized using periodic loading of constant shape and speed. While this idealized traffic load is not completely correct, idealized traffic load is an acceptable approximation because a better approximation is seldom available, owing to the unpredictable and imprecise nature of traffic.

- The asphalt concrete in the pavement layer is assumed to be linearly viscoelastic given that a single traffic load cycle causes small strains.

- The deformation of base and subgrade is often modelled using nonlinear elasticity, but given the uncertainties in load variations, the base and subgrade are idealized as linearly elastic, with the hope that this approximation is not significant compared to the approximate nature of traffic and temperature variations.

These idealizations facilitate significant reduction in computational cost. First, given that the material properties are linear and the load is periodic in time, Fourier series expansion is utilized to eliminate the time variable. Second, given that the pavement is unbounded in the direction of traffic, and the load is periodic in that direction, Fourier series expansion is also utilized to eliminate the spatial variable in the direction of traffic. The three-dimensional, time-dependent problem thus reduces to a set of two-dimensional problems solved for a range of spatial and temporal frequencies, with the analysis domain being the cross section of the pavement. Fortunately, the assumption of constant traffic speed links the spatial and temporal frequencies, thus reducing the number of two-dimensional problems to be analyzed. Standard finite element method is employed in solving the resulting set of two-dimensional problems. Given that the method utilizes Fourier series and Finite Element methods, the resulting method is the FFE method. The next section provides a detailed formulation of the FFE method.

Stress Analysis through Fourier-Finite Element Method

Consider an infinite pavement under traffic load moving with a constant speed V. In this specific section, the research team used the coordinate x for the transverse direction ($x_{min} < x < x_{max}$), y for the depth direction ($0 < y < y_{max}$; $y = 0$ is the top surface), and z for the traffic direction ($-\infty < z < +\infty$). The spatial distribution of the load at $t = 0$ is given by $\mathbf{p}(x,z)$. The pavement analysis problem reduces to solving the elasticity equations with appropriate boundary conditions. The traffic load is applied at the top surface. The precise statement of the problem reduces to solving the following equations.

Strain-displacement relation:

$$\boldsymbol{\varepsilon} = \begin{Bmatrix} \varepsilon_{xx} \\ \varepsilon_{yy} \\ \varepsilon_{zz} \\ \gamma_{yz} \\ \gamma_{zx} \\ \gamma_{xy} \end{Bmatrix} = \begin{bmatrix} \partial/\partial x & 0 & 0 \\ 0 & \partial/\partial y & 0 \\ 0 & 0 & \partial/\partial z \\ 0 & \partial/\partial z & \partial/\partial y \\ \partial/\partial z & 0 & \partial/\partial x \\ \partial/\partial y & \partial/\partial x & 0 \end{bmatrix} \begin{Bmatrix} u_x \\ u_y \\ u_z \end{Bmatrix} = \mathbf{L}\mathbf{u}. \tag{152}$$

Stress strain relation:

$$\boldsymbol{\sigma} = \begin{Bmatrix} \sigma_{xx} & \sigma_{yy} & \sigma_{zz} & \tau_{yz} & \tau_{zx} & \tau_{xy} \end{Bmatrix}^T = \int_0^t \mathbf{C}(t-\tau)\frac{d\boldsymbol{\varepsilon}}{d\tau} d\tau. \tag{153}$$

Equilibrium equations:

$$\mathbf{L}^T\boldsymbol{\sigma} = \mathbf{f}. \tag{154}$$

Top boundary condition:

$$\mathbf{t_r} = \begin{Bmatrix} \tau_{xy} & \sigma_{yy} & \tau_{yz} \end{Bmatrix}^T = \mathbf{p}(x, t - z/V). \tag{155}$$

Where:

u = displacement vector.
ε = strain vector.
L = strain displacement operator.
σ = stress vector.
C = stress-strain matrix.
f = body force vector.
p = load has the argument (t−z/V) indicating that the load is moving with a constant velocity *V*.

Fourier transform in t and z. Given that the material properties and geometry do not vary with t or z, material properties are linear, and t and z are unbounded, Fourier transform can be applied in these two directions to reduce the problem dimension:

$$\hat{f}(z,\omega) = \int_{-\infty}^{+\infty}\int_{-\infty}^{+\infty} f(z,t)e^{-i\omega t}e^{-ikz}dt$$

(156)

Where:

$\hat{f}$ = Fourier transform of a generic function f.
k = wave number (spatial frequency).
ω = (temporal) frequency.

Thus the strain-displacement operator **L** occurring in the problem definition (equations 152 to 155) should be replaced by:

$$\hat{\mathbf{L}}(k) = \begin{bmatrix} \partial/\partial x & 0 & 0 \\ 0 & \partial/\partial y & 0 \\ 0 & 0 & ik \\ 0 & ik & \partial/\partial y \\ ik & 0 & \partial/\partial x \\ \partial/\partial y & \partial/\partial x & 0 \end{bmatrix}$$

(157)

Equations 152 to 155 become:

$$\hat{\boldsymbol{\varepsilon}} = \hat{\mathbf{L}}\hat{\mathbf{u}},$$

(158)

$$\hat{\boldsymbol{\sigma}} = i\omega\hat{\mathbf{C}}(\omega)\hat{\boldsymbol{\varepsilon}},$$

(159)

$$\hat{\mathbf{L}}^{T}\hat{\boldsymbol{\sigma}} = \hat{\mathbf{f}},$$

(160)

$$\hat{\mathbf{t}}_{\mathbf{r}} = \begin{Bmatrix} \hat{\tau}_{xy} & \hat{\sigma}_{yy} & \hat{\tau}_{yz} \end{Bmatrix}^{T} = \hat{\mathbf{p}}(x,k,\omega).$$

(161)

The Fourier transform eliminates the need for convolution in equation and reduces the dimension of the governing equation to two. However, the problem must be solved independently for a sweep of frequencies and wavenumbers, and the resulting response must be inverse Fourier transformed to obtain the response histories and variation in z direction.

Relation Between Wave Number and Temporal Frequency

Since the load is moving with a constant speed, all the responses (stress and deformation profiles) move with the same speed, i.e., the response relative to the location of the load would remain constant. In other words, all the deformations and stresses take the form, f(t−z/V), similar to the expression for the load in equation 155. Fourier transform of such a translating function takes the form:

$$\hat{f}(k,\omega)=\int_{-\infty}^{+\infty}\int_{-\infty}^{+\infty} f\left(t-\frac{z}{V}\right)e^{-i\omega t}e^{-ikz}dtdz=\int_{-\infty}^{+\infty}\int_{-\infty}^{+\infty} f\left(\bar{t}\right)e^{-i\omega \bar{t}}e^{-i\left(k+\frac{\omega}{V}\right)z}d\bar{t}dz \tag{162}$$

Where $\bar{t}$ is $t-z/V$.

It is easy to see that $\hat{f}$ is nonzero only when $k = -\omega/V$, and $\hat{f}$ is equal to

$$\hat{f}(\omega)=\int_{-\infty}^{+\infty} f(t)e^{-i\omega t}dt \tag{163}$$

The implication is that the solution of equations 158 to 161 need not be done for all sets of ω and k, but for all ω, with $k = -\omega/V$. Thus, the assumption of constant speed results in significant reduction in the computational cost.

Reduction to Fourier Series

Finally, note that the load is periodic in time with a period T, meaning that Fourier transform must be replaced by Fourier series

$$\hat{f}(\omega_j)=\sum_{t_n} f_j(t_n)e^{-i\omega_j t_n} \tag{164}$$

with frequencies given by $\omega_j = -2\pi j/T$. Thus, at the end, the analysis reduces to solving the two-dimensional boundary value problem in equations 158 to 161 for $\omega_j = -2\pi j/T$ and $k_j = \omega_j/V$. Once the solutions are obtained for all the frequencies, the responses are obtained by using Fourier series expansion in time and space:

$$f(z,t) = \sum_{\omega_j} \hat{f}_j e^{i\omega_j t} e^{ik_j z}$$

(165)

f is a generic response and represents displacement, stress, or any other state variable for a given x and y.

Finite Element Analysis at a Given ω and k

The material properties vary in both x and y directions in the constitutive relation equation 159. Thus, the equations 158 to 161 cannot be solved using layered models, and warrant the use of more a general numerical method. Given the material property variation and potentially curved boundaries and interfaces, the research team proposes that finite element method be used to solve the problem. The research team follows the standard procedure for this method, as follows:

- Obtain the variational form of the equilibrium equation 160.

$$\delta\pi(\omega,k) = \int_{\Omega} \hat{\boldsymbol{\sigma}}^* \delta\hat{\boldsymbol{\varepsilon}} dxdy - \int_{x_{min}}^{x_{max}} \hat{\mathbf{t}}_r^* \delta\hat{\mathbf{u}}(x,y)\Big|_{y=0} dx = 0$$

(166)

Where:

π = total energy of the system,

$\hat{\boldsymbol{\sigma}}^*$, $\hat{\mathbf{t}}_r^*$ = transposes of stress and traction vectors respectively.

- Perform finite element discretization, where the displacement in the entire domain u(x,y) is interpolated using the nodal displacements $\mathbf{d}_j$. (j=1 … no. nodes):

$$u(x,y) = \sum_j N_j(x,y) d_j = \mathbf{Nd}$$

(167)

- In the previous steps N_j are the shape functions associated with $\mathbf{d}_j$, **N** is the matrix of shape functions and **d** is the vector of nodal displacements. Incorporating the finite element interpolation 167 in the variational form 166 and performing needed algebraic manipulations result in the final finite-element stiffness relation:

$$\mathbf{Kd} = \mathbf{f}$$

(168)

$$\mathbf{K}(\omega,k) = \int_{\Omega} \mathbf{B}^* \hat{\mathbf{C}}(\omega,x,y)\mathbf{B} dxdy$$

(169)

$$\mathbf{B}(k,x,y) = \mathbf{L}(k)\mathbf{N}(x,y) \tag{170}$$

$$\mathbf{f}(\omega,k) = \int_{x_{min}}^{x_{max}} \mathbf{N}(x,y)^* \Big|_{y=0} \hat{\mathbf{p}}(x,\omega,k)\,dx \tag{171}$$

Algorithm and Computational Cost

The algorithm involves the solution of 2-D finite element equation 168 for different values of ω (and corresponding k = −ω/V), and performing inverse Fourier transform using equation 165. The flow chart for the algorithm is shown in source: fhwa.

figure 101. Given the small number of 2D runs, this run time of FFE is several orders of magnitude less than the run time for 3D finite element model with moving load. As noted before and further explained later, pavement performance analysis requires running stress analysis numerous times, making the proposed FFE stress analysis appealing and practical.

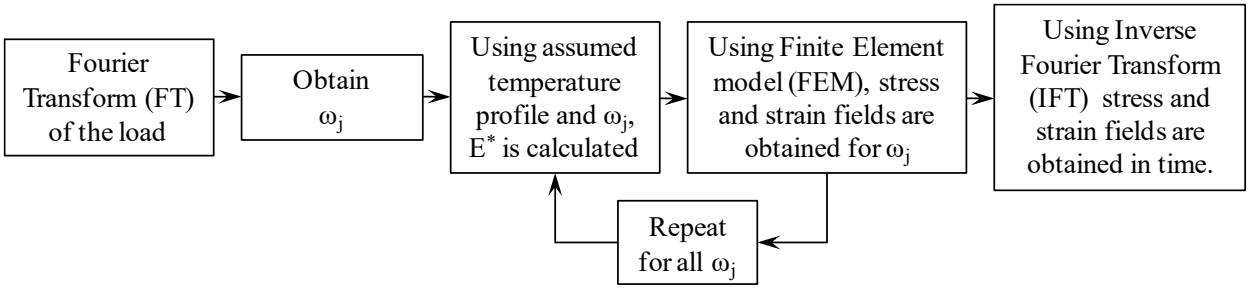

Source: FHWA.

Figure 101. Flowchart. FFE method.

Incorporation of Stress Analysis Approach into Pavement Performance Modeling

Pavement performance modeling requires stress analysis under millions of repeated load cycles with varying pavement damage and rutting levels. This stress analysis is obviously not practical, and the idea of cycle jump often used for fatigue analysis of structures can be adopted here. The cycle jump or extrapolation typically uses the stress analysis once to update the damage level for thousands of cycles; this extrapolation is justified by the fact that the time-scale of damage variation is large compared to the time scale of stress analysis. Such extrapolation is often linear, but sometimes nonlinear extrapolation may be needed for increased accuracy.

Based on this observation, the basic idea is to divide the pavement life into different seasons, with each season characterized by the average damage level. The assumption is that the damage does not change significantly within a season. Typical length of a season is between 2 w and few months, depending on the desired level of accuracy (FlexPAVE 2.0 currently uses 3 mo).[6] Each season is further divided into analysis segments. In addition to constant damage levels, each analysis segment is assumed to have constant temperature and associated thermal stress, and

constant traffic load level and frequency. This characterization is obviously an approximation, and the temperature is typically chosen as an average temperature in an analysis segment. The analysis segment does not have to represent contiguous segment of pavement life. Typically, all mornings of a given season are gathered to form an analysis segment, with afternoons and evenings similarly clubbed together. The number of segments is not restricted to three, but depends on the average temperature and traffic level variation within a day and the desired level of accuracy (FlexPAVE 2.0 currently uses three analysis segments).

In summary, for any given season, for each segment, the damage resulting from a single cycle is computed by post-processing the results from the pavement stress analysis model using FFE. These per-cycle damage for all segments, along with the damage level at the beginning of the season, are processed to obtain the damage level at the end of the season. This procedure is repeated in a sequential manner starting from the first season till the end of pavement life. Naturally, the accuracy increases as the number of seasons and analysis segments for each season are increased, but this increase requires increased computational effort. A balance should be struck between accuracy and efficiency. As mentioned before, at this time, FlexPAVE 2.0 utilizes 3-mo long seasons, and 3 segments per d.[6]

FlexPAVE 2.0 Graphical User Interface

FlexPAVE 2.0 is a completely independent computer code from FlexPAVE 1.1, including the engine.[6,20] The engine is implemented in C++ using an object-oriented approach that is modular, with components related to structural analysis, performance modeling using segmentation, and climatic effects based on EICM, and fatigue, rutting and thermal cracking models discussed in this report.[13] The structural analysis component is further separated into FFE routines and the underlying linear algebra routines developed using efficient Intel® oneAPI Math Kernel library.[159] FlexPAVE 2.0 also builds on the convenient library of Eigen.[160] The distress results from the engine are then passed to FlexPAVE 2.0 GUI based on Microsoft Excel, which performs post-processing to obtain the final outputs shown in the GUI.[24]

Most of the elements of the GUI for FlexPAVE 2.0 are already defined, and few or no modifications are expected from its current development point.[6] This section presents an overview of the GUI elements developed so far that are expected to be present in the final implementation and, consequently, in PASSFlex.[7] One drawback of the previous versions of FlexPAVE is that the GUI development phase did not consider accommodating the needs of users with disabilities in the design (e.g., screen reader software for visually impaired users). The process of making software usable and friendly for users with disabilities is described in Section 508 of the Rehabilitation Act of 1973 (Section 508), which is a requirement for software distributed by Government entities.[19] For that reason, even though FlexPAVE has received FHWA's support over the years, FlexPAVE could not be nationally distributed through FHWA, and its dissemination was reduced.

During the conception phase of FlexPAVE 2.0's GUI, the research team adopted a simplified approach based on two primary factors: easier implementation of Section 508 compliance and simplification of the user training process and adapting that process to ease implementation of the new version.[6,19] The research team combined these factors and generated a GUI using

Microsoft Excel with VBA elements, following the steps used for FlexMAT, which had already been through several Section 508 compliance reviews and received feedback from many users.[5,24,144] The developed GUI for FlexPAVE 2.0 is presented in figure 102. Users who are familiar with FlexPAVE 1.1 may find 2.0 significantly different from previous versions. The differences stem from the simplifying philosophy.

The screen in figure 102 is the main screen, where users handle the projects, materials, structure, project-specific elements, and (when the analysis is complete) the analysis outputs. Four basic groups incorporate the elements handled in the GUI:

- "Project Details," ranging from cell B3 to cell B9, includes project-specific representative characteristics: project name, latitude and longitude of the project's site, altitude of the project's site, water table depth, traffic opening date, and the pavement's design life. The project name selected here will be the identifier for the project created and, when saved, also will be the title of the file generated. Projects with the same name are not allowed.

- "Pavement Structure" includes the following three elements:

    - Use cell B11 to define the number of layers in the pavement structure that, when changed, will adjust the number of rows in "Table 1. Pavement Structure" with the selected number of layers.

    - Use cell B12 to change the unit system between "SI" and "US Customary" and adjust all the units in the GUI accordingly.

    - Use the "Table 1. Pavement Structure" table to define the structure, from top to bottom, i.e., the first row of the table is the surface layer of the pavement, and the last row is the bottom-most layer (normally the subgrade). In the "Table 1. Pavement Structure" table, the "Material" selection is unavailable until a "Layer Type" is selected from among "Asphalt," "Aggregate Base," and "Subgrade," as shown in figure 103.

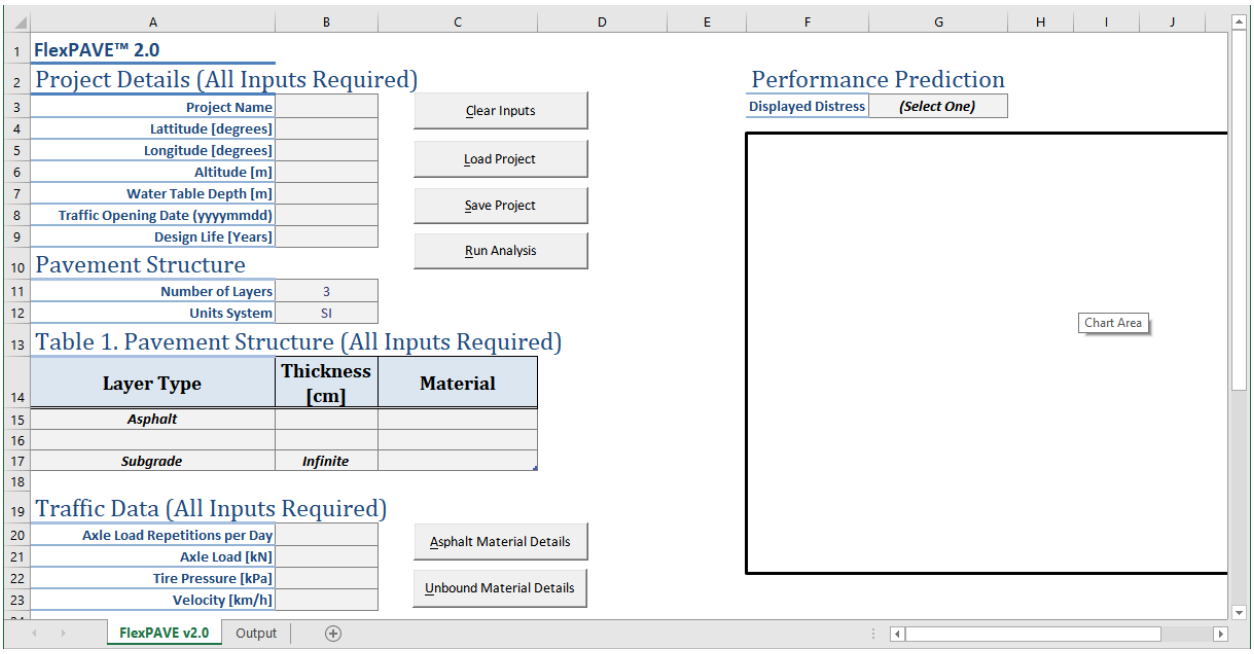

Source: FHWA.

Figure 102. Screenshot. FlexPAVE version 2.0 GUI.

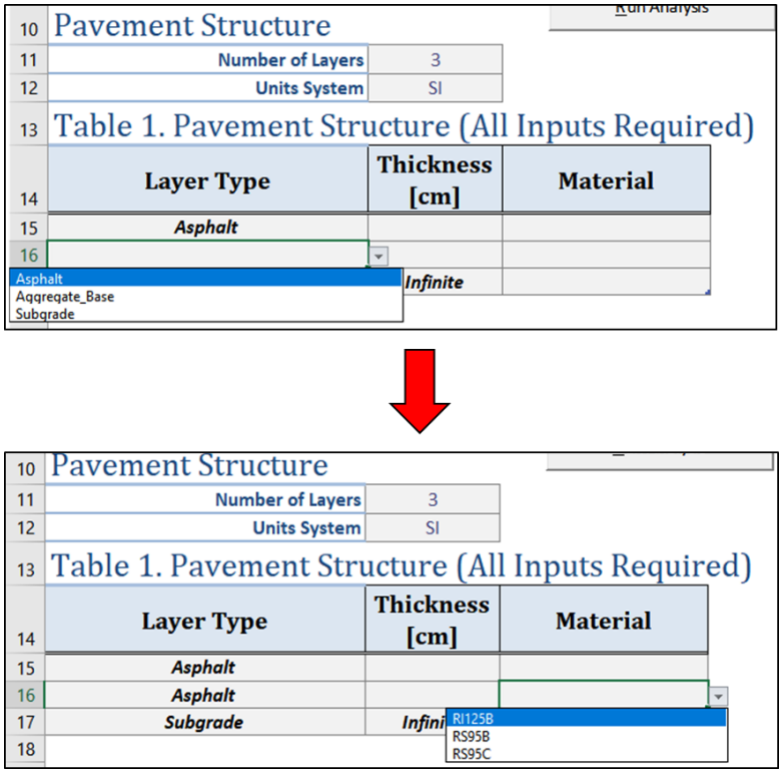

Source: FHWA.

Figure 103. Screenshot. Layer type and material selection in FlexPAVE version 2.0.

- "Traffic Data" information input has a dynamic location on the screen because that information depends on the number of layers selected for the pavement structure table. "Traffic Data" is located two rows below the last layer and includes the input cells for the following information:
    - The daily traffic level in ESALs.
    - The individual axle load.
    - The tire pressure.
    - The traffic speed (velocity).
- Use the "Performance Prediction" screen in figure 104 to select which performance is shown in the graph, i.e., "Fatigue," "Rutting," or "Thermal Cracking."

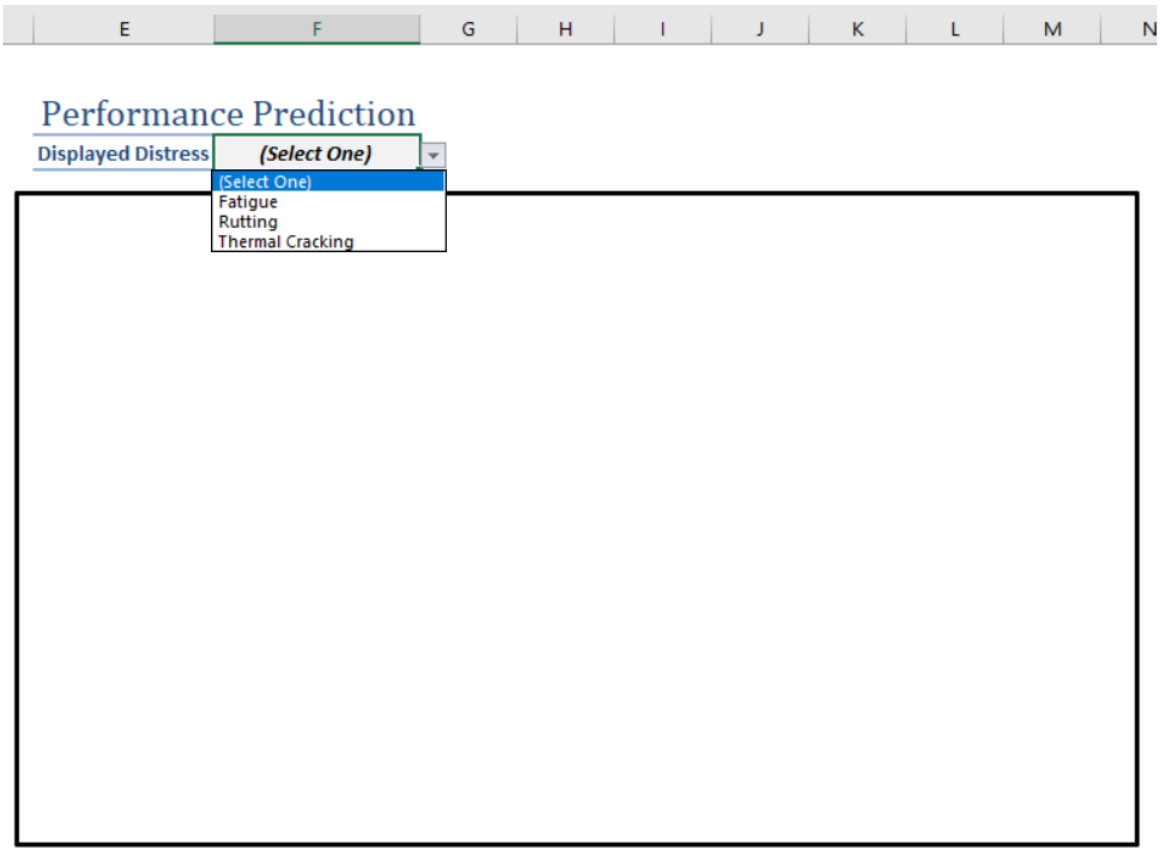

Source: FHWA.

Figure 104. Screenshot. "Performance Prediction" screen in FlexPAVE version 2.0.

Beyond the input selection, the six buttons described in table 39 allow the user to perform actions in FlexPAVE 2.0.[6] The "Clear Inputs," "Save Project," and "Run Analysis," buttons are direct execution buttons that perform their intended functionality when the user clicks them. The other buttons, "Load Project," "Asphalt Material Details," and "Unbound Material Details," require other actions that are more involved with auxiliary screens.

Table 39. Summary of button-related actions in FlexPAVE 2.0.

Button	Functionality
"Clear Inputs"	Deletes all user input information currently present on the screen.
"Load Project"	Opens the "Project Selection" screen for selection of existent projects in the database of FlexPAVE 2.0 projects.
"Save Project"	Saves or updates a project with the name selected in cell B3, storing the current filled information into a project file in the database.
"Run Analysis"	Verifies if the current inputs are valid and generates a warning message with a description of the missing input, if needed. Saves or updates current project. Runs pavement simulation for the current project.
"Asphalt Material Details"	Opens the "Asphalt Material Properties" management screen for adding asphalt materials into the database.
"Unbound Material Details"	Opens the "Unbound Material Properties" management screen for adding asphalt materials into the database.

Clicking the "Load Project" button displays the "Project Selection" dialog box in figure 105, which allows the user to select from existing projects in the database in the "Project Name" list. Once a project is selected, clicking the "Load" button clears the input values on the previous screen and replaces them with the values of the selected project.

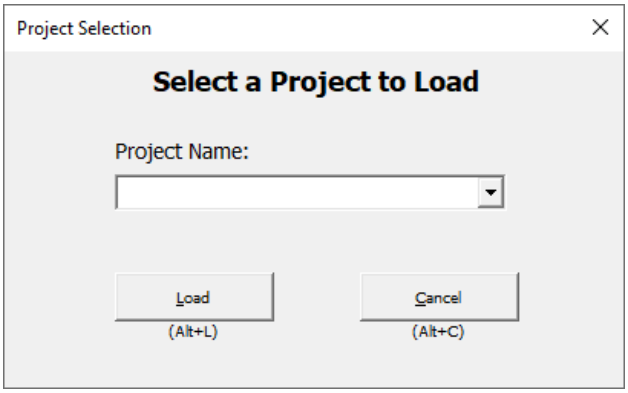

Source: FHWA.

Figure 105. Screenshot. "Project Selection" dialog box in FlexPAVE version 2.0.

If the project contains results from a previously run simulation, those results are loaded and available for verification on graph generated by the selection in the "Performance Prediction" screen in figure 104.

Clicking the "Asphalt Material Details" button displays the "Asphalt Material Properties" dialog box in figure 106. The user can select from the existing asphalt materials in the database in the "Select Material" list. When the user selects a material, the properties of that material are displayed in the boxes. This screen has an inherent set of functionalities, one of which requires an additional handling screen of its own. Table 40Table 40. Summary of actions in "Asphalt Material Details" functionality. presents a summary of the actions, with the functionalities and requirements for each element.

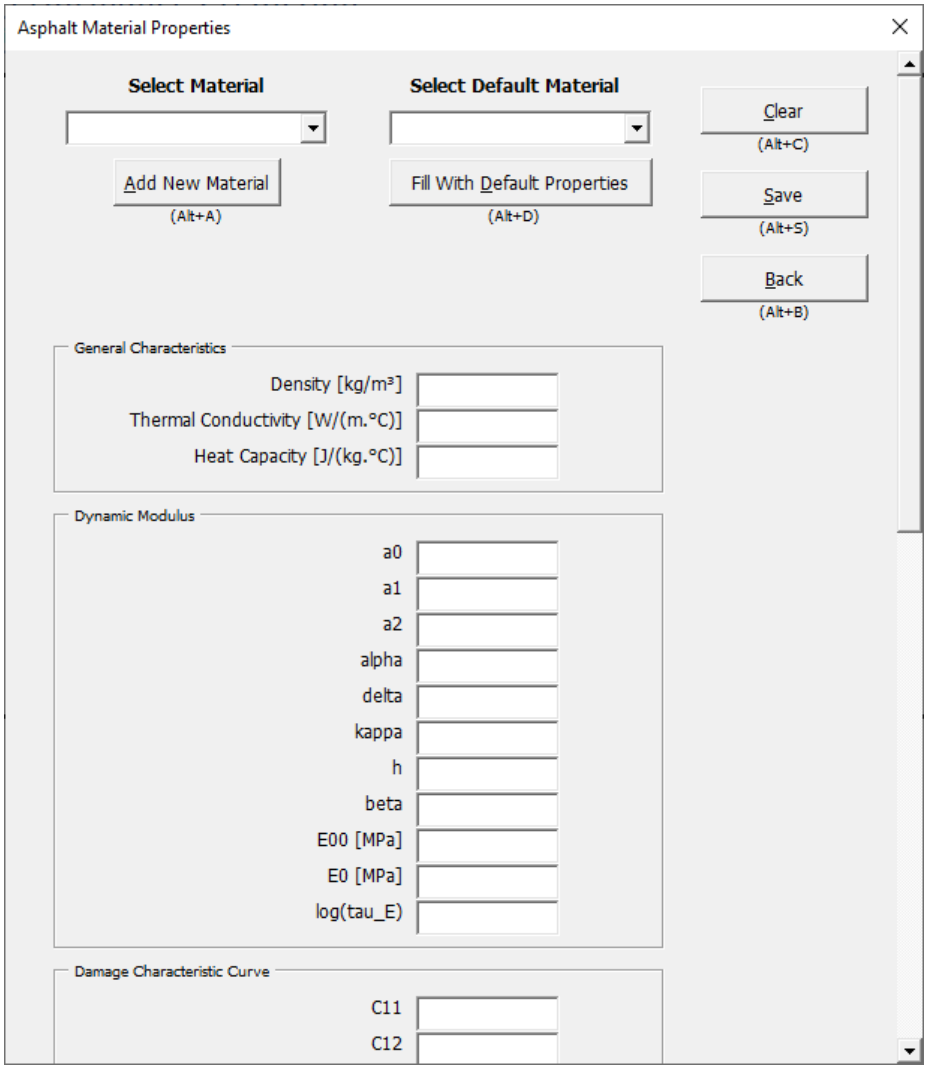

Source: FHWA.

Figure 106. Screenshot. "Asphalt Material Properties" dialog box in FlexPAVE version 2.0.

Table 40. Summary of actions in "Asphalt Material Details" functionality.

Action	Functionality	Requirement
The "Select Material" list	Select a material from the database of existing materials.	At least one material entry in the database.
The "Select Default Material" list	Select a default material to use for empty properties of the selected material.	None.
The "Add New Material" button	Display the "New Asphalt Material" dialog box to add a new material to the database of asphalt materials.	None.
The "Fill With Default Properties" button	Fill empty properties from the currently selected material with a default material's properties.	Selection of a material either from database or recently added. Selection of a default material.
The "Clear" button	Clear the selection of material and properties.	None.
The "Save" button	Save the current material to the database of materials.	Material name identification. All coefficients and properties must have a value.
The "Back" button	Close the "Asphalt Material Properties" dialog box.	None.

The "Add New Material" button requires an additional dialog box for its functionalities. The "New Asphalt Material" dialog box in figure 107 contains a "New Material Name" text box to define the material name and two buttons, the "Load Cracking Properties" button and the "Load Rutting Properties" button, to select FlexMAT files or FlexMAT-generated files to import the coefficients and calibrated models for cracking and rutting from, respectively.[(5)] When a unique name is given (i.e., a name that is not yet in the database) and the intended cracking and rutting files are loaded, click the "Done" button to display the "Asphalt Material Properties" dialog box and load the selected material properties. If no file is selected or any properties are missing for cracking, rutting, or both, the corresponding text boxes will be left empty, and default material properties can be used to fill them.

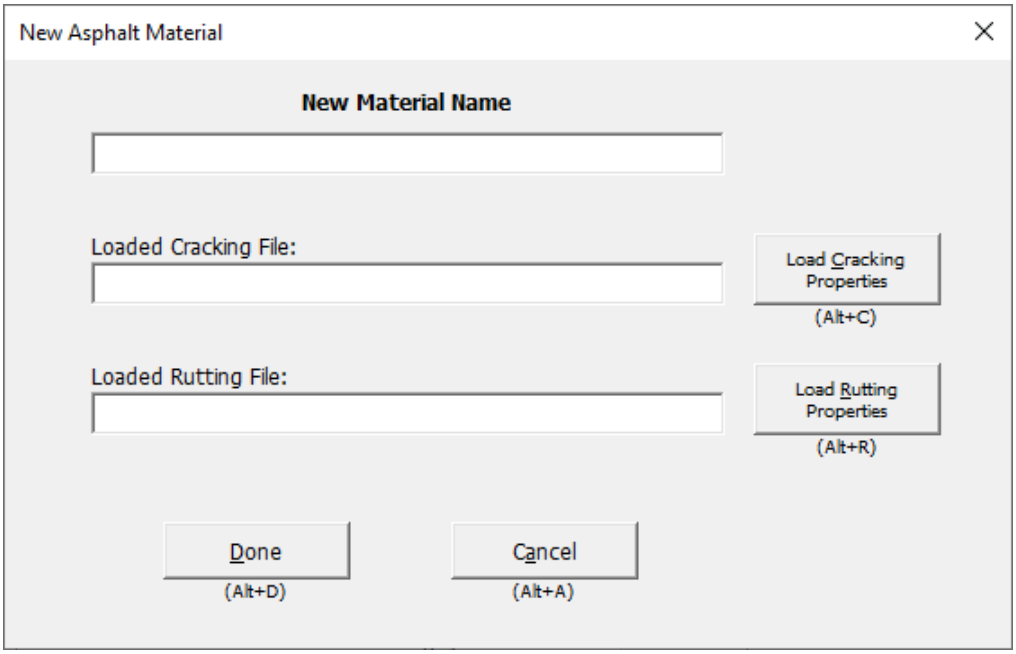

Source: FHWA.

Figure 107. Screenshot. "New Asphalt Material" dialog box in FlexPAVE version 2.0.

The "Unbound Material Details" button on the FlexPAVE 2.0 main screen is similar to the "Asphalt Material Details" button in that the "Unbound Material Details" button is used to add materials to the database and to verify the properties of the materials, except the "Unbound Material Details" button is used for the materials in the "Aggregate Base" and "Subgrade" layer types. Figure 108 presents the "Unbound Material Properties" dialog box where these actions are handled.

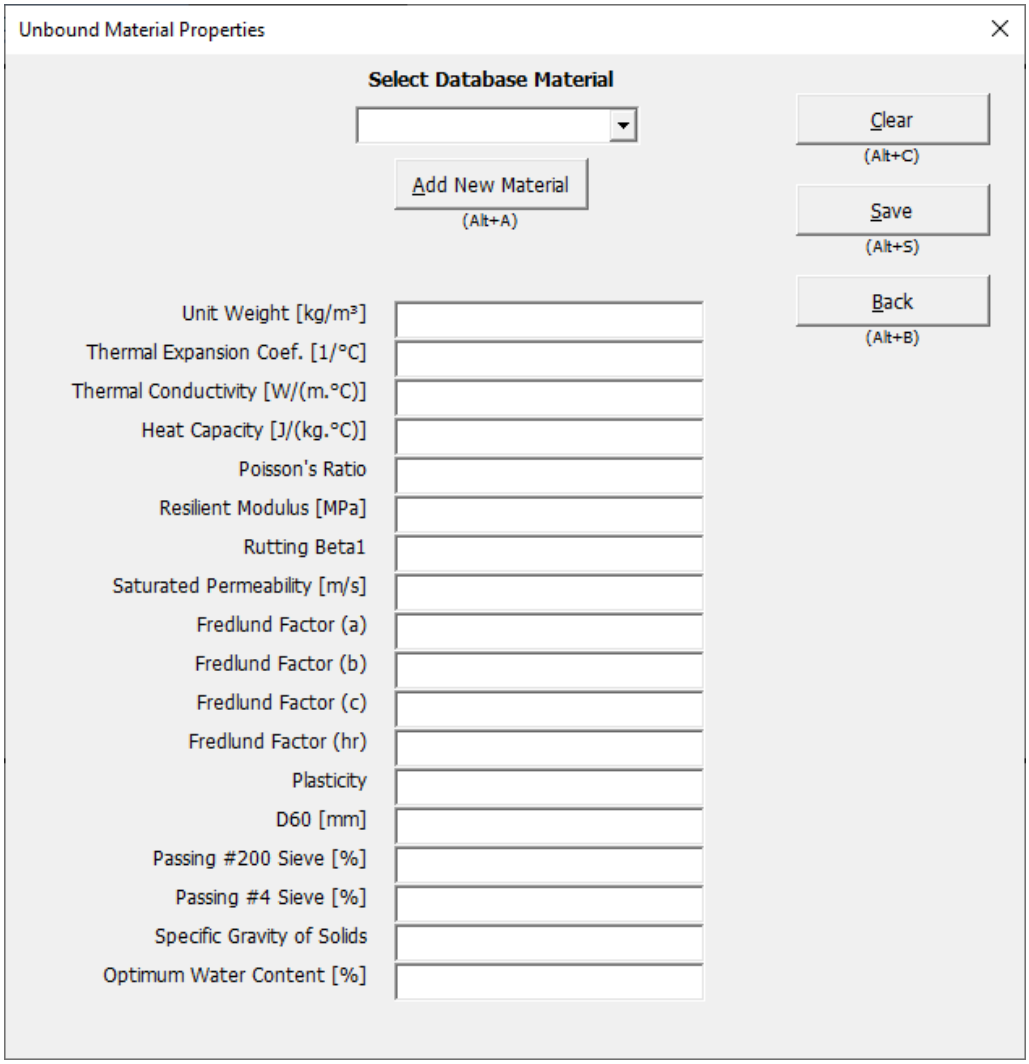

Source: FHWA.

Figure 108. Screenshot. "Unbound Material Properties" dialog box in FlexPAVE version 2.0.

Table 41 presents a summary of the actions available at this stage, with their respective functionalities and restrictions.

Table 41. Actions in "Unbound Material Details" functionality of FlexPAVE 2.0.

Action	Functionality	Requirement
The "Select Database Material" list	Select a material from the database of existing materials.	At least one material entry in the database.
The "Add New Material" button	Activate the "New Unbound Material" dialog box to add a new material to the database of unbound materials.	None.
The "Clear" button	Clear the selection of material and properties.	None.
The "Save" button	Save the current material to the database of materials.	Material name identification. All coefficients and properties must have a value.
The "Back" button	Close the "Unbound Material Properties" dialog box.	None.

The "Add New Material" button is similar to the "Add New Material" button in that it requires another dialog box for its functionalities. The "New Unbound Material" dialog box in figure 109 contains the "Material Type" list to select from default materials characterized by the AASHTO Soil Classification System with properties that are common to materials thus classified.[161] These default values follow those presented in the Input Manual for the Enhanced Integrated Climatic Model (EICM) (2016) and the values reported in the AASHTO Mechanistic-Empirical Pavement Design Guide (2020).[13,162] When a user selects a material type and enters a valid name in the "New Material Name" text box, clicking the "Done" button returns the user to the previous "Unbound Material Properties" dialog box to verify the material's properties and be save the material to the database.

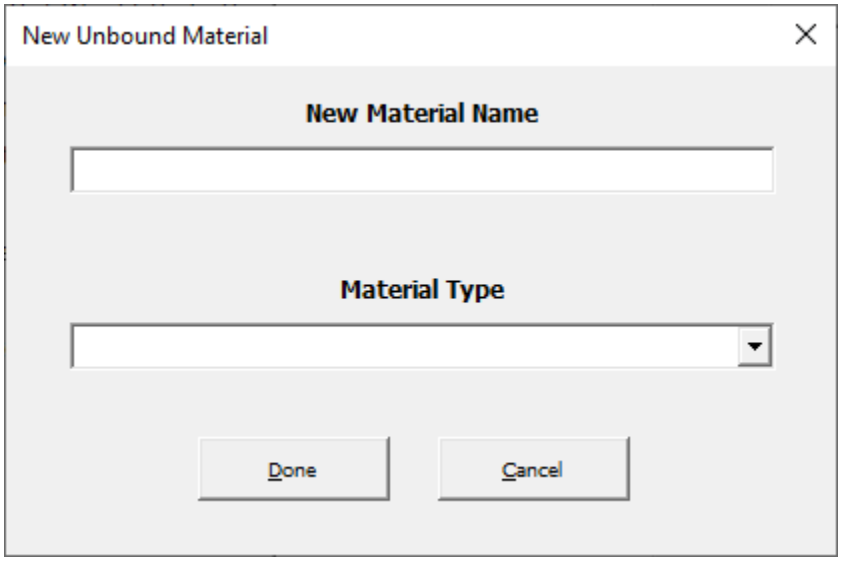

Source: FHWA.

Figure 109. Screenshot. "New Unbound Material" dialog box in FlexPAVE version 2.0.

REFERENCES

1. Underwood, B. S., C. Baek, and Y. R. Kim. 2012. "Simplified Viscoelastic Continuum Damage Model as Platform for Asphalt Concrete Fatigue Analysis." *Transportation Research Record: Journal of the Transportation Research Board* 2296, no. 1: 36–45. https://journals.sagepub.com/doi/10.3141/2296-04, last accessed September 15, 2023.

2. Choi, Y. T., and Y. R. Kim. 2014. "Implementation and Verification of a Mechanistic Permanent Deformation Model (Shift Model) to Predict Rut Depths of Asphalt Pavement." *Road Materials and Pavement Design* 15 no. sup1: 195–218. https://trid.trb.org/view/1316750, last accessed September 15, 2023.

3. Lytton, R. L., C. W. Chen, and D. N. Little. 2001. *Microdamage Healing in Asphalt and Asphalt Concrete, Volume III: A Micromechanics Fracture and Healing Model for Asphalt Concrete*. Report No. FHWA-RD-98-143. Washington, DC: Federal Highway Administration. https://www.fhwa.dot.gov/publications/research/infrastructure/pavements/98143/98143.pdf, last accessed September 15, 2023.

4. AASHTO. n.d. "AASHTO" (web page). https://www.transportation.org/, last accessed April 19, 2023.

5. FHWA. 2022. "FlexMAT™ Asphalt Pavement Analysis Tools" (web page). https://highways.dot.gov/research/infrastructure/pavements/flexmat, last accessed April 19, 2023.

6. FHWA. n.d. *FlexPAVE*™ (software). Version 2.0.

7. FHWA. n.d. *PASSFlex*™ (software).

8. Keshavarzi, B. 2019. "Prediction of Thermal Cracking in Asphalt Pavements Using Simplified Viscoelastic Continuum Damage (S-VECD) Theory." Ph.D. dissertation. North Carolina State University.

9. FHWA. n.d. *FlexTC* (software).

10. SCHOTT AG. n.d. "ZERODUR®" (web page). https://www.schott.com/en-ca/products/zerodur, last accessed April 19, 2023.

11. Minnesota Department of Transportation. 2023. "MnROAD: Minnesota's Cold Weather Pavement Testing Facility" (web page). http://www.dot.state.mn.us/mnroad/, last accessed April 19, 2023.

12. FHWA. 2019. "LTPPBind" (web page). https://highways.dot.gov/research/long-term-infrastructure-performance/ltpp/ltppbind, last accessed April 19, 2023.

13. Larson, G., and B. Dempsey. 1997. *Enhanced Integrated Climatic Model Version 2.0*. Report No. DTFA MN/DOT 72114. Urbana-Champaign, IL: University of Illinois.

14. NASA. 2022. "Modern-Era Retrospective Analysis for Research and Applications, Version 2" (web page). https://gmao.gsfc.nasa.gov/reanalysis/MERRA-2/, last accessed April 19, 2023.

15. FHWA. 2022. "FlexMAT™ for Cracking Version 2.1" (web page). https://highways.dot.gov/research/infrastructure/pavements/flexmat-cracking-version2-1, last accessed April 19, 2023.

16. FHWA. 2022. "FlexMAT™ for Rutting Tool Version 2.1" (web page). https://highways.dot.gov/research/infrastructure/pavements/flexmat-rutting-version2-1, last accessed April 19, 2023.

17. Transportation Research Board. 2022. "NCHRP 09-54 [Completed] Long-Term Aging of Asphalt Mixtures for Performance Testing and Prediction" (web page). https://apps.trb.org/cmsfeed/TRBNetProjectDisplay.asp?ProjectID=3400, last accessed April 19, 2023.

18. AASHTO. 2015. "AASHTOWare Pavement ME Design" (web page). https://me-design.com/medesign/Home.aspx, last accessed April 19, 2023.

19. Electronic and information technology. 2021. 29 U.S. C. § 794(d).

20. FHWA. n.d. FlexPAVE™ (software). Version 1.1.

21. Auburn University. n.d. "About the Test Track" (web page). https://www.eng.auburn.edu/research/centers/ncat/testtrack/index.html, last accessed April 19, 2023.

22. Manitoba. n.d. "Transportation and Infrastructure" (web page). https://www.gov.mb.ca/mit/index.html, last accessed April 19, 2023.

23. Seo, Y., S. M. Kim, and J. H. Lee. 2013. "Operation of the First Full Scale Road Test Facility in Korea and Lessons Learned from 8 Years of Experience." *KSCE Journal of Civil Engineering* 17: 1023–1029.

24. Microsoft®. 2023. *Microsoft® Excel®* (software).

25. Ding, J., Y. D. Wang, S. Gulzar, Y. R. Kim, and B. S. Underwood. 2020. "Uncertainty Quantification of Simplified Viscoelastic Continuum Damage Fatigue Model using the Bayesian Inference-Based Markov Chain Monte Carlo Method." *Transportation Research Record: Journal of the Transportation Research Board* 2674 no. 4: 247–260.

26. AASHTO. 2022. *Standard Method of Test for Stress Sweep Rutting (SSR) Test Using Asphalt Mixture Performance Tester (AMPT)*. TP 134. Washington, DC: AASHTO.

27. Transportation Research Board. 2022. “TFRS 01 [Active] Quality Assurance (QA) Aspects of Performance Related Specifications (PRS)” (web page). https://apps.trb.org/cmsfeed/TRBNetProjectDisplay.asp?ProjectID=4875, last accessed April 19, 2023.

28. Kim, Y. R., B. S. Underwood, M. N. Guddati, A. Ghanbari, B. Keshavarzi, Y. D. Wang, J. Jeong, D. Mocelin, F. D. C. Pivetta, and N. A. H. Saleh. 2024. *Development of Balanced Mixture Design Index Parameters and the Flex Suite of Performance Analysis Tools for Asphalt Pavements—Volume II*. Report No. FHWA-HRT-24-111. Washington, DC: Federal Highway Administration.

29. Elwardany, M., F. Y. Rad, C. Castorena, and Y. R. Kim. 2018. “Climate-, Depth-, and Time-Based Laboratory Aging Procedure for Asphalt Mixtures.” *Journal of the Association of Asphalt Paving Technologists* 87: 467–511.

30. Kim, Y. R., C. Castorena, M. Elwardany, F. Y. Rad, B. S. Underwood, A. Gundha, P. Gudipudi, M. Farrar, and R. Glaser. 2018. *Long-Term Aging of Asphalt Mixtures for Performance Testing and Prediction*. NCHRP Report 871. Washington, DC: Transportation Research Board.

31. Yousefi, R. F., M. D. Elwardany, C. Castorena, and Y. R. Kim. 2018. “Evaluation of Chemical and Rheological Aging Indices to Track Oxidative Aging of Asphalt Mixtures.” *Transportation Research Record: Journal of the Transportation Research Board* 2672, no. 28: 349–358.

32. Kim, Y. R., C. Castorena, N. F. Saleh, E. Braswell, M. Elwardany, and F. Y. Rad. 2021. *Long-Term Aging of Asphalt Mixtures for Performance Testing and Prediction*. NCHRP Report No. 973. Washington, DC: Transportation Research Board.

33. Elwardany, M. D., F. Y. Rad, C. Castorena, and Y. R. Kim. 2017. “Factors Affecting Oxidation Reaction Mechanisms in Asphalt Concrete.” Report 17-05969. Presented at the *96th Annual Meeting of the Transportation Research Board*. Washington, DC: Transportation Research Board.

34. Yousefi, R. F., M. D. Elwardany, C. Castorena, and Y. R. Kim. 2017. “Investigation of Proper Long-Term Laboratory Aging Temperature for Performance Testing of Asphalt Concrete.” *Construction and Building Materials* 147: 616–629.

35. Saleh, N. F., B. Keshavarzi, F. Y. Rad, D. Mocelin, M. Elwardany, C. Castorena, B. S. Underwood, and Y. R. Kim. 2020. “Effects of Aging on Asphalt Mixture Pavement Performance.” *Construction and Building Materials* 258: 120309.

36. Marasteanu, M., A. Zofka, M. Turos, X. Li, R. Velasquez, W. Buttlar, G. Paulino, A. Braham, E. Dave, J. Ojo, H. Bahia, C. Williams, J. Bausano, A. Gallistel, and J. McGraw. 2007. *Investigation of Low Temperature Cracking in Asphalt Pavements-Phase II National Pooled Fund Study 776 Phase I*. Report No. MN/RC 2012-23. St. Paul, MN: Minnesota Department of Transportation Research Services.

37. Alavi, M. Z. 2014. “Comprehensive Methodologies for Analysis of Thermal Cracking in Asphalt Concrete Pavements” Ph.D. dissertation, University of Nevada, Reno.

38. Hass, R., F. Meyer, G. Assaf, and H. Lee. 1987. “A Comprehensive Study of Cold Climate Airport Pavement Cracking.” *Journal of the Association of Asphalt Paving Technologists* 56: 198–245.

39. Hiltunen, D. R., and R. Roque. 1994. “A Mechanics-Based Prediction Model for Thermal Cracking of Asphaltic Concrete Pavements.” *Journal of the Association of Asphalt Paving Technologists* 63: 81–117.

40. Olidis, C., and D. Hein. 2003. *Guide for Mechanistic-Empirical Design of New and Rehabilitated Pavement Structure Appendix HH: Field Calibration of Thermal Cracking Model*. Washington DC: National Cooperative Highway Research Program.

41. Nam, K., and H. U. Bahia. 2004. “Effect of Binder and Mixture Variables on Glass Transition Behavior of Asphalt Mixtures.” *Journal of the Association of Asphalt Paving Technologists* 73: 89–120.

42. Nam, K., and H. U. Bahia. 2009. “Effect of Modification on Fracture Failure and Thermal-Volumetric Properties of Asphalt Binders.” *Journal of Materials in Civil Engineering* 21, no. 5: 198–209.

43. Marasteanu, M. K., H. Moon, E. Z. Teshale, A. C. Falchetto, M. Turos, W. Buttlar, E. Dave, G. Paulino, S. Ahmed, S. Leon, H. Bahia, A. Arshadi, H. Tabatabaee, J. Ojo, R. Velasquez, S. Mangiafico, C. Williams, and A. Buss. 2012. *Investigation of Low Temperature Cracking in Asphalt Pavements National Pooled Fund Study-Phase III*. Final Report. St. Paul, MN: Minnesota Department of Transportation.

44. Kim, S. S., A. Wargo, and D. Powers. 2010. “Asphalt Concrete Cracking Device to Evaluate Low Temperature Performance of HMA.” *Journal of the Association of Asphalt Pavement Technologists* 79: 157–188.

45. Bahia, H., H. Tabatabaee, and R. Velasquez. 2012. “Asphalt Thermal Cracking Analyser (ATCA).” In *7th RILEM International Conference on Cracking in Pavements: Mechanisms*, eds. A. Scarpas, N. Kringos, I. Al-Qadi, A. Loizos, 147–156. New York, NY: Springer.

46. Islam, M. R., and R. A. Tarefder. 2014. “Determining Thermal Properties of Asphalt Concrete Using Field Data and Laboratory Testing.” *Construction and Building Materials* 67, part B: 297–306. https://doi.org/10.1016/j.conbuildmat.2014.03.040, last accessed June 6, 2023.

47. Stoffels, S. M., and F. D. Kwanda. 1996. “Determination of the Coefficient of Thermal Contraction of Asphalt Concrete Using the Resistance Strain Gage Technique.” *Asphalt Paving Technology: Association of Asphalt Paving Technologists—Proceedings of the Technical Sessions* 65: 73–98.

48. Mehta, Y. A., D. W. Christensen, and S. M. Stoffels. 1999. “Determination of Coefficient of Thermal Contraction of Asphalt Concrete Using Indirect Tensile Test.” *Journal of the Association of Asphalt Pavement Technologists* 68: 349–368.

49. Zeng, M., and D. H. Shields. 1999. “Nonlinear Thermal Expansion and Contraction of Asphalt Concrete.” *Canadian Journal of Civil Engineering* 26, no. 1: 26–34. https://doi.org/10.1139/l98-041, last accessed June 6, 2023.

50. Bahia, H. U., and D. A. Anderson. 1993. “Glass Transition Behavior and Physical Hardening of Asphalt Binders.” *Proceedings of the Association of Asphalt Paving Technologists* 62: 93–129.

51. Mansourkhaki, A., M. Ameri, M. Habibpour, and B. S. Underwood. 2020. “Relations Between Colloidal Indices and Low-Temperature Properties of Reclaimed Binder Modified with Soft Binder, Oil-Rejuvenator and Polybutadiene Rubber.” *Construction and Building Materials* 239: 117800. https://doi.org/10.1016/j.conbuildmat.2019.117800, last accessed June 6, 2023.

52. Mansourkhaki, A., M. Ameri, M. Habibpour, and D. Daryaee. 2020. “The Effect of Polybutadiene Rubber (PBR) on Chemical and Theological Properties of the Binder Including RAP.” *Construction and Building Materials* 244: 118320. https://doi.org/10.1016/j.conbuildmat.2020.118320, last accessed June 6, 2023.

53. Alavi, M. Z., E. Y. Bahia, and P. E. Sebaaly. 2015. “A Comprehensive Model for Predicting Thermal Cracking Events in Asphalt Pavements.” *International Journal of Pavement Engineering* 18, no. 9: 871–885. https://doi.org/10.1080/10298436.2015.1066010, last accessed June 6, 2023.

54. Sakhaiefar, M., B. S. Underwood, S. R. Ranjithan, Y. R. Kim, and N. Jackson. 2009. “Application of Artificial Neural Networks for Estimating Dynamic Modulus of Asphalt Concrete.” *Transportation Research Record* 2127: 173–186. https://doi.org/10.3141/2127-20, last accessed June 6, 2023.

55. Akentuna, M. 2017. “Laboratory Investigation of Low-Temperature Performance of Asphalt Mixtures.” Ph.D. dissertation. Ohio University.

56. Jones, M. I., and G. L. Darter. 1968. “Thermal Expansion-Contraction of Asphaltic Concrete,” *Journal of the Association of Asphalt Pavement Technologists* 37: 56–97.

57. Lytton, R. L., D. E. Pugahl, C. H. Michalak, H. S. Liang, and B. J. Dempsey. 1993. *An Integrated Model of the Climatic Effects on Pavements*. Washington, DC: Federal Highway Administration.

58. Kennedy, T. W., and R. J. Cominsky. 1990. *The SHRP Asphalt Research Program: 1990 Strategic Planning Document.* Washington, DC: Strategic Highway Research Program National Research Council.

59. Christensen, D. W., and R. Bonaquist. 2003. “Ternary Property Maps for Asphalt Concrete.” *Journal of the Association of Asphalt Pavement Technologists* 72: 38–73.

60. Alavi, M. Z., N. E. Morian, E. Y. Hajj, and P.E. Sebaaly. 2015. “Influence of Asphalt Binder Oxidative Aging on Critical Thermal Cracking characteristic of Asphalt Mixtures.” *Journal of the Association of Asphalt Paving Technologies* 84: 115–142.

61. Teymourpour, P., and H. U. Bahia. 2014. “Effects of Binder Modification on Aggregate Structure and Thermo Volumetric Properties of Asphalt Mixtures.” *Transportation Research Record* 2445, no. 1: 21–28. https://doi.org/10.3141%2F2445-03, last accessed June 6, 2023.

62. Sefidmazgi, N. R., L. Tashman, and H. Bahia. 2012. “Internal Structure Characterization of Asphalt Mixtures for Rutting Performance Using Imaging Analysis.” *Road Materials and Pavement Design* 13, no. 1: 21–37. https://doi.org/10.1080/14680629.2012.657045, last accessed June 6, 2023.

63. Christensen, D. W., and R. Bonaquist. 2015. “Improved Hirsch Model for Estimating the Modulus of Hot Mix Asphalt.” *Road Materials and Pavement Design* 16, no. 2: 254–274. https://doi.org/10.1080/14680629.2015.1077635, last accessed June 6, 2023.

64. Minnesota Department of Transportation. 2021. “MnROAD Test Cells” (web page). https://perma.cc/FHX6-LQBR, last accessed June 6, 2023.

65. Keshavarzi, B., D. Mocelin, and Y. R. Kim. 2021. “A Composite Model for Predicting the Coefficient of Thermal Contraction (CTC) of Asphalt Concrete Mixtures.” *Journal of Testing and Evaluation* 50, no. 1.

66. MTS®. “Materials Testing” (web page). https://www.mts.com/en/industries/materials, last accessed September 15, 2023.

67. Castorena, C., Y. R. Kim, S. Pape, and K. Lee. 2017. *Development of Small Specimen Geometry for Asphalt Mixture Performance Testing*. NCHRP IDEA N181 Final Report. Washington, DC: Transportation Research Board.

68. National Instruments™. 2023. *National Instruments™ LabView* (software).

69. MathWorks®. 2022. MathWorks® *MATLAB® Nonlinear Curve Fitting Toolbox™* (software).

70. FHWA. *Portland Cement Concrete Pavements Research: Thermal Coefficient of Portland Cement Concrete*. Report. Washington, DC: Federal Highway Administration. https://www.fhwa.dot.gov/publications/research/infrastructure/pavements/pccp/thermal.cfm, last accessed June 6, 2023.

71. Daniel, J. S., T. Bennert, Y. R. Kim, W. Mogawer, and D. Mensching. 2015. *Evaluation of Plant Produced RAP Mixtures in the Northeast Phase III Report*. Report No. TPF5-230. Washington, DC: Federal Highway Administration.

72. Sabouri, M., T. Bennert, J. S. Daniel, and Y. R. Kim. 2015. "A Comprehensive Evaluation of the Fatigue Behavior of Plant-Produced RAP Mixtures." *Road Materials and Pavement Design* 16, sup no. 2: 29–54. https://doi.org/10.1080/14680629.2015.1076997, last accessed June 6, 2023.

73. Daniel, J. S., T. Bennert, Y. R. Kim, W. Mogawer, A. Congalton, D. Mensching, M. Sabouri, and M. Elwardany. 2014. *Evaluation of Plant Produced RAP Mixtures in the Northeast Phase I Interim Report*. Report no. TPF5-230. Washington, DC: Federal Highway Administration.

74. Olard, F., and H. Di Benedetto. 2003. "General 2S2P1D Model and Relation between the Linear Viscoelastic Behaviours of Bituminous Binders and Mixes." *Road Materials and Pavement Design* 4, no. 2: 185–224. https://doi.org/10.1080/14680629.2003.9689946, last accessed June 6, 2023.

75. Underwood, B. S., and Y. R. Kim. 2011. "Experimental Investigation into the Multiscale Behaviour of Asphalt Concrete." *International Journal of Pavement Engineering* 12, no. 4: 357–370. https://doi.org/10.1080/10298436.2011.574136, last accessed June 6, 2023.

76. Houston, W. N., and C. E. Zapata. 2008. *Calibration and Validation of the Enhanced Integrated Climatic Model for Pavement Design*. NCHRP Report No. 602. Washington, DC: Transportation Research Board.

77. Alavi, M. Z., E. Y. Hajj, and P. E. Sebaaly. 2016. "Significance of Oxidative Aging on the Thermal Cracking Predictions in Asphalt Concrete Pavements." In *8th RILEM International Conference on Mechanisms of Cracking and Debonding in Pavements: Material Crack Characterization*, eds. Chabot, A., W. G. Buttlar, E. V. Dave, C. Petit, G. Tebaldi, 127–132. New York, NY: Springer.

78. Jung, D. H., and T. S. Vinson. 1994. *Low-Temperature Cracking: Test Selection.* Report no. SHRP-A-400. Washington, DC: Strategic Highway Research Program.

79. Chehab, G. R., and Y. R. Kim. 2005. "Viscoelastoplastic Continuum Damage Model Application to Thermal Cracking of Asphalt Concrete." *Journal of Materials in Civil Engineering* 17, no. 4: 384–392.

80. Morian, N. E. 2014. "Influence of Mixture Characteristics on the Oxidative Aging of Asphalt Binders." Ph.D. dissertation. University of Nevada, Reno.

81. Cortez, E., E. Y. Hajj, P. E. Sebaaly, and M. Z. Alavi. 2011. "Investigating Low-Temperature Properties of Cylindrical Superpave Gyratory-Compacted Asphalt Concrete Specimens Using the Thermal Stress-Restrained Specimen Test." Presented at the *90th Annual Meeting of the Transportation Research Board*. Washington, DC: Transportation Research Board.

82. Keshavarzi, B., and Y. R. Kim. 2020. "A Dissipated Pseudo Strain Energy-Based Failure Criterion for Thermal Cracking and Its Verification Using Thermal Stress Restrained Specimen Tests." *Journal of Construction and Building Materials* 223: 117199.

83. Wang, Y. D., B. Keshavarzi, and Y. R. Kim. 2018. “Fatigue Performance Prediction of Asphalt Pavements with FlexPAVE^{TM}, the S-VECD Model, and D^R Failure Criterion.” *Transportation Research Record* 2672, no. 40: 217–227.

84. Wang, Y. D., B. Keshavarzi, and Y. R. Kim. 2018. “Fatigue Performance Analysis of Pavements with RAP Using Viscoelastic Continuum Damage Theory.” *KSCE Journal of Civil Engineering* 22, no. 6: 2118–2125.

85. Elwardany, M. D., F. Y. Rad, C. Castorena, and Y. R. Kim. 2018. “Evaluation of Asphalt Mixture Laboratory Long-Term Aging Methods for Performance Testing and Prediction.” *Road Materials and Pavement Design* 18, no. 1: 28–61.

86. Rowe, G., and M. Sharrock. 2011. “Alternate Shift Factor Relationship for Describing Temperature Dependency of Viscoelastic Behavior of Asphalt Materials.” *Transportation Research Record* 2207, no. 1: 125–135.

87. Majidifard, H., N. Tabatabaee, and W. Buttlar. 2019. “Investigation of Short-Term and Long-Term Binder Performance of High-RAP Mixtures Containing Waste Cooking Oil.” *Journal of Traffic and Transportation Engineering (English Edition)* 6, no. 4: 396–406. https://doi.org/10.1016/j.jtte.2018.11.002, last accessed June 6, 2023.

88. Witczak, M., and O. Fonseca. 1996. “Revised Predictive Model for Dynamic (Complex) Modulus of Asphalt Mixtures.” *Transportation Research Record* 1540, no. 1: 15–23.

89. AASHTO. 2019. *Standard Method of Test for Determining the Dynamic Modulus for Asphalt Mixtures Using Small Specimens in the Asphalt Mixture Performance Tester (AMPT)*. TP 132. Washington, DC: AASHTO.

90. AASHTO. 2019. *Standard Practice for Preparation of Small Cylindrical Performance Test Specimens Using the Superpave Gyratory Compactor (SGC) or Field Cores*. PP 99. Washington, DC: AASHTO.

91. Underwood, B. S., Y. R. Kim, and M. Guddati. 2010. “Improved Calculation Method of Damage Parameter in Viscoelastic Continuum Damage Model.” *International Journal of Pavement Engineering* 11, no. 6: 459–476.

92. Schapery, R. A. 1987. “Deformation and Fracture Characterization of Inelastic Composite Materials Using Potentials.” *Polymer Engineering and Science* 27, no. 1: 63–75.

93. AASHTO. 2019. *Standard Method of Test for Determining the Damage Characteristic Curve and Failure Criterion Using Small Specimens in the Asphalt Mixture Performance Tester (AMPT) Cyclic Fatigue Test*. TP 133. Washington, DC: AASHTO.

94. Keshavarzi, B., D. Mocelin, and Y. R. Kim. 2021. “Predicting Thermal Stress Restrained Specimen Test (TSRST) Fracture Temperatures Using the Dissipated Pseudo Strain Energy Criterion.” *ASCE Journal of Transportation Engineering* 147, no. 1.

95. Fromm, H. J., and W. A. Hang. 1972. “A Study of Transverse Cracking of Bituminous Pavements, Proceedings of the Association of Asphalt Paving Technologists.” *Association of Asphalt Paving Technologists Proceedings* 41: 383-423.

96. Buttlar, W. G., R. Roque, and D. R. Hiltunen. 2008. “Prediction of Thermal Cracking with TCMODEL.” In *Modeling of Asphalt Concrete*, ed. Y. R. Kim, 405–425. Reston, VA: American Society of Civil Engineers.

97. Dave, E. V., W. G. Buttlar, S. E. Leon, B. Behnia, and G. H. Paulino. 2013. “IlliTC -Low-Temperature Cracking Model for Asphalt Pavements.” *Road Materials and Pavement Design* 14, no. S2: 57–78.

98. Roque, R., W. G. Buttlar, B. E. Ruth, M. Tia, W. Dickison, and B. Reid. 1997. *Evaluation of SHRP Indirect Tension Tester to Mitigate Cracking in Asphalt Concrete Pavements and Overlays*. Report No. WPI 0510755. Gainesville, FL: University of Florida.

99. Kim, Y. R., and H. Wen. 2002. “Fracture Energy from Indirect Tension Testing.” *Journal of the Association of Asphalt Paving Technologists* 71: 779–793.

100. Zhou, F., S. Hu, D. H. Chen, and T. Scullion. 2007. “Overlay Tester: Simple Performance Test for Fatigue Cracking.” *Transportation Research Record* 2001, no. 1: 1–8.

101. Walubita, L. F., A. N. Faruk, G. Das, H. A. Tanvir, and T. Scullion. 2013. “The Overlay Tester (OT): Using the Fracture Energy Index Concept to Analyze the OT Monotonic Loading Test Data.” *Construction and Building Materials* 40: 802–811.

102. Wu, Z., L. Mohammad, L. Wang, and M. Mull. 2005. “Fracture Resistance Characterization of Superpave Mixtures Using the Semi-Circular Bending Test.” *Journal of ASTM International* 2, no. 3: 129–143.

103. Kim, M., L. Mohammad, and M. A. Elseifi. 2012. “Characterization of Fracture Properties of Asphalt Mixtures as Measured by the Semi-Circular Bend Test and Indirect Tension Test.” *Transportation Research Record* 2296, no. 1: 115–124.

104. Ozer, H., I. L. Al-Qadi, J. Lambros, A. El-Khatib, P. Singhvi, and B. Doll. 2016. “Development of Fracture-Based Flexibility Index for Asphalt Cracking Potential Using Modified Semi-Circle Bending Test Parameters.” *Construction and Building Materials* 115: 390–401.

105. Ozer, H., I. L. Al-Qadi, P. Singhvi, T. Khan, J. Rivera-Perez, and A. El-Khatib. 2016. “Fracture Characterization of Asphalt Mixtures with RAP and RAS Using the Illinois Semi-Circular Bending Test Method and Flexibility Index.” *Transportation Research Record* 2575, no. 1: 130–137.

106. Underwood, B. S., C. Baek, and Y. R. Kim. 2012. “Simplified Viscoelastic Continuum Damage Model as Platform for Asphalt Concrete Fatigue Analysis.” *Transportation Research Record* 2296, no. 1: 35–45.

107. Kim, Y. R., M. N. Guddati, Y. Choi, D. Kim, A. Norouzi, Y. D. Wang, B. Keshavarzi, M. Ashouri, A. Ghanbari, A. D. Wargo, and B. S. Underwood. 2022. *Hot-Mix Asphalt Performance Related Specification Based on Viscoelastoplastic Continuum Damage (VEPCD) Model*. Final Report for FHWA Project-DTFH61-08-H-00005. Report No. FHWA-HRT-21-093. Washington, DC: Federal Highway Administration.

108. Schapery, R. A. 1984. "Correspondence Principles and a Generalized J-Integral for Large Deformation and Fracture Analysis of Viscoelastic Media." *International Journal of Fracture* 25: 195–223.

109. Kim, Y. R., and D. N. Little. 1990. "One-Dimensional Constitutive Modeling of Asphalt Concrete." *Journal of Engineering Mechanics* 116, no. 4: 751–772.

110. Wang, Y., and Y. R. Kim. 2017. "Development of a Pseudo Strain Energy-Based Fatigue Failure Criterion for Asphalt Mixtures." *International Journal of Pavement Engineering* 20, no. 10: 1182–1192. https://doi.org/10.1080/10298436.2017.1394100, last accessed June 6, 2023.

111. Cao, W., L. N. Mohammad, M. Elseifi, S. B. Cooper, and S. Saadeh. 2018. "Fatigue Performance Prediction of Asphalt Pavement Based on Semicircular Bending Test at Intermediate Temperature." *Journal of Materials in Civil Engineering* 30, no. 9.

112. Ozer, H., I. L. Al-Qadi, P. Singhvi, J. Bausano, R. Carvalho, X. Li, and N. Gibson. 2018. "Prediction of Pavement Fatigue Cracking at an Accelerated Testing Section Using Asphalt Mixture Performance Tests." *International Journal of Pavement Engineering* 19, no. 3: 264–278.

113. AASHTO. 2017. *Standard Method of Test for Determining the Dynamic Modulus and Flow Number for Asphalt Mixtures Using the Asphalt Mixture Performance Tester (AMPT)*. T 378. Washington, DC: AASHTO.

114. AASHTO. 2018. *Standard Method of Test for Determining the Damage Characteristic Curve and Failure Criterion Using the Asphalt Mixture Performance Tester (AMPT) Cyclic Fatigue*. TP 107. Washington, DC: AASHTO.

115. Wang, Y. D., B. S. Underwood, and Y. R. Kim. 2020. "Development of Fatigue Index Parameter, Sapp, for Asphalt Mixes Using Viscoelastic Continuum Damage Theory." *International Journal of Pavement Engineering* 23, no. 2: 438–452. https://doi.org/10.1080/10298436.2020.1751844, last accessed June 6, 2023.

116. West, R., D. Timm, R. Willis, B. Powell, N. Tran, D. Watson, M. Sakhaeifar, R. Brown, M. Robbins, A. Vargas-Nordcbeck, F. L. Villacorta, X. Guo, and J. Nelson. 2012. *Phase IV NCAT Pavement Test Track Findings*. Report No. 12-10. Auburn, AL: National Center for Asphalt Technology.

117. Sabouri, M., T. Bennert, J. S. Daniel, and Y. R. Kim. 2015. "Fatigue and Rutting Evaluation of Laboratory-Produced Asphalt Mixtures Containing Reclaimed Asphalt Pavement." *Transportation Research Record* 2506, no. 1: 32–44.

118. Jeong, J., Y. D. Wang, A. Ghanbari, C. Nash, D. Nener-Plante, B. S. Underwood, and Y. R. Kim. 2020. “Pavement Performance Predictions Using Performance-Volumetric Relationship and Evaluation of Construction Variability: Example of MaineDOT Shadow Project for the Development of Performance-Related Specifications.” *Construction and Building Materials* 263: 120150.

119. Guo, X. 2013. “Local Calibration of the MEPDG Using Test Track Data.” Master’s thesis. Auburn University.

120. Ingevity™. 2023. “Ingevity™ Evotherm®” (web page). https://www.ingevity.com/products/evotherm/, last accessed June 3, 2023.

121. Li, X., and N. Gibson. 2016. “Comparison of Laboratory Fatigue Characteristics with Full-Scale Pavement Cracking for Recycled and Warm-Mix Asphalts.” *Transportation Research Record* 2576, no. 1: 100–118.

122. Wang, Y. D., A. Ghanbari, B. S. Underwood, and Y. R. Kim. 2019. “Development of a Performance-Volumetric Relationship for Asphalt Mixtures.” *Transportation Research Record* 2674, no. 6: 416–430. https://doi.org/10.1177/0361198119845364, last accessed June 6, 2023.

123. Vavrik, W. R., G. Huber, W. J. Pine, and S. H. Carpenter. 2002. “Bailey Method for Gradation Selection in Hot-Mix Asphalt Mixture Design.” *Transportation Research Circular* E-C044: ISSN 0097-8515. Washington, DC: Transportation Research Board of the National Academies. http://onlinepubs.trb.org/onlinepubs/circulars/ec044.pdf, last accessed January 15, 2014.

124. Eslaminia, M., S. Thirunavukkarasu, M. N. Guddati, and Y. R. Kim. 2012. “Accelerated Pavement Performance Modeling Using Layered Viscoelastic Analysis.” In *7th RILEM International Conference on Cracking in Pavements*, eds. A. Scarpas, N. Kringos, I. Al-Qadi, and A. Loizos, 20–22. New York, NY: Springer.

125. FHWA. 2021. “Pavement Testing Facility Overview” (web page). https://highways.dot.gov/laboratories/pavement-testing-laboratory/pavement-testing-facility-overview, last accessed June 6, 2023.

126. Gibson, N., X. Qi, A. Shenoy, G. Al-Khateeb, M. Kutay, A. Andriescu, K. Stuart, J. Youtcheff, and T. Harman. 2012. *Performing Testing for Superpave and Structural Validation*. Report No. FHWA-RT-11-045. Washington, DC: Federal Highway Administration.

127. AASHTO. 2022. *Standard Method of Test for Resistance to Plastic Flow of Asphalt Mixtures Using Marshall Apparatus*. TP 245. Washington, DC: AASHTO.

128. AASHTO. 2022. *Standard Method of Test for Determining the Permanent Shear Strain and Stiffness of Asphalt Mixtures Using the Superpave Shear Tester (SST)*. T 320. Washington, DC: AASHTO.

129. AASHTO. 2022. *Standard Method of Test for Hamburg Wheel-Track Testing of Compacted Asphalt Mixtures*. T 324. Washington, DC: AASHTO.

130. European Committee for Standardization (CEN). 2020. *EN 12697-22 Bituminous Mixtures—Test METHODS—Part 22: Wheel tracking*. Brussels, Belgium: CEN.

131. AASHTO. 2010. *Standard Method of Test for Determining Rutting Susceptibility of Hot Mix Asphalt (HMA) Using the Asphalt Pavement Analyzer (APA)*. T 340. Washington, DC: AASHTO.

132. AASHTO. 2022. *Standard Method of Test for Rutting and Fatigue Resistance of Asphalt Mixtures Using Incremental Repeated Load Permanent Deformation (iRLPD)*. TP 116. Washington, DC: AASHTO.

133. Jahangiri, B., H. Majidifard, J. Meister, and W. G. Buttlar. 2019. "Performance Evaluation of Asphalt Mixtures With Reclaimed Asphalt Pavement and Recycled Asphalt Shingles in Missouri." *Transportation Research Record* 2673, no. 2: 392–403.

134. Witczak, M., C. Schwartz, and H. Von Quintus. 2001. *Superpave Support and Performance Models Management*. Interim Report no. NCHRP Project 9-19. Washington, DC: National Cooperative Highway Research Program.

135. Choi, Y. T., V. Subramanian, M. N. Guddati, and Y. R. Kim. 2012. "Incremental model for prediction of permanent deformation of asphalt concrete in compression." *Transportation Research Record* 2296, no. 1: 24–35.

136. Subramanian, V., M. N. Guddati, and Y. R. Kim. 2013. "A Viscoplastic Model for Rate-Dependent Hardening for Asphalt Concrete in Compression." *Mechanics of Materials* 59: 142–159.

137. AASHTO. 2022. *Standard Method of Test for Bulk Specific Gravity (Gmb) of Compacted Asphalt Mixtures Using Saturated Surface-Dry Specimens*. T 166. Washington, DC: AASHTO.

138. Ghanbari, A., B. S. Underwood, and Y. R. Kim 2020. "Development of a Rutting Index Parameter Based on the Stress Sweep Rutting Test and Permanent Deformation Shift Model." *International Journal of Pavement Engineering* 23, no. 2: 1–13. https://doi.org/10.1080/10298436.2020.1748190, last accessed June 6, 2023.

139. Witczak, M. W., and M. M. El-Basyouny. 2004. "Calibration of Permanent Deformation Models for Flexible Pavements." In *Guide for Mechanistic–Empirical Design of New and Rehabilitated Pavement Structures*, App. gg-1. Champaign, IL: ARA, ERES Division.

140. Kim, Y. R., C. Castorena, Y. Wang, A. Ghanbari, and J Jeong. 2018. *Comparing Performance of Full-Depth Asphalt Pavements and Aggregate Base Pavements in NC*. Report no. HWY-2015-02. Raleigh, NC: NC Department of Transportation.

141. Sreedhar, S., and E. Coleri. 2018. “Effects of binder content, density, gradation, and polymer modification on cracking and rutting resistance of asphalt mixtures used in Oregon.” *Journal of Materials in Civil Engineering* 30, no. 11: 04018298.

142. Mogawer, W., T. Bennert, J. S. Daniel, R. Bonaquist, A. Austerman, and A. Booshehrian. 2012. “Performance Characteristics of Plant-Produced High RAP Mixtures.” *Road Materials and Pavement Design* 13, no. 1: 183–208.

143. Buttlar, W. G., J. Meister, B. Jahangiri, H. Majidifard, and P. Rath. 2018. *Performance Characteristics of Modern Recycled Asphalt Mixes in Missouri, Including Ground Tire Rubber, Recycled Roofing Shingles, and Rejuvenators*. Report No. cmr 19-002, 68–77. Jefferson City, MO: Missouri Department of Transportation.

144. Microsoft®. 2023. *Microsoft® Visual Basic for Applications®* (software).

145. Bonaquist, R. 2008. *Ruggedness Testing of the Dynamic Modulus and Flow Number Tests with the Simple Performance Tester*. NCHRP Report No. 629. Washington, DC: Transportation Research Board. https://doi.org/10.17226/14200, last accessed September 15, 2023.

146. Kim, D., and Y. R. Kim. 2017. “Development of Stress Sweep Rutting (SSR) Test for Permanent Deformation Characterization of Asphalt Mixture.” *Construction and Building Materials* 154: 373–383.

147. Eslaminia, M., and M. N. Guddati. 2016. “Fourier-Finite Element Analysis of Pavements Under Moving Vehicular Loading.” *International Journal of Pavement Engineering* 17, no. 7: 602–614.

148. Rahbar-Rastegar, R., J. S. Daniel, and G. Reinke. 2017. “Comparison of Asphalt Binder and Mixture Cracking Parameters.” *Road Materials and Pavement Design* 18, no. 4: 211–233.

149. Wang, Y. D., A. Norouzi, and Y. R. Kim. 2016. “Comparison of Fatigue Cracking Performance of Asphalt Pavements Predicted by Pavement ME and LVECD Programs.” *Transportation Research Record* 2590, no. 1: 44–55.

150. Wang, Y., B. Keshavarzi, and Y. R. Kim. 2018. “Fatigue Performance Predictions of Asphalt Pavements Using FlexPAVE™ with the S-VECD Model and D^R Failure Criterion.” *Transportation Research Record* 2672, no. 40: 217–227. https://doi.org/10.1177/0361198118756873, last accessed June 6, 2023.

151. Cao, W., A. Norouzi, and Y. R. Kim. 2016. “Application of Viscoelastic Continuum Damage Approach to Predict Fatigue Performance of Binzhou Perpetual Pavements.” *Journal of Traffic and Transportation Engineering* (English Edition) 3, no. 2: 104–115.

152. NCHRP. 2004. *Guide for Mechanistic–Empirical Design of New and Rehabilitated Pavement Structures*. Report No. NCHRP 1-37A. Washington, DC: National Cooperative Highway Research Program.

153. Wang, Y. D., A. Ghanbari, B. S. Underwood, and Y. R. Kim. 2021. "Development of Preliminary Transfer Functions for FlexPAVE™." *Construction and Building Materials* 266, Part B: 121182. https://doi.org/10.1016/j.conbuildmat.2020.121182, last accessed June 6, 2023.

154. Seo, Y. 2010. "Distress Evolution in Highway Flexible Pavements: A 5-Year Study at the Korea Highway Corporation Test Road." *Journal of Testing and Evaluation* 38, no. 1: 1–10.

155. Miller, J. S., and W. Y. Bellinger. 2003. *Design Identification Manual for the Long-Term Pavement Performance Program* (Fourth Revised Edition). Report No. FHWA-RD-03-031. Washington, DC: Federal Highway Administration

156. Jackson, N., and J. Puccinelli. 2006. *Long-Term Pavement Performance (LTPP) Data Analysis Support: National Pooled Fund Study TPF-5(013): Effects of Multiple Freeze Cycles and Deep Frost Penetration on Pavement Performance and Cost*. Report no. FHWA-HRT-06-121. Washington, DC: Federal Highway Administration.

157. West, R., D. Timm, B. Powell, M. Heitzman, N. Tran, C. Rodezno, D. Watson, F. Leiva, and A. Vargas. 2019. *Phase VI (2015-2017) NCAT Test Track Findings*. Report No. 18-04. Auburn, AL: National Center for Asphalt Technology, Auburn University.

158. FHWA. "LTPP InfoPave™" (web page). https://infopave.fhwa.dot.gov/, last accessed September 15, 2023.

159. Intel®. "Intel oneAPI Math Kernel Library (oneMKL)" (web page). https://www.intel.com/content/www/us/en/docs/oneapi/programming-guide/2023-0/intel-oneapi-math-kernel-library-onemkl.html, last accessed September 15, 2023.

160. Eigin. "Eigen 3.4.90 (git rev 67eeba6e720c5745abc77ae6c92ce0a44aa7b7ae)" (web page). https://eigen.tuxfamily.org/dox/, last accessed September 15, 2023.

161. AASHTO. 1991. *Standard Specification for Classification of Soils and Soil–Aggregate Mixtures for Highway Construction Purposes*. M 145. Washington, DC: AASHTO.

162. AASHTO. 2008. *Mechanistic-Empirical Pavement Design Guide, a Manual of Practice*. Publication no. MEPDG-1. Washington, DC: AASHTO.

Recommended citation: Federal Highway Administration, *Development of Balanced Mixture Design Index Parameters and the Flex Suite of Performance Analysis Tools for Asphalt Pavements—Volume I* (Washington, DC: 2024) https://doi.org/10.21949/1521558

HRDI-20/06-24(WEB)E